

BRNO UNIVERSITY OF TECHNOLOGY

Faculty of Electrical Engineering
and Communication

MASTER'S THESIS

Brno, 2021

Bc. Vladimír Bílek



BRNO UNIVERSITY OF TECHNOLOGY

VYSOKÉ UČENÍ TECHNICKÉ V BRNĚ

FACULTY OF ELECTRICAL ENGINEERING AND COMMUNICATION

FAKULTA ELEKTROTECHNIKY
A KOMUNIKAČNÍCH TECHNOLOGIÍ

DEPARTMENT OF POWER ELECTRICAL AND ELECTRONIC ENGINEERING

ÚSTAV VÝKONOVÉ ELEKTROTECHNIKY A ELEKTRONIKY

ELECTROMAGNETIC ANALYSIS AND MODELING OF A SOLID ROTOR INDUCTION MACHINE

ELEKTROMAGNETICKÁ ANALÝZA A MODELOVÁNÍ ASYNCHRONNÍHO STROJE S PLNÝM ROTOREM

MASTER'S THESIS
DIPLOMOVÁ PRÁCE

AUTHOR
AUTOR PRÁCE

Bc. Vladimír Bílek

SUPERVISOR
VEDOUCÍ PRÁCE

Ing. Jan Bárta, Ph.D.

BRNO 2021

Master's Thesis

Master's study program **Power Electrical and Electronic Engineering**

Department of Power Electrical and Electronic Engineering

Student: Bc. Vladimír Bílek

ID: 195658

**Year of
study:** 2

Academic year: 2020/21

TITLE OF THESIS:

Electromagnetic analysis and modeling of a solid rotor induction machine

INSTRUCTION:

1. Review of the state-of-the-art electrical machines with a solid rotor.
2. Describe and evaluate the methodologies of electromagnetic analysis of induction machines with a solid rotor.
3. Create a surrogate model for fast estimation of the parameters of a solid rotor induction machine
4. Optimize a solid rotor induction machine by using a surrogate model.

RECOMMENDED LITERATURE:

- [1] PYRHONEN, J.; JOKINEN t.; HRABOVCOVÁ V. Design of rotating electrical machines. John Wiley and Sons, 2007. ISBN 978-0-470-69516-6.
- [2] J.R. HENDERSHOT, T.J.E. MILLER . Design of Brushless Permanent-Magnet Machines. Motor Design Books LLC; Second Edition edition, 2010. ISBN 978-0984068708.
- [3] A. E. Fitzgerald, Ch. Kingsley, S. Umans "Electric Machinery", McGraw-Hill Companies Inc., 2003. 688 s. ISBN 0-07-112193-5

**Date of project
specification:** 8.2.2021

Deadline for submission: 24.5.2021

Supervisor: Ing. Jan Bárta, Ph.D.

doc. Ing. Ondřej Vítek, Ph.D.
Chair of study program board

WARNING:

The author of the Master's Thesis claims that by creating this thesis he/she did not infringe the rights of third persons and the personal and/or property rights of third persons were not subjected to derogatory treatment. The author is fully aware of the legal consequences of an infringement of provisions as per Section 11 and following of Act No 121/2000 Coll. on copyright and rights related to copyright and on amendments to some other laws (the Copyright Act) in the wording of subsequent directives including the possible criminal consequences as resulting from provisions of Part 2, Chapter VI, Article 4 of Criminal Code 40/2009 Coll.

Abstract

This Master's thesis deals with the electromagnetic analysis and modeling of a solid rotor induction machine. The work includes a state-of-review on the topic of high-speed electrical machines, with the description of their advantages and disadvantages compared to conventional electrical machines with gearboxes, division of high-speed electrical machines with solid rotors, and comparison of their advantages and disadvantages, where the emphasis is placed mainly on high-speed induction machines with solid rotors and their use and applications in industry. Furthermore, the work deals with methods of calculation of electrical induction machines with solid rotors. Thus, methods for analytical calculation and finite element calculation of induction machines with solid rotors are described here. Above all, the emphasis is placed on the finite element method in a 2D space using correction end-effect factors, which are divided and described in detail here. Based on the obtained literature, an electric machine with a solid rotor is calculated using electromagnetic FEM analysis. The calculation of the machine is automatized with Python script. As another main objective of this work is to describe the so called surrogate models, their advantages and disadvantages, their use in industry and especially the application of surrogate models to a electrical machines with a solid rotor. Using surrogate models, the case study machine with a solid rotor is then optimized using SymSpace and Optimizer. For the optimizations, 3 machine designs were considered and eventually compared with each other from an electromagnetic performance point of view.

Keywords

High-speed electrical machine, Induction machine, Electrical machine with a solid rotor, Correction end-effect factor for a solid rotor, FEM, Ansys Maxwell, Python, FreeCAD, Electromagnetic calculation, Electromagnetic analysis, Surrogate model, Surrogate modeling, Optimization, SymSpace, Optimizer

Abstrakt

Tato diplomová práce se zabývá elektromagnetickou analýzou a modelováním asynchronního stroje s plným rotorem. Tato práce tedy zahrnuje literární rešerši na téma vysokootáčkových elektrických strojů s porovnáním s klasickými elektrickými stroji s převodovkou a popisem jejich výhod či nevýhod, rozdělení vysokootáčkových elektrických strojů s plnými rotory a srovnání jejich výhod či nevýhod, kde se tato práce nejvíce soustřeďuje na vysokootáčkové asynchronní stroje s plnými rotory a jejich použití v průmyslu. Dále se tato práce zabývá metodami výpočtu elektrických asynchronních strojů s plnými rotory. Proto jsou zde uvedeny a popsány metody výpočtu stroje mezi které patří analytické metody i metoda konečných prvků. Vzhledem k povaze elektrických strojů s plnými rotory je hlavně kladen důraz v této práci na výpočet stroje pomocí metody konečných prvků ve 2D prostoru s využitím korekčních činitelů konců plných rotorů, které jsou zde velmi detailně popsány a rozděleny. Na základě dostupné literatury je vypočítán elektrický stroj s plným rotorem pomocí MKP analýzy. Elektromagnetický výpočet stroje je automatizován pomocí skriptu vytvořeného v Pythonu. Dalším hlavním cílem této práce je popis tzv. náhradních modelů, uvedení jejich výhod či nevýhod, použití v jiných průmyslových odvětvích a hlavně použití náhradních modelů na elektrický stroj s plným rotorem. S využitím náhradních modelů je dále optimalizovaný vybraný asynchronní stroj s plným rotorem a to pomocí programů SymSpace a Optimizer. Pro samotnou optimalizaci byly uvažovány 3 návrhy stroje, které byly na závěr mezi sebou porovnány a to hlavně z hlediska jejich elektromagnetického výkonu.

Klíčová slova

Vysokootáčkový elektrický stroj, Indukční stroj, Elektrický stroj s plným rotorem, Korekční činitele konců plných rotorů, MKP, Ansys Maxwell, Python, FreeCAD, Elektromagnetický výpočet, Elektromagnetická analýza, Náhradní model, Náhradní modelování, Optimalizace, SymSpace, Optimizer

Rozšířený abstrakt

Tato diplomová práce se zabývá elektromagnetickou analýzou a modelováním asynchronního stroje s plným rotorem. Elektrické stroje s plnými rotory jsou v dnešní době požadovány hlavně v průmyslových aplikacích, kde jsou nutné vyšší otáčky stroje. Důvodem využití právě vysokootáčkových strojů s plnými rotory je jejich robustnost, odolnost vůči vysokým centrifugálním a tahovým silám, dosahuje vysokých obvodových rychlostí rotoru, kompaktnost bez nutnosti použití převodovky, bezúdržbovost a jsou výhodné zejména z ekonomického a ekologického hlediska. Z těchto důvodů jsou elektrické stroje s převodovkou nahrazovány vysokootáčkovými stroji. Díky rozsáhlému výzkumu a vývoje frekvenčních měničů je to možné. Navíc frekvenční měniče v dnešní době dosahují vysokých účinností s mnohem dostupnější cenou než tomu bylo dříve. Elektrické vysokootáčkové stroje s plnými rotory mají navíc tu výhodu, že dosahují lepších elektromagnetických parametrů při vyšších rychlostech.

V první kapitole jsou více popsány výhody a nevýhody vysokootáčkových elektrických s plnými rotory, oproti klasickým elektrickým strojům s převodovkou. Navíc tato práce obsahuje literární rešerši na téma vysokootáčkových elektrických strojů a jejich rozdělení. Mezi tyto typy vysokootáčkových strojů s plnými rotory patří např. indukční stroje, synchronní reluktanční stroje, homopolární stroje a další. Všechny tyto typy vysokootáčkových strojů jsou vypsány s jejich výhodami a nevýhodami, popřípadě vlastnostmi. Dále jsou zde vypsány materiálové požadavky těchto strojů, které by měli být dodrženy pro dosažení nejlepších parametrů stroje. Ze všech vypsanych typů vysokootáčkových strojů, je největší důraz kladen na vysokootáčkový indukční stroj s plným rotorem, který je nejvíce rozšířený, nejlevnější, nejjednodušší na výrobu a dosahuje při vyšších rychlostech dobré elektromagnetické parametry. Pro tento typ stroje byly vypsány a detailně popsány různé typy rotorových konstrukcí. Mezi tyto rotorové konstrukce patří například hladký plný rotor, axiálně drážkovaný plný rotor a další. Nakonec této kapitoly bylo vypsáno několik aplikací a použití vysokootáčkových strojů s plnými rotory v průmyslovém odvětví, mezi které patří např. turbo cirkulátor, plynový kompresor, turbomolekulární čerpadla a další.

Ve druhé kapitole se práce zabývá metodami výpočtu elektrických indukčních strojů s plnými rotory. Jsou zde popsány dvě základní metody výpočtu elektrických strojů: analytická metoda výpočtu a metoda konečných prvků. Pro analytické metody je zde popsáno několik postupů a metodik pro výpočet indukčního stroje s plným rotorem, včetně jejich výhod a nevýhod. V další části je uvedena metoda konečných prvků a její možnosti. Je tu hlavně popsán rozdíl mezi programy využívající metodu konečných prvků pro simulaci elektromagnetického modelu, a to buď ve 2D nebo 3D

prostředí s jejich výhodami a nevýhodami. V rámci použití metody konečných prvků pro výpočet stroje v této práci, se další část zabývá postupy a uskálími 2D simulací pomocí metody konenčných prvků. V rámci těchto simulací jsou uvedeny a podrobně popsány korekční faktory konců pevného rotoru, pro různé typy pevných rotorů, které mají za úkol upravit vodivost materiálu ve 2D modelu. Hlavní korekční faktory jsou mezi sebou porovnány a v určitých případech jsou uvedeny i příklady jejich výpočtu.

Ve třetí kapitole je popsán proces tzv. Náhradního modelování. Jedná se v podstatě o aproximaci závislostí mezi vstupními a výstupními parametry stroje, kdy se vytvoří tzv. náhradní model. Jinými slovy by se náhradní modely daly popsat jako statistické modely, které jsou strojově učeny. Hlavní výhodou této metody je tedy značné zrychlení při optimalizaci návrhu stroje, neboť se v podstatě jedná o rychlé vyhodnocení a predikci možné hodnoty výstupního parametru stroje. Konvenční optimalizace stroje zahrnuje hlavně výpočet stroje pomocí metody konečných prvků, který je značně časově náročnější. V této kapitole je tedy obecně popsána práce s procesem náhradního modelování, jeho výhody či nevýhody, použití ve průmyslu a možné využití i právě na indukční stroje s plnými rotorem.

Ve čtvrté kapitole je uveden stroj pro případovou studii. Uvažovaný stroj byl indukční axiálně drážkovaný s plným rotorem. Stroj je napájeny rovnou ze sítě z důvodu jednoduššího výpočtu pomocí MKP simulací a potencionálně možného měření vyrobeného vzorku. Dále byl zde popsán algoritmus pro výpočet a vyhodnocení simulovaných výsledků. Algoritmus a vyhodnocení výsledků je zprostředkováno pomocí programovacího jazyka Python. Vytvoření geometrie je provedeno v programu FreeCAD, což je open-source program pro tvorbu 2D a 3D modelů či výkresů. Samotná simulace byla provedena v programu Ansys maxwell, kde byla využita 2D tranzientní simulace. Veškeré vlastnosti a důvody výběru programů byly popsány v této kapitole.

V páté kapitole jsou uvedeny a popisány dosažené výsledky všech simulací vybraného stroje. Jsou zde ukázány zejména momentová charakteristika stroje, výkonové charakteristiky v závislosti na elektromagnetické účinnosti, účinníku, fázového proudu a ztrát ve stroji. Nakonec byl pro stroj vybrán pracovní bod, který byl dále použit pro potřeby náhradního modelování stroje.

Šestá kapitola ukazuje přímou implementaci náhradního modelu na vybraný indukční stroj. Tato operace se sestává z několika kroků, kde první krok byl určení celkový počet všech vstupních parametrů stroje. Druhý krok je pak citlivostní analýza stroje s využitím určených vstupních parametrů stroje, která slouží pro zjištění možného dalšího zlepšení výkonu stroje a hlavně pro zjištění charakteristik mezi vstupními a

výstupními parametry stroje. Po tom následuje vybrání vhodného vzorkovacího schématu, který slouží jak podklad pro výpočet počátečních dat pro učení náhradních modelů. Posledním krokem je určení správné aproximační funkce jako základ pro náhraní model. Pro vybraný typ stroje byla vybrána jako aproximační funkce radiální bázová funkce. Po vytvoření náhradního modelu práce ukazuje jejich přesnost a zda-li jsou náhradní modely vhodné pro vybraný typ stroje.

Sedmá kapitola pojednává o optimalizaci návrhu stroje s využitím náhradních modelů. Optimalizace návrhu stroje byla provedena pomocí programů SymSpace a Optimizer. V této kapitole jsou tedy uvedeny postupy optimalizace stroje, vybrání vhodného optimalizačního algoritmu, požadavky pro optimalizovaný stroj během optimalizace a také aktivní učení náhradních modelů.

V osmé a poslední kapitole jsou uvedeny elektromagnetické analýzy optimalizovaných návrhů stroje. Proces elektromagnetické analýzy je stejný jako v paté kapitole. Jsou ale provedeny pro více návrhů stroje, kde jsou všechny návrhy stroje mezi sebou porovnány.

Bibliographic citation:

BÍLEK, Vladimír. Electromagnetic analysis and modeling of a solid rotor induction machine. Brno, 2021. Available also at: <https://www.vutbr.cz/studenti/zav-prace/detail/133105>. Master's Thesis. Vysoké učení technické v Brně, Fakulta elektrotechniky a komunikačních technologií, Department of Power Electrical and Electronic Engineering. Supervisor Jan Bárta.

Bibliografické citace:

BÍLEK, Vladimír. Elektromagnetická analýza a modelování asynchronního stroje s plným rotorem. Brno, 2021. Dostupné také z: <https://www.vutbr.cz/studenti/zav-prace/detail/133105>. Diplomová práce. Vysoké učení technické v Brně, Fakulta elektrotechniky a komunikačních technologií, Ústav výkonové elektrotechniky a elektroniky. Vedoucí práce Jan Bárta.

Declaration

I declare that I have written the Master's thesis titled "Electromagnetic analysis of the solid rotor electrical machine" independently, under the guidance of the advisor and using exclusively the technical references and other sources of information cited in the thesis and listed in the comprehensive bibliography at the end of the thesis.

As the author I furthermore declare that, with respect to the creation of this Master's thesis, I have not infringed any copyright or violated anyone's personal and/or ownership rights. In this context, I am fully aware of the consequences of breaking Regulation §11 of the Copyright Act No. 121/2000 Coll. of the Czech Republic, as amended, and of any breach of rights related to intellectual property or introduced within amendments to relevant Acts such as the Intellectual Property Act or the Criminal Code, Act No. 40/2009 Coll., Section 2., Head VI., Part 4.

Prohlášení

Prohlašuji, že svou diplomovou práci na téma „Elektromagnetická analýza elektrických strojů s plnými rotory“ jsem vypracoval samostatně pod vedením vedoucího diplomové práce a s použitím odborné literatury a dalších informačních zdrojů, které jsou všechny citovány v práci a uvedeny v seznamu literatury na konci práce.

Jako autor uvedené diplomové práce dále prohlašuji, že v souvislosti s vytvořením této diplomové práce jsem neporušil autorská práva třetích osob, zejména jsem nezasáhl nedovoleným způsobem do cizích autorských práv osobnostních a jsem si plně vědom následků porušení ustanovení § 11 a následujících autorského zákona č. 121/2000 Sb., včetně možných trestněprávních důsledků vyplývajících z ustanovení části druhé, hlavy VI. díl 4 Trestního zákoníku č. 40/2009 Sb.

Brno, May 24, 2021

.....
author's signature

Acknowledgement

I am sincerely grateful to my supervisor Ing. Jan Bárta, Ph.D. for professional guidance, consultation, patience, and invaluable suggestions for the work.

I would like to thank Dipl.-Ing. Dr. Gerd Bramerdorfer for providing me with helpful literature and advice during our online meetings. Due to the current situation, I was, unfortunately, unable to do my Master's thesis at the Johannes Kepler University in Linz, as planned. I am therefore grateful to Dr. Gerd Bramerdorfer for at least this collaboration with Johannes Kepler University in Linz.

Poděkování

Děkuji vedoucímu diplomové práce Ing. Janu Bártovi, Phd. za účinnou metodickou, pedagogickou a odbornou pomoc a další cenné rady při zpracování mé diplomové práce.

Chtěl bych dále poděkovat Dipl.-Ing. Dr. Gerdu Bramerdorferovi za poskytnutí literatury a rad během našich online schůzek. Kvůli současné situaci jsem bohužel nemohl vypracovat svou diplomovou práci na Univerzitě Johanneše Keplera v Linci, jak to bylo původně plánováno. Jsem proto vděčný Dr. Gerdu Bramerdorferovi alespoň za tuto spolupráci s Univerzitou Johanneše Keplera v Linci.

Brno, May 24, 2021

.....

author's signature

Contents

List of Figures	1
List of Tables	8
Introduction	11
1 High-speed electrical machines	13
1.1 Introduction and motivation	13
1.2 Division of high-speed electrical machines	15
1.3 Construction of high-speed IM with solid rotors	18
1.3.1 High-speed IM with smooth solid rotor	20
1.3.2 High-speed IM with axially slitted solid rotor	22
1.3.3 High-speed IM with squirrel cage solid rotor	27
1.3.4 High-speed IM with radial rotor surface grooves	29
1.4 Applications of high-speed electrical machines	30
1.4.1 High-speed electrical machines for more electric engines (Automotive/Power Generation)	30
1.4.2 Flywheel energy storage systems applications	31
1.4.3 High-speed spindle applications	31
1.4.4 Turbomolecular pumps applications	32
1.4.5 Gas compressor applications	33
1.4.6 Industrial air compressors and air blowers applications	34
1.4.7 Microturbines applications	34
1.4.8 Naval applications	35
1.4.9 Aerospace applications	35
2 Electromagnetic analysis of high-speed IM with solid rotors and calculation of solid rotor end-effects correction factors	37
2.1 Analytical analysis of high-speed IM with a solid rotors	37
2.2 FEM analysis of high-speed IM with a solid rotors	44
2.3 Finite length of the solid rotor and solid rotor end-effects	45
2.4 Corrective end-effect factors	49
2.4.1 Corrective end-effect factors for a solid rotor	49
2.4.2 Corrective end-effect factors for a smooth solid rotor and copper coating	58
2.4.3 Corrective end-effect factors for a solid rotor with high-conductive end-rings	60

2.4.4	Corrective end-effect factors for a solid rotor with a radial rotor surface grooves.....	61
3	Surrogate modeling	65
3.1	<i>Introduction</i>	65
3.2	<i>Workflow of surrogate modeling</i>	66
3.2.1	Sampling	68
3.2.2	Output evaluations	70
3.2.3	Construction of the surrogate model	70
3.2.4	Active learning	71
3.2.5	Adding new samples	72
3.3	<i>Deployment of surrogate model</i>	72
4	Electromagnetic analysis of the case study IM with a solid rotor	74
4.1	<i>Case study electric machine</i>	74
4.2	<i>Simulation procedure of the analyzed case study electrical machine</i>	76
4.2.1	FreeCAD	78
4.2.2	Ansys Maxwell	79
4.2.3	Python	86
5	Electromagnetic analysis results of the case study IM with a solid rotor	87
6	Creation of surrogate model based on case study IM with a solid rotor	91
6.1	<i>Selection of suitable machine parameters for the surrogate model</i>	91
6.2	<i>Sensitivity analysis of the case study IM with a solid rotor</i>	93
6.3	<i>Design of experiments and output evaluations</i>	100
6.4	<i>Construction of surrogate model</i>	102
7	Optimization of the case study induction machine with a solid rotor using surrogate model and active learning of surrogate model	117
7.1	<i>Selecting a suitable optimization algorithm for a case study machine with a solid rotor</i>	117
7.2	<i>Optimization process of the case studies with a solid rotor</i>	118
7.3	<i>Results of the first optimization of the case study machine with a solid rotor</i>	123
7.4	<i>Results of the second optimization of the case study machine with a solid rotor</i>	136
8	Electromagnetic analysis of optimized designs of case study IM with solid rotors	147
	Conclusion	155
	References	159
	List of symbols and abbreviations	179
	List of Appendices	184

List of Figures

Fig. 1.1	Illustration of a system with electric motor, gearbox and gas compressor unit [2].	13
Fig. 1.2	Illustration of a system with high-speed electrical machine integrated into compressor unit [2].	14
Fig. 1.3	Powers limited by the rotor material yield stress (700 MPa) versus rotational speed [11].	18
Fig. 1.4	Constructions of solid smooth rotor for high-speed IM: (a) simple smooth rotor, (b) smooth rotor with copper end rings and (c) smooth rotor coated with conductive material according to [2], [11] and [23].	21
Fig. 1.5	Constructions of axially slitted solid rotor for high-speed IM: (a) axially slitted rotor, (b) axially slitted rotor where every second slit is deeper, (c) axially slitted rotor with copper end rings and (d) axially slitted rotor coated with conductive/resistive material according to [2].	24
Fig. 1.6	Construction of shielded axially slitted solid rotor for high-speed IM according to [32].	26
Fig. 1.7	Construction of axially slitted solid rotor with skewed slits in radial and axial directions with: (a) normal depth and (b) every second slit is deeper according to [33].	27
Fig. 1.8	An example of constructions of solid rotor with: (a) rectangular open slots with brazed squirrel cage, (b) embedded squirrel cage by isostatic pressure and (c) round embedded copper bars inserted in a solid rotor core with drill holes according to [35].	28
Fig. 1.9	An example of construction of axially slitted solid rotor with radial grooves for high-speed IM according to [43].	29
Fig. 1.10	High-speed electrical machines for the more-electric engine [44].	30
Fig. 1.11	High-speed composite flywheel [44].	31
Fig. 1.12	High-speed 200 W 300000 rpm PCB drilling spindle [44].	32
Fig. 1.13	Cross section of a turbomolecular pump driven by a high-speed motor [44].	33

Fig. 1.14	(Left) Conventional compressor and (right) integrated compressor [44].	34
Fig. 1.15	Typical layout of a micro gas turbine [44].	35
Fig. 2.1	Equivalent electrical circuit for high-speed IM with smooth solid rotor [87].	39
Fig. 2.2	Distribution of relative permeability in: (a) smooth solid rotor and (b) axially slitted solid rotor.	42
Fig. 2.3	Distribution of eddy-current losses in: (a) smooth solid rotor and (b) axially slitted solid rotor.	43
Fig. 2.4	Assumed curved current paths in the solid-rotor with long (left) and short (right) end iron lengths [106].	46
Fig. 2.5	Distribution of current density in: (a) smooth solid rotor and (b) axially slitted solid rotor.	47
Fig. 2.6	Solid rotor induction machine total impedance at the rated operational point (left) and solid rotor impedance consisting of active and end region part [104].	49
Fig. 2.7	Graph comparing classic and modified formula of the Russell's end-effect factor.	54
Fig. 2.8	Assumed curved current path in the solid rotor with very long rotor end region.	54
Fig. 2.9	Sketch of the smooth solid rotor with a copper coating [23].	58
Fig. 2.10	Rotor induced eddy current paths: (a) without copper end-rings, (b) with copper end-rings [22].	61
Fig. 2.11	Detail of distribution of current density in: (a) smooth solid rotor and (b) axially slitted solid rotor.	62
Fig. 2.12	The geometry of the radial grooves on the stator surface according to [22].	62
Fig. 2.13	Air gap flux density variation with its harmonic spectrum.	63
Fig. 3.1	Demonstration of the advantages of the surrogate model over conventional simulations and optimization [111].	65
Fig. 3.2	Diagram of the workflow of surrogate modeling [111].	67
Fig. 3.3	Illustration of simulated function of input and output parameters with approximated surrogate model function.	68
Fig. 3.4	Sampling scheme of: two-parameters Latin hypercube sampling (a) [119] and three-level Box-Behnken sampling (b) [120].	69
Fig. 3.5	Comparison of surrogate model predictions data and simulated data [131].	71

Fig. 3.6	Comparison of the optimization processes for a conventional generational MOEA-based optimization (ConvOpt) and a hybrid optimization run (HybridOpt) that uses surrogate models during the MOEA execution, according to [142] and [143].	73
Fig. 4.1	Sketch of slitted solid rotor construction used for the case study electromagnetic analysis.	75
Fig. 4.2	Algorithm of the whole process of electromagnetic model simulation.	77
Fig. 4.3	The whole initially created geometry of the electrical machine with the axially slitted solid rotor in FreeCAD.	79
Fig. 4.4	B-H curve for stator material - M470-50A.	81
Fig. 4.5	B-H curve for rotor material - Steel 1008.	83
Fig. 4.6	Imported and modified geometry in Ansys maxwell of the axially slitted solid rotor.	84
Fig. 4.7	Created initial mesh for axially slitted solid rotor.	85
Fig. 4.8	Detail of created initial mesh for axially slitted solid rotor.	85
Fig. 5.1	Torque-speed characteristics of the case study IM with an axially slitted solid rotor.	87
Fig. 5.2	Efficiency, Phase current and Power factor vs Output power characteristics of the case study IM with an axially slitted solid rotor.	88
Fig. 5.3	Stator core losses, Rotor losses and Winding losses vs Output power characteristics of the case study IM with an axially slitted solid rotor.	89
Fig. 5.4	Distribution of magnetic flux density in the whole machine for IM with an axially slitted solid rotor.	90
Fig. 6.1	Sketch of all parameters consider for optimization in: (a) cross-section of the machine and (b) solid rotor.	92
Fig. 6.2	Sketch of all parameters consider for optimization in: (a) stator slot and (b) rotor slit.	92
Fig. 6.3	Results of sensitivity analysis for the function of: Torque (a), Output power (b), Electromagnetic efficiency (c), Power factor (d), Torque ripple (e), Phase current (f), Total losses (g), Fundamental component of the flux density in the air-gap (h), Current density (i) and Linear current density of stator slot (j) on normalized value of input variable.	99
Fig. 6.4	Determination of the accuracy of the constructed surrogate models using training and validation data for Torque (a), Power factor (b), Electromagnetic efficiency (c), Torque ripple (d), and Fundamental component of the flux density in the air-gap (e).	106

Fig. 6.5	The dependence of relative torque error of the surrogate models on samples of: Active length of the machine (a), Rotor slit depth (b), Rotor slit width (c), and Number of stator conductors (d).	108
Fig. 6.6	The dependence of relative power factor error of the surrogate model on samples of: Active length of the machine (a), Rotor slit depth (b), Rotor slit width (c), and Number of stator conductors (d).	108
Fig. 6.7	The dependence of relative electromagnetic efficiency error of the surrogate model on samples of: Active length of the machine (a), Rotor slit depth (b), Rotor slit width (c), and Number of stator conductors (d).	109
Fig. 6.8	The dependence of relative torque ripple error of the surrogate model on samples of: Active length of the machine (a), Rotor slit depth (b), Rotor slit width (c), and Number of stator conductors (d).	109
Fig. 6.9	The dependence of relative fundamental component of flux density in the air-gap error of the surrogate model on samples of: Active length of the machine (a), Rotor slit depth (b), Rotor slit width (c), and Number of stator conductors (d).	110
Fig. 6.10	The torque dependence on samples of: Active length of the machine (a), Rotor slit depth (b), Rotor slit width (c), and Number of stator conductors (d) for all values from initial training data.	111
Fig. 6.11	The power factor dependence on samples of: Active length of the machine (a), Rotor slit depth (b), Rotor slit width (c), and Number of stator conductors (d) for all values from initial training data.	112
Fig. 6.12	The electromagnetic efficiency dependence on samples of: Active length of the machine (a), Rotor slit depth (b), Rotor slit width (c), and Number of stator conductors (d) for all values from initial training data.	112
Fig. 6.13	The torque ripple dependence on samples of: Active length of the machine (a), Rotor slit depth (b), Rotor slit width (c), and Number of stator conductors (d) for all values from initial training data.	113
Fig. 6.14	The fundamental component of flux density in the air-gap dependence on samples of: Active length of the machine (a), Rotor slit depth (b), Rotor slit width (c), and Number of stator conductors (d) for all values from initial training data.	113
Fig. 7.1	Demonstration of the SymSpace graphical environment and the created input and output parameters of the calculated case study machine.	120
Fig. 7.2	Block diagram for the process of machine design optimization using surrogate model and its active learning.	122

Fig. 7.3	Initial optimization results for the main optimization objectives of the case study machine without any constraints in Optimizer, displayed in a per unit system.	124
Fig. 7.4	Distribution of input parameters and their number of uses in the Optimizer in the initial optimization without any constraints.	126
Fig. 7.5	The flux density in the air-gap as a function of other output parameters in the initial optimization results of the machine without any constraints in Optimizer.	127
Fig. 7.6	Initial optimization results for the main optimization objectives of the case study machine with defined constraints in Optimizer, displayed in a per unit system.	129
Fig. 7.7	The flux density in the air-gap as a function of other output parameters in the initial optimization results of the machine with defined constraints in Optimizer.	130
Fig. 7.8	Verification of the accuracy of the surrogate models using the results obtained from the initial optimization, where the verification samples are oriented to the highest possible electromagnetic efficiency of the machine for Torque (a), Power factor (b), Electromagnetic efficiency (c), Torque ripple (d), and Fundamental component of the flux density in the air-gap (e).	132
Fig. 7.9	Verification of the accuracy of the surrogate models using the results obtained from the initial optimization, where the verification samples are oriented to the highest possible torque of the machine for Torque (a), Power factor (b), Electromagnetic efficiency (c), Torque ripple (d), and Fundamental component of the flux density in the air-gap (e).	134
Fig. 7.10	Verification of the accuracy of the surrogate models using the results obtained from the initial optimization, where the verification samples are oriented to the lowest price of the machine with respect to the highest torque of the machine for Torque (a), Power factor (b), Electromagnetic efficiency (c), Torque ripple (d), and Fundamental component of the flux density in the air-gap (e).	135
Fig. 7.11	Second optimization results for the main optimization objectives of the case study machine with defined constraints in Optimizer, displayed in a per unit system.	137
Fig. 7.12	The flux density in the air-gap as a function of other output parameters in the second optimization results of the machine with defined constraints in Optimizer.	138

Fig. 7.13	Verification of the accuracy of the surrogate models using the results obtained from the second optimization, where the verification samples are oriented to the highest possible electromagnetic efficiency of the machine for Torque (a), Power factor (b), Electromagnetic efficiency (c), Torque ripple (d), and Fundamental component of the flux density in the air-gap (e).	140
Fig. 7.14	Verification of the accuracy of the surrogate models using the results obtained from the second optimization, where the verification samples are oriented to the highest possible torque of the machine for Torque (a), Power factor (b), Electromagnetic efficiency (c), Torque ripple (d), and Fundamental component of the flux density in the air-gap (e).	141
Fig. 7.15	Verification of the accuracy of the surrogate models using the results obtained from the second optimization, where the verification samples are oriented to the lowest price of the machine with respect to the highest torque of the machine for Torque (a), Power factor (b), Electromagnetic efficiency (c), Torque ripple (d), and Fundamental component of the flux density in the air-gap (e).	142
Fig. 7.16	Comparison of the original machine design (a) with optimized machine designs focusing on: the highest possible electromagnetic efficiency (b), the highest possible torque (c) and the lowest machine price respecting the highest achievable torque (d).	145
Fig. 8.1	Torque-speed characteristics of the original and optimized designs of the IM with an axially slitted solid rotor.	148
Fig. 8.2	Electromagnetic efficiency vs. Output power characteristics of the original and optimized designs of the IM with an axially slitted solid rotor.	148
Fig. 8.3	Phase current vs. Output power characteristics of the original and optimized designs of the IM with an axially slitted solid rotor. . .	149
Fig. 8.4	Power factor vs. Output power characteristics of the original and optimized designs of the IM with an axially slitted solid rotor. . .	150
Fig. 8.5	Stator core losses vs. Output power characteristics of the original and optimized designs of the IM with an axially slitted solid rotor.	151
Fig. 8.6	Rotor losses vs. Output power characteristics of the original and optimized designs of the IM with an axially slitted solid rotor. . .	151
Fig. 8.7	Stator winding losses vs. Output power characteristics of the original and optimized designs of the IM with an axially slitted solid rotor.	152

Fig. 8.8 Distribution of magnetic flux density in the whole machine
with a solid rotor for: Original design (a), Design 2 (b), Design 1 (c),
Design 3 (d). 154

List of Tables

Tabel 1.1	Overview of the properties of electrical machines with gear-box and high-speed electrical machines integrated into system [2]. . .	15
Tabel 1.2	Overview of high-speed electrical machines with their attributes [17].	16
Tabel 1.3	Classification of main material requirements for high-speed induction machines [18].	17
Tabel 1.4	Typical milling applications speed [52].	32
Tabel 4.1	Overview of electric parameters for the case study machine. . .	74
Tabel 4.2	Overview of geometric dimensions and used material for the case study machine.	74
Tabel 5.1	Performance of analyzed case study IM with an axially slitted solid rotor at the selected operating point.	90
Tabel 6.1	Range of limits for normalized values of input parameters of the case study IM with a solid rotor.	94
Tabel 6.2	Narrowed selection of input parameters and their normalized narrowed range of values for the surrogate model of the case study IM with a solid rotor.	101
Tabel 6.3	Determination of the strength of the linear relationship between machine output parameters using Pearson's R coefficient for training data.	114
Tabel 6.4	Determination of the strength of the linear relationship between machine output parameters using Pearson's R coefficient for verification data.	115
Tabel 6.5	Determination of the strength of the linear relationship between machine input and output parameters using Pearson's R coefficient for all data.	115
Tabel 6.6	Determination of the linear relationship between machine input and output parameters using covariance coefficient for all data.	115
Tabel 7.1	Determination of input parameter constraints including their step and possible combinations during optimization.	120

Tabel 7.2	Determination of optimization objectives and output parameter constraints in per unit system for the initial optimization.	121
Tabel 7.3	Naming of machine output parameters, their absolute value and their value in per unit system, in Optimizer.	121
Tabel 7.4	Determination of optimization objectives and output parameter constraints in per unit system for the results of the initial optimization.	128
Tabel 7.5	Limits of machine output parameter values in absolute values obtained from reduced results of the initial optimization in the Optimizer.	128
Tabel 7.6	Errors of the surrogate model results after re-evaluation of the initial optimization results with respect to the highest electromagnetic efficiency of the machine.	132
Tabel 7.7	Errors of the surrogate model results after re-evaluation of the initial optimization results with respect to the highest torque of the machine.	134
Tabel 7.8	Errors of the surrogate model results after re-evaluation of the initial optimization results with respect to the lowest price of the machine considering the highest possible torque of the machine.	135
Tabel 7.9	Limits of machine output parameter values in absolute values obtained from reduced results of the second optimization in the Optimizer.	136
Tabel 7.10	Errors of the surrogate model results after re-evaluation of the second optimization results with respect to the highest electromagnetic efficiency of the machine.	140
Tabel 7.11	Errors of the surrogate model results after re-evaluation of the second optimization results with respect to the highest torque of the machine.	141
Tabel 7.12	Errors of the surrogate model results after re-evaluation of the second optimization results with respect to the lowest price of the machine considering the highest possible torque of the machine.	142
Tabel 7.13	Comparison of input parameters and machine price with the original design and optimized machine designs respecting the highest possible electromagnetic efficiency, the highest possible torque and the lowest machine price with respect to the highest possible torque.	145
Tabel 7.14	Comparison of the evaluated values of the surrogate models with the simulated values of the machine after the optimization considering the highest possible electromagnetic efficiency.	146

Tabel 7.15	Comparison of the evaluated values of the surrogate models with the simulated values of the machine after the optimization considering the highest possible torque.	146
Tabel 7.16	Comparison of the evaluated values of the surrogate models with the simulated values of the machine after the optimization considering the lowest price with the respect to the highest possible torque.	146
Tabel 8.1	Performance of analyzed original and optimized designs of the case study IM with an axially slitted solid rotor at the selected operating point.	152

Introduction

Since the invention of the induction machine by Nikola Tesla in 1888, the induction machine has played a major role in the development of the electrotechnical industry. After this invention, more attention was focused on electrical machines with a solid ferromagnetic rotor. The design problem of such a rotor has been an interesting research topic since the invention of the induction machine. The solid rotor is made of a single piece of ferromagnetic material and is ideal with respect to the fluid dynamical and mechanical performance, with excellent heat resistance. It is also very cheap, easy to manufacture and the ferromagnetic materials are in most cases easily available. However, in most of the early prototypes, the rotor was a simple smooth cylinder, and the power supply used for the machine was a conventional network with lower frequency. Hence, the performance of the solid-rotor induction machine was very poor compared with laminate-rotor squirrel-cage induction machines [1].

In the late 1950s and early 1960s, with the increasing interest in solid rotor technology, research and development started to be more active in the field of solid rotors. Most of the early studies on solid rotors were accomplished with various simplifications and simplified models. This was due to the fact, that computer technology was not very advanced and most of the calculations were done by analytical equations. For example one of the simplifications was the assumption of an unsaturated rotor having a constant permeability, which resulted in poor validity. Later on, more complex and advanced models of high-speed induction machines with solid rotors were proposed. These models included three-dimensional nature of the solid rotor as for example end-effects of the rotor [2]. Some of the issues and research are mentioned in publications [3] - [10], where later on, some of the authors continued in this research.

In recent years, the demand for high-speed electrical machines has increased. This is due to the fact that some industrial applications require high rotational speed. For example compressors, turbo-compressors, turbo-circulators, pumps, and machine tools can often achieve better performance at higher speeds. Also, the energy efficiencies of such applications improve at higher speeds, so it is a great option from an economic and ecological point of view. With the extensive research and development in the field of frequency converter technology, it has become feasible to apply the variable speed technology of different high-speed machines to such a range of applications [11].

With better and more advanced frequency converters, the emphasis is also placed on the research and development of high-speed machines. High-speed machines are characterized by high efficiency, great mechanical properties, and better electromagnetic

parameters than regular electric machines with a mechanical gearbox. Therefore, the best solution and design in terms of electromagnetic, mechanical, and thermal parameters for high-speed electrical machines are constantly being sought. These best solutions and designs include mechanical modification of the rotor. For example, a high-speed induction machine with a solid rotor is mechanically modified with axial slits, radial grooves, a conductive layer, etc. Those modifications help to improve electromagnetic parameters and cooling. But in some cases can worsen mechanical parameters and can be challenging to manufacture. Another challenging aspect of designing a high-speed electrical machine is its calculation itself, from the electromagnetic point of view [12].

For this purpose, modern numerical methods are used for the calculation of electrical machines, in general. The most used numerical method is FEM, where a lot of the programs are using this method for multi-physical calculations. These programs, used for designing electrical machines, are in some cases faster and more accurate than analytical calculations. But in the case of the high-speed electrical machine, these FEM based calculations can take large amounts of time. The best type of analysis for high-speed electrical machines would be 3D analysis. But it could even take months to finish this analysis and without proper experience with this analysis, the accuracy of outcome results could be questionable. A better option for this is 2D analysis, which is less time-consuming. However, it does not capture all aspects that 3D simulation can offer. For this purpose, corrective factors of electric current bending at the end of the rotor were introduced. These corrective factors help bring the results, of the calculated model, closer to a real electrical machine. Despite these simplifications, the analysis still takes too much time. And mainly because, time-transient analysis is used in this case which is also the most suitable for accurate results. This is due to the fact that high-speed electrical machines, mainly stator and rotor, have large electromagnetic constants [13].

For this reason, a new method of calculation of electrical machines with solid rotors has been proposed, which will help to reduce the time consumption of optimization of machine design even more. This method consists of using FEM-based analysis and statistical models that approximate the results of FEM-based analysis. These statistical models are also called surrogate models and are used in many other engineering fields. Surrogate models are often used with optimization algorithms to find the best machine design. The advantage of surrogate models is that they are an approximate function of the results, so optimizing the machine design is many times faster than using conventional optimization. This Master's thesis deals with the possibilities and methods of calculation of induction machines with solid rotors and its accelerated design optimization using surrogate model.

1 High-speed electrical machines

1.1 Introduction and motivation

Nowadays, there is increasing pressure to shift technology in the field of high-speed electrical machines with an increasing demand for reducing the electricity consumption of electrical machines and increasing their efficiency, reliability, lifetime, improve maintenance, and reduce their size. For that reason, in several branches of industry, electrical machines with gearboxes are being replaced with high-speed electrical machines. According to [2], speed-increasing gearboxes are commonly used between the normal speed electric machines and the higher speed compressors. The speed ratios in such gearboxes vary generally from 2:1 to 6:1. However, a gearbox has an efficiency penalty of 1-1.5% loss per gear stage at full load. It is also noteworthy that the efficiency of the gearbox drops as the load decreases. Another drawback is the need for lubrication of gears, a cooling system, and the need for additional space. Moreover, the overall efficiency is lower. On the other hand, for example, the construction of an electric machine with a gearbox and compressor is simple. And better external cooling for the electrical machine can be applied. An illustration of this system is shown in Fig. 1.1.

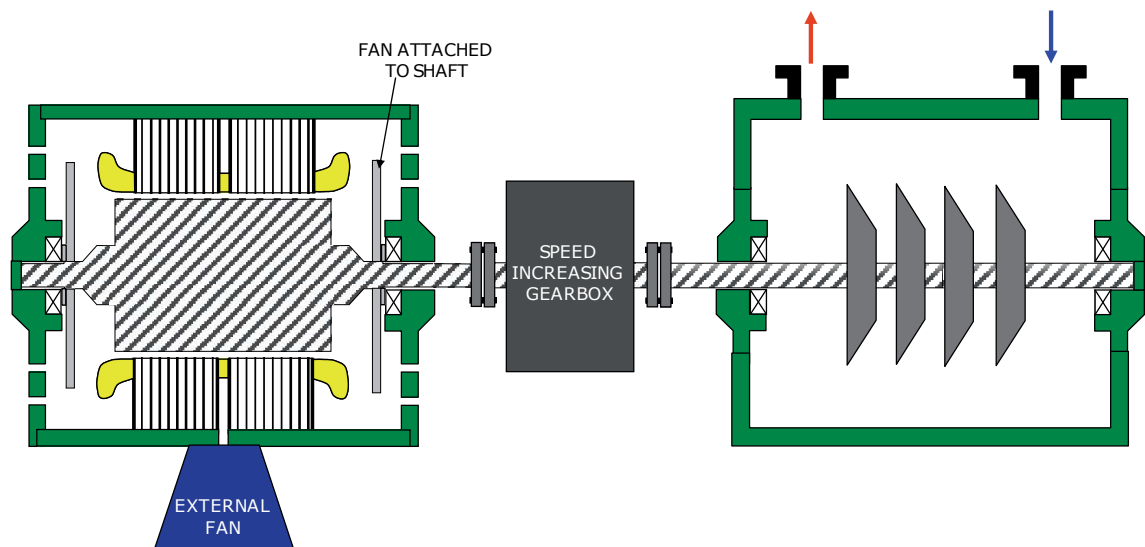


Fig. 1.1: Illustration of a system with electric motor, gearbox and gas compressor unit [2].

For these reasons, high-speed electrical machines are being used more in areas where higher speeds are required. From this point of view, high-speed electrical machines are integrated into single systems. For example, they are integrated into compressors, turbo-compressors, turbo-circulators, pumps, etc. According to [14], this integration system helps to improve the reliability, maintenance, efficiency of the electrical machine (and

whole system) and the construction is more robust with mechanical rigidity and resistance to centrifugal forces. The biggest advantage of this system is less space requirement because the load is connected directly to the machine, which can be in some cases crucial. Basically, it eliminates the total length of the train and the alignment of the drive train is greatly simplified. Also, power frequency converters are nowadays much more advanced and their efficiency is close to the efficiency of the gearboxes (in some cases even better). And the price of these converters is, in some cases, very close to the price of gearboxes. An illustration of this system is shown in Fig. 1.2. With the use of converters (and with the possibility of using magnetic bearings or air bearings) the following properties are eliminated or improved in the whole system:

- Need for lubrication of gearbox
- Lower losses caused by gearbox
- Positive contribution to vibrations behavior

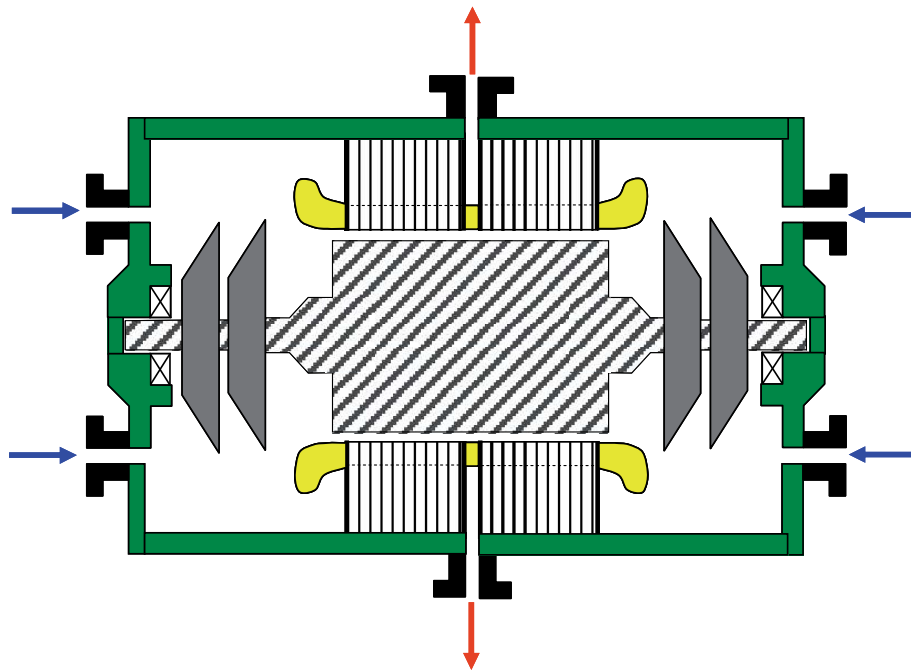


Fig. 1.2: Illustration of a system with high-speed electrical machine integrated into compressor unit [2].

On the other hand, the cooling of the high-speed electrical machine can be in some cases, difficult. It is mainly due to a closed construction of the system, where cooling depends on internal air exchange and heat exchangers, where the electrical machine is cooled by the internal fluid. According to [15], the cooling system must be extremely reliable and efficient. The reasons for that are to avoid over temperatures of the stator winding, rotor

(rotor cage/ magnets), bearing, and shaft deformations. Therefore, the cooling system of a high-speed machine is of primary importance and strongly dependent on the application. Another main issue with this type of machine can be manufacture difficulties. For example, a high-speed induction machine with a coated solid rotor or a high-speed synchronous machine with permanent magnets can be in some cases very difficult to produce. With increasing machine size, the manufacturing problems are increasing.

All the features of these two systems can be summarized, according to [2], in the following table:

Table 1.1: Overview of the properties of electrical machines with gearbox and high-speed electrical machines integrated into system [2].

Electrical machines with gearbox	Highs-speed electrical machines
<ul style="list-style-type: none"> • Direct/Non-direct drive • Non-integrated casing • External cooling for motor • Simple construction • Non-integrated casing • Gas seals 	<ul style="list-style-type: none"> • Direct drive • Integrated bearing • Integrated and sealed casing • Internal gas cooling for motor • Thermal stresses affecting on motor • Compact size • Lower costs • No shaft seals

In the next sections of this work, an emphasis will be placed on division, design and application of high-speed electrical machines.

1.2 Division of high-speed electrical machines

The use of a particular high-speed electrical machine highly depends on the application, manufacture possibilities and in some cases price. Another crucial parameter for a high-speed electrical machine is its size. According to [16], with increasing size, a high power density, good dynamic performance, and also mechanical durability is needed. The permanent magnet machine is usually the first candidate for a high-speed machine application due to its good electromagnetic behavior. However, the permanent magnet material has small tensile strength and can not withstand the large centrifugal force due to the high rotation speed. For this reason, high-speed IM are widely used in many applications due to their good mechanical performance. But its electromagnetic performance is worse. Another type of high-speed machine can be used as an alternative, but this machine also has its advantages and disadvantages. Based on these properties and attributes, a high-speed electrical machine is chosen for its application.

According to [17], the main division of high-speed machines with their advantages and disadvantages is shown in the following table:

Table 1.2: Overview of high-speed electrical machines with their attributes [17].

Types	Positive attributes	Negative attributes
PMBM	<ul style="list-style-type: none"> • High power density • High efficiency in the full speed range • Large air gap length • Simple power converter (Self-excitation at all times) • High phase inductance to limit short-circuit currents 	<ul style="list-style-type: none"> • Rotor robustness (require careful rotor construction design) • Intolerance to elevated temperature • Iron loss at idling Field weakening • High cost
SRM	<ul style="list-style-type: none"> • High intrinsic fault tolerance • High reliability • High rotor/inertia ration • High efficiency • Robust rotor structure • Simpler construction • Thermal management easier • Without magnet saturation concern • Wide speed operational capability • Low copper and iron loss • Field adjustment 	<ul style="list-style-type: none"> • Inferior power and torque density than PMBM • High torque ripple • High ventilation losses • High vibration • High windage losses • Small air gap length • Sophisticated power converter
IM	<ul style="list-style-type: none"> • Constant voltage over a reasonable speed range • Robust rotor structure • High reliability • Easy starting • Open loop speed regulation • Low cost 	<ul style="list-style-type: none"> • Lower power • High rotor loss • Sophisticated power converter to provide both control and excitation • Low fault tolerance
CPM	<ul style="list-style-type: none"> • High power factor • Field adjustment 	<ul style="list-style-type: none"> • Complicated rotor structure • Rotor loss
HM	<ul style="list-style-type: none"> • High power factor • Field adjustment • Simple rotor structure 	<ul style="list-style-type: none"> • High windage losses • High iron losses

Syn. RM	<ul style="list-style-type: none"> • Simple rotor structure • Singly excited • Low rotor losses • Field adjustment 	<ul style="list-style-type: none"> • Low power factor • Low torque density • High windage losses • Small air gap length
---------	--	---

For high-speed electrical machines, it depends not only on their properties but also on the properties of the materials. Due to increasing demand for these machines, more types of new materials are being created. According to [18], these new materials are specifically designed to meet higher demands in mechanical strength (Yield strength, Young's modulus, elongation), whilst at the same time trying to preserve or improve their electromagnetic characteristics (efficiency, lower losses, lower saturation of material). For high-speed electrical machines mentioned in Table 1.2, five material classes are considered as main properties of interest. These material classes are shown in table 1.3:

Table 1.3: Classification of main material requirements for high-speed induction machines [18].

Material class	Location	Properties of interest
Soft magnetic	<ul style="list-style-type: none"> • Rotor • Stator 	<ul style="list-style-type: none"> • Saturation flux density • Yield and tensile strengths • Ductility and Brittleness • Low iron loss behaviour over a wide frequency range
Hard magnetic	<ul style="list-style-type: none"> • Rotor • Stator 	<ul style="list-style-type: none"> • Coercivity • Reminiscent flux • Yield and tensile strengths • Operating temperature • Temperature variation • Low electrical conductivity
Conductors	<ul style="list-style-type: none"> • Rotor • Stator 	<ul style="list-style-type: none"> • Conductivity • Mechanical strength
Electrical insulation systems	<ul style="list-style-type: none"> • Rotor • Stator 	<ul style="list-style-type: none"> • Maximum operating temperature • Method of application • Ageing mechanisms • Thermal conductivity
Retention systems	<ul style="list-style-type: none"> • Rotor 	<ul style="list-style-type: none"> • Yield strength • Magnetic properties • Electrical conductivity • Thermal conductivity

Despite all the advantages and disadvantages, High-speed IM are the most used high-speed electrical machines with solid rotors in the industry. It is due to its low cost, mechanical rigidity, robust rotor structure and high reliability. In this work, an emphasis will be placed mainly on this type of high-speed electrical machine.

1.3 Construction of high-speed IM with solid rotors

High-speed IM with solid rotors made of a solid single piece of ferromagnetic material, which is able to reach very high speed. For high-speed applications, centrifugal forces and peripheral speed play an important role to decide the construction type. For this reason, this type of rotor is preferred mainly in megawatt range power and higher rotational and peripheral speeds over a laminated rotor, as can be seen in Fig. 1.3.

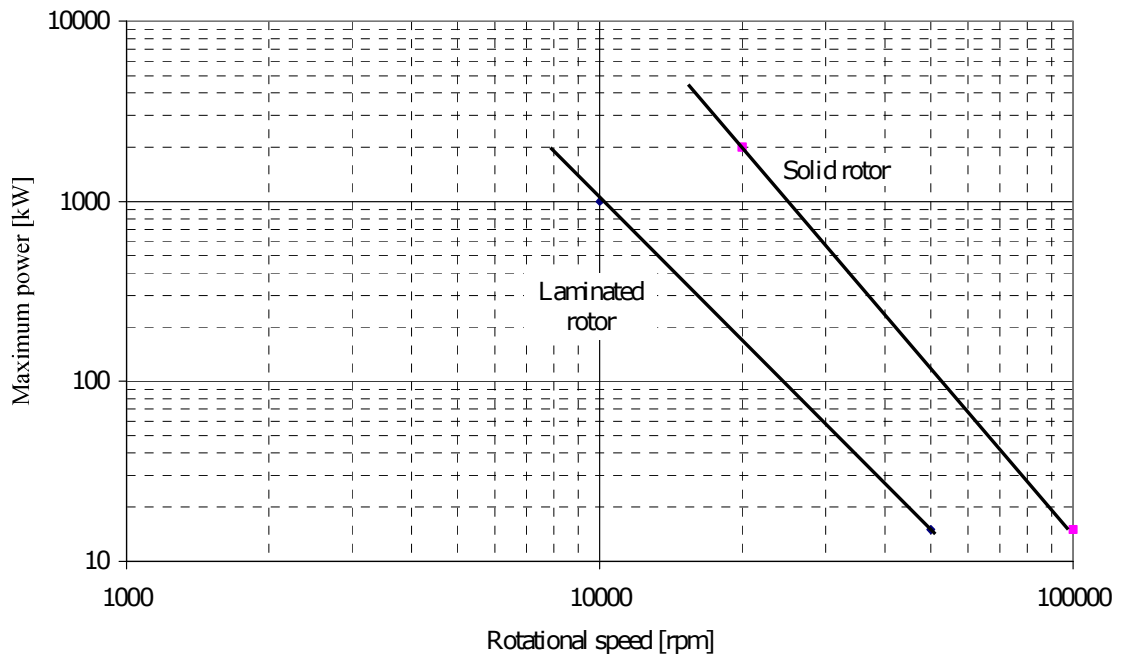


Fig. 1.3: Powers limited by the rotor material yield stress (700 MPa) versus rotational speed [11].

In order to have good efficiency, the rotor of a high-speed IM should usually provide the following two basic functions, according to [24]:

- High permeability flux path is needed so that most of the magnetic field energy generated is usable at the air gap for the production of the torque
- The rotor has to have low resistivity flow paths for the electric currents induced so that the ohmic losses relating to torque producing currents are low.

Ferromagnetic materials have high permeability, but they lack low resistivity compared to other metals. This problem is usually solved in such a way, that those two functions are performed by different parts of the rotor.

According to [11], the simplest solid rotor is a smooth steel cylinder, which has the best mechanical properties. However, such a type of solid rotor has the worst electromagnetic properties. Hence, some modifications of the solid smooth rotor have to be made in order to improve electromagnetic properties. On the other hand, these modifications can be very expensive and also can raise manufacturing demands. But they are essential in order to improve every electromagnetic aspect of the machine and to ensure the economical operation of the machine. So the possibilities of the manufacturer and itself should be taken into account.

Emphasis should also be placed on choosing the right material for a solid rotor, to achieve the best electromagnetic and mechanical properties. The biggest problem with choosing the right material is the low availability of information for these materials, especially in terms of electromagnetic properties. Manufacturers often provide enough information on mechanical properties, but sometimes they only provide basic electric properties such as electric resistivity of the material. For this purpose, publications [19] and [20] provides a comparison of materials used for the solid rotors. It also shows necessary electromagnetic properties, such as the B-H curve for some materials. So it can be easier for some engineers, who are less experienced in designing high-speed IM, to choose the most suitable material for a solid rotor.

Overall, high-speed IM with solid rotor construction offers these advantages according to [11]:

- High mechanical integrity, rigidity and durability. The solid rotor is the most stable and of all rotor types it maintains best its balance.
- High thermal durability.
- Simple to protect against aggressive chemicals.
- High reliability.
- Simple construction, easy and cheap to manufacture.
- Very easy to scale at large power and speed ranges.
- Low level of noise and vibrations (if smooth surface).

In the next sections, all types and modifications of solid rotors for high-speed IM will be described with their advantages and disadvantages.

1.3.1 High-speed IM with smooth solid rotor

As was mentioned above, solid smooth rotors have the worst electromagnetic properties, such as the slip and losses of the rotor tends to be large and the power factor is low. It is due to a poor flux density penetration into the rotor caused by high rotor frequencies and low electric conductivity of a material, which leads to large apparent resistance, a low magnetization inductance, and an over-saturated surface of the solid rotor. This results in very poor electromagnetic torque. But this type of rotor is also simplest in its construction. According to [2], [11], [12] and [23] it is easy to manufacture, cheap and has the best mechanical and fluid-dynamical properties for low air friction. It also offers the best solution to minimize the parasitic effects of mechanical nature. This type of rotor can be seen in Fig. 1. 1.4 (a).

For better electromagnetic performance and increasing torque, adding non-magnetic high-conductivity (either copper or aluminum) end-rings helps to improve these parameters, according to [11], [22] and [24]. It is due to rotor current flow in the solid iron that tends to be more aligned into the axis-parallel direction, which increases the Lorentz force. Publications [16], [21] and [22] states that for example, a two-pole smooth solid rotor equipped with copper end-rings produces twice as much torque at a certain slip compared to an ordinary smooth rotor. This type of rotor can be seen in Fig. 1. 1.4 (b).

The last and best modification of a smooth solid rotor, according to [2], [11] and [12], is adding a conductive layer on the surface of the rotor, which covers the whole rotor from one end-ring to another end-ring. In most cases, the thickness of the copper layer is bigger on the end rings to increase conductivity for the end-ring rotor current. Publications [16], [21] and [22] states that for coat it is either used low or high conductivity non-magnetic material, to improve electromagnetic properties of high-speed IM. In most cases, a high conductive copper layer is used for coating this type of rotor. This copper coat is acting both as an infinite number of bars and as the end rings. Due to its high conductivity, it is the main circuit path of the fundamental currents. Some part of the fundamental current circulates in the solid steel part of the rotor cross-section. According to [23] and [24], it also acts as a high-frequency filter for air gap harmonics and does not let higher-frequency stator slot harmonics to penetrate through the coating layer. This helps to reduce rotor eddy-current losses and losses in the stator winding. To achieve the best electromagnetic properties with the highest electromagnetic torque, the thickness of copper should be thick enough to carry induced rotor currents. But the layer should be thin enough not to decrease air gap flux. Of course, with regard to the mechanical limits of copper. This type of rotor can be seen in Fig. 1.4 (c).

The only problem with these two modifications is their higher cost and demanding manufacturing. It can even degrade the mechanical properties of the rotor because copper does not have such great tensile strength as the material used for the solid rotor. In some cases, these modifications can not be used or another conductive material has to be used, such as copper alloys. On the other hand, it dramatically improves every electromagnetic property compared to the construction of a simple solid smooth rotor.

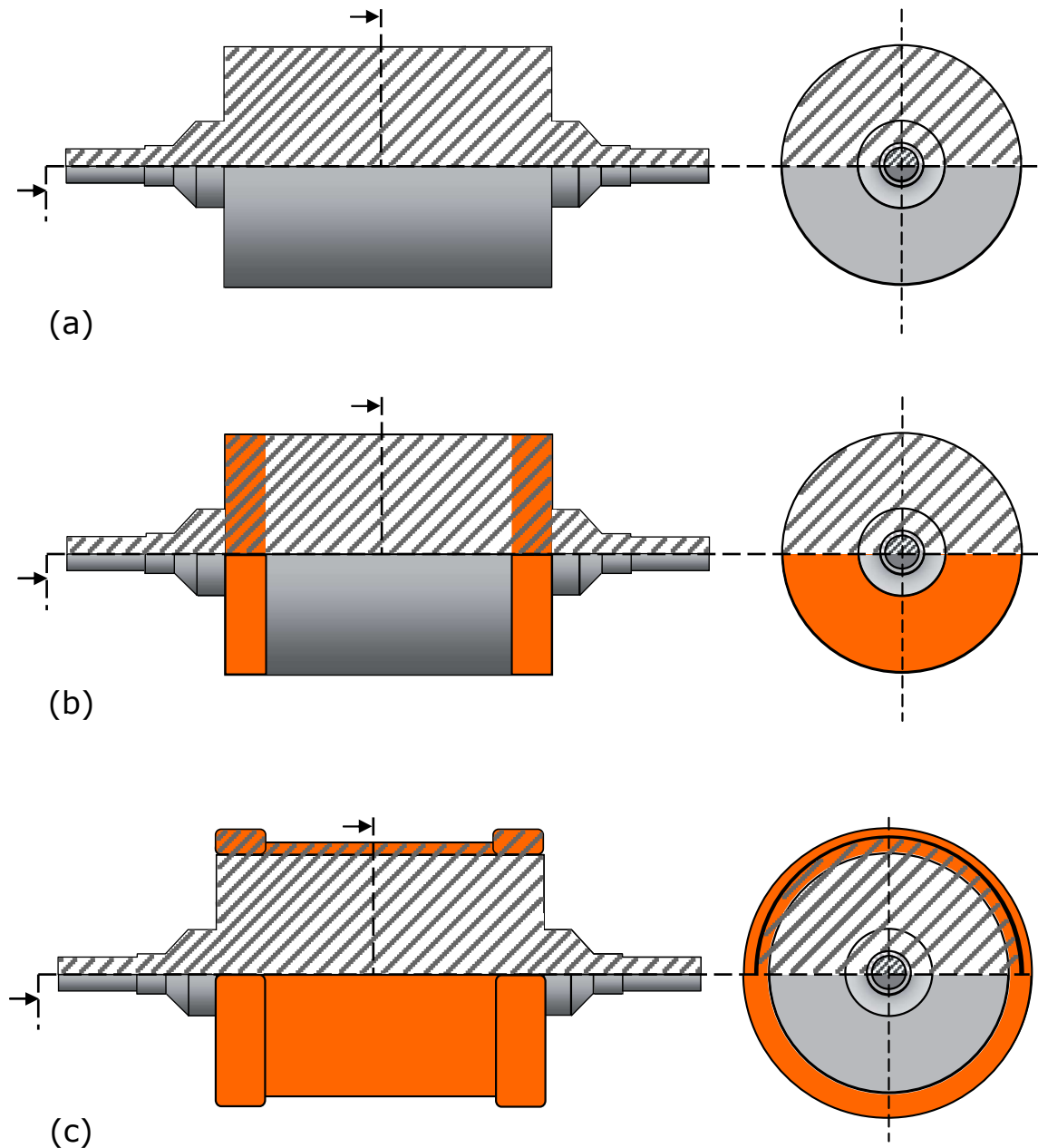


Fig. 1.4: Constructions of solid smooth rotor for high-speed IM: (a) simple smooth rotor, (b) smooth rotor with copper end rings and (c) smooth rotor coated with conductive material according to [2], [11] and [23].

1.3.2 High-speed IM with axially slitted solid rotor

To further improve the electromagnetic properties of high-speed IM, a modification of the smooth solid rotor was developed in such a way, that better flux penetration into the rotor is enabled. This is achieved by axially slitting the cross-section of the rotor, as it is illustrated in Fig. 1.5 (a). According to [2], [16], [25] and [26]. The slit makes the fundamental flux component into the rotor much easier. Also, slitting the rotor decreases the low-frequency impedance of the rotor, thus producing more torque and increase efficiency. Moreover, it increases the high-frequency surface impedance of the rotor, which decreases the rotor eddy-current loss. The drawback of axial slitting is that the ruggedness of the solid rotor is partially lost and at very high speeds, the friction between the rotating rotor and air increases significantly. However, the axial slitting intensifies the cooling of the rotor, due to the increased cooling surface of the rotor.

From the electromagnetic point of view, it is very important to choose the right amount of slits. In publication [21], it is stated that to achieve a smooth torque the stator slot and the rotor combinations producing synchronous torques must be avoided, which is the same case for selecting rotor bars in common IM. According to another study in [11] and [27], the output torque of the machine as a function of the number of rotor slits has a form of a downward-opening parabola. In [11] the number of stator slots was 48 and the number of the rotor slits, that achieved the highest torque, lied between 34 and 42, with increasing slip, sliding to the higher number. Also with a higher number of slits at the same slip, the electromagnetic torque is increased. The study was only limited to even numbers of the rotor slits. That is because the use of odd numbers of rotor slits is not allowed in most of the recommendations for slit numbers on the construction and operation of an electrical machine. The main reason for that is because the magnitude of the unbalanced magnetic pull may be large (even larger than the weight of the rotor) or it can create unwanted vibrations. This is caused by the odd number of rotor slits. On the other hand, the ripple of electromagnetic torque is decreased. Another study [28], recommends that the optimal number of the slits is between 5 and 15 per pole pair.

Another crucial aspect of designing an axially slitted solid rotor is the depth of the slits. According to [21] and [34], the depth of the rotor slits has a significant effect on motor performance. The slits should reach very deep inside the rotor. The 60% radius is the best choice to produce the best electromagnetic properties. Unfortunately, the mechanical strength of the rotor may become too weak. Depending on the maximal stress to maximize the fatigue life in zero to full speed cycles the rotor slit depth should be selected to be approximately 50% of the radius of the solid rotor. In reality, the depth of the slits varies between 40-50% of the radius of the solid rotor, depending on the size and speed of the machine.

Also, the selection of the width of the slits is based on the number of slits. It is

also limited by mechanical stress that is created at the bottom of the slit where the highest concentration of mechanical stress is located. For this reason, if it is possible, the bottom of the slit is rounded, which further decreases the mechanical stress of the material at the bottom of the slit. It is also limited by the amount of coolant flow (which should be as large as possible) and the production capabilities of the manufacturer.

This construction can be modified as it is illustrated in Fig. 1.5 (b). Here slit depths vary, where every second slit is deeper than the previous one. The reason why such construction was proposed is that, when the depth of the rotor slitting is too deep, the rotor material between the slits is highly saturated. The depth of the axial slits is then restricted by the saturation of the rotor between slits. This is the reason why the maximum electromagnetic torque can be reached at 60% of the radius of the solid rotor, as it was stated in previous construction. With very deep slits the material between the slits is highly saturated and the flux flow in the rotor teeth is restricted. With various slit depth, this high saturation is limited. The biggest drawback of such construction is its mechanical limitation. If the longer slits become too deep, the rotor becomes too fragile. And also the longer slits are restricted to some extent as was described in the previous construction. In study [2], it is stated that from the electromagnetic point of view, it gives very similar results as the construction with equal slit depths, in terms of electromagnetic torque and the power factor.

Next construction of high-speed IM is illustrated in Fig. 1.5 (c). This construction holds the advantages of the axially slitted rotor and copper end rings. It is a very similar construction as it was described for a smooth solid rotor with copper end rings in chapter 1.3.1, except for axial slits. Here the current flow also tends to be more aligned to the axis-parallel direction. The torque and efficiency are increased according to [29].

The construction illustrated in Fig. 1.5 (d) is an axially slitted solid rotor coated with either highly-conductive or resistive non-magnetic material. According to [2], if the rotor is coated with a highly conductive material (such as copper), the machine will have the best electromagnetic properties with the highest torque, higher efficiency, and better power factor. This improvement holds the same electromagnetic properties as it was described in chapter 1.3.1 with the coated solid smooth rotor. The main advantage of this construction is that the machine holds both advantages of axial slits and copper coat. If the rotor is coated with resistive non-magnetic material it behaves similarly as with high-conductive material, according to a study in [30]. This coat creates high-surface impedance which damps the air gap harmonic effects in the coating layer. So it also works as a high-frequency filter. The highest value of the rotor surface impedance can be achieved if the coating material has high permeability and low conductivity.

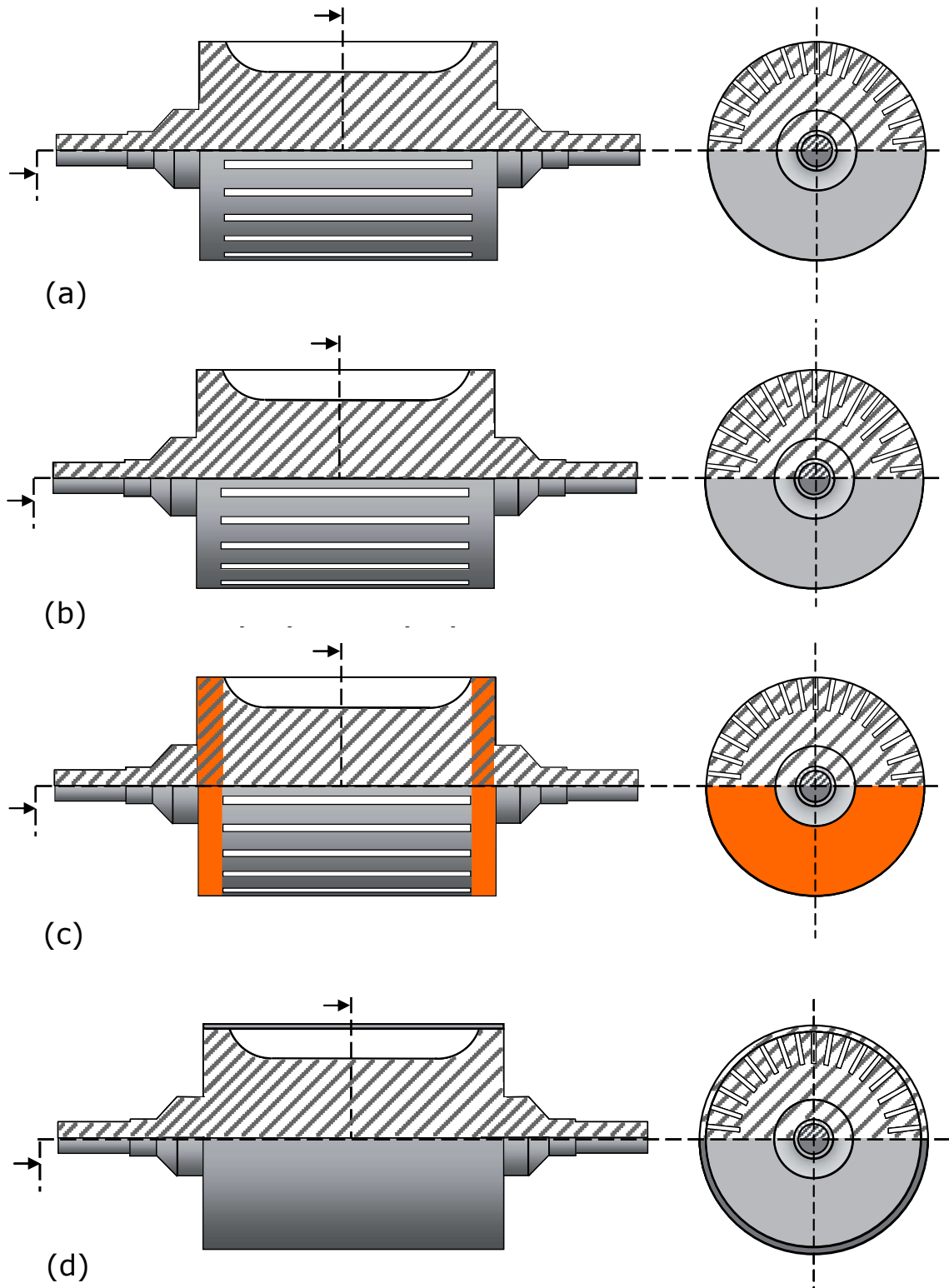


Fig. 1.5: Constructions of axially slitted solid rotor for high-speed IM: (a) axially slitted rotor, (b) axially slitted rotor where every second slit is deeper, (c) axially slitted rotor with copper end rings and (d) axially slitted rotor coated with conductive/resistive material according to [2].

With this material, the effectiveness of rotor loss reduction is significant. No matter which type of coat is used, the penetration depth of higher air gap harmonics is reduced. Furthermore, the coating material can reduce the transient unbalanced magnetic force.

Another use for coating is mechanical reinforcement of the rotor. When the axial slits are created, the mechanical rigidity and robustness of the solid rotor is partially lost, as was stated. Using non-magnetic material, for example titan, helps to improve the mechanical properties of the solid rotor. The disadvantage of this procedure is that the titan is electrically conductive, but its conductivity is similar to that of the material used for the solid rotor. So it is not highly resistive or conductive compared to the material used for the solid rotor and in some cases can create additional eddy current losses in the rotor, because in this state, it does not behave as a high-frequency filter.

Regardless of the coat type used, every coat helps to reduce mechanical losses caused by friction between air and the solid rotor. The biggest drawback of this technology is its price and mainly the demand for manufacturing. The coat should be welded to the material of the solid rotor, and the joint should have higher tensile strength than the coating material. In the case of using titan, a solid rotor can be inserted into a titan tube which is less demanding from the manufacturing point of view. But with increasing machine size, it can become a challenging task.

Based on all the construction described above, a special construction was designed to have the best possible electromagnetic parameters. This construction is called shielded axially slitted solid rotor and is illustrated in Fig. 1.6. This construction is composed of axially slitted solid rotor, copper end rings and copper coating which covers only rotor teeth, according to [31] and [32]. It, therefore, creates a hybrid technology, which resembles a solid rotor with a squirrel cage. This construction combines all advantages and electromagnetic properties of all used components which are described above, and besides, the benefits of squirrel cage are added. While the slits help to lower impedance of the rotor and penetration of flux density into the rotor, the copper coat on slit teeth acts as rotor bars, where end-rings collect the induced rotor current. It also helps to filter higher-frequency air gap harmonics and reduce eddy current losses. Most of the induced rotor current passes through the teeth coat, while some of the current induced in the solid rotor is extruded to the surface of the rotor due to higher rotor frequencies and better axially-aligned as a result of copper end rings. Thus, most of the induced current is located on the surface, which creates the highest electromagnetic torque possible, with the reduction of torque ripple and eddy-current losses. In study [32], a comparison is made between the axially slitted solid rotor, copper-coated smooth solid rotor and shielded axially slitted solid rotor. The shielded axially slitted solid rotor had the highest torque and output power. Compared to the copper-coated smooth solid rotor, the starting torque was remarkably increased. In terms of rotor loss, this construction placed

second due to eddy-current losses induced in the copper layer. But the efficiency was the highest of all three constructions. The authors of the study even showed the power factor of these machines. But the analysis was done in 2D FEM program with transient magnetic analysis. In such analysis, it is known that the accuracy of power factor calculation is not very high and serves only to determine a kind of idea how the power factor changed based on different topology or construction of the machine.

The construction of this solid rotor is made by axially slitting a smooth rotor and coating it with copper. Then end-rings are placed on both sides of the solid rotor. Finally, the slits are opened. This type of construction is quite new and has not been described well enough and tested in the industry yet. The biggest drawback of such construction is its price and highly demanding manufacturing. It is also not entirely determined whether such a solid rotor can withstand centrifugal forces and tensile strength, especially in places of copper coating, with a higher power range and speed.

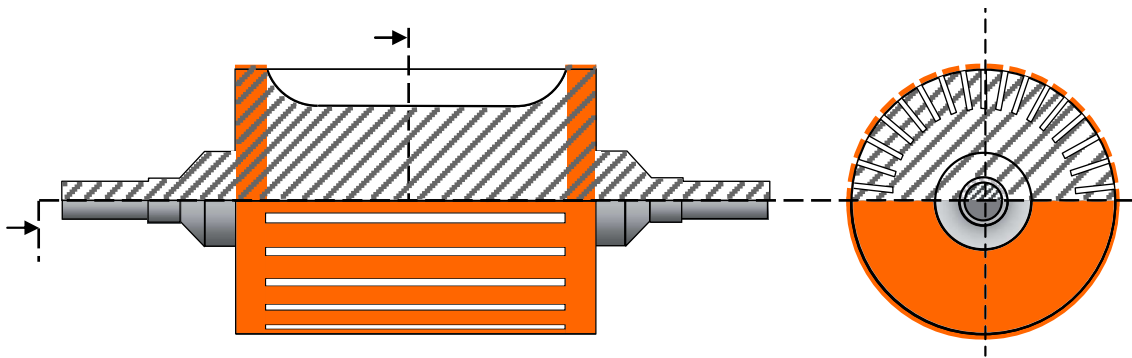


Fig. 1.6: Construction of shielded axially slitted solid rotor for high-speed IM according to [32].

A further modification can be applied on the axially slitted solid rotor as illustrated in Fig. 1.7. Here the slits are skewed in a radial direction and according to [33], this modified topology increases electromagnetic torque. In the case of Fig. 1.7(a), the electromagnetic torque, was in the study, increased by 10.7% compared with the construction with non-skewed rotor slits. This topology was even improved by creating rotor slits where every second slit is deeper than the previous one and skewed in the radial direction. This optimized topology improved the electromagnetic torque by 37.7%. Due to skewing, this topology does not have such drawbacks as those in topology with non-skewed slits. Here the slits do not go deep enough and can be longer. In the study, the machine was calculated with a skew angle of 15°, 30°, 45° and 60°. The study showed that with the skew angles increases, the output electromagnetic torque increases slightly. However, with skewed slits, the torque ripple increased by 40.3%. The torque ripple was improved by skewing the rotor slits in the radial direction by 30° and additionally skewing the rotor slits in the axial direction by 26°. The torque ripple was significantly reduced to nearly

1% of its output torque. This topology can be used in combination with the described slitted solid rotors above. The drawback of this topology is demanding to manufacture and it may not withstand high centrifugal forces and tensile strength at higher speeds.

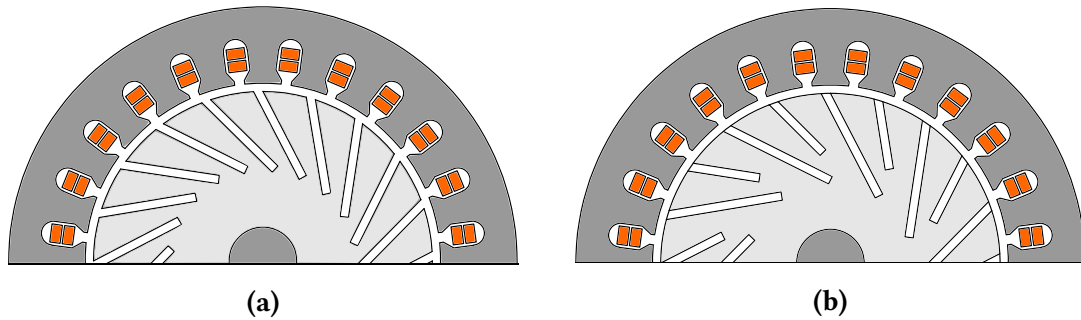


Fig. 1.7: Construction of axially slitted solid rotor with skewed slits in radial and axial directions with: (a) normal depth and (b) every second slit is deeper according to [33].

1.3.3 High-speed IM with squirrel cage solid rotor

This construction is very similar to a common induction machine with a squirrel cage. For high-speed applications, even the laminated rotor can be used, but only to some extent. It is due to large centrifugal forces and high tensile strength which the laminated rotor would not withstand, according to [36]. For this reason, the rotor is made of solid ferromagnetic material with inserted copper bars into the drilled bores or cut slots and a copper short-circuit ring is added that connects the rotor bars. Some of the construction of a solid rotor with squirrel cage is illustrated in Fig 1.8. According to [37] and [38] most, of the current, is induced in rotor bars, so the current flowing in the solid rotor is reduced. Additionally, eddy current losses in the solid rotor are also reduced, and better than any other construction previously described, as stated in [39] and [40]. It is due to the remarkably lower rotor resistance of the copper cage. With low resistance also comes the lower slip of the IM. Moreover, the power factor is highest compared to all IM with a solid rotor and efficiency is also high. However, inserting the rotor bars inside the solid rotor increases the rotor leakage inductance to a high value, which limits the rotor performance. And the steel bridges between the rotor bars are saturated, as it is stated in study [21]. These two factors reduce the power factor of the squirrel cage rotor. Even with these drawbacks, if the high-speed IM with squirrel cage is designed properly, it can achieve the best electromagnetic parameters of all described IM with solid rotors.

For further improvement of electromagnetic properties, the opening of rotor slots would be beneficial from the magnetic point of view, mainly in construction Fig 1.8(c). But this will also remarkably increase frictional losses and from the mechanical point of view, opening the rotor slots is not preferred. So smooth rotor construction is the right choice. So for higher speed, construction Fig. 1.8(a) and Fig. 1.8(b) are not very ideal.

The main disadvantage of this construction is challenging and complicated manufacturing. This is the reason why it is not preferred in high-speed applications. According to study [41] and [42], the most critical part of a squirrel-cage rotor is the short-circuit ring, which must be designed differently compared to the traditional one. Here, the joint between the short-circuit ring and rotor bar must be designed properly from the mechanical and thermal point of view. Otherwise, the rotor would not withstand centrifugal forces, dynamic bending and high temperatures during operation.

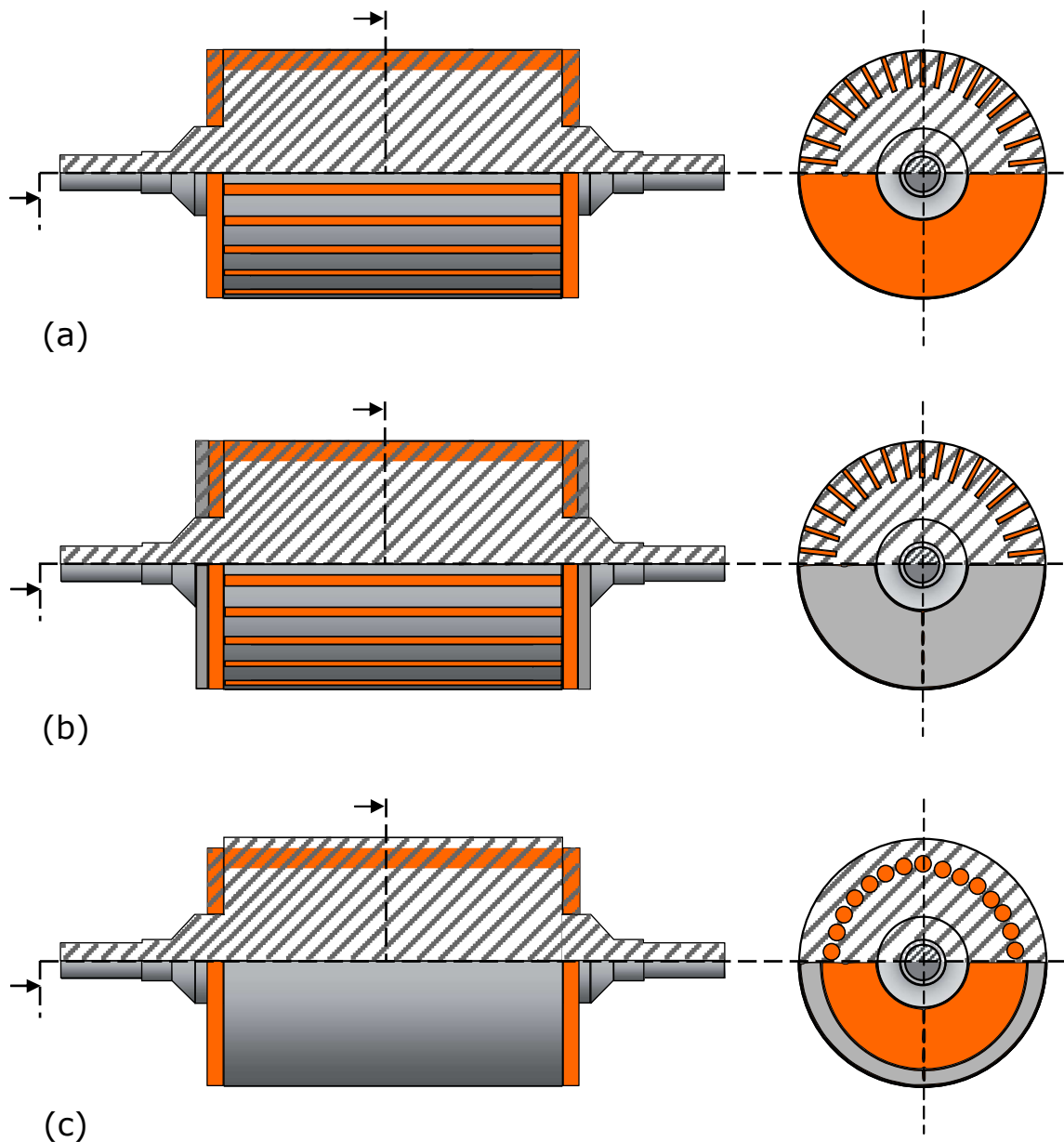


Fig. 1.8: An example of constructions of solid rotor with: (a) rectangular open slots with brazen squirrel cage, (b) embedded squirrel cage by isostatic pressure and (c) round embedded copper bars inserted in a solid rotor core with drill holes according to [35].

1.3.4 High-speed IM with radial rotor surface grooves

This special case of solid rotor modification is illustrated in Fig. 1.9. In this case, radial grooves are created on the surface of the solid rotor and they act as a coating for a solid rotor. It increases the surface impedance of the solid rotor and therefore behaves as a highly resistive coating material. Thus acts as a high-frequency air gap harmonic filter which reduces rotor losses. The high resistivity of the solid rotor surface is made intentionally by choosing the correct distance between individual radial grooves, but the radial grooves have to be on the active length of the rotor (not on end rings). The depth of radial grooves should be as deep as penetration depth for high-frequency harmonic components of induced rotor current. The width of radial grooves should be designed concerning the active length of the rotor and the distance between each groove. With all these rules applied, the conductivity of the surface of the solid rotor should be at least 80% less conductive than the rest of the rotor. According to [43], if the radial grooves are designed correctly the rotor surface eddy current losses can be decreased up to 60% and total rotor eddy current losses can be decreased up to 30%. As a result of that, the efficiency of the machine then increases. This modification can be done on any type of high-speed IM with a solid rotor, which does not contain other coating material. The main advantage of this modification is its simplicity and easy manufacturing. It also does not affect the mechanical or thermal properties of the solid rotor.

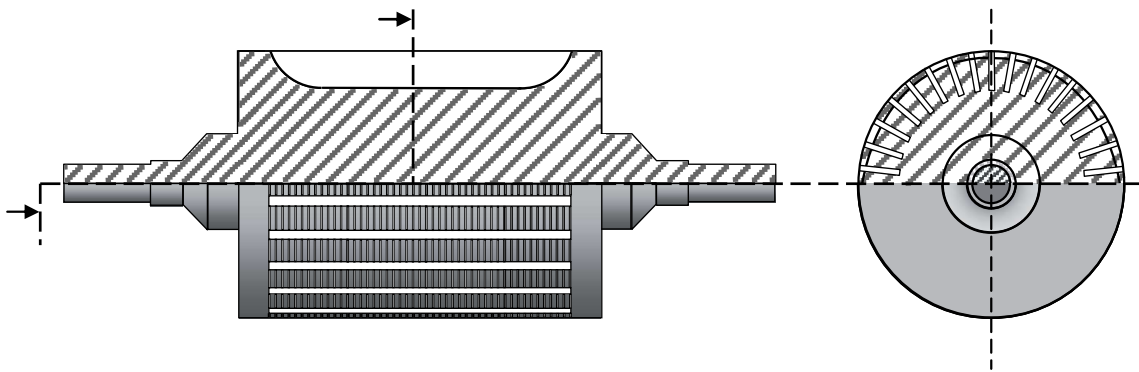


Fig. 1.9: An example of construction of axially slitted solid rotor with radial grooves for high-speed IM according to [43].

1.4 Applications of high-speed electrical machines

As it was stated, due to simple construction, low production cost and excellent mechanical/thermal stress withstanding capabilities, high-speed IM with solid rotors structure are widely used in many high-speed, high-pressure application fields. As reported by [44], an advantage of high-speed machines is the reduction of system weight for a given magnitude of power conversion. This is particularly desirable in mobile applications, where any saving in weight results directly in reduced fuel burn and emissions. Also, another benefit in adopting high-speed machines in certain applications is the improvement in reliability as a result of the elimination of intermediate gearing. In this section, an overview of some applications for high-speed IM will be shown and described.

1.4.1 High-speed electrical machines for more electric engines (Automotive/Power Generation)

According to [44] - [48], the concept is to have high-performance traction machines integrated within hybrid drive trains to improve fuel efficiency and reduce emissions. Due to increasing calls for emission and fuel efficiency improvement, further electrification for engines is being used for automotive and power-generating applications. Mainly by using high-speed machines. The potential applications of high-speed electrical machines within a more-electric engine are several, as it is for example shown in Fig. 1.10. This application shows the layout of four possible high-speed electrical machines around an engine. The electrical machine M1 is placed on the same shaft as the turbine and the compressor wheels in a turbocharger. It has two functions: First, it is used for speeding up the compressor to the required speed. And second, at high loads when excessive en-

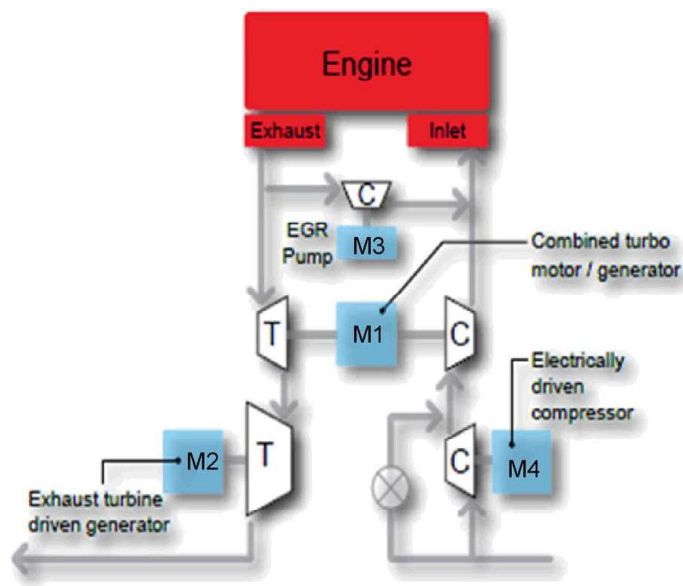


Fig. 1.10: High-speed electrical machines for the more-electric engine [44].

ergy is created in the exhaust, the machine is used as a generator. The electrical machine M2 improves driveline efficiency. It is done by installing this machine downstream of the turbocharger to extract waste heat from the exhaust gases. The recovered energy is then used to supply the vehicle's electrical load, including the traction machine if used within a hybrid drivetrain architecture. The electrical machine M3 drastically reduces the pumping energy required in comparison with more conventional EGR systems.

1.4.2 Flywheel energy storage systems applications

As stated in [44] and [49]-[51], this system operates by mechanically storing energy in a rotating flywheel. Electric energy is stored by using a machine that spins the flywheel, therefore converting the electric energy into mechanical energy. The process of recovering mechanical energy is using the same machine to slow down the flywheel. Hence converting the mechanical energy back to electrical energy. Modern flywheels have commonly large diameters, rotate at higher speeds, and have higher power and lower energy densities. They have higher power densities than the NiMH batteries typically used in hybrid vehicles or aerospace applications, although their energy densities are lower. These systems also offer several advantages over battery technologies such as more compact solutions, higher efficiency, longer lifetime, greater depth of discharge than batteries, and wider operating temperature range.



Fig. 1.11: High-speed composite flywheel [44].

1.4.3 High-speed spindle applications

Nowadays, in the machine tool industry, there is increased demand for higher rotational speeds, speed control, low vibration levels, power density, and more compact systems, as it is described in [44] and [52]-[54]. For this, high-speed electrical machines are used for spindle applications.

The electrical spindles applications can be divided into two main areas:

- Milling applications
- Grinding applications

The maximum rotational speed achieved during the different milling applications depends on the processed material type, as it is shown in Table 1.4.

Tabel 1.4: Typical milling applications speed [52].

Applications	Speed
Metal	4500 - 12000 rpm
Stones	8000-12000 rpm
Glass/Marble	8000 - 14000 rpm
Wood	18000 - 25000 rpm
Aluminum	30000 - 40000 rpm

For the grinding applications, the machine tools rotational speed is higher than the typical range for milling applications. Speed is achieved up to hundreds of thousands of revolutions per minute in the ultra-precision machining application such as mesoscale dimension range and mega-speed drive systems. Some typical spindle applications are grinding of bearings, screw, constant velocity joints, injectors pumps, etc. An example of an high-speed drilling spindle is illustrated in Fig. 1.12.



Fig. 1.12: High-speed 200 W 300000 rpm PCB drilling spindle [44].

1.4.4 Turbomolecular pumps applications

As stated in [44] and [55]-[57], the turbomolecular pumps are used to obtain and maintain a high vacuum. They are portable, fast-starting, and require little in the way of a

support system. The principle of these pumps is that gas molecules can be given momentum in the desired direction by repeated collision with a moving solid surface. In a turbopump, a rapidly spinning turbine rotor hits gas molecules from the inlet of the pump toward the exhaust to create or maintain a vacuum. For this purpose, high-speed machines are a great choice for this application, where the speeds reach higher rotational speeds of up to 100 000 rpm at low power density (a few hundred watts). These pumps are used to get a very high vacuum condition up to 10^{-10} mbar. Because of that, the rotor runs in a deep vacuum, with extreme thermal exchange problems. An example of a turbomolecular pump is shown in Fig. 1.13.



Fig. 1.13: Cross section of a turbomolecular pump driven by a high-speed motor [44].

1.4.5 Gas compressor applications

As reported by [44] and [58]-[61], gas compression is needed at many places in the chemical, oil, and gas industries. It is mainly for gathering, transmitting, and processing the gas downstream. Due to an increasing call for lowering emissions and increasing difficulty of installation due to environmental restrictions, gas-fired drives are being replaced with high-speed electrical machines. The idea of using high-speed electrical machines is to minimize the environmental, regulatory and maintenance issues. The main advantage of electric high-speed gas compressors is placing the machine with a compressor on a single shaft, which minimizes the demand for additional space. The electric high-speed compressor is integrated into the whole system, which additionally, improves the mechanical robustness of the whole system. Also, these machines do not need lubrication systems, so they are more suitable than electrical machines with a gearbox. It is due to the extensive use of magnetic bearings lately these days. Magnetic bearings also increase availability, safety, and efficiency, which reduce maintenance costs. Therefore, electric high-speed drives are the most environment-friendly compressor drives. An example of a conventional and integrated compressor is shown in Fig. 1.14.

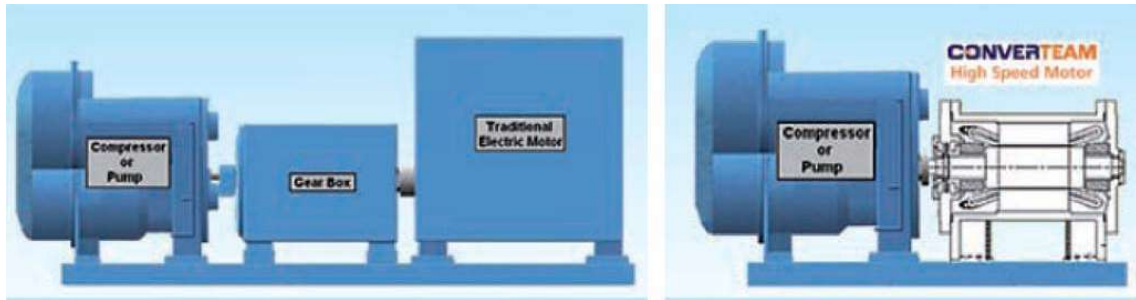


Fig. 1.14: (Left) Conventional compressor and (right) integrated compressor [44].

1.4.6 Industrial air compressors and air blowers applications

According to [44], [61]-[62], the demand for higher quality and oil-free compressed air is also increasing in industrial applications such as the food, beverage, and pharmaceutical industry. Any oil contamination can lead to unsafe products and consumer health hazards. In the automotive industry, it is essential to achieve oil-free air. In the electronics industry, moisture can affect sensitive processes and cause oxidation of micro terminal strips, which results in product failure. If oil contamination occurs in any of the aforementioned industries, it can lead to expensive product recalls and in the worst-case plant shutdown. Nowadays, high-speed electrical machines that operate at power levels of 100-500 kW and speeds of 80-15000 rpm, using magnetic or air bearings, are being used lately as oil-free direct drive industrial compressors, in the range of 4-9 bars. Also in wastewater treatment plants, over 60% of power demand is required for the delivery of air to provide oxygen for biological treatment of waste streams and mixing to solids. In the last decade, there is a rapid growth in the use of turbo blowers driven by high-speed motors. The advantages of these blowers are higher reliability and durability, reduced noise, 25% reduction in ecological footprint, and energy savings above 35% with respect to conventional blowers.

1.4.7 Microturbines applications

As stated in [44] and [53], microturbines are small combustion turbines of a size comparable to a refrigerator. The typical output power is 30-400kW. They are typically used for stationary energy generation applications at sites with space limitations for power production. These machines are very fuel-flexible and can run on natural gas, biogas, propane, butane, diesel and kerosene. Microturbines have few moving parts, high efficiency, low emissions, and have waste heat utilization opportunities. They are lightweight and compact in size. Waste heat recovery can be used in combined heat and power systems to achieve energy efficiency levels greater than 80%. Fig. 1.15 shows the typical layout of a micro gas turbine. It consists of a compressor, a combustor, a turbine, an alternator, a recuperator (optional), and a generator. Recently, there is an

interest in using microturbines as a range extender within serial hybrid vehicles, as well as all-electric vehicles. It would be used as a power unit that can charge the vehicle's batteries. It is claimed that such technology can be just 5% of the size, weight, and parts of an equivalent piston engine.

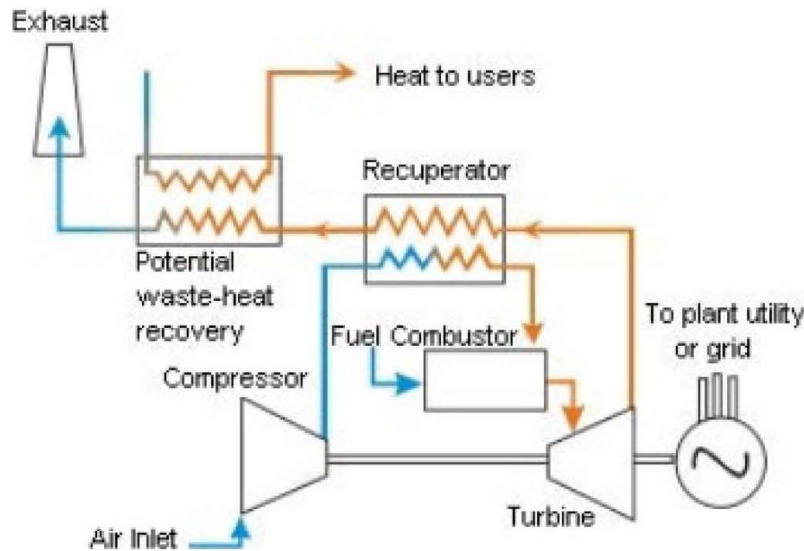


Fig. 1.15: Typical layout of a micro gas turbine [44].

1.4.8 Naval applications

According to [18], [63]-[64], this sector was the first one to implement more electrical craft concept. The main reason for that is better weight distribution and reduced man shaft lengths, which reduces hull vibrations and transmission power loss issues. Nowadays, additional motives are behind extensive electrification of naval applications, namely: reduced Noise/vibration signatures, increased fuel efficiency, and reduced/eliminated mechanical gearing. The main concepts of naval applications are IEP and IFEP. Both of these concepts find the industrial backing of military and commercial outfits and allow for a reduction in prime mover count. IFEP eliminates the need for the traditional auxiliaries generator sets and caters to a centralized grid having several generators operating at their optimum loading. Here high-speed IM is the most suitable choice for such an application. It is mainly used for its lower cost, mechanical robustness, higher-speeds, controllability, and most importantly for a wide flux-weakening operation, where high-speed IM excels and naval applications demands. High-speed IM are in naval applications used for example as assisted turbochargers.

1.4.9 Aerospace applications

As described by [18] and [65]-[67], nowadays, the research takes place in two main concepts of aerospace applications: MEA and MEE. The MEE aims at replacing functions of

critical nature to the engine traditionally driven off by mechanical systems by using the electrical drive. Thus potentially eliminating external gearboxes and the strategic relocation of components such as starter/generators and hydraulic systems. The MEE concept also increases global propulsion efficiency by targeting three main areas, namely:

- A reduction of existing pumping losses
- Replacing the conventional pneumatic engine starting methods
- Reducing to a certain degree, or even eliminate, the number of utility bleed-offs required for systems such as cabin pressurization and compressor deicing

The MEE also caters to enabling emergency power extraction through wind-milling of the main power plant. The goal of MEA is to include MEE with all the engine auxiliaries being driven by electrical variable speed drives, together with electrically driven control surface actuators and landing gear. High-speed machines are therefore preferred in such applications. For example, high-speed machines are directly coupled to the auxiliary power turbine, flywheels, or engine-starting functions which demands a wide operating speed range.

2 Electromagnetic analysis of high-speed IM with solid rotors and calculation of solid rotor end-effects correction factors

2.1 Analytical analysis of high-speed IM with a solid rotors

In the past, there has been an effort to create analytical methods for the design and calculation, of the performance, of high-speed IM. However as it was stated before, these analytical methods included some simplifications. The first thought of the researchers was the assumption of an unsaturated rotor having constant permeability. This resulted in poor validity of the calculated electrical machine. Later on, the three-dimensional nature of the solid rotor was included in the analytical method, which improved the results of analytical methods.

In today's modern analytical methods, the saturation of a solid rotor is included. For this reason, many researchers are trying to divide the solid rotor into several layers. This helps to better describe the solid rotor with analytical equations. For example, one of the more comprehensive analytical methods for the analysis of a high-speed induction machine with solid rotors was presented in work [68], where it combines the three-dimensional linear method and transfer matrix method for calculation of the performance of the machine. Additionally, both the saturation and finite-length effects were taken into account. Here, the active region of the solid rotor is divided into saturated and unsaturated parts, with an assumption of sinusoidal time dependence and phasor quantities used in the solution. But this method was applied only on the calculation of smooth solid rotors where different materials were tested on the machine performance, with an assembly of the equivalent electrical circuit for steady-state performance. The results obtained by the method had agreed fairly well with the measured results. The main drawback of this analytical method is its limitation to only one type of a solid rotor. However, this type of rotor is very rarely used in the industry, and besides, the analytical method is rather complicated.

Newer analytical methods, which are dividing the solid rotor into several parts, are trying to get even better results by using other numerical methods than those in the literature described above. Some of these analytical methods are presented in [69] - [77]. These analytical methods are trying to estimate torque, power, or eddy-current losses accurately. Nonetheless, they are limited mainly to smooth solid rotors with or without a copper coat. A publication [78] that is not related directly to the high-speed induction machine, focuses on the issue of analytical solution of electromagnetic field

problem of the high-speed spinning ball. This publication is more related to applied physics but can be useful in the determination of some aspects of the performance of high-speed IM with the solid rotor for example torque or eddy-current losses. The ball can be considered as a rotor with a round shape and the physical principle, used for the ball, can be applied for a cylindrical rotor. Overall, these analytical methods are also rather complicated and do not provide satisfactory results compared to measured results.

Another attempt of the researchers was to create even more simplified analytical methods with emphasis on the assembly of an equivalent electrical circuit for the steady-state performance of the machine. These analytical methods are much more comprehensible and easier to use for calculating the machine performance of the high-speed IM with solid rotors. One of the older literature [79], is using for the design of a high-speed IM equivalent electrical circuit in the shape of Γ for steady-state performance. To achieve some parameters of the equivalent electrical circuit, it additionally uses a circular diagram. Such a method is outdated and in some cases not very accurate. Newer and more optimized analytical methods, where some of them are proposed in [80] - [83], are using the different equivalent electrical circuit in the shape of T, which is a more traditional and general shape used for other types of an induction machine. These methods are focusing on increasing the accuracy of calculated results with the measured results, which is done using empirical formulas. Other literature such as [84] is even proposing analytical methods for the preliminary design of high-speed IM with an assembly of equivalent electrical circuit and steady-state performance calculation. A publication [85] shows an analytical calculation of other electromagnetic parameters such as resistance and leakage reactance of the end ring of the solid rotor. A special case of single-phase IM with the copper coated smooth solid rotor is also analyzed via an electric equivalent circuit, as it is suggested in [86]. Here, the machine is analyzed via d-q axes, where each axis has its own equivalent electrical circuit. Each of the elements of the equivalent electrical circuit is then calculated with analytical formulas.

These analytical methods provide one major advantage compared to those that are dividing rotor into several parts. They can be used on other solid rotor constructions and are not limited to a smooth solid rotor only. But they also do not provide the wanted accuracy of the calculated results. As an example, an analytical method for the calculation of an equivalent electrical circuit for the steady-state performance of a solid smooth rotor will be shown below. This method is proposed in [87] and has very good agreement with calculated results from a FEM program.

The calculation is based on the equivalent electrical circuit shown in Fig. 2.1. Here iron losses are neglected and for the calculation, the fundamental harmonic component

is considered only. The parameters of the equivalent electrical circuit are as follows: R_s is stator resistance, which is determined by a classical analytical formula, L_1 is the magnetizing inductance (stator inductance), $N'_2(s)$ is the leakage inductance expressed in the rotor frame (which depends on the slip) and $R'_2(s)$ is the equivalent resistance expressed in the rotor frame (which depends on the slip). The magnetizing inductance L_1 can be determined by performing either a simulation of no-load operation (i.e., $s = 0$) or by any analytical calculation. The formula proposed in this publication for the calculation of magnetizing inductance for phase a is:

$$L_1 = \frac{\Psi_a}{I_m}, \quad (2.1)$$

where Ψ_a is flux linkage of phase a and I_m is stator peak current. This formula can be used only in assumption that input currents have sinusoidal waveform.

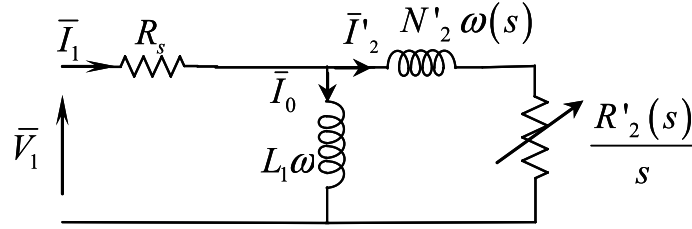


Fig. 2.1: Equivalent electrical circuit for high-speed IM with smooth solid rotor [87].

The secondary current I'_2 is determined for phase A by:

$$I'_2(s) = I_m - \frac{\Psi_a(s)}{L_1}. \quad (2.2)$$

The secondary impedance $Z'_2(s)$ of phase a can be calculated by:

$$Z'_2(s) = \frac{j \cdot \omega \cdot \Psi_a(s)}{I'_2(s)} = \frac{R'_2(s)}{s} + j \cdot N'_2(s) \cdot \omega, \quad (2.3)$$

$$R'_2(s) = s \cdot \Re\{Z'_2(s)\}, \quad (2.4)$$

$$N'_2(s) = \frac{\Im\{Z'_2(s)\}}{\omega}, \quad (2.5)$$

where ω is angular frequency of the stator field. With the assumption that the machine is fed with constant three phase's voltage, the stator current of the phase a for each slip can be determined as:

$$I_1(s) = \frac{V_1}{[Z_{op}(s) + R_s]}, \quad (2.6)$$

$$Z_{op}(s) = \frac{j \cdot L_1 \cdot \omega \cdot \left[\frac{R'_2(s)}{s} + j \cdot N'_2(s) \cdot \omega \right]}{j \cdot L_1 \cdot \omega + \left[\frac{R'_2(s)}{s} + j \cdot N'_2(s) \cdot \omega \right]}, \quad (2.7)$$

where V_1 is input voltage. For electromagnetic torque an electromotive force has to be calculated:

$$E_1(s) = V_1 - R_s \cdot I_1(s). \quad (2.8)$$

Then calculation of transmitted rms apparent power to the rotor:

$$S_{tr}(s) = \frac{3}{2} \cdot E_1(s) \cdot I_1^*(s) = P_{tr}(s) + j \cdot Q_{tr}(s), \quad (2.9)$$

where P_{tr} is active power and Q_{tr} is reactive power. Then the torque is calculated with:

$$T_{em}(s) = \frac{P_{tr}(s)}{\Omega}, \quad (2.10)$$

$$\Omega = \frac{2 \cdot \pi \cdot n}{60}, \quad (2.11)$$

where n is rotational speed of the solid rotor. The formula for the torque can be even used for calculation of torque-slip characteristics, which can help to determine starting torque or pull out torque of the machine.

Overall, using the analytical methods for designing or calculating the performance of high-speed IM can be in some cases fast and simple process. But for this type of electrical machine, it mostly comes with rather complicated formulas that hold some simplifications, which impairs the accuracy of the calculated results compared to the measured results. Moreover, some analytic methods can be applied only on some specific rotor construction, which are defined using empiric formulas. So they are not usable on every type of high-speed IM. From the description above, the reason for the inaccuracies can be described and summarized with one following formula:

$$d = \sqrt{\frac{2}{\omega_p \sigma \mu}}, \quad (2.12)$$

where ω_p is the angular frequency of the penetrating field, σ is electrical conductivity of material, and μ is permeability of material. Permeability of material can be written as:

$$\mu = \frac{B}{H} = \mu_r \cdot \mu_0, \quad (2.13)$$

where B is magnetic flux density, H is magnetic field strength, μ_r is relative permeability and μ_0 is permeability of vacuum.

Formula (2.12) is called penetration depth of magnetic field and it states how deep the magnetic field of the higher harmonic components penetrates into the solid rotor. So the most crucial part of the solid rotor is the outer layer of the solid rotor, which is the most sensitive to higher harmonic components of the magnetic field. The formula will be discussed and described further in this part.

The formula contains three variables, where two of the variables mostly complicate the assembly of the analytical method. The first variable is the conductivity σ of the material, which can be considered constant in the material. One could say that the conductivity of the material is dependent on the temperature of the solid rotor, and thus the conductivity varies depending on the temperature and location of the solid rotor. But the value of conductivity does not change that drastically and the most important part, for penetration depth, is the outer layer of the solid rotor. So the conductivity of the solid rotor material does not complicate the assembly of analytical methods.

The angular frequency ω_p is complicating the assembly of the analytic method much more. For example, let's assume the high-speed IM with a smooth solid rotor that is supplied with very high frequency. The stator magnetic field induces eddy currents into the rotor, with varying slip-dependent rotor frequency, which creates electromagnetic torque as well as high rotor losses. The higher the rotor frequencies are, the more of the rotor eddy-currents are pushed outwards to the surface of the solid rotor. This makes penetration of the flux density difficult, and most of the flux lines are located on the surface of the solid rotor, which creates rotor losses. Additionally, higher air-gap frequencies, that penetrate through the outer layer of the solid rotor, create most of the rotor losses. For penetration depth, the number of stator slots and frequency of power supply is very crucial, because it determines the value of higher air-gap frequencies and thus the depth of the penetration. For the smooth solid rotor, the assembly of the analytic formulas can be considered the simplest, compared to other solid rotor construction. It is due to the simple shape of the solid rotor, so the distribution of electromagnetic fields is easier to determine. But these electromagnetic fields are still complicated to analytically describe because they are time and spatially dependent. To further improve the electromagnetic parameters of the high-speed IM with a solid rotor, it is quite common to create axial slits in the solid rotor, which helps to penetrate flux lines deeper into the rotor. With this rotor modification, it is almost impossible to analytically describe electromagnetic fields in the solid rotor, due to the complexity of the rotor geometry.

The last variable is the permeability of material μ , which defines the conductivity of rotor material for magnetic fields. This variable complicates the description of analytical

methods the most because it highly depends on the type of used material, where every material has a different non-linear B-H curve. So the analytic formulas have to be, in nature, non-linear. The main problem with the permeability lies in the saturation of the solid rotor, which is directly related to the rotor field's angular frequency. As was stated above, because of the high rotor field's angular frequencies, the penetration depth of flux lines is very low. Thus, most of the rotor current is located at the outer layer of the solid rotor, mainly, in the case of a smooth solid rotor. The higher density of the rotor current located at this layer causes high saturation of rotor material. With the high saturation of rotor material, the permeability of the material is decreasing, making it more difficult to enter the fundamental component of magnetic fields into the solid rotor, because of low magnetic conductivity on the rotor surface. However, if the permeability is low, the penetration depth is high for higher air-gap frequencies. So magnetic field with a higher harmonic component penetrates deeper into the rotor, causing high rotor losses. Overall, the assembly of analytical formulas for the solid smooth rotor is the simplest, but for the axially slitted solid rotor, it is incredibly difficult.

All these described assumptions can be easily verified in some of the 2D FEM programs. In this work, Ansys maxwell was used for the calculation of high-speed IM and verification of the assumptions. For example permeability of material for smooth solid rotor can be seen in Fig. 2.2(a). Here the relative permeability of the

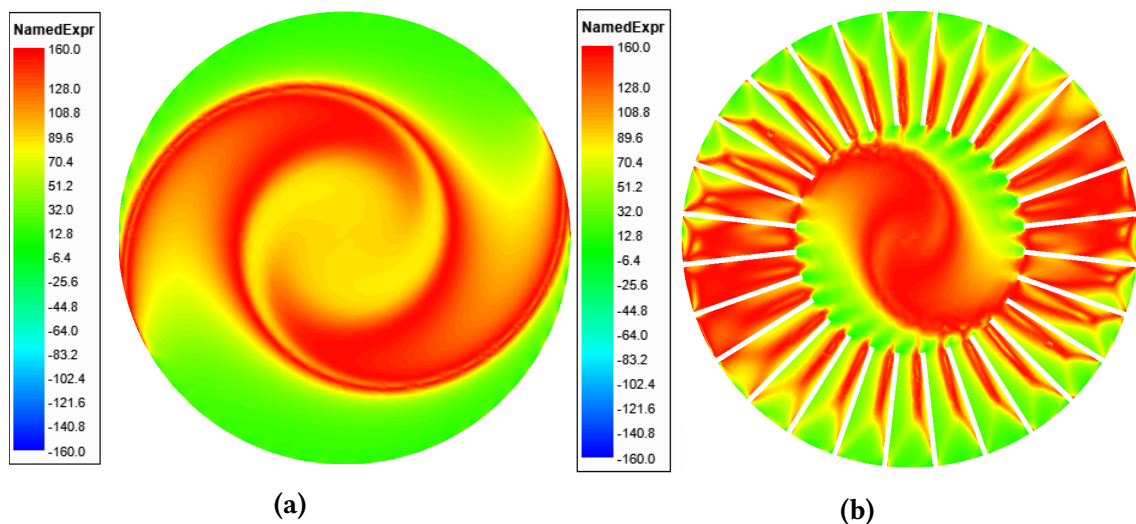


Fig. 2.2: Distribution of relative permeability in: (a) smooth solid rotor and (b) axially slitted solid rotor.

rotor material is lowest at the outer part of the solid rotor and increases towards the rotor yoke. This is caused by the higher rotor frequencies that push the rotor current outwards to the rotor surface. Although, it does not apply to some parts of the solid rotor, where it can be seen that on two sides the value of the permeability is high. And

even the rotor yoke does not have the same value of permeability and is changing due to higher rotor frequencies. It can also be seen the reaction of the stator and rotor magnetic fields, which causes curvature of the field when the machine is loaded. In Fig. 2.2(b), the permeability of the rotor material is further affected by axial slits in the solid rotor. Here the field is much less periodical than in the previous construction.

Another example can be seen in Fig. 2.3(a), where is shown the distribution of rotor losses in the smooth solid rotor. It can be seen that most rotor losses are found on the rotor surface. This proves, that the most rotor current is located on the outer layer of the solid rotor, due to high rotor frequencies. Additionally, most of the rotor losses are caused by higher air-gap harmonic components of the magnetic field, where the largest concentration of rotor losses is right below the rotor surface. The depth of penetration indicates how deep the largest concentration of rotor losses will be. Thus, it highly depends on the conductivity of the material, rotor frequency and permeability of the material. The concentration of rotor losses then decreases towards the rotor yoke. The distribution of the rotor losses for the axially slitted solid rotor can be seen in Fig. 2.3(b). Here the largest concentration is as well, under the surface of the rotor.

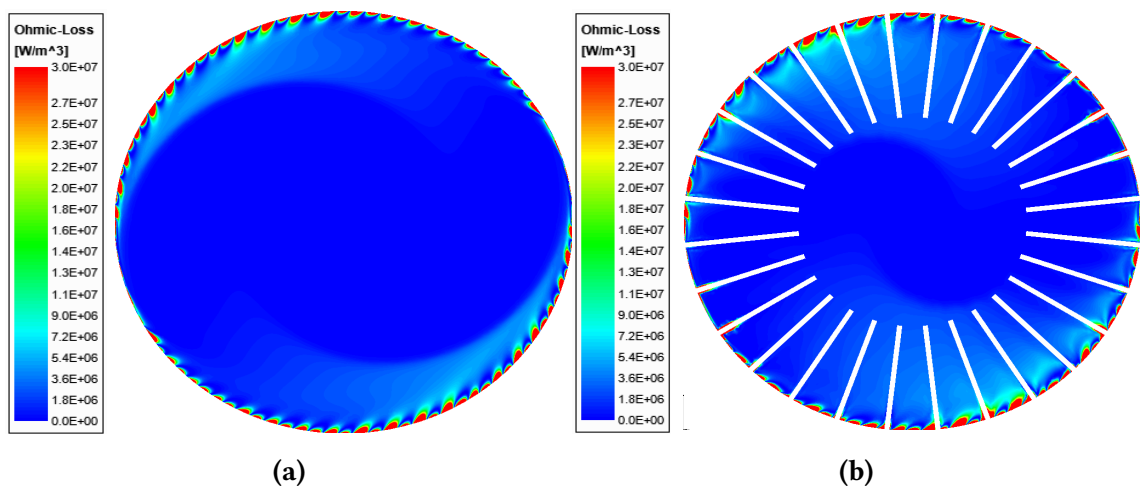


Fig. 2.3: Distribution of eddy-current losses in: (a) smooth solid rotor and (b) axially slitted solid rotor.

In conclusion, it can be assumed that the issue of analytical methods is very extensive and complex. This work will not focus on those issues or procedures on how to assembly the analytical formulas. Some of the problems behind it were outlined above. For this reason, it is nowadays much more effective and easier to use FEM programs, that use modern numerical methods. As was shown above, it is quite easy to calculate a high-speed IM with solid rotors and verify all the physical principles behind it. Moreover, it can analyse the machine in space and time. In the next section, the possibilities of high-speed IM with a solid rotors analysis using FEM programs will be discussed.

2.2 FEM analysis of high-speed IM with a solid rotors

This section will deal with the possibilities of high-speed IM with a solid rotor using FEM programs. Therefore, the main goal will not be to describe the principle of calculation using the FEM method. For further information, literature [88] - [93] explains the principle of calculation using FEM, where some of this literature even shows direct use in electrical engineering.

As it was stated, the best choice for calculating high-speed IM with solid rotors is using FEM based software. It is due to very good agreement with measured results. However, compared to analytical methods, it can become time-consuming. In general, high-speed IM with solid rotors are, from the physical point of view, complex electromagnetic systems. For that reason, simulation of such a machine is recommended to be carried out in 3D space, to capture all of the 3D aspects of the machine and to reach the best possible agreement with measured results. Unfortunately, according to [94] - [97], a complex geometry must be created in 3D space with very fine mesh. On top of that, to improve the accuracy of the results a time-stepping method is used. With this method, the transient states of the machine are simulated, but it is very time consuming, expensive, and requires a large amount of memory. On the other hand, this type of simulation includes effects of eddy-currents, a saturation of material, and non-linear properties. The benefits of 3D simulation are, for example, taking into account that magnetic flux can pass from one pole to another in multiple ways, as stated in [98]. In another instance, [99], complex distribution of eddy-currents and the changes in the magnetic flux density distribution is included and can be simulated with very good accuracy. As stated in publication [100], the stator end-winding leakage inductance is taken into account with all 3D aspects. And as reported by [101], the 3D simulation takes into account leakage inductance of the solid rotor ends.

Although 3D simulations have the best agreement with the measured results, it has a major drawback, due to which this type of simulation is not recommended. And that is time-consumption, which can take even months. For simulation time reduction, time-harmonic analysis can be considered, or combined 3D numerical and analytical computation approach for analysis, as publication [102] suggests. However, it still takes a lot of time due to the 3D nature of geometry, which is complex and needs to have a very fine mesh in order to calculate the results correctly. Another disadvantage of 3D simulations is the precision of setting up the simulations themselves. If anyone, who is setting up the simulation makes a mistake, it can lead to false simulation results. Considering the nature of 3D simulation, which can take even months, the design of such a machine can get very expensive.

A much better option is to simulate the machine in 2D space. A major advantage of this is a significant reduction of simulation time consumption. Time consumption can be reduced from months to days or even hours. Moreover, the needed space for memory is reduced, and using such simulation is less expensive. On the other hand, 2D simulations lose all the benefits of 3D simulation. That includes calculation of end-winding leakage inductance, the leakage inductance of the solid rotor ends, complex distribution of eddy-currents and other described or related benefits. This leads to very poor agreement with measured results. Fortunately, nowadays the abilities of 2D electromagnetic field computation programs are much more advanced, as publication [103] suggests. These shortcomings can be included in the model and simulation in such a way that the accuracy of calculated results is very close to those of 3D simulation and measured one.

In the next section, an emphasis will be placed on how to include 3D aspects of high-speed IM machine with solid rotors in 2D simulations.

2.3 Finite length of the solid rotor and solid rotor end-effects

When 2D FEM based programs are used for calculations of high-speed IM with solid rotors, the whole rotor is treated as an infinitely long solid conductor. Hence, the inductances of the rotor ends are not taken into account in the coupled circuit modeling. Therefore, some assumptions have to be established in order to calculate the machine properly and correctly.

The first one is, the rotor power factor angle remains too small, and thus the power factor of the whole machine in the 2D analysis is too optimistic. According to [104], the power factor of the smooth solid rotor can be estimated. If the rotor surface impedance is solved using linear materials, where formula (2.12) of penetration depth is used, its angle will be 45° . This corresponds to the phase shift between the electric field strength and the surface current, which is also 45° when using linear theory. This produces for a non-saturating smooth rotor a power factor of $\cos\varphi = 0.707$. Such a power factor is wrong and contrary to other obtained results with the practical experiments, the phase angle of the solid rotor is far less than 45° . For this reason, Agarwal's limiting non-linear theory assumes idealized rectangular magnetization characteristics for smooth steel surface. Agarwal's model also assumes that the flux density within the material may exist only at a magnitude up to a saturation level, either positive or negative. For estimation of surface impedance Agarwal's depth of penetration is used:

$$d_{\text{Agarwal}} = \sqrt{\frac{2}{\omega_r \sigma \mu}} = \sqrt{\frac{2H_0}{\omega_r \sigma B_s}}, \quad (2.14)$$

where H_0 is the peak value of the sinusoidal applied surface magnetic field strength, ω_r is angular frequencies of the rotor fields, and B_s is the saturation value of magnetic field flux density. The phase shift of the impedance of the solid rotor calculated with Agarwal's limiting non-linear theory is then 26.6° , which corresponds to a totally saturated smooth solid rotor. Hence, the power factor of solid rotor is $\cos\varphi = 0.894$. Based on these two theories, the rotor power factor angle should vary between 26.6° and 45° . So the value of the power factor of the solid rotor should vary between $\cos\varphi = 0.707 - 0.894$, depending on the circumstances. In [105], a non-linear variation of the fundamental B-H curve was used in the calculation. It was concluded that the rotor impedance phase angle varies between $35.3^\circ - 45^\circ$, which corresponds to the value of power factor $\cos\varphi = 0.707 - 0.816$. The test results showed that the real phase angle of the rotor impedance approaches the lower value when the slip increases and the magnetic field strength drives the surface of the rotor steel into magnetic saturation. So the values in both methods come very similar in size. These methods unfortunately do not apply to every type of rotor construction. For example, if the solid rotor is slitted the rotor power factor angle is 22° , which corresponds to the value of power factor $\cos\varphi = 0.927$, as stated in [104]. But this interval still gives an idea of the size of the power factor.

The second assumption is the path of the rotor currents. As it was stated, due to high slip-dependent rotor frequencies, the rotor current is pushed outwards to the outer layer of the solid rotor. In the rotor ends region the skin effect forces the currents to flow at the end ring surface. So the path for the rotor currents will be mainly under the surface of the solid rotor, as is illustrated in Fig. 2.4.

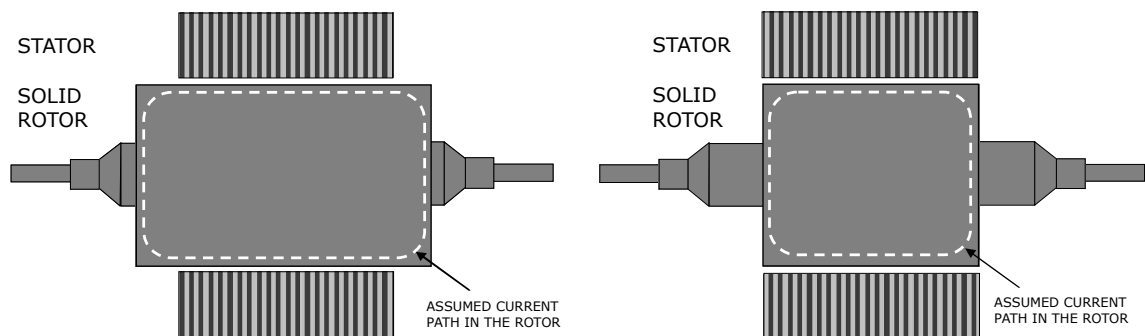


Fig. 2.4: Assumed curved current paths in the solid-rotor with long (left) and short (right) end iron lengths [106].

This can be easily verified in 2D FEM simulation on some simple machine with a solid rotor. In 2D FEM simulation, it is not common to calculate the path of rotor currents in the axis along with the solid rotor. But a current density can be shown in the cross-section of the solid rotor. This can at least partially verify the assumption with sufficient

accuracy. The distribution of current density is shown in Fig. 2.5. It can be seen that in both, the solid smooth and axially slitted solid rotor, the highest density of current is right under the surface of the solid rotor. This confirms the assumption of the current path. At a closer look, smaller regions right under the rotor surface can be seen there, and each of the regions has the opposite polarity of current density than the rest of the rotor. These regions are currents induced by higher air-gap frequencies. The location of these currents matches those of the rotor losses in Fig. 2.3. The only part of the current path which cannot be verified with 2D FEM simulation is in the rotor end. But, this part of the solid rotor is also very important.

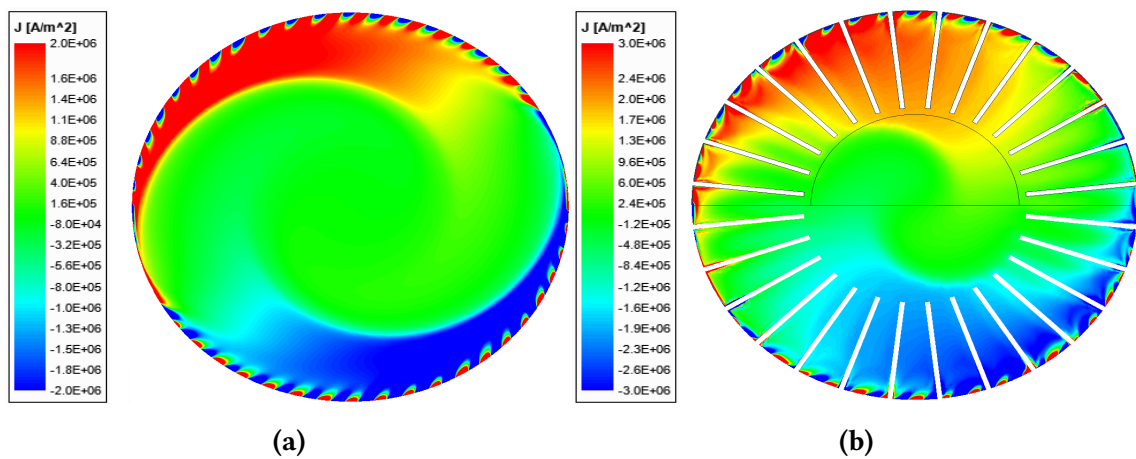


Fig. 2.5: Distribution of current density in: (a) smooth solid rotor and (b) axially slitted solid rotor.

As stated in [105], the longer the rotor end is, the higher will be apparent resistance, which is caused by the skin effect that forces the current to the rotor surface. So the skin effect basically lengthens the current path. This is also assumed in Fig. 2.4. For the optimal end ring length, Agarwall's formula for depth penetration can be used for the calculation of end rotor regions. This way, it is possible to achieve the lowest apparent resistance and at the same time the best efficiency of the machine, as [106] suggests.

The third and last assumption is directly related to the rotor end regions and is the most crucial for 2D FEM calculations. When the solid rotor is modeled in 2D space, the main problem is related to the rotor impedance behavior, which is tightly related to the rotor field solution. The reason is that in 2D space (or 2D FEM based programs) it is only possible to specify the axial stator length of the whole model. So the rotor end regions cannot be directly specified or modeled in the 2D space. However, a lot of 2D FEM based programs allows specifying bond between objects, for example, in induction machines with squirrel cage the rotor bars are connected with a copper ring. In 2D FEM programs these rotor bars are connected by resistance and leakage inductance between 2 rotor

bars. In the case of a solid rotor, it is much more complicated, because the whole rotor geometry has to be taken into account instead of just rotor bars. So it is not an easy task to correctly determine, how to split a solid rotor into parts and which parts of the solid rotor to connect with the resistance and leakage inductance. There is also no guarantee if this procedure is correct, due to the absence of calculations and visualization of magnetic fields along the rotor axis. This is the biggest drawback of 2D FEM simulation, compared to 3D FEM simulation. But this issue can be bypassed as stated in [104], by modifying the solid rotor impedance. The modification of the solid rotor impedance acts as the much needed 3D rotor end-effect and it is done with a simple formula:

$$Z_{\text{fix}} = k_{\text{er}} Z_r, \quad (2.15)$$

where Z_{fix} is corrected solid rotor impedance, k_{er} is complex corrective end-effect factor, and Z_r is solid rotor impedance. Also the phase angle of the rotor impedance can be calculated as:

$$\cos\varphi_r = \frac{R_r}{Z_r} = \frac{R_r}{\sqrt{R_r^2 + (\omega_r L_{r\sigma})^2}} = \frac{R_r}{\sqrt{R_r^2 + (s\omega_s L_{r\sigma})^2}}, \quad (2.16)$$

where R_r is resistance of the solid rotor, ω_s is the angular frequency of the stator field, and $L_{r\sigma}$ is leakage inductance of the solid rotor.

The complex corrective end-effect factor has the function of increasing the impedance of the active part of the solid rotor by the impedance of the rotor end regions. Without it, the solid rotor impedance will be too small and the output power of the machine too optimistic. In 2D FEM calculations, the 3D rotor end-effects are traditionally taken into account by modifying the rotor effective resistivity by an end-factor, because the reactance of the solid rotor cannot be changed in these programs. The corrected effective resistance can lead to a very accurate calculation of the machine torque, but the calculation of the power factor of the rotor and also the entire machine will undoubtedly fail. This is demonstrated in Fig. 2.6.

In the figure, it can be seen that the magnitude of calculated and measured total impedance differs. That is due to the impossibility of changing the rotor reactance in the 2D model, which has to be increased due to the absence of the rotor end regions. This difference just indicates the unchanged reactance of the solid rotor. Also, the phase shift of both total impedances naturally differs, which is most important for the power factor. The phase shift of the calculated total impedance has a lower value, which leads to a higher power factor. The phase shift of the measured total impedance, on the other hand, has a higher value. This leads to a lower value of the power factor. In the literature [2], a high-speed IM with a solid rotor was studied on this effect. It was concluded that

calculated power factor had value of $\cos\varphi = 0.68$, but the real measured machine had power factor value of $\cos\varphi = 0.61$. The difference is large, given the power factor, so using this method will inevitably lead to incorrect power factor determination.

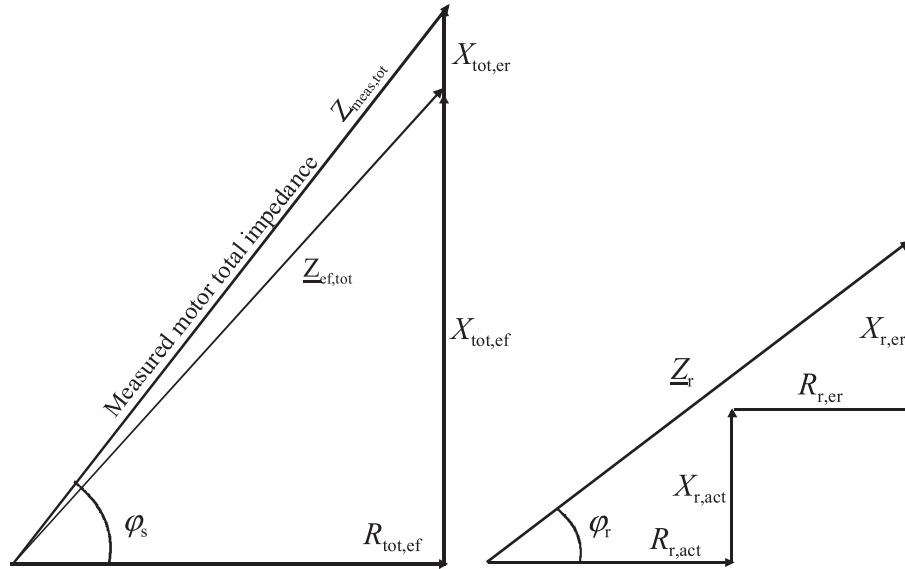


Fig. 2.6: Solid rotor induction machine total impedance at the rated operational point (left) and solid rotor impedance consisting of active and end region part [104].

In the vast majority of cases, it is possible to change only the rotor conductivity in 2D FEM programs. The conductivity of the rotor is directly related to the effective resistivity of the rotor, which is very convenient in this case. Instead of changing the resistivity of the rotor, the conductivity of the rotor will be changed instead. This can be done by the end-effect factor for conductivity in the same way, as for the resistivity. The next section, of this work, will provide an overview of most of the correction end-effect factors used for rotor conductivity correction, from various authors.

2.4 Corrective end-effect factors

2.4.1 Corrective end-effect factors for a solid rotor

The formula for correction of the solid rotor conductivity, in the case of 2D FEM calculations, is the same as for correction of the solid rotor impedance in the formula (2.15):

$$\sigma_{\text{Corr}} = k\sigma, \quad (2.17)$$

Here, corrected conductivity is given by modified conductivity of the rotor material by end-effect factor. The rotor conductivity must be recalculated for the operating temperature of the machine, but the issue of heat calculation is out of the scope of this work. The end-effect factor k is represented here in general and many publications

show its different shape.

According to Russell [10], the rotor ends can be taken into account in the computations by modifying the rotor resistivity by the end-factor depending on the length and the pole pitch of a solid rotor:

$$k_{\text{Russell}} = 1 - \frac{2\tau_p}{\pi L_r} \tanh\left(\frac{\pi L_r}{2\tau_p}\right) \quad (2.18)$$

where τ_p is the pole pitch and L_r is the rotor length.

As reported by O'Kelly [107], for calculation of end-factor that reduces the rotor equivalent conductivity, the end-effect corrective factor is dependent on the length, the pole pair number, and average rotor radius:

$$k_{\text{O'Kelly}} = \frac{L_r}{L_r + \frac{\pi r_{\text{ave}}}{p}}, \quad (2.19)$$

where r_{ave} is the average rotor radius and p is the pole pair number.

Woolley's [8] formula for the end-factor depends on length, outer diameter, and additional parameters of a solid rotor and is defined as:

$$k_{\text{Woolley}} = \left[\frac{1}{2} \left(Q_1 + \sqrt{Q_1^2 + 4k_1 \cdot \tanh\left(\frac{pL_r}{D_r}\right)} \right) \right], \quad (2.20)$$

where D_r is the rotor outer diameter. The variables Q_1 and k_1 are defined as:

$$Q_1 = 1 - \left(\frac{D_r}{pL_r} + k_1 \right) \tanh\left(\frac{pL_r}{D_r}\right), \quad (2.21)$$

$$k_1 = \frac{z_{\text{er}}\rho_c}{y_{\text{slit}}\rho_{\text{er}}}, \quad (2.22)$$

where z_{er} and ρ_{er} represent the end region thickness and the resistivity, y_{slit} is the slit depth and ρ_c is the cylindrical shell region resistivity.

In study presented by Yee [7], it is assumed that the rotor current density is confined in a thin shell around the rotor. The end-factor for a smooth solid rotor is defined as:

$$k_{\text{Yee}} = \frac{aL_r \left(1 + \coth\left(\frac{aL_r}{2}\right) \right)}{aL_r \left(1 + \coth\left(\frac{aL_r}{2}\right) \right) - 2}, \quad (2.23)$$

The variable a is defined as:

$$a = \frac{\pi}{\tau_p} \quad (2.24)$$

According to Trickey [5], the end-factor depends on the inner and outer diameters and the pole pair number of the rotor, and is defined as:

$$k_{\text{Trickey}} = \frac{p}{2} \left[\frac{1 + \left(\frac{D_{\text{in}}}{D_r}\right)^p}{1 - \left(\frac{D_{\text{in}}}{D_r}\right)^p} \right], \quad (2.25)$$

In the case of a slitted solid rotor, the inner diameter D_{in} can be defined according to the rotor slit depth:

$$D_{\text{in}} = D_r - 2y_{\text{slit}}. \quad (2.26)$$

It should be noted, that (2.25) does not take into account the rotor length. Thus, according to Trickey's formula, the correction factor is a constant value for all rotor lengths.

The corrective end-effect factors listed above, are the most basic and well know. The studies in [2] and [108], presented a comparison between all of these corrective end-effect factors on a real machine. For the case study, a three-phase, two-pole 170 Hz induction machine equipped with a slitted solid steel rotor with an output power of 120 kW was chosen. The solid rotor had at the beginning long "end rings", which were gradually shortened piece by piece. For achieving the most comparable results between the measured and FEM calculated values, the machine was supplied directly from the 50 Hz network instead of the frequency converter. This led to a reduction of supply voltage, which had to be reduced to keep the air-gap flux density and the machine performance at rated values. Thus, the nominated output power of the machine was reduced to around 35 kW. This also led to a higher nominal slip of the machine.

The main goal of the work was to show the difference between each corrective end-effect factor with respect to the length of the rotor. The study showed that the corrective factor according to Trickey (2.25), had the highest value of all corrective factors. However as was expected, the value was the same regardless of the length of the rotor. The lowest value, on the other hand, had a corrective factor according to Russell (2.18). Each of the corrective factors was then applied in the 2D FEM simulation of the electrical machine with the solid rotor and calculated with different load conditions. The real machine was also measured with the same load conditions.

The main two investigated quantities were the torque and power factor of the machine. In terms of machine torque, the corrective factor for Woolley (2.20), Yee (2.23),

and mainly Trickey (2.25) had the worst agreement with the measured results. On the other hand, Russell (2.18) and O’Kelly (2.19) had the best and quite accurate agreement. In terms of the power factor of the machine, all of the corrective end-effect factors noticeably failed, for the reasons described in the previous section. Only Russell’s and O’Kelly’s came closest to the measured characteristics. Overall, O’Kelly end-effect factor gave quite accurate results and provided a good approximation in a wide rotor angular frequency range. However, the calculation with O’Kelly’s factor failed, because the behavior of the correction factor is more linear than the real measured torque-speed characteristics. This was most noticeable in the characteristics of the power factor. For this reason, Russell’s end-factor was chosen as the best option. As the author suggested, the results are not too realistic as the rotor frequency increases, but the generated electromagnetic torque had a great accuracy when the machine is close to the synchronous speed. That is because the solid rotor is not heavily saturated.

The biggest issue of all listed end-effect factors is that most of them are partly based on the calculation of the penetration depth. So this basically means that the conductivity (or apparent resistance) of the solid rotor is adjusted only on the basis of the geometry of the solid rotor. This is not entirely correct, because the same machine, with the same geometrical dimensions, may have a different rotor slip in a given operation. This assumption was verified for example in [12], using 3D FEM simulation. For that reason, an additional function that includes a rotor slip frequency should be added, because the magnetic flux in the rotor end-regions is associated with the most heavily saturated parts of the rotor. Due to the skin effect to the rotor currents, the rotor end-regions drifts in a deep saturation, which additionally increases the apparent resistance of the solid rotor when the slip increases. Thus, an additional correction factor that includes a slip was presented in [108] by Aho. This factor was used with Russell’s end-factor as a basis for the slip-corrected end-factor. Total correction factor then contains both of the factors is written as:

$$k_{\text{tot}} = k_{\text{Russell}} \cdot k_{\text{Aho}}, \quad (2.27)$$

where k_{Aho} is the slip-corrected factor by Aho. The correction factor k_{Aho} further increases the rotor resistivity. This formula was created with experimental measurements and finite element calculations. The factor is written as:

$$k_{\text{Aho}} = \left(\frac{n}{n_s} \right)^4. \quad (2.28)$$

With the Aho correction factor, the calculated results of the torque compared with the measured values showed much better accuracy and almost matched the measured torque-speed characteristics. Unfortunately, the power factor of the whole machine still did not show the desired accuracy. But the calculated results approached a little

bit more the measured values. So it can be concluded, that despite very accurately calculated results of the torque, the power factor cannot be calculated correctly in 2D FEM calculations, if this type of end-effect corrective factor is used. That is due to the lower phase angle of the solid rotor impedance, which is caused by not including the reactance of the rotor end regions.

For even better results of the calculated torque and power factor of the slitted solid rotor, a modified version of Russell's correction end-factor formula (2.18) was presented in [109]. A classic Russell's correction factor has a minor disadvantage and that is using only the whole length of the rotor in the calculation. So it is not possible to enter the length of the rotor end region in the formula. Considering the length of the active part and additionally the end regions of the rotor in the formula, will result in different values of the correction factor and better agreement between calculated and measured results. The shape of modified Russell's formula is:

$$k_{\text{Russell,M}} = 1 - \frac{\tau_p}{\pi l_s} \frac{\tanh\left(\frac{\pi l_s}{\tau_p}\right)}{\left(1 + \tanh\left(\frac{\pi l_s}{\tau_p}\right) \tanh\left(\frac{\pi l_{\text{end}}}{\tau_p}\right)\right)}, \quad (2.29)$$

where l_s is the half of the active stator-pack length and l_{end} is the length of the rotor end beyond the active stator pack. For a more detailed comparison between the classic and modified version of Russell's corrective coefficient, let's assume for example a machine with the following parameters needed for calculation:

- Outer diameter of rotor $D_r = 500 \text{ mm}$,
- Number of poles $2p = 2$,
- Length of stator pack $l_s = 750 \text{ mm}$.

By entering these values into the formulas (2.18) and (2.29) with a gradual increase in the length of the rotor ends from 0 to 675, the graphs are created and shown in Fig. 2.7. The length of the rotor end is deliberately high in the graph to explain the difference between the two formulas. In reality, such a long rotor end could not of course be realized, due to much worse electromagnetic performance and the dynamics of the solid rotor. Here it is shown for demonstration purposes only. In the graph, it can be seen that both of the characteristics have noticeably different courses, which is caused by adding the length of the rotor end to modified Russell's corrective factor. However, one thing is very important to note because it diametrically distinguishes the two formulas. The course of modified Russell's corrective factor formula tends to be constant with increasing rotor length, where the classical formula is still rising. Hence, at some point of the rotor length,

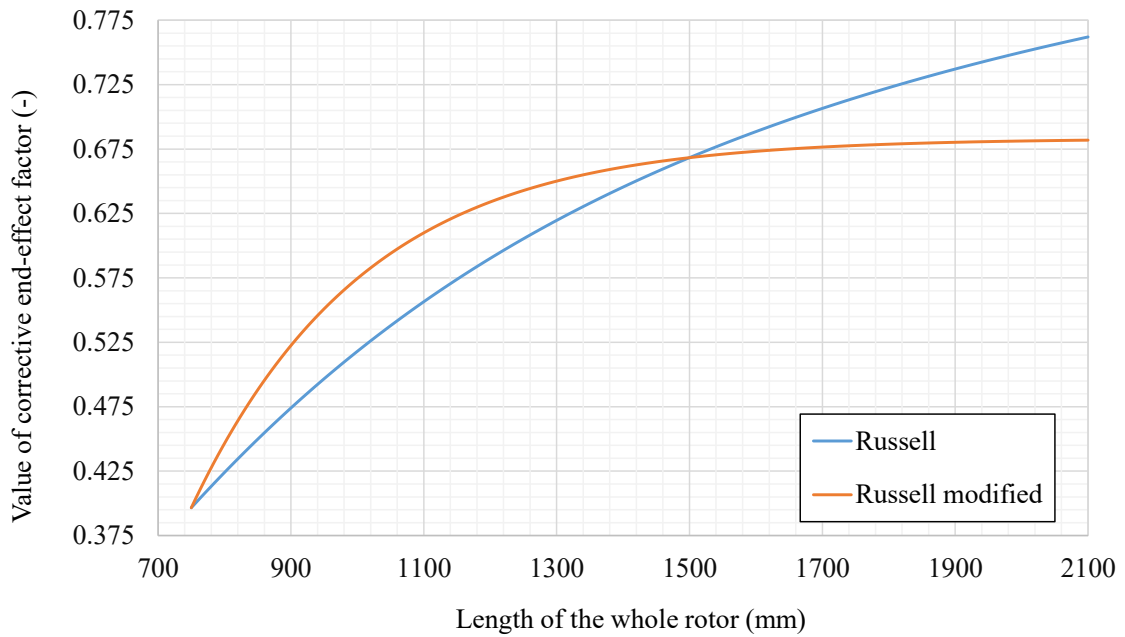


Fig. 2.7: Graph comparing classic and modified formula of the Russell's end-effect factor.

the corrective factor of the modified formula will be constant. Where on the other hand, the corrective factor of the classical formula will rise to a value of one, with a very long rotor. But this is not correct, because if very long rotor ends would be considered, the current in the rotor would not flow to its end. Instead, it would be dispersed beyond the stator pack end in a way that it flows through the path of least resistance, no matter how long is the solid rotor or how large is the total impedance of the solid rotor. This is approximately demonstrated in Fig. 2.8 on one half of the whole machine.

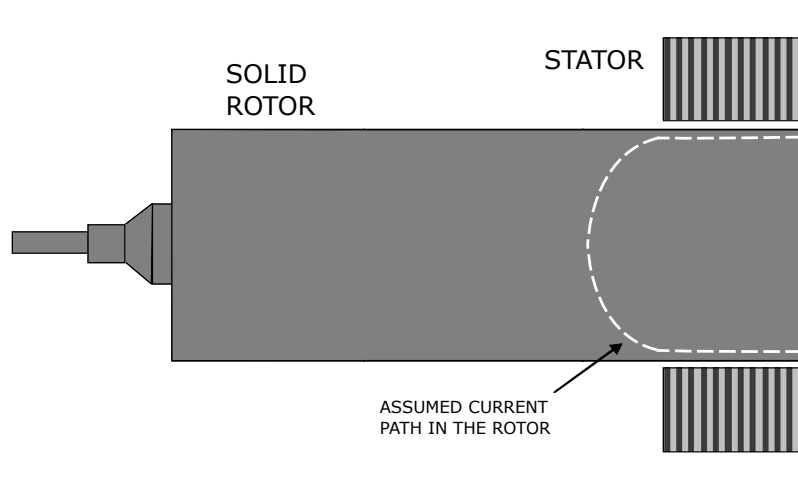


Fig. 2.8: Assumed curved current path in the solid rotor with very long rotor end region.

The modified Russell's formula, therefore, ensures that the value of the final conductivity of the solid rotor will not rise beyond some point of the rotor length. If

the classic Russell's formula would be used in a case with very long rotor ends, it could result in an incorrect value of final conductivity, which would result in bad results of 2D FEM simulation.

It could be pointed out that the current path in the rotor also depends on the rotor frequency, which will have some effect on the value of the modified Russell's end-effect factor. This is true, thus the slip-correction factor has to be applied in this case as well. In the same study, a new slip-correction factor was proposed which corrects the modified Russell's end-effect factor:

$$k_{\text{tot}} = k_{\text{Russell,M}} \cdot k_{\text{PAN}}, \quad (2.30)$$

where k_{PAN} is the slip-correction factor by Pyrhonen, Aho and Nerg. This factor is based on Agarwal's depth of penetration, which is further improved by experimental measurements in a way that has good agreement with the measured results:

$$k_{\text{PAN}} = 1 - c \cdot \omega_r^{\frac{3}{4}}, \quad (2.31)$$

where c is an adaptation coefficient.

The adaptation coefficient c is used for further correction of slip-correction factor k_{PAN} . In the study, the adaptation coefficient was determined based on measured results with the polyfitting technique to obtain good agreement between the simulations and measurements. For the case study, a three-phase, two-pole 170 Hz induction machine equipped with a slitted solid steel rotor with an output power of 120 kW was chosen. On this machine, the value of the adaptation coefficient was determined to be $c = 0.022$. But, the value of the adaptation coefficient may slightly differ with another machine. Therefore, the slip-correction factor by Aho can be used instead, because it purely depends on the slip of the rotor.

Despite an even better agreement between calculated and measured results, the value of the calculated power factor of the whole machine is still not satisfactory due to the lower phase angle of the rotor impedance. For this reason, a method for correction of power factor was proposed in [2], [104], and [109]. This correction method can be used for both formulas of Russell's correction factor and it is even compatible with both slip-correction factors. The correction of the power factor is based on Agarwal's nonlimiting theory. Using this theory a total rotor impedance is raised by end-region inductance, which is not included in the 2D FEM calculation and creates an error between calculated and measured results. This was described and demonstrated in previous section in Fig. 2.6. It is assumed that the smooth ferromagnetic end rings are heavily saturated under load and produces an inductance corresponding to the phase angle of 26.6° . This correction approach is also called Agarwal's inductance at the rotor

end. This procedure will be shown in the following example:

Let's assume a machine with a slitted solid rotor with the following parameters needed for calculation:

- Outer diameter of rotor $D_r = 197.5 \text{ mm}$,
- Number of poles $2p = 2$,
- Length of stator pack $l_s = 280 \text{ mm}$,
- Length of rotor end region $l_{\text{end}} = 20 \text{ mm}$,
- Supply frequency $f = 170 \text{ Hz}$,
- Angular frequency of the rotor fields $\omega = 13.9 \text{ rad/s}^{-1}$.

First, the conductivity of the solid rotor is modified by Russell's factor. In this case, a modified Russell's factor is used:

$$k_{\text{Russell,M}} = 1 - \frac{\tau_p}{\pi l_s} \frac{\tanh\left(\frac{\pi l_s}{\tau_p}\right)}{\left(1 + \tanh\left(\frac{\pi l_s}{\tau_p}\right) \tanh\left(\frac{\pi l_{\text{end}}}{\tau_p}\right)\right)} = 0.46. \quad (2.32)$$

Then the slip-dependent correction factor is applied. Here, correction factor k_{PAN} is used:

$$k_{\text{PAN}} = 1 - 0.022\omega_r^{\frac{3}{4}} = 0.84 \quad (2.33)$$

where the total correction factor for the solid rotor is:

$$k_{\text{tot}} = k_{\text{Russell,M}} \cdot k_{\text{PAN}} = 0.386. \quad (2.34)$$

As it can be seen in 2.34, the rotor conductivity must be lowered to 38.6% to take the rotor end effects into account in the torque production. So the resistivity of the rotor material is then increased by a factor of:

$$\frac{1}{k_{\text{tot}}} = \frac{1}{0.386} = 2.59. \quad (2.35)$$

So it can be said, that the slitted part producing torque accounts only for 38.6% of the total rotor resistive impedance. Thus, 61.4% of the rotor resistance comes from the end effects. This illustrates how dominating the end effects in a purely solid rotor really are. For further calculation, let's assume that the value of rotor impedance is in the per-unit system $Z_r = 1 \angle 22^\circ$, which can be calculated with 2D FEM programs. According to Agarwal, the impedance phase angle is assumed to be 26.6° , in the smooth end areas.

The rotor total inductance is calculated so that 38.6% of the rotor has an inductance corresponding to the phase angle of 22° and 61.4% of the rotor will have an inductance corresponding to the rotor angle of 26.6° . The rotor end-leakage reactance is:

$$X_{er} = j0.614 \cdot \tan(26.6^\circ) = j0.305. \quad (2.36)$$

Then this reactive part of Agarwal's impedance has to be added to the active part impedance $Z_r = 1 \angle 22^\circ = 0.927 + j0.375$ of the rotor, which will result in the rotor total impedance in the per-unit system:

$$Z_r = 0.927 + j(0.375 + 0.305) = 0.927 + j0.68 = 1.15 \angle 36^\circ. \quad (2.37)$$

This newly recalculated impedance is used for the correction of the calculated power factor of the whole machine. It also should be noted, that the corrected impedance of the rotor is changing based on the slip of the machine. This has to be included in the calculation if the torque slip characteristics are investigated. Using this approach in the study proved to be very accurate for the correction of the power factor.

Aside from both main factors described above, a corrective factor given by Yee [6] can be written in a way that it includes slip dependency. The shape of the formula is:

$$K_{Yee,M} = 1 + \frac{\frac{2}{a \cdot L_r}}{\coth\left(\lambda \cdot \frac{L_r}{2}\right) + \frac{a \cdot \coth\left(\gamma \cdot \frac{L_r}{2}\right)}{\gamma} - \frac{2 \cdot a}{L_r \cdot \gamma^2}}, \quad (2.38)$$

where l_{gap} is the length of the air gap. Where variables a , λ , and γ are written as follows:

$$a = \frac{\pi}{\tau_p}, \quad (2.39)$$

$$\lambda = \sqrt{j \cdot \omega_r \cdot \mu \cdot \sigma}, \quad (2.40)$$

$$\gamma = \sqrt{a^2 + \frac{\lambda}{l_{gap} \cdot \mu_r}}. \quad (2.41)$$

In case of very small rotor frequencies, $\coth\left(\frac{a \cdot L_r}{2}\right) \approx 1$ and in addition, setting $\gamma \approx a$, the formula (2.38) gets the form of (2.23). Therefore, with smaller rotor frequencies, the formula becomes frequency independent, as [103] states. This may result in an incorrect 2D FEM calculation of the torque. For this reason, this corrective factor is not very accurate, which was proven in the study [2] and [104].

2.4.2 Corrective end-effect factors for a smooth solid rotor and copper coating

These corrective end-effect factors are mainly for high-speed machines with a smooth solid rotor and a copper coating. In the study [23], a corrective factor for a smooth solid rotor with a copper coating was presented. Each of the factors is calculated and applied separately to each part in the rotor for the best and most accurate 2D FEM simulation results. The reason for the separate calculation is the different behavior of each part from a physical point of view. Both of these corrective factors have been verified with measurements on a real machine. In this case, for correction of a smooth solid rotor conductivity, the following formula is applied:

$$\sigma_{\text{Corr}} = \frac{1}{k_z^2} \cdot \sigma, \quad (2.42)$$

where k_z is the corrective end-effect factor for the smooth solid rotor with the following shape:

$$k_z = 1 + \frac{2 \tau_p}{\pi L}. \quad (2.43)$$

The corrective factor for the copper coating depends on several following factors, which has to be included in the calculation:

- For better electromagnetic performance, if the manufacturer's capabilities allow it, a copper coat is thicker on the end regions of the solid rotor. This minimizes the solid rotor impedance.
- The length of the copper coat.
- The number of space harmonic.

Based on these factors, a sketch is created and illustrated in Fig. 2.9.

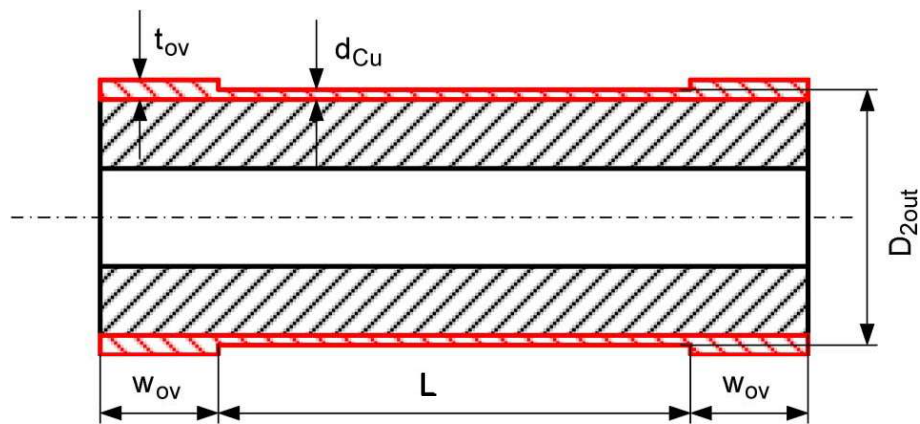


Fig. 2.9: Sketch of the smooth solid rotor with a copper coating [23].

For the correction of the copper layer conductivity, the Russell-Northworthy's coefficient is used. This correction factor has a very similar shape to that of modified Russell's

correction factor but is adjusted to the stated factors. The formula for correction of the copper coat conductivity has a classic shape:

$$\sigma_{\text{Corr}} = k_{\text{RN}}\sigma, \quad (2.44)$$

where k_{RN} is the Russell-Northworthy's correction end-effect factor:

$$k_{\text{RN}} = 1 - \frac{\tanh(0.5\beta_\nu L)}{0.5\beta_\nu L [1 + k_t \tanh(0.5\beta_\nu L) \tanh(\beta_\nu w_{\text{ov}})]}, \quad (2.45)$$

where k_t is the correction factor for the thicker layer of the copper coat and β_ν is constant that depends on the number of space harmonic. The correction factor k_t is very important in 2D FEM calculation because a thicker layer of the end-regions on the copper coat cannot be modeled in a 2D space. So the conductivity of the copper coat on the active part of the solid rotor is changed based on the thickness of the thicker layer. The formula for this corrective factor is:

$$k_t = 1 + \frac{1.2(t_{\text{ov}} - d_{\text{Cu}})}{d_{\text{Cu}}}, \quad (2.46)$$

where t_{ov} is the thickness of the copper coat at the rotor end regions and d_{Cu} is the thickness of the copper coat on the active part of the rotor. After a closer look at the formula (2.46), it can be seen that the corrective factor k_t does not depend on the thickness of each part of the copper layer but rather on the thickness ratio of both copper layers. The thicker is the copper layer at the rotor end regions the higher conductivity of the copper layer on the active part of the rotor will be in the 2D FEM model. The thickness of both copper layers can be the same but this will result in lower conductivity of the copper coating in the 2D FEM model.

And the last variable β_ν is written as:

$$\beta_\nu = \nu \frac{\pi}{\tau_p}, \quad (2.47)$$

where ν is the number of space harmonic. The formula (2.47) acts as a constant, that changes the conductivity of the copper layer based on the number of space harmonic components. That means with a higher number of space harmonic components the copper layer will be more conductive. So it acts as a higher harmonic frequency filter where it let the fundamental harmonic component of the magnetic fields pass. In 2D FEM simulation, the most important is the fundamental harmonic component so in that case $\nu = 1$.

The only drawback of both corrective factors is that they are slip independent. Thus, slip correction for end-factor (2.28) and (2.31) can be applied. Also, the formula (2.45) for correction of the copper layer can be used for any other rotor construction that contains the copper coat.

2.4.3 Corrective end-effect factors for a solid rotor with high-conductive end-rings

If the solid rotor is equipped with end-rings made of a high-conductive material, e.g. copper or aluminum, the rotor end-effects should be also considered. The studies [11], [22], and [29], presented an approach to obtain fairly accurate 2D FEM calculation results. The approach is very similar to that in the previous cases. For example, the copper end rings represent a 3D end-effect that cannot be included in the 2D model. So, an equivalent conductivity for the rotor material has to be calculated. The equivalent conductivity takes the resistivity of the end rings into account when the rotor conductivity is considered.

The equivalent conductivity for the solid rotor is:

$$\sigma_{\text{Corr}} = k_e \cdot \sigma, \quad (2.48)$$

where k_e is corrective end-factor for copper end rings:

$$k_e = 1 + C \cdot (\alpha - 1), \quad (2.49)$$

where $c = 0.3$ for thick copper end-rings and $C = 1$ for rotors without copper end rings. The coefficient α represents copper end-rings resistance contribution to the solid rotor and is expressed with Russell end-effect factor:

$$\alpha = \frac{1}{k_{\text{Russell}}} = \frac{1}{1 - \frac{2\tau_p}{\pi L} \tanh\left(\frac{\pi L}{2\tau_p}\right)}, \quad (2.50)$$

where L is the active part of the solid rotor.

The calculation of the correction factor for copper end-ring is based on the assumption of eddy-current paths in the solid rotor as it is demonstrated in Fig. 2.10(a). In Fig. 2.10(b) it is assumed that the rotor current flows more or less axially in the solid rotor and in circumference direction in the copper end-rings. Hence, the approximation of the conductivity of the solid rotor, equipped with copper end-rings, fits the current flow much better than without copper end-rings.

And additionally, for the preliminary design of the width of the copper rings, it is possible to use the formula for Agarwal's depth of penetration (2.14). Or another method for calculation of copper end-rings thickness can be used, which is based on the analogy of the squirrel cage induction machine. This method is proposed in [22].

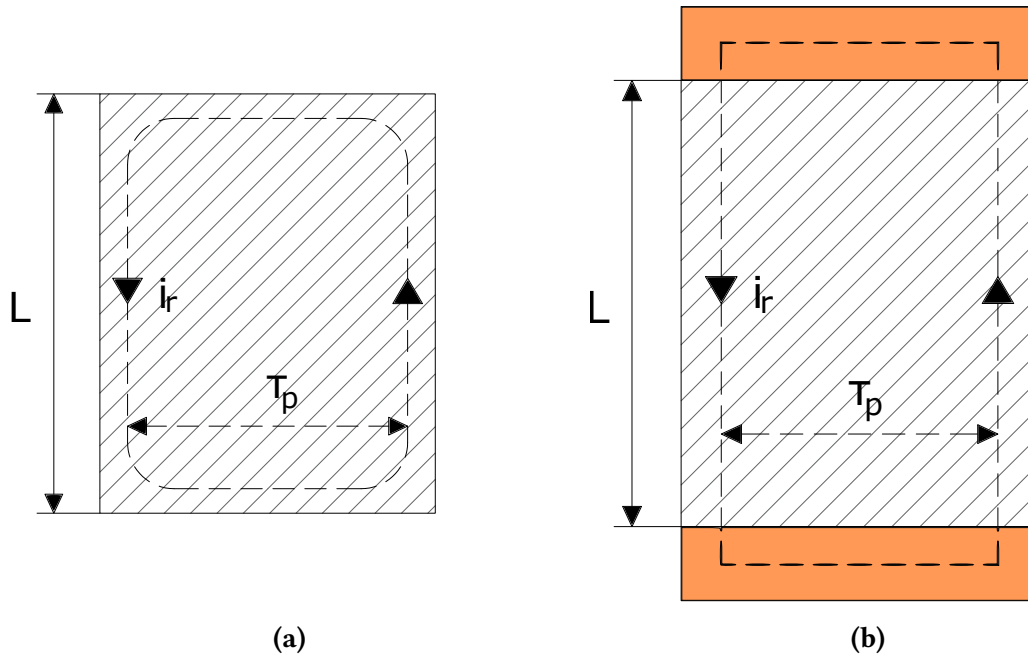


Fig. 2.10: Rotor induced eddy current paths: (a) without copper end-rings, (b) with copper end-rings [22].

2.4.4 Corrective end-effect factors for a solid rotor with a radial rotor surface grooves

This is a special case of rotor surface modification to improve the electromagnetic performance of the electrical machine with a solid rotor. As it was mentioned before, higher air-gap frequencies, which are caused by stator slotting and additionally (depending on rotor construction) rotor slitting, penetrates through the surface of the solid rotor and causing high-frequency rotor eddy currents mainly underneath the rotor surface. These high-frequency rotor eddy currents are demonstrated in Fig. 2.11. The rotor eddy currents additionally cause high rotor losses, which increases the rotor temperature. For this reason, radial grooves are created on the rotor, which has the task of disrupting these high-frequency eddy currents, according to, [22] and [43].

As it was stated, for coating of the solid rotor either high conductive or high resistive material is used. In this case, by grooving the solid rotor surface, the surface becomes effectively more resistive and thereby cutting the path of high-frequency harmonic currents. Thus, radial grooves are acting as a high resistive coating for the solid rotor. In studies [22] and [43] radial grooves were used on the case study machine. The rotor eddy current losses beneath the outer surface were decreased significantly by 75% for 400 Hz, 70% for 600 Hz, and 65% for 800 Hz. For 800 Hz operating frequency the total rotor eddy current losses were decreased by 30%. In the 2D model, the radial grooves

are created as an outer layer of the solid rotor with defined depth. The end-effect factors for correction of the rotor conductivity are defined for the outer layer and the rest of the rotor separately. The conductivity of the outer layer, which represents the radial grooves, should be decreased by approximately 80-90%, depending on the machine. A method for calculating the correction factor for the radial grooves will be shown below.

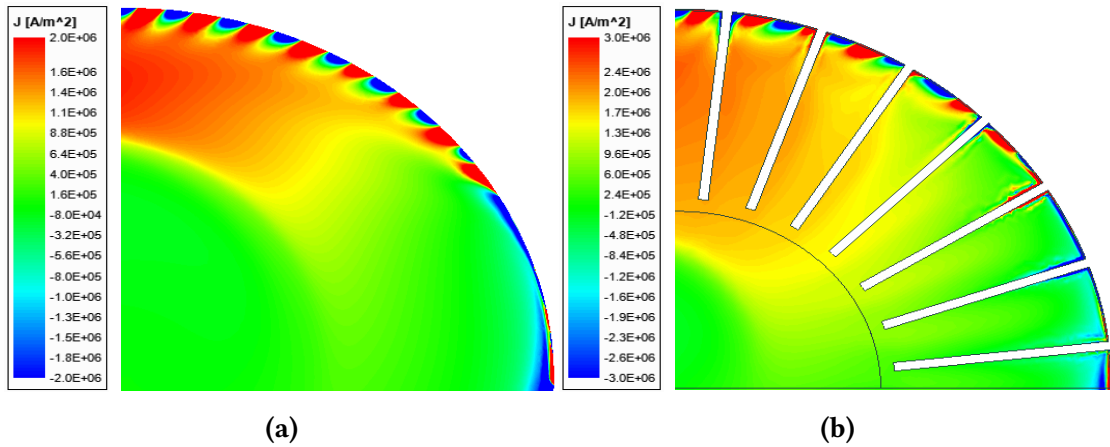


Fig. 2.11: Detail of distribution of current density in: (a) smooth solid rotor and (b) axially slitted solid rotor.

The geometry of the radial grooves consists of three main parameters as is shown in Fig. 2.12. The width of the radial grooves (a) depends mainly on the capabilities of the manufacturer. It can vary between 0.1 - 1 mm, also depending on the machine size. The depth of the radial grooves (c) depends on the penetration depth of the higher air-gap frequencies. It can be easily calculated with a classic formula for penetration depth (2.12). The distance between each radial groove (b) is the most important for the calculation and determines the conductivity of the radial grooves in the 2D model.

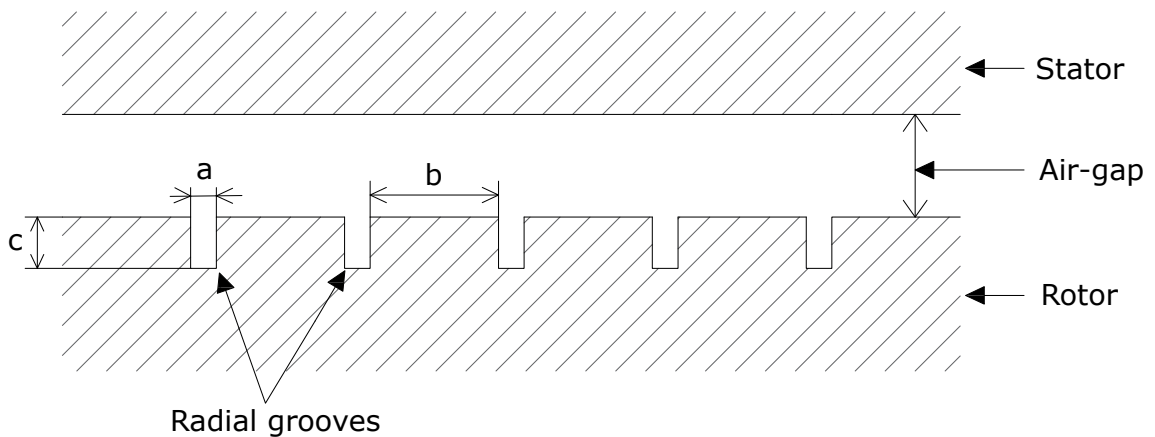


Fig. 2.12: The geometry of the radial grooves on the stator surface according to [22].

As an example, let's assume an electrical machine with the 3-phase stator winding with shortening of the winding step to 5/6 equipped with an axially slitted solid rotor with the following parameters needed for calculation:

- Number of stator slots $Q_1 = 24$,
- Number of rotor slits $Q_2 = 28$,
- Outer rotor diameter $D_r = 150 \text{ mm}$,
- Number of poles $2p = 2$,
- Length of the active part of the rotor $L = 250 \text{ mm}$.

First, to determine the conductivity of the radial grooves, a 2D FEM simulation is needed to get the distribution of flux density in the air gap. Then FFT analysis is performed to get all the components of the air-gap flux density. For this example, a graph containing all harmonic components of the air-gap flux density is shown in Fig. 2.13. The graph shows that the air-gap flux density is composed of fundamental and higher harmonic components caused by stator slotting and rotor slitting. So the most dominant higher harmonic components are with ordinal numbers -23, 25, -27, and 29. According to [43], for the calculation of the correction factor, all higher harmonic components were used. But newer study [22] shows that the highest value of the higher harmonic components is preferred. So for the calculation, higher harmonic components with ordinal numbers -27 and 29 are used, which corresponds to the rotor slits.

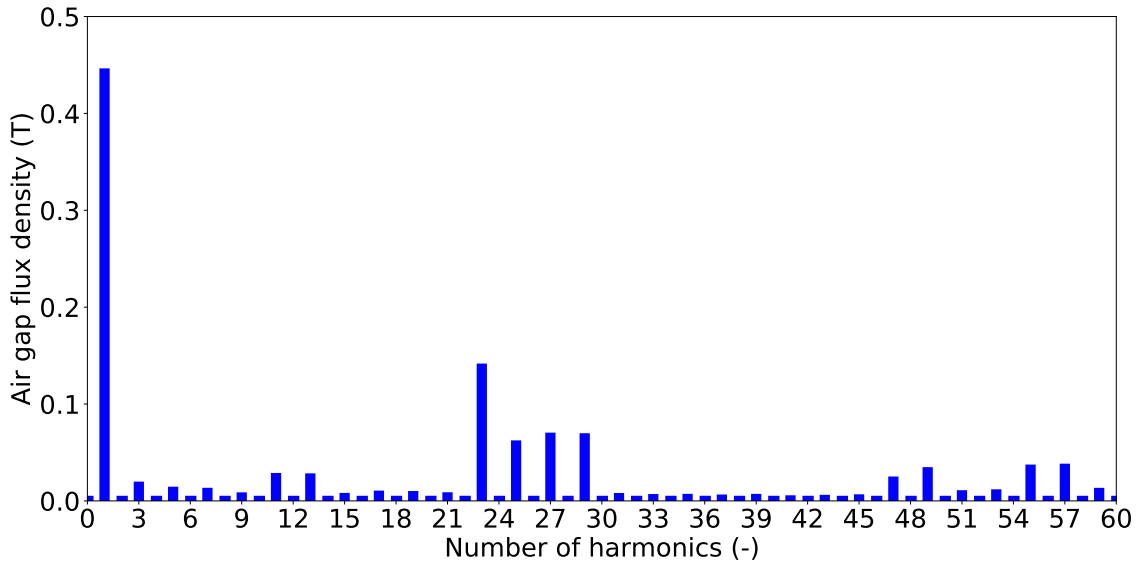


Fig. 2.13: Air gap flux density variation with its harmonic spectrum.

For the calculation of the corrected conductivity for the radial grooves, Russell's end-effect factor is used, which takes into account the rotor ends by decreasing conductivity

in the 2D computation. However, instead of calculating one corrective factor, an average equivalent Russell end-effect factor (2.51) is calculated, which consists of corrective end-effect factors for fundamental (2.52) and higher harmonic (2.53) air-gap fields.

$$k_{R,eq} = \frac{k_{R,\nu=1} + k_{R,\nu}}{2}, \quad (2.51)$$

$$k_{R,\nu=1} = 1 - \frac{2 \cdot \tau_p}{\pi \cdot l_{Fe\nu}} \tanh\left(\frac{\pi \cdot l_{Fe\nu}}{2 \cdot \tau_p}\right), \quad (2.52)$$

$$k_{R,\nu} = 1 - \frac{2 \cdot \tau_{p\nu}}{\pi \cdot l_{Fe\nu}} \tanh\left(\frac{\pi \cdot l_{Fe\nu}}{2 \cdot \tau_{p\nu}}\right), \quad (2.53)$$

where $l_{Fe\nu}$ is the distance between each individual radial groove and represents dimension (b) in Fig. 2.13, ν_{ave} is average value of higher harmonic component, and $\tau_{p\nu}$ is the average pole pitch of the stator slot harmonic fields. Dimension $l_{Fe\nu}$ is assumed as an iron length path for high-frequency harmonic currents and is selected and designed with respect to the active length of the rotor and width of the radial grooves. $\tau_{p\nu}$ is assumed as the length of the pole pitch for high-frequency eddy currents under the rotor surface. The following example shows the whole process of calculating the correction factor for the radial grooves and is based on previously determined machine parameters:

In this case, the width of the radial grooves is selected to 0.5 mm and thus with the respect to the active part of the rotor, the length between the radial grooves is 8 mm:

$$k_{R,\nu=1} = 1 - \frac{2 \cdot \tau_p}{\pi \cdot l_{Fe\nu}} \tanh\left(\frac{\pi \cdot l_{Fe\nu}}{2 \cdot \tau_p}\right) = 9.471 \cdot 10^{-4} \quad (2.54)$$

$$\nu_{ave} = \frac{|-27| + 29}{2} = 28 \quad (2.55)$$

$$\tau_{p\nu} = \frac{\tau_p}{\nu_{ave}} = 13,09 \text{ mm} \quad (2.56)$$

$$k_{R,\nu} = 1 - \frac{2 \cdot \tau_{p\nu}}{\pi \cdot l_{Fe\nu}} \tanh\left(\frac{\pi \cdot l_{Fe\nu}}{2 \cdot \tau_{p\nu}}\right) = 0.225 \quad (2.57)$$

$$k_{R,eq} = \frac{k_{R,\nu=1} + k_{R,\nu}}{2} = 0.113 \quad (2.58)$$

So, according to (2.58), the radial grooves will have reduced conductivity up to 89%. Accordingly, in the 2D model, applying only 11% of the rotor conductivity to the outer layer of the solid rotor with the penetration depth, the rotor surface eddy current losses should be decreased significantly. Moreover, the electromagnetic torque of the machine is hardly affected by this modification of the solid rotor, according to [22].

3 Surrogate modeling

3.1 Introduction

In the last few decades, numerical design methods and models have been widely used for engineering purposes. They have become a key aspect in designing and optimizing the final product in a wide range of fields, both in science and industry. It is also due to their increasing accuracy and complexity. However, in the vast majority of cases, running these numerical design methods and models on computers takes a lot of computational time and power. To accelerate the design and optimization of the final product a surrogate modeling is used.

According to [110], surrogate modeling is often used to reduce computational time of all tasks by replacing expensive numerical simulations with approximate functions that are much faster to evaluate. Surrogate models are constructed by evaluating the original model at a set of points, called training points and using the corresponding evaluations to construct an approximate model based on mathematical functions. In other words, surrogate model is statistical model that accurately approximate the simulation outputs. It does not require large number of simulations and is able to perform hundreds and thousands of output evaluations, which would be extremely time-consuming with

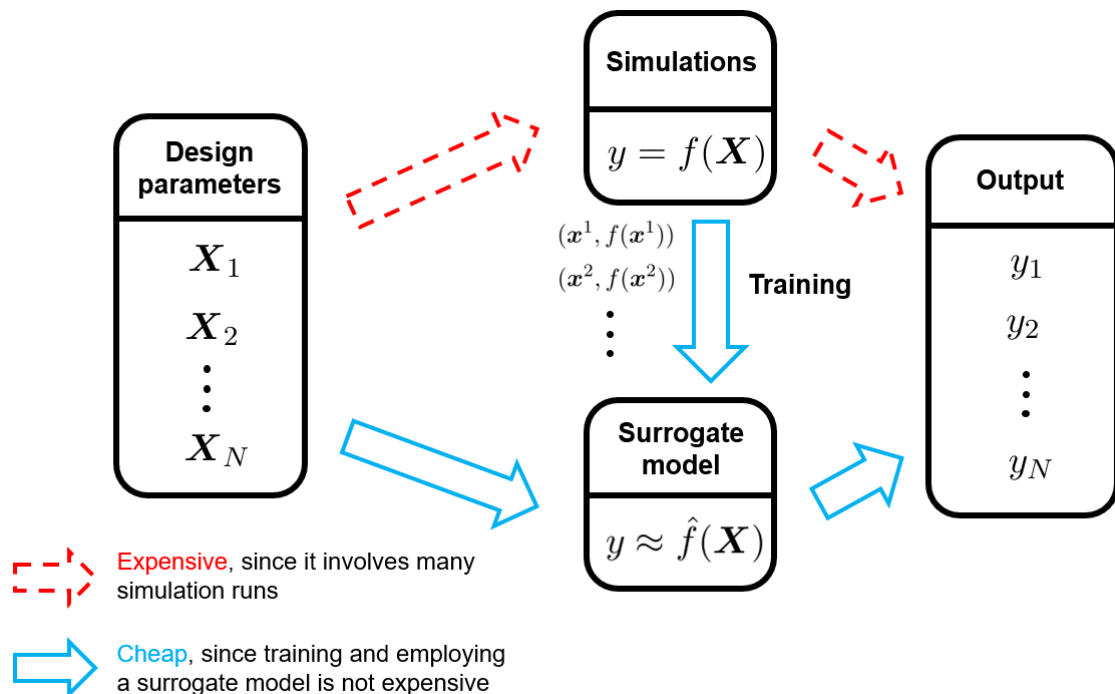


Fig. 3.1: Demonstration of the advantages of the surrogate model over conventional simulations and optimization [111].

conventional simulation and optimization. Simply put, a surrogate model is a predictive model that is trained with a set of initial simulations or calculations of some specific object or model. So, surrogate modeling is a special case of supervised machine learning. This idea is illustrated in Fig. 3.1.

Another advantage of the surrogate modeling is its easy use. Due to this reason it is gaining popularity in a wide range of scientific and engineering fields. Just to name few fields for example: medical [112], automotive [113], electronics [114], oil industry [115], chemical process engineering [116], fluids [117] and many others. Surrogate modeling is additionally very suitable for the design and optimization of electrical machines, especially the ones with solid rotors. The next section will deal more with the basic idea about surrogate modeling and its use for electrical machines with a solid rotor.

3.2 Workflow of surrogate modeling

As stated in [111], a surrogate model is trained using a data-driven approach. Its training data is obtained via probing the simulation outputs at several suitably selected locations in the design parameter space. At each of these locations, a full simulation is conducted to calculate the corresponding simulation output. By assembling the pairs of inputs (design parameters) and their corresponding outputs into a training dataset, a statistical model can be build based on the obtained dataset.

For an electrical machine, this means that a sensitivity analysis of the machine must be performed. So, the first step to create a surrogate model is to make a list of all input variables of the proposed electrical machine. For example number of conductors, depth of slits, width of slits and others. One of the disadvantages of the surrogate model is that it cannot work very well with too many input parameters of the designed product. The acceptable number of input parameters is up to around 10. However, if the investigated object (electric machine) had around 50 input parameters, the surrogate model would not be able to accurately evaluate the output parameters of the object (electric machine). The electrical machine with a solid rotor has low number of input parameters, so the surrogate model can be applied. On the other hand, for example, Line-start synchronous machines would be problematic because they have a high number of input parameters. In that case, another methodology for machine design and optimization would have to be chosen, such as optimization using a genetic algorithm, as [118] suggests. After selecting all suitable input parameters, it is also necessary to select the important and monitored output parameters, such as electromagnetic torque, electromagnetic efficiency, power factor and other. Based on the selected input and output parameters a sensitivity analysis must be preformed to show the

relationship between input and output parameters. This is done by executing several calculations, where each input parameter is individually changed in a wide range of values with reasonable limits. Here, the calculations can be preformed by FEM-based program, preferably in 2D space for electrical machines with a solid rotor, as it was discussed in section 2.2. Based on all calculated results, graphs are created, which show the dependence of all input parameters on each monitored output parameter of the calculation. If the input variables differ in their size and physical unit, it is preferable to convert all input parameters to per unit system. This will achieve relative growth of each input parameter and better comparison between them. The graphs could also reveal if the function of the input parameter to the output parameter does not have some very complex function shape. This could be problematic and the approximation of the function with the surrogate model would not be possible. This would mean that the surrogate model would show poor accuracy of the output results. The best possible case scenario is when all function of input parameters to output parameters have a linear or quadratic course of the function. The reason behind this will be explained later.

Based on sensitivity analysis of the electrical machine and all available graphs with function of all input and output parameters, it can be determines which input parameters improve, or conversely degrade, the output parameter of the machine. This can help to predict the behaviour of the machine even better and narrow the selection for the input parameter limit even more. The limit of the input parameters is on of the most crucial parts of the surrogate modeling. After the selection of the most suitable limit for all input parameters, the surrogate model is ready to be made. The workflow of creating

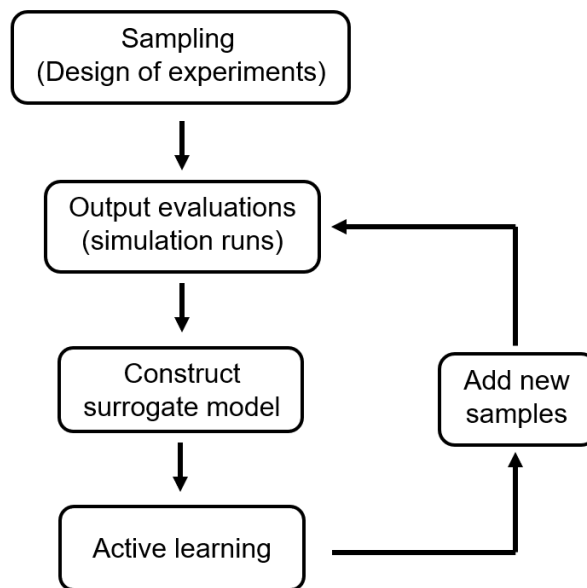


Fig. 3.2: Diagram of the workflow of surrogate modeling [111].

surrogate model, according to [111], is shown in Fig. 3.2. Each step shown in the diagram will be discussed and described in the following sections.

3.2.1 Sampling

Sampling is used to create training data for surrogate model. This is done by selecting samples from the full range of each input parameter, where each input parameter has its reasonable limit. This practice is known as design of experiments. It is preferable to have samples that are spread evenly across the input parameter space. However, this varies from case to case. For example, in most cases, it is appropriate to use a linear distribution of samples in the range of the input parameter. But, in some cases, the sampling of the input parameter could have a completely different course of the distribution. This is important, because the sampling of input parameters will affect the predicted output parameters of surrogate model. This situation is illustrated in Fig. 3.3. Here, the original function (blue line) of input parameter (X) to output parameter (Y) has some unspecified course of the function. The samples are here linearly distributed, but the samples do not reveal the minima and the maxima of the function. If this sampling would have been used in surrogate model, the surrogate model would evaluate and approximate this sampling as a linear function. This would lead to a huge error in evaluating the output values of the surrogate model. To avoid this problem, a sensitivity analysis was performed. Another task of sensitivity analysis was to reveal the course of functions between input and output parameters and, if necessary, to determine the

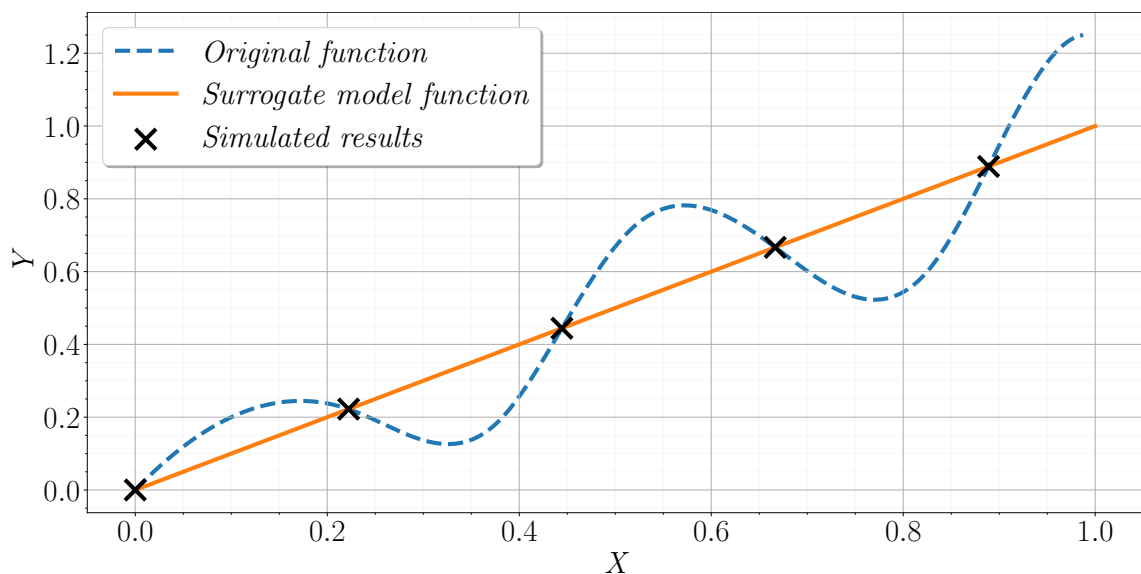


Fig. 3.3: Illustration of simulated function of input and output parameters with approximated surrogate model function.

most suitable sampling for input parameters for the most optimal approximation of the

functions for surrogate modeling.

However, to create initial training data, it is not enough to simply select suitable samples of input parameters. It is also necessary to create space-filling sampling schemes, which creates all sample combinations for the selected input parameters. Many sampling schemes exist, but the most well-known are Latin Hypercube scheme or Box-Behnken scheme. The general difference between the sampling schemes is the prediction error of the surrogate model, which is very important. So each scheme has its application to a given situation. The difference between Latin hypercube and Box-Behnken scheme is shown in Fig. 3.4. The Latin hypercube scheme is presented as 2D dimensional layout with samples in it. The Box-Behnken scheme is created as three-level cube. This work will not deal with these schemes in detail. For further information, publications

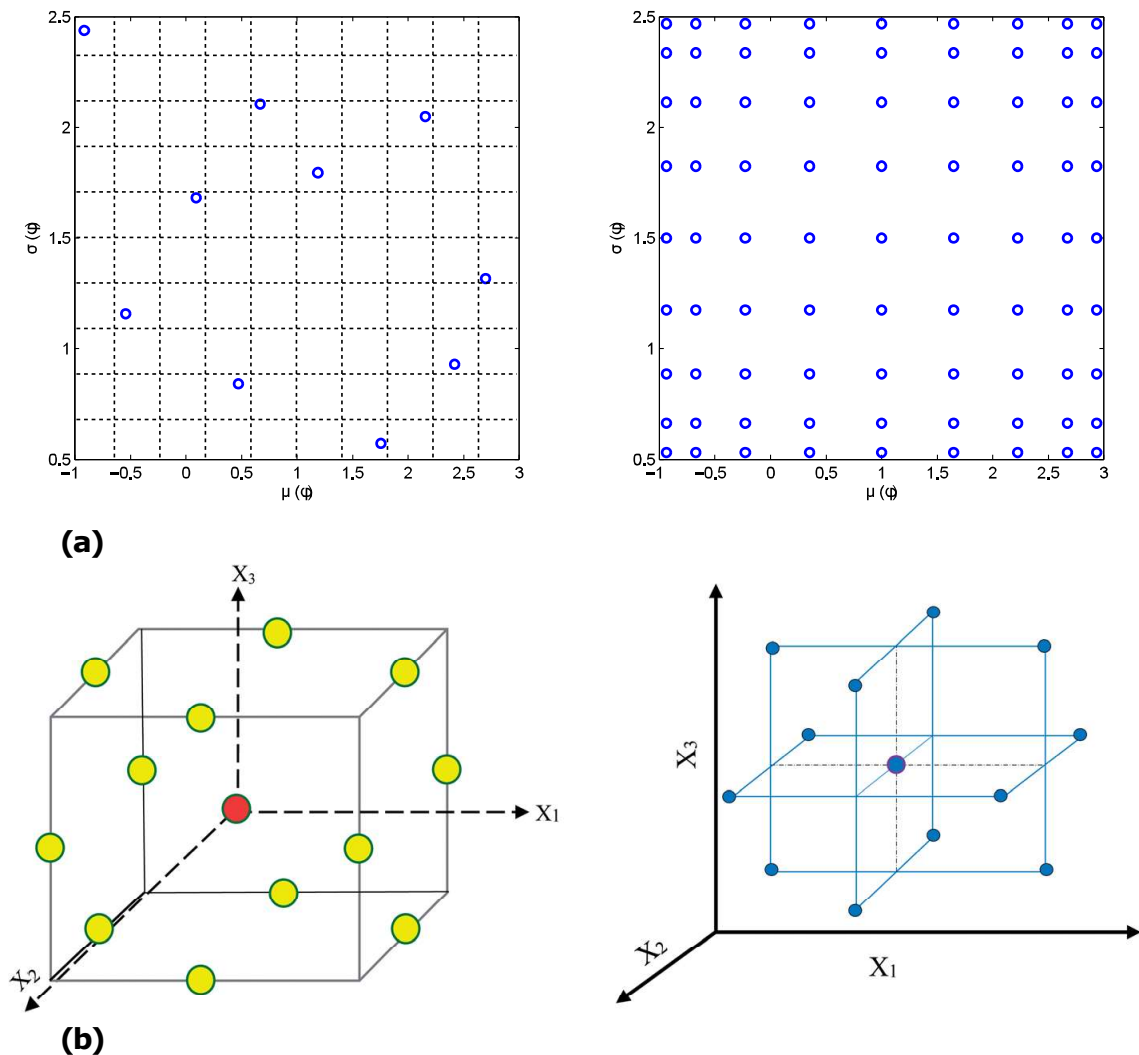


Fig. 3.4: Sampling scheme of: two-parameters Latin hypercube sampling (a) [119] and three-level Box-Behnken sampling (b) [120].

[121] - [125] provides more information on Latin hyper cube sampling scheme, where publications [126] - [130] provides more information on Box-Behnken sampling scheme.

3.2.2 Output evaluations

After the sampling scheme for initial data were determined, all these sampling points have to be simulated or calculated. After all of the simulations or calculations are completed, both input parameters and output parameters of the simulations/calculations, are assembled together in their correspondence. All data are then conveniently stored for further use on the surrogate model.

3.2.3 Construction of the surrogate model

In this step, the surrogate model is constructed by using collected training data from previous step. As the core for surrogate modeling, multiple machine learning technique exists. This work will not deal with each of the machine learning techniques in-depth or which one is the best. Publications [132] - [137] deal in depth with the surrogate modeling and possible different machine learning techniques used in it. These machine learning techniques include, for example:

- Response surface models,
- Splines with tensions,
- Gaussian processes,
- Sparse Gaussian process,
- Radial basis function,
- Polynomial regression,
- And others ...

The surrogate model itself is then created by using one of such methods mentioned above (the one that is most suitable for a given application) with the initial training data. This creates trained predictive model, that is almost ready to be used. Before the surrogate model is further used, it is also advantageous to plot surrogate model data and simulations data from initial training, as it is shown in Fig. 3.5. This way, it can be determined whether the surrogate model is creating an unwanted error, when evaluating the output parameter. If the plotted data of model predictions and simulated data have a purely linear course, then surrogate model has practically no error and is now ready to be used. If some points deviates, then the surrogate modeling is not suitable for a given application. For better testing of surrogate model, some of the initial training data (about

10%), can be taken out before creating the surrogate model and used for verification of the model. These verification data would be plotted in the same graph, but this time the error between model predictions and simulation data would be much more noticeable. This is because verification data are not included in the training data. So, naturally the surrogate model has to predict them, where in process of evaluation creates an error between predicted and simulated data.

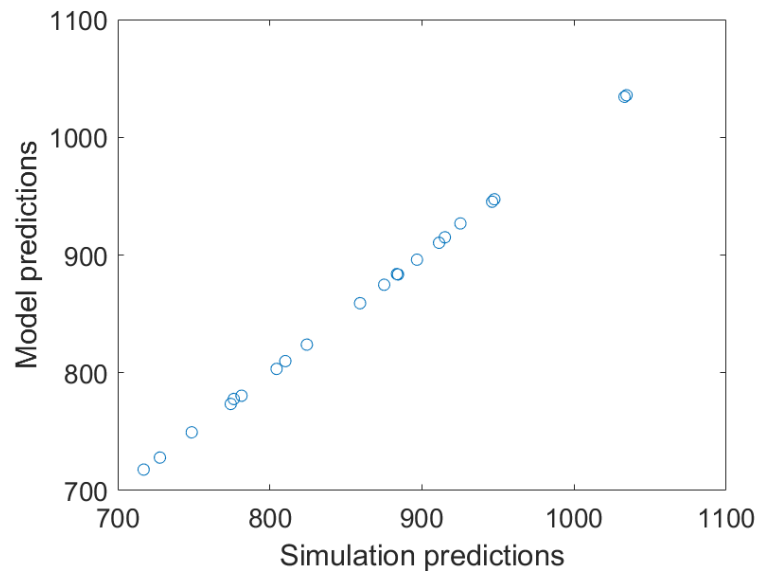


Fig. 3.5: Comparison of surrogate model predictions data and simulated data [131].

To determine how much is the linear relationship between the predicted and simulated data, and possibly see how big is the evaluation error of the surrogate model, the Pearson R coefficient can be used. This coefficient shows the strength of the linear relationship between two set of data. The value of this coefficient ranges from -1 to 1. If the coefficient is 1 then the it is purely positive linear correlation. When one parameters increases, the other increase as well with no deviation. When the value is -1 then it is purely negative linear correlation and when one parameter increases, the other is decreasing with no deviation. If the value is 0 than there is practically no linear correlation between two parameters. In addition to the pearson R coefficient, covariance can also be used. This one shows only linear relationship like the Pearson R coefficient (not its strength). The range of this coefficient is much higher, which can reveal a much greater linear correlation between the two parameters. Publication [138], deals more with these two coefficients, its characteristics, and its use.

3.2.4 Active learning

When creating a sampling scheme for initial training data, it is not possible to predict the total number of samples or sometimes the correct sampling of input parameters. There-

fore, most of the time the Surrogate model is not accurate when it is first constructed. This is determined by the complexity of the approximated input-output relation. So, in the vast majority of cases, it is necessary to enrich the initial training data of the surrogate model as the training progresses. This practice is known as Active learning.

This process has two possible approaches, where both of these approaches are done iteratively. The first one is to use learning functions, which helps to identify the next sample with the highest information value. In other words, as stated in [111] and [131], those learning functions are designed to allocate samples to regions where:

- the surrogate model is thought to be inaccurate, uncertain or where the model has the largest expected error,
- or to regions where particularly interesting combinations of design parameters lie, such as the region that possibly contains the globally optimum values of the design parameters.

This way the surrogate model can learn the fastest way. In the second approach, the samples are picked manually. Thus, the samples can be selected evenly across the limits of the input parameters, or based on the size of the monitored output parameter, or selected completely randomly. Regardless of the approach used, the accuracy of the surrogate model should increase. Publications [139] - [141] deal in more depth with the active learning of the surrogate model.

3.2.5 Adding new samples

Once the new samples have been identified, new simulations or calculations are performed in order to get new corresponding simulation data. These new data are stored in existing training data. Subsequently, the surrogate model is re-trained on the enriched training dataset. This process is iterative and is repeated until the surrogate model produces satisfying results with the highest possible accuracy and lowest possible errors. In practice, the number of iterations is often around 2 to 3.

3.3 Deployment of surrogate model

Based on the previous sections, the surrogate model is, at this point, ready to be used in the final design and optimization of the object (in this case electrical machine). The main advantage of the surrogate model, as it was mentioned at the very beginning of this chapter, namely that it can significantly reduce the time consumption of all calculations or simulations with good accuracy. It is then possible to use for example multi-objective evolutionary algorithms to determine the best design using a surrogate model. This case

was shown in publications [142] and [143] for electrical machines and electric drives. In these publications, it was also shown, the difference between conventional and hybrid surrogate modeling design using MOEA-based optimization. It has been shown that the conventional process of designing an electrical machine or drive using FEM-based analysis with MOEA-based optimization is considerably longer than using a hybrid surrogate model with MOEA-based optimization. This is illustrated in Fig. 3.6. For the conventional MOEA-based optimization, the FEM-based analysis was used during all M generations. Where on the other hand the hybrid optimization with the surrogate model, FEM-based analysis was used only in sampling and creating initial training data for N generations and for final FEM-based re-evaluation and verification of Pareto front computations. The Pareto front computations only required surrogate model, which is basically function with some data. And of course, there was an option with some of the steps were repeated due to active learning of the surrogate model. But nonetheless, the total number of FEM-based simulations were reduced and this type of optimization was proved to be less time consuming with very good accuracy of the evaluated designs for electrical machine and drive.

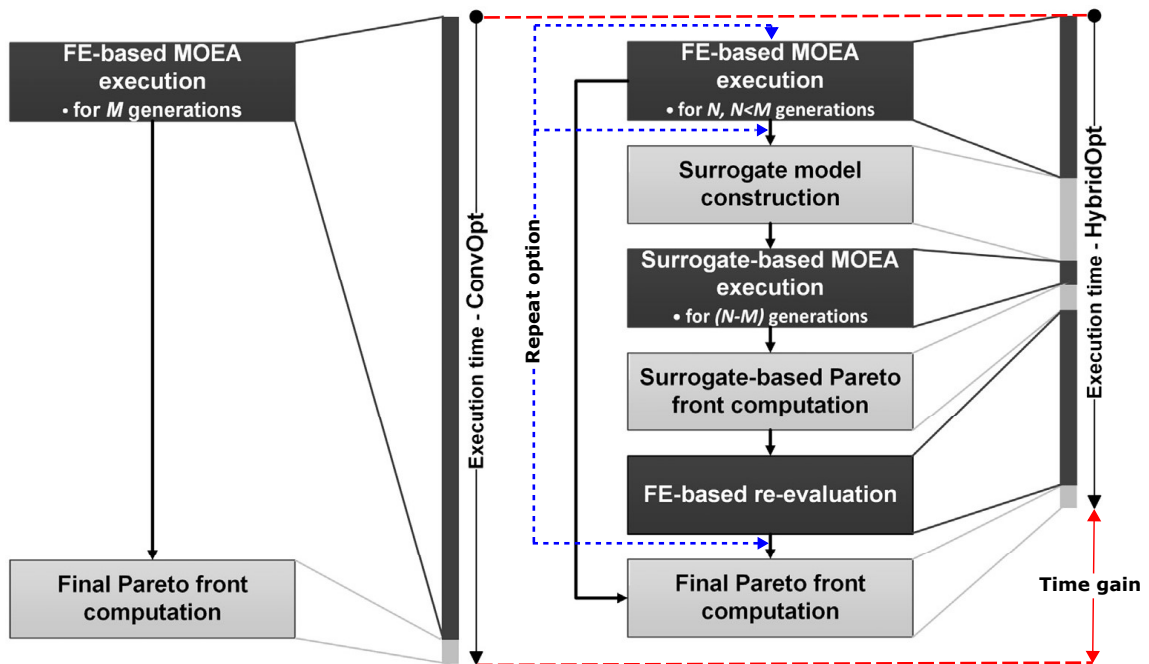


Fig. 3.6: Comparison of the optimization processes for a conventional generational MOEA-based optimization (ConvOpt) and a hybrid optimization run (HybridOpt) that uses surrogate models during the MOEA execution, according to [142] and [143].

The next chapters of this work will be devoted to the analysis of an electric machine with a solid rotor and its subsequent use for a surrogate model and possible optimization of the design of the selected machine.

4 Electromagnetic analysis of the case study IM with a solid rotor

4.1 Case study electric machine

For the case study, a 3-phase induction machine with a squirrel cage rotor and a single layer stator winding with 35 conductors was chosen. Electrical parameters, of the machine, are shown in Table 4.1 and its dimension with used material in Table 4.2.

Table 4.1: Overview of electric parameters for the case study machine.

Parameters	Unit	Value
Rated power	kW	1.5
Rated torque	Nm	9.905
Rated voltage	V	400
Efficiency	%	84.62
Power factor	-	0.744
Rated current	A	3.43
No-load current	A	2.23
Relative short-circuit current	-	7.67
Relative short-circuit torque	-	3.925
Pull out torque	Nm	42.112
Winding connection	-	Y
Number of poles	-	4
Frequency	Hz	50
Slip	%	3.588
Slip at pull out torque	%	30.273
Speed	min^{-1}	1446.2

Table 4.2: Overview of geometric dimensions and used material for the case study machine.

Dimension	Unit	Value	
		Stator	Rotor
Outer diameter	mm	145	83.4
Inner diameter	mm	83.9	35
Length of the active part	mm	170	
Air-gap length	mm	0.25	
Number of slots	-	36	28
Used material	-	M470-50A	M470-50A

Due to the nature and goals of this work, the squirrel cage rotor was replaced with a solid rotor. In this case study, only one type of solid rotor is examined, and that is an axially slitted solid rotor. The solid rotor is made of a single piece of ferromagnetic material, so naturally, the material was also replaced with shaft steel 1008. The material was chosen based on its price and easy availability. For this reason, it is easy to produce a prototype for the measurement of the case study. The dimensions of the new solid rotor are illustrated in Fig. 4.1.

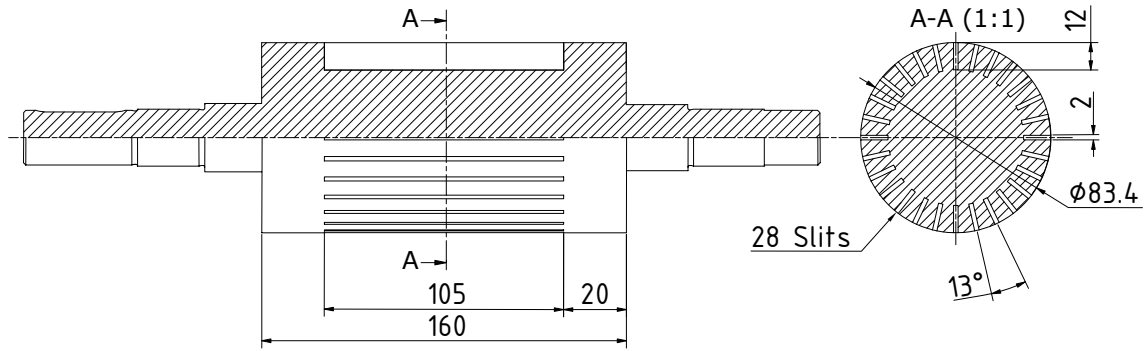


Fig. 4.1: Sketch of slitted solid rotor construction used for the case study electromagnetic analysis.

Here, the dimensions of the new rotor is limited by the dimensions of the original electric machine. So the length of the end-regions can be a maximum of 20 mm, which is the thickness of the original end ring of the squirrel cage. The optimal length of end-regions for the solid rotor can be verified with Agarwal's depth of penetration formula. For the calculation, the rated slip of the original machine is used because at this moment the slip of the modified machine is not known. At the slip of 0.036, the corresponding electrical angular frequencies of the rotor currents is 11.31 rads^{-1} . The steel 1008 has a conductivity of $2 \cdot 10^6 \text{ Sm}^{-1}$ at a temperature of 20°C and the saturation flux density is 1.9 T with a corresponding saturation field strength of 15915 Am^{-1} .

$$d_{\text{Agarwal}} = \sqrt{\frac{2H_0}{\omega_r \sigma B_s}} = \sqrt{\frac{2 \cdot 15915}{11.31 \cdot 2 \cdot 10^6 \cdot 1.9}} = 27.2 \text{ mm} \quad (4.1)$$

Based on this result, it may be concluded that the optimal end-region length of the solid rotor at this slip is about 27.2 mm. But it is already known that a solid rotor tends to have a large slip, especially a smooth solid rotor. Therefore, the optimal length of the end-region, in the end, may be higher. For slip 0.05 the optimal length of the end-region is 23.1 mm and for slip 0.07 is 19.52 mm. For this reason, the proposed end-region length in Fig. 4.1 may be correct or at least be very close to the optimal length calculated with Agarwal's penetration depth formula. Even with this difference, the match of the two end-region lengths is relatively good. And as mentioned, it cannot be changed due to the size of the whole electric machine, which is the limiting factor for the rotor

end-region length.

The depth of the axial slits in the axially slitted solid rotor, in Fig. 4.1, is only about 29% of the rotor radius. Ideally could be deeper up to 50%, to achieve better electromagnetic parameters. The speed and mechanical properties of the rotor would be able to allow this. However, it is due to the limited capabilities of the manufacturer. The same goes for the width of the axial slits, which could be narrower. But it is also limited and this is the narrowest possible width which can be manufactured.

Even with these shortcomings, the modified electrical machine, with a solid rotor, should be able to produce some reasonable results for the study in this work. Besides, the main advantage of this approach is the much simpler comparison of simulated and measured results. That is because the electrical machine is powered directly from the 50 Hz network.

These shortcomings can be also improved by optimization of the machine using the surrogate model, which is the main focus of this work. So it will be very interesting to see how much the parameters improve after optimization and if the improvements will correspond with the theory that was described in the first chapter of this work. So basically, this “bad” machine design will also serve to test the capabilities of the surrogate model.

4.2 Simulation procedure of the analyzed case study electrical machine

The process of electromagnetic analysis, of the case study electrical machine, consists traditionally of three main steps: pre-process, process and post-process. Each of the steps is performed by using one of the following programs: Python, FreeCAD and Ansys maxwell. Python script controls and manages the entire analysis process and creation of the electromagnetic model. This script also contains all needed input variables, for other programs, such as geometric dimensions, input voltage and more. In addition, it also holds a post-process function at the end of the machine electromagnetic analysis, where is it able to show characteristics and calculated performance of the analyzed machine. FreeCAD represents the pre-process function, where the geometry of the electromagnetic model is created and exported for electromagnetic analysis. And finally, Ansys maxwell imports and performs the electromagnetic analysis of the electromagnetic model created in FreeCAD. The algorithm of the whole machine analysis procedure is shown in Fig. 4.2. Each program will be more discussed in the following sections.

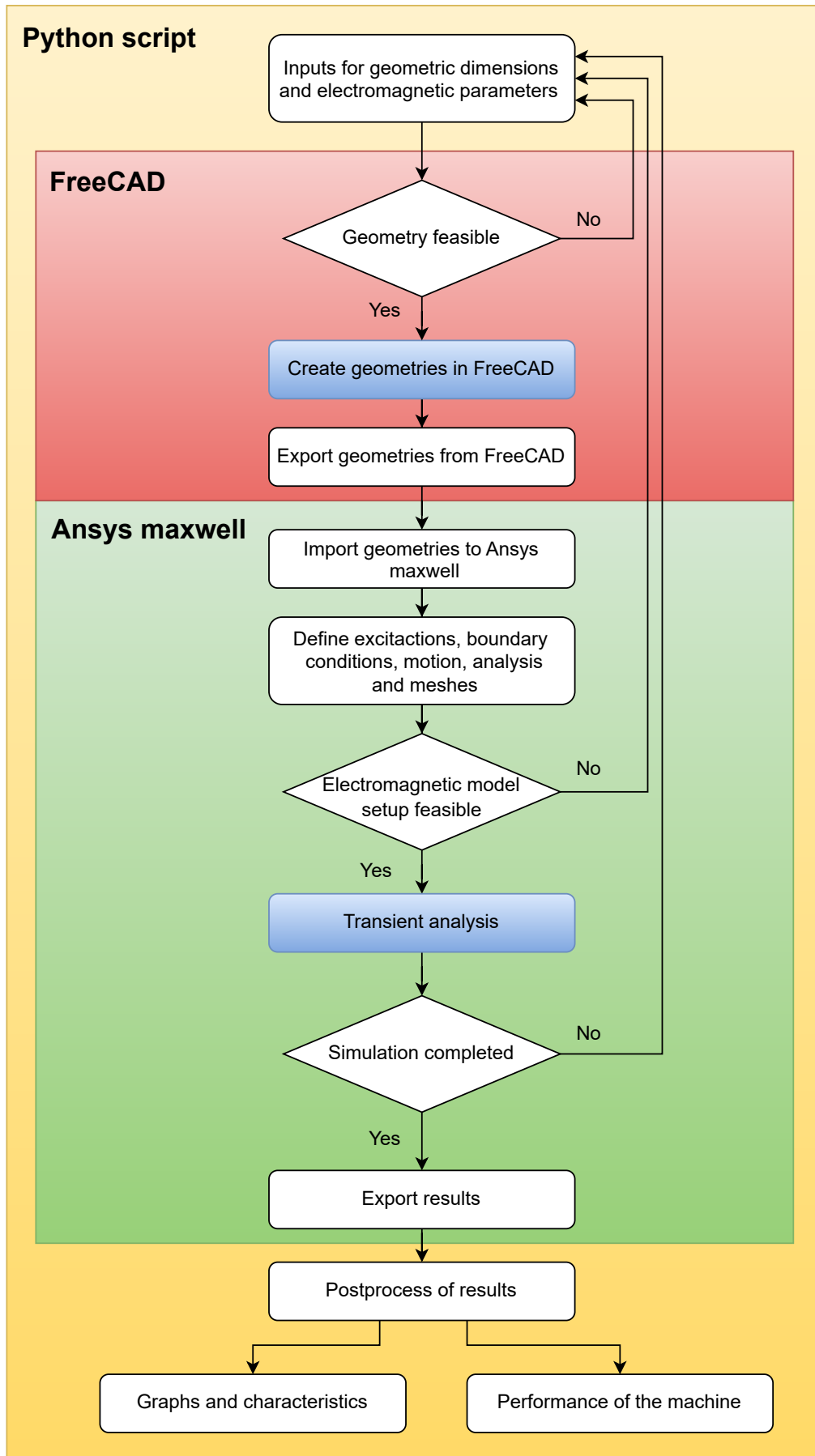


Fig. 4.2: Algorithm of the whole process of electromagnetic model simulation.

4.2.1 FreeCAD

For the pre-process of the electromagnetic model, the FreeCAD program was chosen. One reason is that it is free and can be used freely commercially. It is also very similar to other CAD programs and has very similar controls with a possibility of 2D and 3D drawing. Users familiar with other CAD environments should not have much trouble controlling this program. Also, it has multi-platform support and it is able to export geometries with a various file extension, as *.dxf, *.dwg, *.step, etc., that are compatible with most of the CAD and FEM programs. So it is possible to either use it directly in a FEM program for simulation or change some dimensions in another CAD program. Additionally, FreeCAD can create a mesh in the model. This is done by either built-in Netgen or Gmsh mesher. It is also able to do other FEM related tasks such as the definition of material, boundary conditions and some post-process features. All of the features are listed in [144].

Another reason is the ability to fully control FreeCAD using Python. This feature is also common with other open-source or paid CAD programs, but here it is made in a very convenient way. So, the FreeCAD can be controlled with internal macros, can create internal macros, be directly controlled with an external Python script, or can be controlled from a built-in Python console. With all these features, it is possible to automate the creation of different geometries that can be exported and used for other purposes in a fast and efficient way. The creation of an internal macro or external python script can be either written directly by the user or is created by sequentially creating geometry in the FreeCAD environment by the user. The second option is way more easier and convenient. Basically when the user is creating some geometries at the same time python commands are written in the built-in python console. The created Python script can be copied and further modified according to the user's needs. The main advantage of scripting is the creation of geometry as a background process without the use of a FreeCAD GUI. On the other hand, the main disadvantage of scripting in FreeCAD is the requirement of Python ver. 3.6, which is only supported Python version for scripting. More information and all the necessary procedures and tips on how scripting works in Python in FreeCAD can be found in [145].

Based on all the features mentioned above, a geometry of the axially slitted solid rotor was created in FreeCAD, in accordance with specified parameters. The creation procedure itself consisted of, first creating the axially slitted rotor geometry manually. The created Python script in the in-built Python console was copied and parameterized for further possible changes in geometry. This script was executed as an external Python script, that was controlling and managing the creation of geometry in FreeCAD.

This created geometry is shown in Fig. 4.3. Additionally, the stator was divided into several parts for better and more controlled meshing. So each, stator yoke and teeth were divided into two half parts. This was also done for the rotor, which was divided into four parts in total. The first layer is very thin and it is done for better meshing and visualization of higher stator slot air-gap frequencies currents. The height of this layer is normally determined with the formula for penetration depth (2.12), but with these low power supply frequencies it is set manually otherwise the height would be too small. Other layers were then divided equally. This also helps to better determine loss density in each part of the machine. Unfortunately, the in-built meshing of the geometries cannot be used here, because Ansys maxwell doesn't support it and often can't work imported mesh. The meshing of the geometries was carried out later in the Ansys maxwell. Even another FEM related pre-processing features cannot be used here because Ansys maxwell does not support them. This geometry was then exported with *.step extension, which is supported by Ansys maxwell.

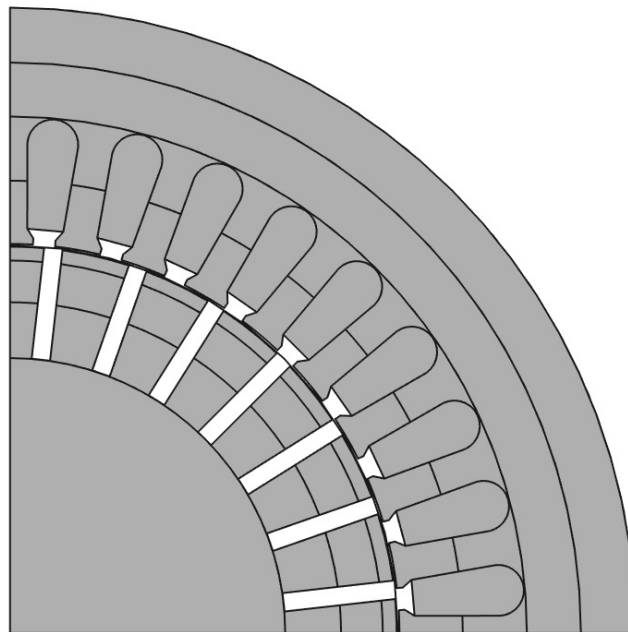


Fig. 4.3: The whole initially created geometry of the electrical machine with the axially slitted solid rotor in FreeCAD.

4.2.2 Ansys Maxwell

For the analysis of the case study electrical machine, the Ansys maxwell software was chosen. It is a commercial program that is widely used to solve multi-physical problems. Therefore, it can be used for a wide variety of simulations for example electromagnetic, thermal, mechanical, fluids, electromechanical, etc. The big advantage of the program is good support from the developers and robustness of the program. If used correctly,

Ansys maxwell can produce a very good agreement between measured and simulated results. Besides, it is user-friendly, which is very important for inexperienced users. It also has very good documentation with a lot of practical examples that serve as a tutorial. On the other hand, this program is very expensive and for this reason, most of the smaller businesses are not able to afford it despite its very good properties.

For this work, Ansys maxwell software for low frequencies electromagnetic field simulations was used. It can simulate either the steady-state of the machine or the transients of the machine. In this case, a transient simulation was used due to more accurate results of the simulation. And because the induction machine is a complex electromechanical and electromagnetic system that creates transients during its operation, which must stabilize. This type of simulation also allows visualizing the behavior of the machine over time. Aside from simulation, Ansys maxwell is also able to create geometries in its environments, but the tools and way of creating geometries are not very practical. For this reason, the geometry was created in FreeCAD. However, even with imported geometry, some parts have to be added, which will be discussed later. Either, the imported or created geometries, have to be further defined with their properties for the simulation. This includes defining materials for each part, excitation, core losses, boundary conditions and others. In this work, the procedure of setting the simulation will not be shown, but only described in general. For further information on this topic, manuals [146] and [147] show the complete procedure of importing/creating geometry with the setting of the electromagnetic model and executing its simulation with a post-process.

In addition, Ansys maxwell has the option of scripting using Python, Java or VBA. It is able to create macros, be controlled by macros, or be controlled by external scripts as well as FreeCAD. Ansys maxwell has also an in-built command window with the possibility of creating a macro simply by manual control of the program itself. Each sequential step performed by the user is written in the form of a command to an external script. Basically, Ansys maxwell has very similar scripting options, with minor differences, as FreeCAD. Due to this, Python is a very good choice for controlling Ansys maxwell and overall automation of the whole machine analysis. Therefore, Python was used for automatizing all steps described below. For further information, the manual [148] provides all the necessary information on scripting.

In terms of the analysis of the case study machine itself, only a quarter of the electromagnetic model was created in FreeCAD. That is because the machine has 4 poles where in each pole the distribution of electromagnetic field is the same, at least in terms of FEM simulation. This creates symmetry in the electromagnetic model that can be

used to reduce the simulation time. After the import of geometries from FreeCAD, a few changes had to be made in order to analyze the electromagnetic model correctly. First, three more parts had to be added, where all of the parts represent the air region in the machine. This helps to generate better mesh, mainly in the air gap where it is needed the most. The next step was to define the materials for each part of the electromagnetic machine. For stator parts, a material M470-50A was used that is typical for stator sheets. All necessary parameters were obtained from [149], mainly the B-H curve. However, most of the time the B-H curve is incomplete, so it is necessary to extend this curve further. If the curve is not further extended or is poorly extrapolated, it may lead to poor simulation results. So there are two ways to extend the B-H curve, either extend it manually, which requires some experience, or use extrapolating methods for the B-H curve. The second option is better for inexperienced people and in addition, the extrapolated values for some methods show a very good agreement with the measured values of the B-H curve behind the saturation point. Some of the methods are presented in [150] and [151]. The extrapolated B-H curve of the stator material is shown in Fig. 4.4.

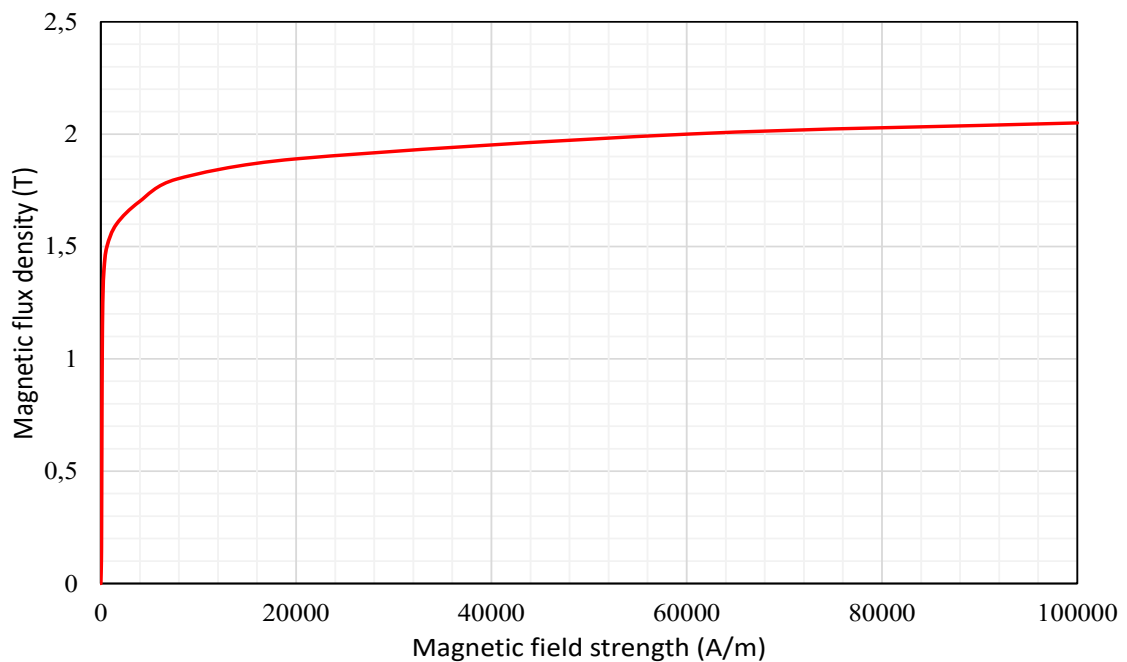


Fig. 4.4: B-H curve for stator material - M470-50A.

For the rotor parts, a material Steel 1008 was used which is typical for the steel shafts of the rotors. This material is widely used and easy to get. In this case, this material was selected directly from the Ansys maxwell libraries, which already has extrapolated B-H curve values. It also contains all other needed parameters for the electromagnetic calculation. The B-H curve of the rotor material is shown in Fig. 4.5. However, the conductivity of the steel had to be changed in order to include end-regions of the solid rotors, because the Ansys maxwell does not allow to define either the length of the solid rotor

or length of the end-regions. The rotor is a single piece of the ferromagnetic material without any additional modification, aside from the axial slits. That means that it does not contain any additional conductive layer, which improves electromagnetic parameters, such as copper coating. For this reason, a modified Russell end-factor corrective factor [109] was chosen. This corrective end-effect factor was applied to the conductivity of the axially slitted solid rotor and was calculated based on the sketch presented in Fig. 4.1:

$$\begin{aligned}
k_{\text{Russell,M}} &= 1 - \frac{\tau_p}{\pi l_s} \frac{\tanh\left(\frac{\pi l_s}{\tau_p}\right)}{\left(1 + \tanh\left(\frac{\pi l_s}{\tau_p}\right) \tanh\left(\frac{\pi l_{\text{end}}}{\tau_p}\right)\right)} \\
&= 1 - \frac{65.5 \cdot 10^{-3}}{\pi \cdot 0.16} \frac{\tanh\left(\frac{\pi \cdot 0.16}{65.5 \cdot 10^{-3}}\right)}{\left(1 + \tanh\left(\frac{\pi \cdot 0.16}{65.5 \cdot 10^{-3}}\right) \tanh\left(\frac{\pi \cdot 20 \cdot 10^{-3}}{65.5 \cdot 10^{-3}}\right)\right)} \\
&= 0.851.
\end{aligned} \tag{4.2}$$

But this correction factor was applied only in terms of rotor geometry. Thus, it is a slip independent and for this reason, another correction factor, which includes a slip of the machine, had to be added. In this case, two correction factors were used to compare them. The nominal values of the original machine were used as an example and the first correction factor used is according to Aho [108]:

$$k_{\text{Aho}} = \left(\frac{n}{n_s}\right)^4 = \left(\frac{1446.2}{1500}\right)^4 = 0.864. \tag{4.3}$$

The second correction factor is according to Pyrhonen, Aho and Nerg [109]:

$$k_{\text{PAN}} = 1 - c \cdot \omega_r^{\frac{3}{4}} = 1 - 0.022 \cdot (50 \cdot 0.0359 \cdot 2 \cdot \pi)^{\frac{3}{4}} = 0.865. \tag{4.4}$$

Both of the slip correction factors proved to have almost identical values. However, with increasing supply frequency, this difference will become more noticeable. With this conclusion, the slip correction factor according to Pyrhonen, Aho and Nerg was chosen. According to the authors, it shows the best results with measured data. With calculated both of the correction factors, the total correction end-effect factor is:

$$k_{\text{tot}} = k_{\text{Russell,M}} \cdot k_{\text{PAN}} = 0.851 \cdot 0.865 = 0.736. \tag{4.5}$$

It can be seen that, the resistivity of both solid rotors is raised by 26.4%. Due to the low supply frequency and slip, the effect of end-region is not so crucial. But with higher supply frequencies and slip, the effect of end-region would be much more noticeable and in some instances would also be dominant. Even the rotor construction can noticeably

affect the correction end-effect factor. The final conductivity of both solid rotors, used in the electromagnetic model, is then:

$$\sigma_{\text{Corr}} = k_{\text{tot}} \cdot \sigma = 0.736 \cdot 2 \cdot 10^6 = 1.472 \cdot 10^6 \text{ Sm}^{-1}. \quad (4.6)$$

And last, a material for machine winding was also defined, which is copper that was also used directly from Ansys maxwell library.

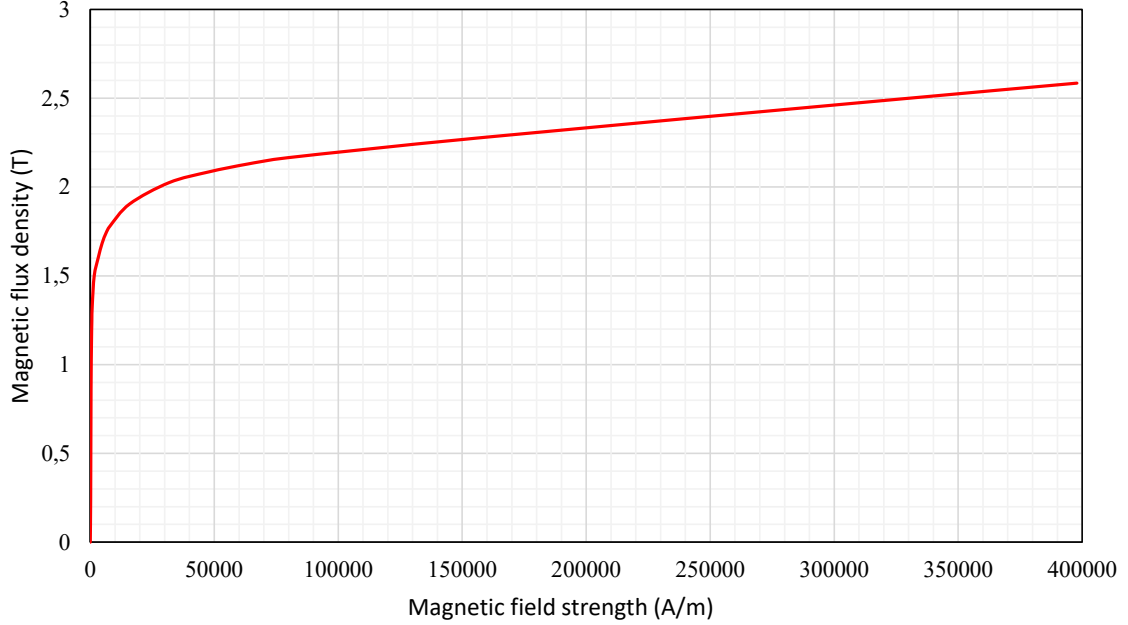


Fig. 4.5: B-H curve for rotor material - Steel 1008.

After the definition of material, a few other steps had to be made, which will be described only in general. The boundary conditions were defined in two main sections. The outer edge of the model, which represents 0 vector potential, and the inner edges of the model, which determine the direction of flux lines. Next, the motion of the rotor had to be defined, where several parameters are declared: initial position, initial speed, the moment of inertia, load torque and damping. The initial speed and the position is considered zero because the machine spins from the starting position. Load torque can be variable and for the first simulation, its value was entered from the original machine. The moment of inertia had to be calculated for the solid rotor. The new calculated value for the moment of inertia was for the slitted solid rotor $5.95 \cdot 10^{-3} \text{ kg} \cdot \text{m}^2$. The damping of the rotor was calculated with two main variables: mechanical frictional losses and speed of the solid rotor. The damping is calculated with the following formula:

$$C_R = \frac{M_{\text{Mech}}}{\Omega} = \frac{P_{\text{Mech}}}{\Omega^2}, \quad (4.7)$$

where M_{Mech} is the mechanical frictional moment of the rotor and P_{Mech} is the mechanical frictional losses of the rotor. Mechanical frictional losses of the solid rotor can be

considered constant, even though the value is changing with the speed of the solid rotor. But the speed of the solid rotor is in this case low, therefore the value of mechanical losses does not differ that much. Thus, a constant value of mechanical losses was considered for the calculation. The value was taken from the original machine which was measured to be 15 W. For example, at the rated speed of the original machine, the damping is calculated with the following formula:

$$C_R = \frac{P_{\text{Mech}}}{\Omega^2} = \frac{P_{\text{Mech}}}{\left(\frac{2 \cdot \pi \cdot n}{60}\right)^2} = \frac{15}{\left(\frac{2 \cdot \pi \cdot 1446.2}{60}\right)^2} = 6.54 \cdot 10^{-4} \text{ N} \cdot \text{m} \cdot \text{s} \cdot \text{rad}^{-1}. \quad (4.8)$$

In another step, a few other parameters had to be set up. These parameters include defining phase winding, excitation, setting core losses, setting eddy effects, the connection of winding, and others. Additionally, an analysis setup had to be created, which includes the frequency of the power supply and simulation length with time step. Simulation length was set up to be 0.3s which is long enough for the machine to go into a steady state. The time step was set up to 600 steps per frequency period of the power supply. Such a time step is very fine, with respect to the supply frequency, for the best possible simulation results. Also, all colors of the machine have been changed for better clarity. This modified electromagnetic model in Ansys maxwell is shown Fig. 4.6.

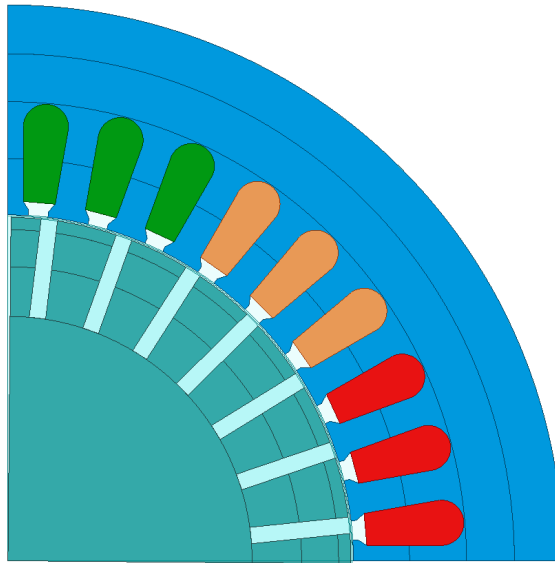


Fig. 4.6: Imported and modified geometry in Ansys maxwell of the axially slitted solid rotor.

One last thing had to be done, in order to calculate the electromagnetic model correctly and that is the meshing of the model. As was stated above, the whole model was divided into several parts for better meshing. Here, both stator and rotor yoke have coarser mesh and stator and rotor tooth (outer layers) have finer mesh. All coils have

coarse mesh because it is not that relevant for the magnetic calculation. On the other hand, the air-gap region has a very fine mesh, due to large energy changes in this place. Air-gap region meshing is always the most important. If the meshing is done poorly it could lead to poor simulation results. For that reason, 4 elements in height were created for good and accurate results. With all these rules, the created initial mesh for the machine had about 20 000 elements. Overall, the model has a very fine mesh and the electromagnetic model should show good simulation results. The whole mesh of the machine with axially slitted solid rotor is shown in Fig. 4.7 and detail of the air-gap mesh region is shown in Fig. 4.8.

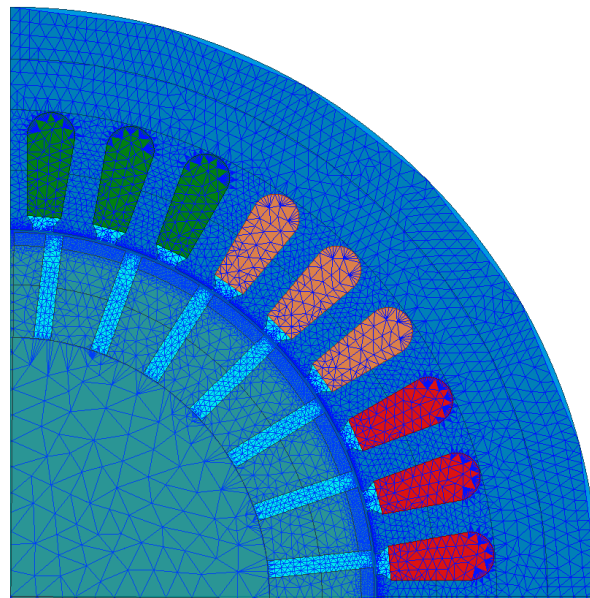


Fig. 4.7: Created initial mesh for axially slitted solid rotor.

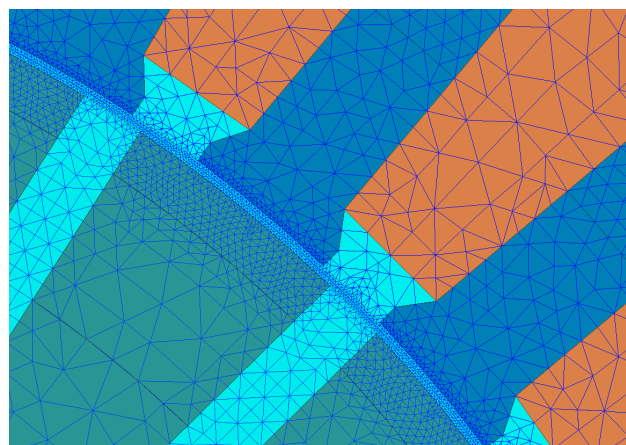


Fig. 4.8: Detail of created initial mesh for axially slitted solid rotor.

4.2.3 Python

Python was chosen for automation of the control algorithm and post-process for two main reasons. The first reason is that it is an open-source programming language with great developer support, multi-platform support and an ever-expanding community. The second reason is its simplicity and easy to understand syntax with intuitive scripting. Basically, an experienced programmer is able to orient himself very quickly in the given syntax and an inexperienced programmer or newcomer to the programming should not have much trouble learning this programming language. And that is also due to the fact that it has very great documentation on every aspect of the scripting with constantly new versions of the program is being released. Alternatively, if anyone has a problem orienting in the documentation, there are various forums with the Python community that is able to answer and advise on any question. In recent years, Python as a programming language has been directly supported by many paid and unpaid programs and can directly control them, as for example stated before on FreeCAD and Ansys maxwell. Also, the Python community is constantly creating new modules for python, where for example some of them are focused on customizable high-quality graphs, complex mathematical calculations and even there is a model that is able to calculate physical equations in the style of Simulink from Matlab. This module is called SimuPy and unfortunately is in the early stage of development.

The aim of this work is not to show the process of working with Python. But to test and verify the functionality and efficiency of the created python script for case study electrical machine analysis. This work also wants to introduce python as a possible choice for automation and post-process of the simulation results obtained. Because it is an easy to use, fast and efficient programming language. For further information with all key features and documentation containing tutorials with practical examples which are related to python scripting can be found in [152].

5 Electromagnetic analysis results of the case study IM with a solid rotor

For the analysis of IM with an axially slitted solid rotor, a torque-speed characteristic was first performed. The analysis of the machine was performed using a transient simulation with constant speed in Ansys maxwell, which is described in previous section. This characteristic is shown in Fig. 5.1. It can be seen, that the machine is not able to achieve the torque at the rated speed or pull out torque of the original squirrel cage rotor. The curve does not also corresponds to the shape of the torque and speed characteristics of the original machine. So the overall performance of the machine with axially slitted solid rotor is worse. Which was expected. Here, in order to obtain higher torque, the slip of the machine is increased. This behavior was also expected and described in previous sections. Furthermore, it can be observed that the starting torque is very high. This implicates that the solid rotors have very high impedance.

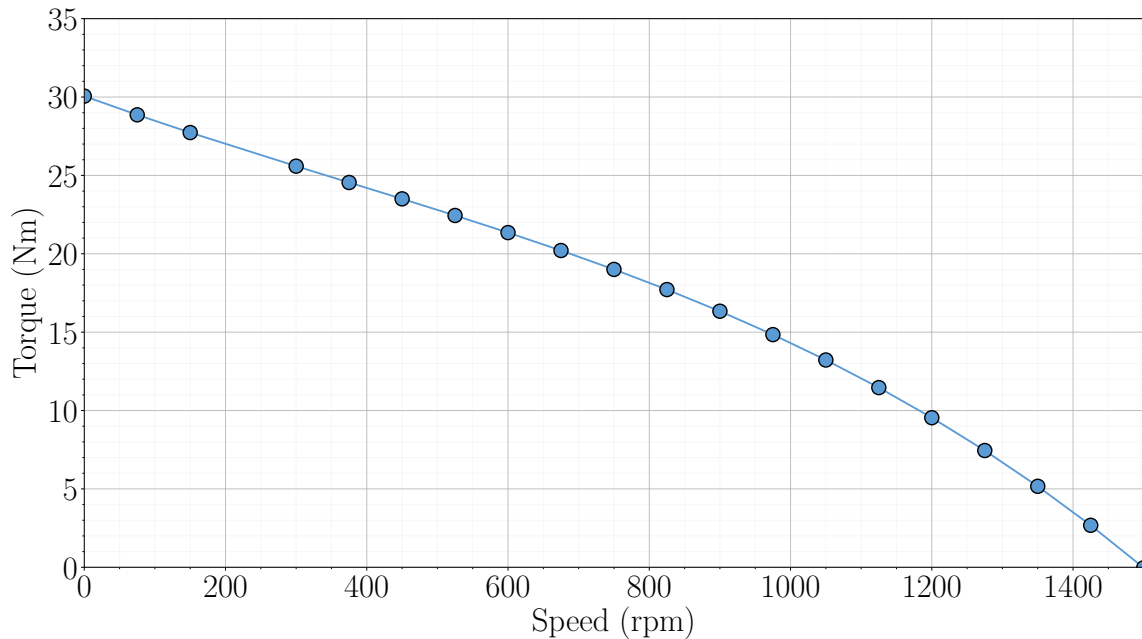


Fig. 5.1: Torque-speed characteristics of the case study IM with an axially slitted solid rotor.

For another characteristic, a number of simulations were performed, but here with transient analysis with defined machine load. In this characteristic, electromagnetic efficiency, phase current (rms) and power factor were observed as a function of machine output power for the machine with solid rotors. This characteristic is shown in Fig. 5.2. The machine reached a maximum output power of about 860 W. As expected, the machine with a slitted solid rotor has failed compared to the original machine in terms of the output power, where the output power was much higher at lower slip. Here, when

the electromagnetic efficiency hits the highest point, it then starts to decrease to lower values. So, the output power is even lower at the highest electromagnetic efficiency. The maximum efficiency of the slitted solid rotor is 68.32 %. The IM with an axially slitted solid rotor has worse electromagnetic efficiency compared to the original machine. Furthermore, the highest efficiency occurs at higher slip. So, these characteristics prove the assumptions that the machine with a solid rotor operates at a higher slip with higher efficiency compared to conventional IM with a squirrel cage. The power factor has an almost linear course. The maximum power factor of the machine is about 0.615. So again, this IM with an axially slitted solid rotor has a very poor power factor, compared to the IM with a squirrel cage. For the phase current, the curve has a course resembling a quadratic function. The machine has a maximum of rms phase current 3.471 A. At lower slip, the phase current is lower compared to the original machine.

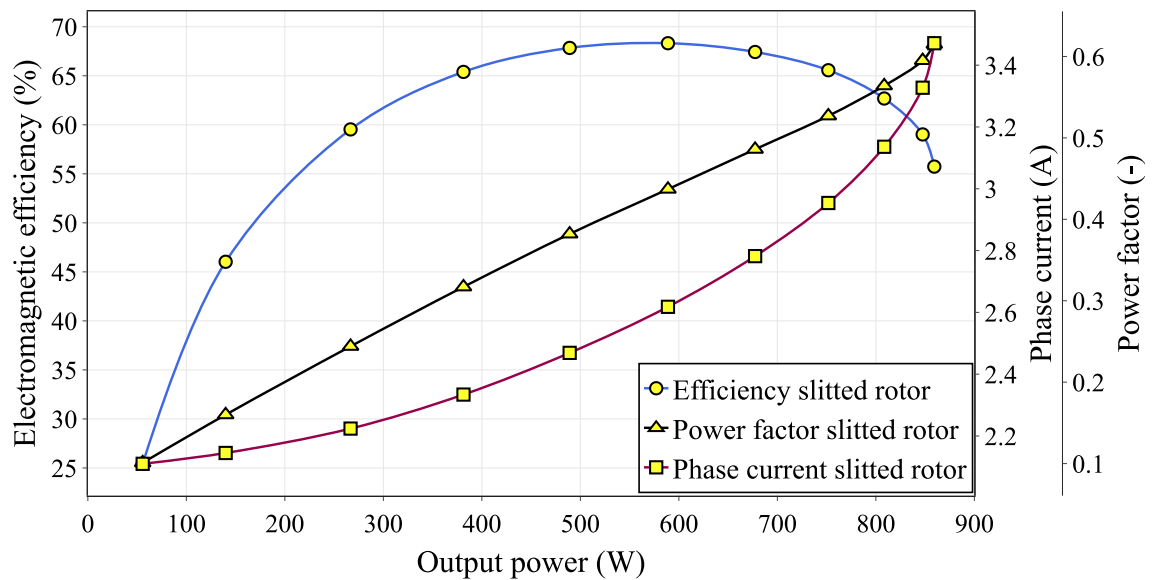


Fig. 5.2: Efficiency, Phase current and Power factor vs Output power characteristics of the case study IM with an axially slitted solid rotor.

The last characteristic shows the dependence of Stator core losses, Rotor losses and Winding losses on the output power of the machine. Here, the stator losses had to be multiplied by the recommended coefficient to bring the simulated values closer to real values. For this reason, it was very convenient to divide the stator core into several parts in the electromagnetic model. Losses obtained from the stator yoke were multiplied by 1.5 and the stator tooth losses were multiplied by 1.8, as it is stated in [153]. In the characteristic, it can be seen that the stator core losses, for solid rotor, have an almost linear course. The higher the output power is the stator losses are lower. The characteristics for rotor losses have a course of a quadratic function. The winding losses have as well a quadratic course of the characteristics. Overall, the highest losses are concentrated in the solid rotor. This is expected because the machine is operating at low speed with high

slip. This results in high rotor frequencies that further increases the rotor losses due to the construction of a solid rotor.

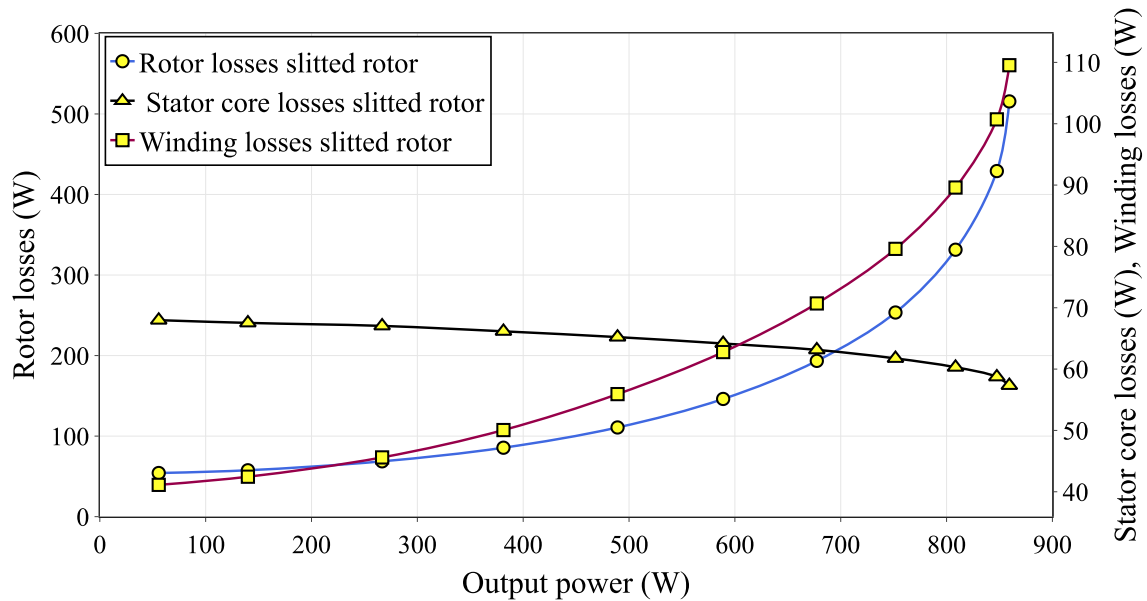


Fig. 5.3: Stator core losses, Rotor losses and Winding losses vs Output power characteristics of the case study IM with an axially slitted solid rotor.

Based on all characteristics shown above, it is clear that the case study IM with a solid rotor has overall poor performance, compared to the original IM with a squirrel cage rotor. So, in order to further increase the performance of this machine by using the surrogate model and its subsequent optimization, it is necessary to select the operating point of this machine. Multiple approaches could be taken to select the operating point, such as selecting the point with the maximum possible torque, output power, electromagnetic efficiency, and others. In this work, the most suitable working point was selected as the one with the highest electromagnetic efficiency. The machine performance at this operating point is shown in the Table 5.1. But, even with the highest electromagnetic efficiency, the overall machine performance is very poor. The torque is low, torque ripple high, slip is very high and the power factor is very poor. But it is very likely, that the machine performance will increase after the optimization.

Additionally in Fig. 5.4 is shown the distribution of the magnetic flux density in the whole machine in the steady-state at the operating point shown in the table above. It can be seen that the maximum value of the magnetic flux density is about $2 T$. The highest value of the magnetic flux density is located mainly in the stator tooth and under rotor slits. It is evident that the flux lines are penetrating much deeper into the rotor, due to slits. This phenomenon was described in first chapter and results in much better machine performance and higher efficiency. Another thing that can be noticed is that in the rotor

Table 5.1: Performance of analyzed case study IM with an axially slitted solid rotor at the selected operating point.

Parameter	Unit	Performance
Torque	Nm	4.255
Torque ripple	%	38.56
Speed	rpm	1322
Output power	W	589
Phase current (rms)	A	2.62
Power factor	–	0.437
Electromagnetic efficiency	%	68.32
Air-gap flux density	T	0.7583
Stator core losses	W	64.17
Rotor losses	W	146.14
Stator winding losses	W	62.77

yoke the field is curved into a vortex shape. This is due to the high slip of the machine, which results in higher rotor frequencies. But because of the slits the rotor frequencies are much lower. If the machine would operate at a higher slip, this vortex phenomenon would be much more noticeable.

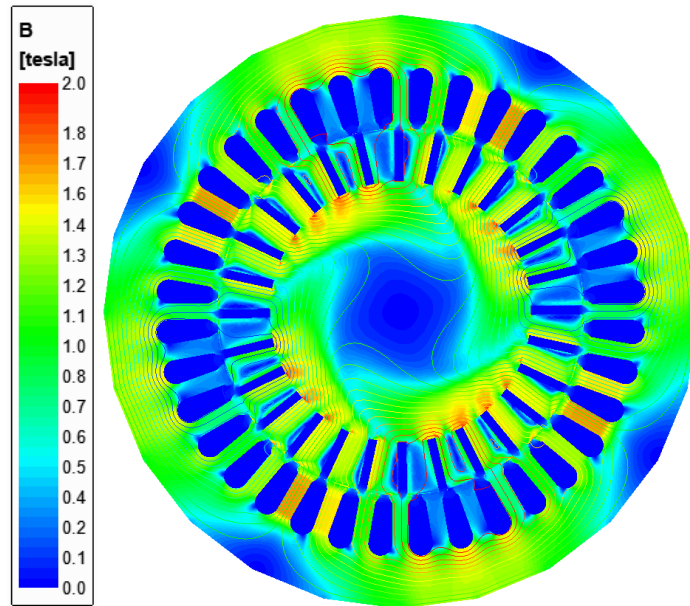


Fig. 5.4: Distribution of magnetic flux density in the whole machine for IM with an axially slitted solid rotor.

In the next chapter, this case study machine with all analyzed results will be used for the construction of surrogate model.

6 Creation of surrogate model based on case study IM with a solid rotor

In this chapter, the procedure for creating a surrogate model based on case study IM with an axially slitted solid rotor will be presented. This procedure of creating a surrogate model is related to Chapter 3 of this thesis. Therefore, some procedures and steps will not be explained in detail again. Thus, mainly a practical procedure will be shown on the selected case study machine of this work.

6.1 Selection of suitable machine parameters for the surrogate model

The first step is to define all possible machine parameters that will be optimized, in order to improve the overall design of the machine. In this case for this machine, it was assumed that its outer diameter would remain the same. So this parameter will not be considered, as well as the number of stator slots and rotor slits. This is because, from an electromagnetic point of view, the number of stator slots and rotor slots are in good agreement and suitable for this machine and its performance. Based on these 3 excluded parameters, only 8 possible machine parameters remain, which is perfect for surrogate modeling. All these parameters are chosen to have a direct effect on the electromagnetic properties of the machine. So parameters that would affect the machine in terms of temperature change or mechanical properties of the machine are not considered. The list of all parameters for machine optimization is as follows:

- Active length of the machine (L),
- Length of the rotor end region (L_{End}),
- Length of the air-gap (l_{gap}),
- Stator slot height (H_{Slot}),
- Stator slot width (W_{Slot}),
- Number of stator conductors (N_{S}),
- Depth of rotor slits (H_{Slit}),
- Width of rotor slits (H_{Slit}).

All of these parameters are illustrated in the Fig. 6.1 and Fig. 6.2.

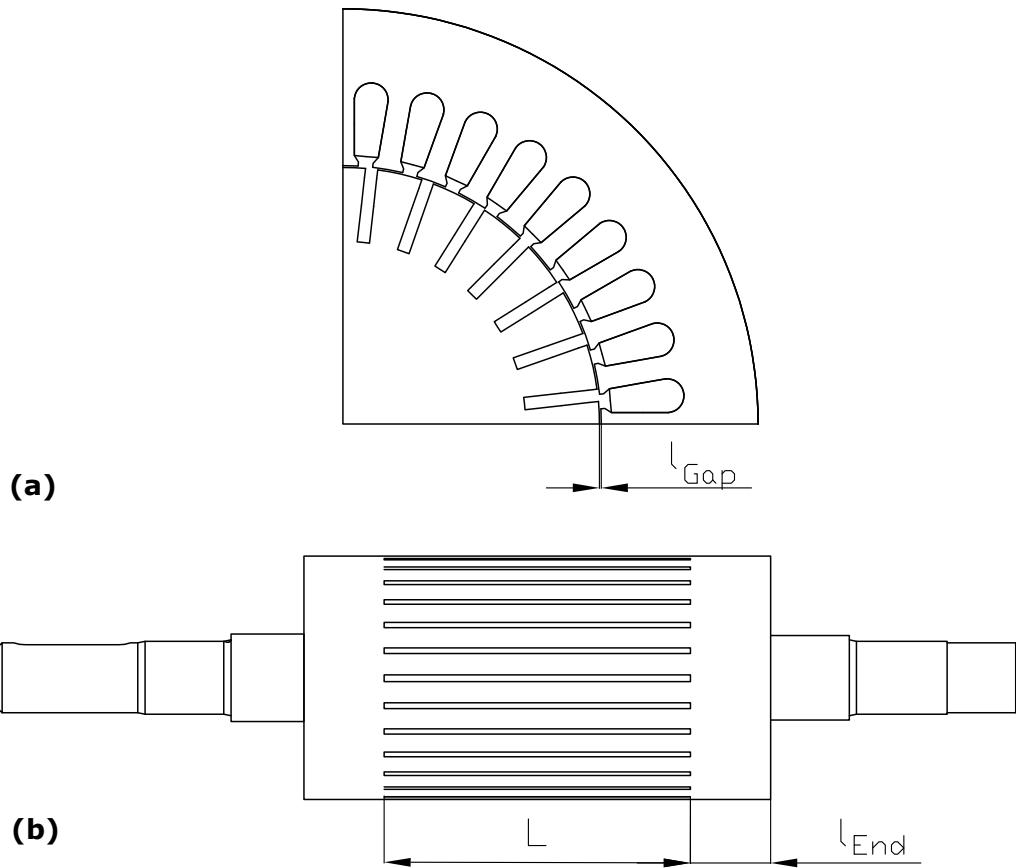


Fig. 6.1: Sketch of all parameters consider for optimization in: (a) cross-section of the machine and (b) solid rotor.

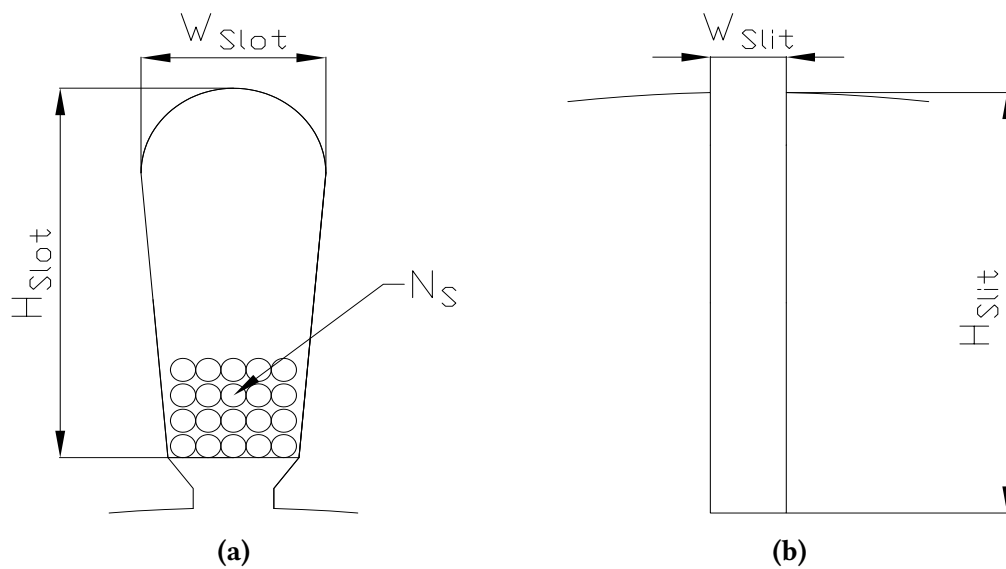


Fig. 6.2: Sketch of all parameters consider for optimization in: (a) stator slot and (b) rotor slit.

6.2 Sensitivity analysis of the case study IM with a solid rotor

The sensitivity analysis was done by changing individually the value, in a wide range with reasonable limits, of all 8 parameters listed in section 6.1. The range of limits was carefully selected based mainly on the limitations of machine construction, best potential improvement of electromagnetic parameters, and price of the machine.

For the active length of the machine, the most crucial factor was mainly the improvement of electromagnetic parameters and price. But otherwise, there is more freedom of choice. The length of the rotor end region is limited mainly in terms of rotor dynamics. So, it should not be too long so as not to affect the operation of the machine too much. Another factor is also price. The length of the air-gap is limited by the construction and by the electromagnetic performance of the machine. The length should not be too long to avoid high stator currents and too low to avoid potential rotor damage to the stator due to rotor eccentricity. Stator slot height and width are limited mainly by the electromagnetic performance of the machine. The slot height should not be too high otherwise the stator yoke will be over-saturated and the stator slot width should not be too wide, which will also cause over-saturation for the stator tooth. At the other extreme, the performance of the machine would also deteriorate. These two parameters are limited by the production limits because it is not possible or easy to produce stator sheets with either big slot and thin stator tooth and yoke or very small stator slots. The number of stator conductors is limited by the machine construction and more precisely by the filling factor of the stator slots. And finally, the depth and width of rotor slits are limited mainly by machine construction. For the rotor slit depth, a maximum depth of approximately 50% of the rotor radius is recommended in terms of mechanical stresses on the rotor. The upper depth limit is therefore known, the choice of the lower one depends only on the possible electromagnetic performance of the machine. In terms of mechanical stress on the rotor, the recommended minimum rotor slit width should be approximately 5 - 10% of the rotor pitch. At lower speeds this limit can be lower. The upper limit of the rotor slit width then depends on the electromagnetic performance of the machine. If the rotor slit width is too wide then the rotor material could become over-saturated in the deepest part of the rotor slit.

Based on all of these assumptions and rules, a lower and upper limit for each machine input parameter has been set. A list of all machine input parameters with their limits is provided in Table 6.1. However, these limits are normalized and related to the base values of the machine input parameters. This makes it easier to see how much each input parameter has increased or decreased. The given step for each input parameter is different, which is of course influenced by the character of the parameter. Moreover,

it is affected by the relationship between the input and output parameters of the simulations. That is, if the step for the input parameter is too large, the function between the input and output parameters of the simulation may be incorrect. Therefore, during sensitivity analysis, it is necessary to check all of these functions and consequently add more simulations with smaller input parameter step. This is an optional iterative process.

Table 6.1: Range of limits for normalized values of input parameters of the case study IM with a solid rotor.

Input parameters	Unit	Minimum	Maximum
Active length of the machine	%	25	187.5
Length of the rotor end region	%	0	255
Length of the air-gap	%	16.67	233.33
Stator slot height	%	33	128.37
Stator slot width	%	42.2	121.7
Number of stator conductors	%	85.7	171.43
Depth of rotor slits	%	8.33	175
Width of rotor slits	%	30	195

The process of simulation, using Ansys maxwell, is the same as described in section 4.2, with algorithm shown in Fig. 4.2. The type of simulation is in this case, transient analysis with constant speed. In this type of simulation, the damping and moment of inertia of the machine do not have to be considered. And since the speed is constant, only the other simulation outputs such as torque, electromagnetic efficiency, etc. can change. For the sensitivity analysis purpose, it is very convenient, because it can be seen how the overall performance of the machine will change at this speed. Whether the overall performance of the machine will improve or also deteriorate. It is therefore necessary to select optimum operation point of the machine with the desired machine speed. In this case, it is the one that was selected in chapter 5 in Table 5.1, where the machine has highest possible electromagnetic efficiency. This type of simulation with the selected operation point of the machine will be further used in other simulations related to surrogate modeling.

After all simulations were completed, a set of several graphs was created. Each graph contains all 8 input parameters, which are displayed as a function of the selected simulation output parameter. The total number of the selected and most interesting output parameters of simulations is 10 in total. All graph with all selected results are shown in Fig. 6.3. Here, on the x-axis of the graphs, is the normalized value of input parameter, which represents the relative growth of changed parameters. On the y-axis of the graphs, the output parameter of the simulations is displayed as the absolute

value. In this way, it is possible to display all simulation results in the most readable way. Other results not used in this section are plotted in the appendix of this paper.

By dividing and considering the influence of each input parameter on the overall machine performance, it can be seen that the active length of the machine has the greatest influence on the machine torque (Fig. 6.3 (a)). The relationship between torque and active length of the machine is purely linear. This means that, with increasing active length of the machine the torque rises as well. This rule applies for the output power of the machine as well (Fig. 6.3 (b)), but even for the total losses of the machine (Fig. 6.3 (g)). This results in only a slight increase in the electromagnetic efficiency of the machine (Fig. 6.3 (c)), where compared to the base active length of the machine the efficiency does not increase that much. The phase current of the machine is also linearly increased (Fig. 6.3 (f)), but the current density (Fig. 6.3 (i)) and linear current density (Fig. 6.3 (j)) do not increase so much and are almost constant. On the other hand power factor (Fig. 6.3 (d)) is increasing with the active length and its course is very similar to electromagnetic efficiency. The torque ripple is decreasing with increasing active length and after the base value of the machine active length it is almost constant (Fig. 6.3 (e)). The flux density in the air-gap is practically constant because the ratio of conductors and active length of the machine is kept constant (Fig. 6.3 (h)). It is clear that as the active length of the machine increases, the overall performance of the machine improves. On the other hand, the overall price of the machine also increases. If the length went to much higher values, the price of the machine would be too high and the performance of the machine might not be that much better.

The length of the rotor end region has very little effect on the overall performance of the machine. As the length increases, the torque (Fig. 6.3 (a)), output power (Fig. 6.3 (b)), electromagnetic efficiency (Fig. 6.3 (c)), power factor (Fig. 6.3 (d)), and total losses (Fig. 6.3 (g)) of the machine increase slightly. All curves have the same shape. From the base length of the rotor end region, all these parameters have a constant value. The phase current (Fig. 6.3 (f)) is nearly constant, as well as current density (Fig. 6.3 (i)) and linear current density (Fig. 6.3 (j)) of the stator slot. However, as the length increases, the torque ripple (Fig. 6.3 (e)) of the machine improves. But only up to the base length. The flux density in the air-gap is again constant (Fig. 6.3 (h)) and the length of the end-region does not have direct impact on its value. From the results it can be concluded that the length of the rotor end is sufficiently designed in its base value and increasing it would only result in an absolute minimal improvement. However, increasing it would lead to a higher machine cost, weight, and a possible deterioration of the overall rotor dynamics. This would result in a deterioration of the overall performance of the machine.

By reducing the number of conductors in the stator it is possible to drastically increase the torque (Fig. 6.3 (a)) and output power (Fig. 6.3 (b)) of the machine. The shape of the function is parabolic and if the number of conductors would raise both of the output parameters would drastically drop. This is due to the different saturation of the stator yoke, tooth and air-gap. As the number of stator conductors decrease, the saturation increases, resulting in increased power and consequently torque. This situation can be seen with the flux density in the air-gap (Fig. 6.3 (h)). If the number of conductors increased the flux density in the air gap would decrease, causing a decrease in torque and power. In [153], it is stated that recommended value of the flux density in the air-gap is between $0.7 - 0.9 T$, for low speed machines. So, number of conductors below base value, do not satisfies this recommendation. However, with the increased number of conductors, the total losses of the machine (Fig. 6.3 (g)) also increase due to higher saturation of the stator tooth and yoke, which leads to higher losses in stator sheets. However, this is not the only reason for the increase in total losses. With decreased number of conductors, the cross-section of the conductor is higher which results in a higher phase current of the machine (Fig. 6.3 (g)). This is also big contribution to the total losses of the machine, because the losses of the stator winding are increased. Thus, reducing the conductors will also increase the current density and linear current density of the stator slot. On the other hand, with increased total losses, the electromagnetic efficiency (Fig. 6.3 (c)) is slightly higher with lower number of conductors. However, it seems that power factor (Fig. 6.3 (d)) has the highest value at the base value of the stator conductors. Either with increasing or decreasing conductors the power factor is decreasing, after this point. The torque ripple (Fig. 6.3 (e)) in this case is also decreasing with the lower number of conductors. So overall, with lower number of stator conductors the overall performance of the machine rises. But they are limited to the fill factor of the stator slot and possibly capabilities of the producer.

In the case of the length of the air-gap, with increasing length, the torque (Fig. 6.3 (a)) and output power (Fig. 6.3 (b)) are slightly rising. But the improvement is very small and negligible. However, torque ripple (Fig. 6.3 (e)) is the dramatically decreasing with increasing air-gap length. On the other hand, the increased length of the air-gap also dramatically increases stator phase current (Fig. 6.3 (f)) and current density (Fig. 6.3 (i)) and linear current density (Fig. 6.3 (j)) of the stator slot. This is due to the large magnetizing inductance, which is caused by the large air-gap. The large magnetizing inductance results in a high magnetizing current, which is directly dependent on the B-H curves of the stator plates. This further causes over-saturation of the stator plates which further generates higher losses in the stator plates. Also, the higher current increases the losses in the stator winding. But with a large air-gap, the rotor losses are decreased. This is due to the fact that with a large air gap, the higher harmonic

components of the stator field do not reach the rotor surface. These higher harmonic components have the effect of generating high losses in the rotor, due to the formation of eddy currents in the rotor. When the length of the air gap is changed, three different types of losses are directly affected: rotor losses, stator winding losses and stator sheet losses. So it is necessary to find such a length of the air gap when the total machine losses are the smallest. In this case, the total losses (Fig. 6.3 (g)) have the lowest value at the base value of the air-gap length. Which means, that at this length of the air-gap, the electromagnetic efficiency is the highest (Fig. 6.3 (c)). So from this point of view, the air-gap length is perfectly designed. The power factor (Fig. 6.3 (d)) is higher at lower length of the air-gap, which corresponds with the low stator current. Flux density in the air-gap is almost constant (Fig. 6.3 (h)). The base value of the air-gap is in this machine is very well designed. The power factor could be higher or the torque ripple could be improved, but at this length, the machine has the highest efficiency, which is most important.

Increased slit depth and decreased slit width considerably increases torque (Fig. 6.3 (a)) and output power (Fig. 6.3 (b)). This confirms the theory that with higher slit depth and narrow slit width the torque increases and with it the output power as well. The total losses of the machine (Fig. 6.3 (g)) are with narrower width of the rotor slits, but with increased slit depth the rotor losses raise. This results in high electromagnetic efficiency (Fig. 6.3 (c)) with very narrow rotor slits. On the other hand, the electromagnetic efficiency rises to a point of 150% of the rotor slot depth. After that point, the efficiency begins to drop. The same rules apply to the power factor (Fig. 6.3 (d)), where the curves for the depth and width of the rotor slits are the same as for the electromagnetic efficiency. The phase current (Fig. 6.3 (f)) is increased with deeper slits but is decreased with narrow slits. Again, this rule also applies to the current density (Fig. 6.3 (i)) and linear current density (Fig. 6.3 (j)) of the stator slot, where the course of the curves is the same. The flux density in the air-gap (Fig. 6.3 (h)) is not affected by these two parameters. However, in the terms of torque ripple (Fig. 6.3 (e)), the deeper slits decrease it. But the width of the rotor slit induces multiple extremes in the magnitude of the moment ripple across the entire range of simulations. With very wide rotor slit the torque ripple is at the maximum value. As the width of the rotor slits narrows, the magnitude of the torque ripple decreases, roughly to the point of the base width of the rotor slit. After this point, the moment ripple increases again, up to a point 90% of the slot width. Then it starts to decrease again. This phenomenon could be explained by the fact that the value of the moment ripple is influenced by the geometry of the rotor and the possible current value of the flux density in the air-gap. But again, this type of machine is very complex, from the physical point of view. Therefore, it is not easy to explain all phenomena that are happening in the machine in detail. But

otherwise, in terms of overall machine performance, it is best if the rotor slit is as deep and narrow as possible. This again confirms the pre-established theory. But the depth and width of the rotor slot is in practice very dependent on the manufacturer's capabilities.

Finally, two parameters remain: the height and width of the stator slot. Each parameter, either alone or together, affects the area of the stator slot, which mainly results in affecting the current density of the stator slot (Fig. 6.3 (i)). Thus, with a small slot height or width, the stator slot current density is very high, which is due to the small stator slot area for both parameters. On the other hand, stator phase current (Fig. 6.3 (f)) has the lowest value, because the fill factor of the stator slot is constant and thus, the stator winding resistance is high at low slot area. As the area of the stator slot increases, the current density quadratically decreases, and phase current is almost linearly increasing, because the stator winding resistance is gradually decreasing. However, at the point 110% of the slot height and tooth width, the current density of the stator slot will slightly increase again. This is due to constant value of fill factor of the stator slot. As the slot area increases, the cross-sectional area of the stator conductors increases, and stator winding resistance decreases. This results in a significant increase in phase stator current. The linear current density (Fig. 6.3 (j)) is then correlated with the phase stator current curve. This is because the area of the stator slot is again increasing. The area of the stator slot also has a further influence on the total losses of the machine (Fig. 6.3 (g)). Initially, as the stator area increases, the total losses decrease as the current density and winding resistance decrease. But with the large slot area, the phase current is also high, which increases the losses in the stator winding much more. At high values of slot height and width, the yoke and stator tooth are very narrow. So the stator sheets start to become over-saturated. This results in high losses in the stator plates. This is directly reflected in the electromagnetic efficiency (Fig. 6.3 (c)), where the efficiency increases up to about the base value of the height and width of the stator slot and then decreases again with increasing phase current. However, the power factor (Fig. 6.3 (d)) is increasing with smaller stator slot area. The torque (Fig. 6.3 (a)) and output power (Fig. 6.3 (b)) increase only slightly to approximately the point of the base value of the height and width of the stator slot. It can be considered that the length and height of the stator slot does not have too much influence on these two parameters. The torque ripple (Fig. 6.3 (e)) is rather increasing after the base value of the slot height and width, especially with the large slot area. But at the base value of the width and height, the torque ripple has the lowest value. After this point, it starts to very slightly increase. Finally, as the size of the slot area increases, the value of the flux density in the air-gap (Fig. 6.3 (h)) increases substantially. At the base value of height and width, the flux density stabilizes and remains more or less constant. The reason behind this is that the

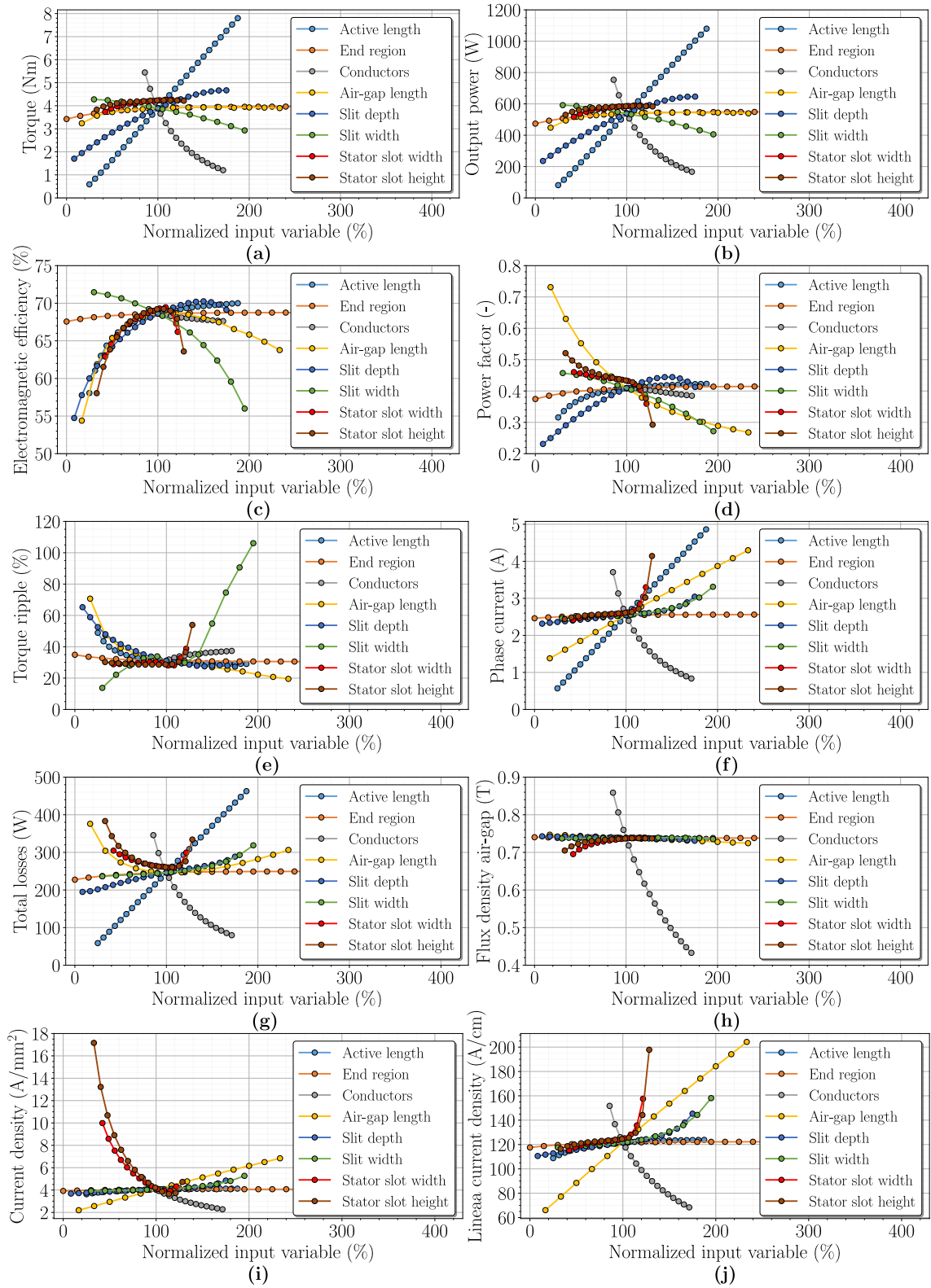


Fig. 6.3: Results of sensitivity analysis for the function of: Torque (a), Output power (b), Electromagnetic efficiency (c), Power factor (d), Torque ripple (e), Phase current (f), Total losses (g), Fundamental component of the flux density in the air-gap (h), Current density (i) and Linear current density of stator slot (j) on normalized value of input variable.

air-gap flux density value shown in the graph is calculated as the radial fundamental component of the air-gap flux density. So, the flux density distribution in the air-gap is slightly different in a small slot width and a large slot width. The magnitude of the flux density is, however, approximately the same. Mainly, the shape of the distribution changes. So when the air-gap flux density curve is converted to the radial fundamental component of the air-gap flux density, the value may be different. Which can be seen in the graph directly. But overall, the height and width of the slot is well designed. Changing them would either make a small improvement or a large deterioration in the overall performance of the machine.

Based on the results of the sensitivity analysis, it was concluded that the performance of the machine could be significantly improved. It was also found that the overall performance of the machine is mainly influenced by 4 parameters:

- Active length of the machine,
- Number of stator conductors,
- Depth of rotor slits,
- Width of rotor slits.

The other parameters had either very little effect or changing them would degrade the performance of the machine. The behaviour and possible poor consequences for machine performance for these parameters are justified above. In addition, the exclusion of these parameters will make the whole process of creating a surrogate model easier and faster. And potentially, with fewer parameters, its accuracy will increase. This is also sufficient for the demonstration and optimization of the case study IM with a solid rotor.

6.3 Design of experiments and output evaluations

From the obtained results of the sensitivity analysis in section 6.2, four main input parameters were selected as the most influential to the performance of the machine. These four parameters were then used later for the initial training data of the surrogate model. However, in order to make the machine optimization more efficient, the limit of the range of values of these parameters has been narrowed. The limit was chosen to take into account the final highest possible performance of the machine, the lowest possible cost of the machine, the feasibility of the machine in terms of construction, and possibly to simplify the function between input and output of the simulation, given in Fig. 6.3. Newly set limits for selected input parameters are shown in Table 6.2.

Table 6.2: Narrowed selection of input parameters and their normalized narrowed range of values for the surrogate model of the case study IM with a solid rotor.

Input parameters	Unit	Minimum	Maximum
Active length of the machine	%	75	150
Number of stator conductors	%	65.71	134.29
Depth of rotor slits	%	75	175
Width of rotor slits	%	30	135

A suitable sampling scheme also had to be selected to generate the initial training data. For the case study machine with a solid rotor, Box-Behnken sampling scheme was chosen. The reason for the decision was that this sampling scheme is suitable for this type of machine and a very convenient toolbox for Python exists that can easily generate this scheme. The name of this toolbox is pyDOE2, where DOE stands for design of experiments. As stated on the official website [154], this toolbox is created for the construction of suitable experimental designs. But the most interesting feature of this toolbox is that it can effectively reduce the total number of all points in the sampling scheme. This will be explained later.

Before the actual sampling scheme was created, it had to be determined how and into how many samples the input parameters would be divided. It was concluded that based on the sensitivity analysis results in Fig. 6.2 and newly set range limits for input parameters, all input parameters were divided into five samples that are evenly distributed across their whole range. In this case, five samples should be a sufficient number to cover the entire function between any input and output parameter. With five samples and four input parameters, the total number of all input parameter combinations for the sampling scheme is $5^4 = 625$. These input parameters were entered into the pyDOE2 toolbox, which generated a matrix of all possible combinations of input parameters. This matrix had a size of 625×4 . Thus, 625 simulations had to be performed to generate the initial training data for the surrogate model. However, the great advantage of the pyDOE2 toolbox is that it can reduce this total number so that the sampling scheme covers statistically as large an area as possible for all possible combinations of input parameters. Reduction of the total number of all possible combinations is only possible by an integer. So the number could be reduced by e.g. 2 or 3. The total number would be $625/2 = 313$ and $625/3 = 208$. So the total number of simulations needed for the initial training data would be 2-3 times smaller. However, note that this function does not guarantee that the total reduced number will statistically cover all possible combinations for the input parameters. So this step is more or less trial and error. And during the initial construction of the surrogate model,

it may happen that a new sampling scheme with a higher number of total points has to be generated. The function for reducing the total number of sampling scheme will not be discussed further in this work. Publication [154] shows the principles on which this function works and its nature in terms of statistics.

For the case study machine with a solid rotor, it was concluded that the best sampling scheme is $5^4 = 625$, without any reduction. This conclusion was reached by trial and error, where the sampling scheme was altered based on the initial surrogate model and its observed accuracy. The initial sampling scheme will not be presented in this work because it is too long and can be easily created. The procedure for creating a sampling scheme using the pyDOE2 toolbox and a detailed description of all the toolbox functions is given in [156].

With the established sampling scheme, all 625 simulations were performed. The type of used simulation was already described, where each simulation took about 3 – 4 hours. In total, all simulations ran for approximately one week. This may seem like a long time, but after the construction of the surrogate model, the optimization of the machine design is very fast. After all simulations were completed, all relevant machine performance data was saved in an excel file. This collection of all stored machine performance data with predefined combinations of input parameters formed the initial training data for the surrogate model.

6.4 Construction of surrogate model

To create a surrogate model, it is essential to choose the right machine learning technique to create it. There are many machine learning functions, where some have been listed in Chapter 3 under Section 3.2.3. For this work, the Radial basis function (RBF) was chosen from all possible machine learning techniques.

According to [157], the RBF is a method that interpolates scattered data sets in k -dimensional space, in general. This approach is convenient especially for a higher dimension $k > 2$, as the conversion to an order data set, for example using tessellation, is computationally very expensive. The RBF interpolation is not separable and is based on distance of two points, where it leads to a solution of a Linear system of equations. Nevertheless, because of the scattered and un-ordered data, RBF is computationally more expensive. On the other hand, RBF offers very interesting applications at an acceptable computational cost, as for example solution of partial differential equations, image reconstruction, neural networks and more. However, to select the correct interpolation technique, it is necessary to know whether the datasets are ordered or un-ordered. The

data sets can be classified as follows:

- Un-ordered
 - Scattered
 - Clustered
- Ordered
 - Unstructured
 - Structured
 - * Non-regular
 - * Semi-regular
 - * Regular

Based on these data classifications, the correct RBF method is selected. The RBF interpolation is then based, as stated above, on computing the distance of two points in the k - dimensional space and defined by a function:

$$f(x) = \sum_{j=1}^M \lambda_j \varphi(\|x_i - x_j\|) = \sum_{j=1}^M \lambda_j \varphi(r) \quad (6.1)$$

$$r = \|x - x_j\|,$$

where λ_j are weights coefficients to be computed and $\varphi(r)$ are the corresponding basis functions, which can be written in the following linear systems:

$$Ax = b, \quad (6.2)$$

where A is interpolation matrix containing radial functions, x is a vector of coefficients and b is a vector of values. Due to some stability issues, usually a polynomial $P_k(x)$ of a degree k is added to the form:

$$f(x) = \sum_{j=1}^M \lambda_j \varphi(\|x_i - x_j\|) + P_k(X_i) \quad (6.3)$$

$$i = 1, \dots, M$$

For practical use, the linear polynomial, which is simple to use, is widely used in many applications. So the RBF interpolation function has form:

$$f(x) = \sum_{j=1}^M \lambda_j \varphi(\|x_i - x_j\|) + a^T x_i + a_0 = \sum_{j=1}^M \lambda_j \varphi(r) + a^T x_i + a_0 \quad (6.4)$$

$$i = 1, \dots, M$$

However, this is a general RBF interpolation function. In fact, the RBF is additionally divided into two main groups:

- Global
- Local

The two main groups differ in solvability and stability. The global group interpolates the data set in its entirety. While the local group focuses mainly on interpolation in specific locations of the data. For this work, the RBF function in the framework of global interpolation and more precisely the Thin-plate spline (TPS) was chosen. As it is stated in [158], TPS are one of the most used techniques in RBF interpolation. It is due to excellent interpolation properties, the physical motivation (minimization of a bending energy), the computational efficiency, the ease of implementation, and the mathematical theory is fully understood. A disadvantage is that the locality of the transformation cannot be controlled except by specifying additional landmarks, which is lengthy and time-consuming. But it is fully sufficient for use in this work and the drawback of this method does not affect the surrogate model result much. The shape of this function is as follows:

$$\varphi(r) = r^2 \log r \quad (6.5)$$

This function is then substituted into the formula 6.4. For the reasons mentioned above TPS is suitable for many engineering applications including surrogate modeling. For further information regarding the RBF interpolation method and TPS, the publications [159] - [163] provide extensive theory, application procedure, and other practical applications.

With the selected RBF interpolation technique, a surrogate model was created, again using the programming language Python. There are several Python libraries that can create a surrogate model using RBF functions, or in some cases even initial training data as in the publication [164]. For the purpose of this work, the very well known SciPy library was chosen, which is mainly used for mathematics, science and engineering [165]. It additionally includes RBF interpolation and even TPS with other methods such as cubic or Gaussian [166]. Its use is very easy. Several input matrices are inserted into the function, where the output is the approximated function for the given inputs. But it is advisable to change the range of all values, both input and output, in the way that they all have the same range. After all, it is not simple to interpolate some data, where one set of data ranges from 1 to 10 and the other set of data ranges from 3000 to 9000. In this case, the input matrices are the data from the initial training, where all data have been converted so that the range of all values is up to 1000. In practice, the input parameters of the machine (active length, number of conductors in the stator, rotor slit depth and rotor slit width) and, in addition, one output parameter of the simulation (torque, power factor, efficiency, etc.) are always inserted into this function. The surrogate model is therefore created separately for each output of the machine simulation, where the input machine

parameters are always the same. However, it is not necessary to create a surrogate model for each output parameter of the simulation, as some of these parameters are linked to each other. The output power of the machine for the example directly increases with torque, since the machine was considered to have a stator speed; from the magnitude of the power factor, the magnitude of the current, current density and linear current density can be estimated; and from the magnitude of the electromagnetic efficiency, it can be discerned whether the overall losses of the machine are higher or lower. By this logic, not all the parameters used in the sensitivity analysis in Fig. 6.3 were used, but their selection was further narrowed down to the following five parameters:

- Torque,
- Torque ripple,
- Power factor,
- Electromagnetic efficiency,
- Fundamental component of the flux density in the air-gap.

This further reduces the complexity of optimizing the machine design, which is possibly a desirable feature. For each of these parameters, using the machine input parameters, surrogate models were created, but with only 90% of the initial training data, which serves as training data. The reason is to establish the initial accuracy of all surrogate models, using the remaining 10% of the data, which serves as verification data. This will be explained later. The method of selecting verification data was completely random. In some cases, these data can be selected evenly from the entire volume of initial training data or by using a special algorithm. It depends on the application and experience in working with the surrogate model. At this point, all the machine input parameters from the defined training data (active length, number of stator conductors, rotor slit depth and rotor slit width) were taken and inserted into the already established surrogate models which returned the approximated output values. The same process was repeated for the remaining verification data. At this point, two sets of data were available. One where the approximated values were directly used in the creation of the surrogate models and the other where they were completely excluded in the creation of the surrogate models. Data that was not used in the creation of the surrogate model then creates a certain error that is always present. In this part, the Pearson's R coefficient was used to determine the accuracy of all surrogate models, which determines how strong the linear association between two sets of data is. Its calculation was again performed in Python using the SciPy library. Its use and calculation is shown in [167]. In this case, the two sets of data were approximated output values from surrogate models and output values from simulations from the initial training data, both for training data and for the remaining

verification data. Based on all the results obtained, graphs were plotted for all the selected machine output parameters, where the y-axis was the surrogate model output values and the x-axis was the simulation output values taken from the initial training data. Correspondence Pearson's R coefficients were given for each plot for both training and verification data. These graphs are shown in Fig. 6.4.

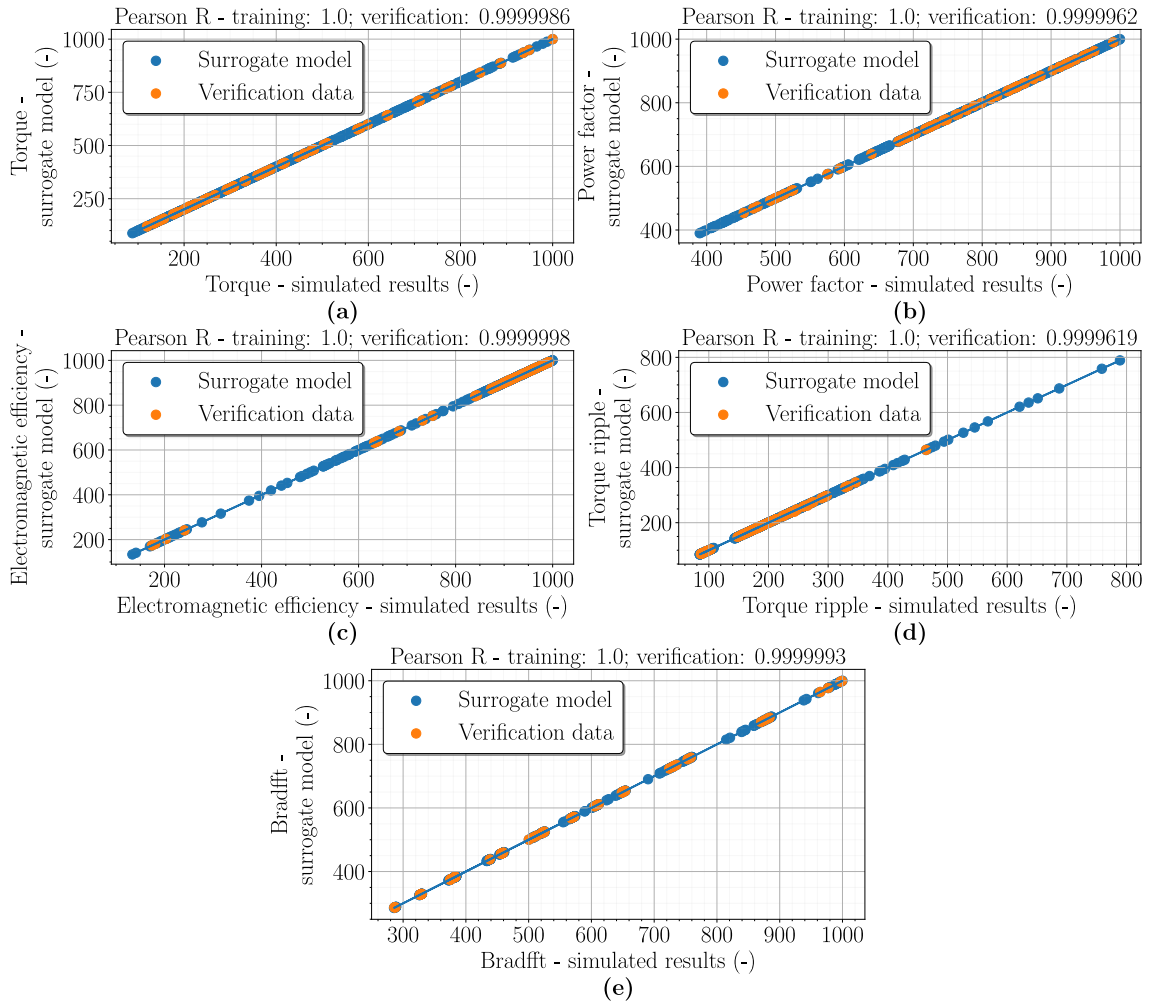


Fig. 6.4: Determination of the accuracy of the constructed surrogate models using training and validation data for Torque (a), Power factor (b), Electromagnetic efficiency (c), Torque ripple (d), and Fundamental component of the flux density in the air-gap (e).

From all plotted graphs, it can be seen that the surrogate model for each output parameter does not have practically any error at all. Which means that no point on the blue curve deviates from the linear dependence and the Pearson's R coefficient is equal to 1. Which is very good and means the surrogate models themselves don't create any error. For verification data, the situation is slightly different. Here the Pearson's R coefficient is less than one, indicating that some points deviate from linear dependence, even if it doesn't seem like it at first glance. But even though Pearson's R coefficient is

less than one, it is very close to this value for each parameter. This was expected because the surrogate model cannot predict the value of the parameter accurately and always creates an error compared to real or simulated values. After all, it is an interpolation of values. But that doesn't change the fact that all surrogate models are very accurate. However, if the values of Pearson's R coefficients were much less than 1 for the example of 0.8 – 0.95, the surrogate model would only be accurate within the average. And this is not desirable for the accurate determination of the output parameter, in that case the surrogate model would be unsuitable for such application. To possibly increase the accuracy of the surrogate model, in that case, it would have to be necessary to use a different combination for the sampling scheme or completely use a different sampling scheme.

To accurately determine the error between the approximated value and the simulated value of all output parameters, for both training and verification data of all surrogate models, several graphs were created. Each graph shows the dependence of the relative error of a given output parameter, referenced to the value of the surrogate model output, to each sample of each input parameter. So this means that each graph contains 4 subplots, where each subplot has the relative error of that parameter on the y-axis and all samples for that input parameter on the x-axis. Thus, the relative errors for each output parameter are shown in Fig. 6.5 - 6.9.

In all plots, it is proved that all the approximated output of the surrogate models for the training data is equal to zero. The individual highest relative errors are for: Torque (Fig. 6.5) 1.5%, Power factor (Fig. 6.6) 0.4%, Electromagnetic efficiency (Fig. 6.7) 0.06%, Torque ripple (Fig. 6.8) 1.5%, and fundamental component of the flux density in the air-gap (Fig. 6.9) 0.5%. So in the result, the highest relative error of the surrogate models is around 1.5%, which is a very good result. This largest relative error may have been due to the smaller number of input parameter samples or poorer local approximation that is characteristic of TPS interpolation, as mentioned above. But some error will always be present in a surrogate model and if it is around 1% then such a surrogate model can be considered very accurate. In this case, it is not even necessary to do additional simulations at the locations with the highest relative error and add the subsequent results to the initial training data or using adaptive sampling. At this point, all surrogate models, in terms of maximum possible relative error, were ready to be used for machine design optimization. But before the optimization, several graphs were plotted showing how and by how much the performance of the machine could potentially be increased. Which in some cases is important if the ranges and sampling of input parameters have been done correctly.

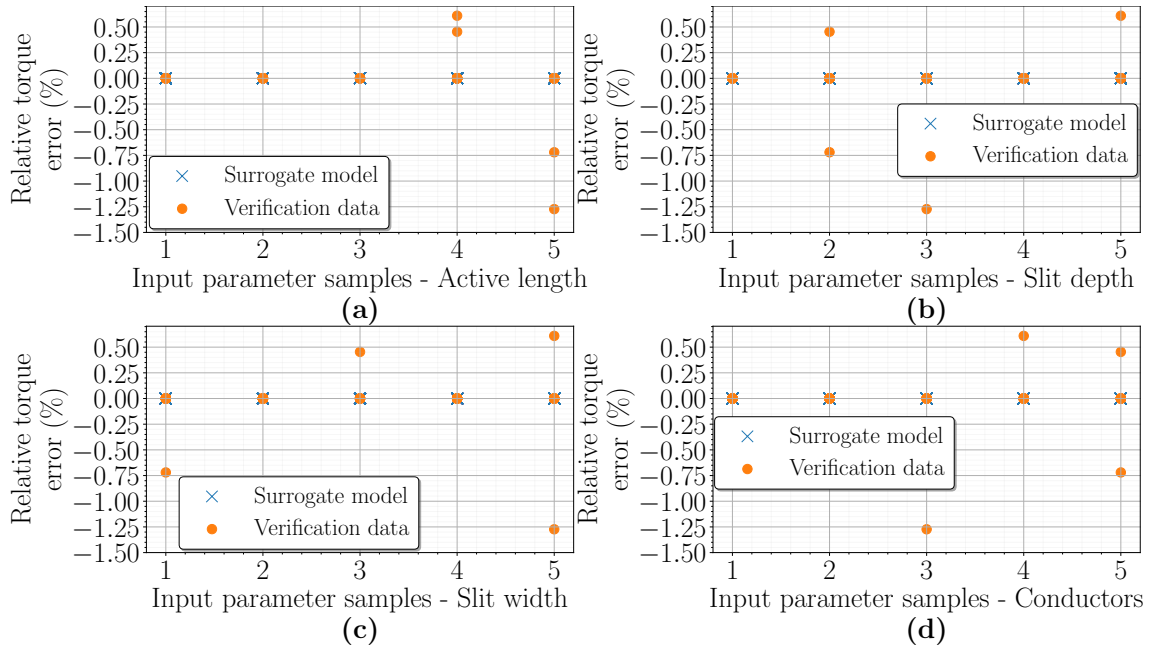


Fig. 6.5: The dependence of relative torque error of the surrogate models on samples of: Active length of the machine (a), Rotor slit depth (b), Rotor slit width (c), and Number of stator conductors (d).

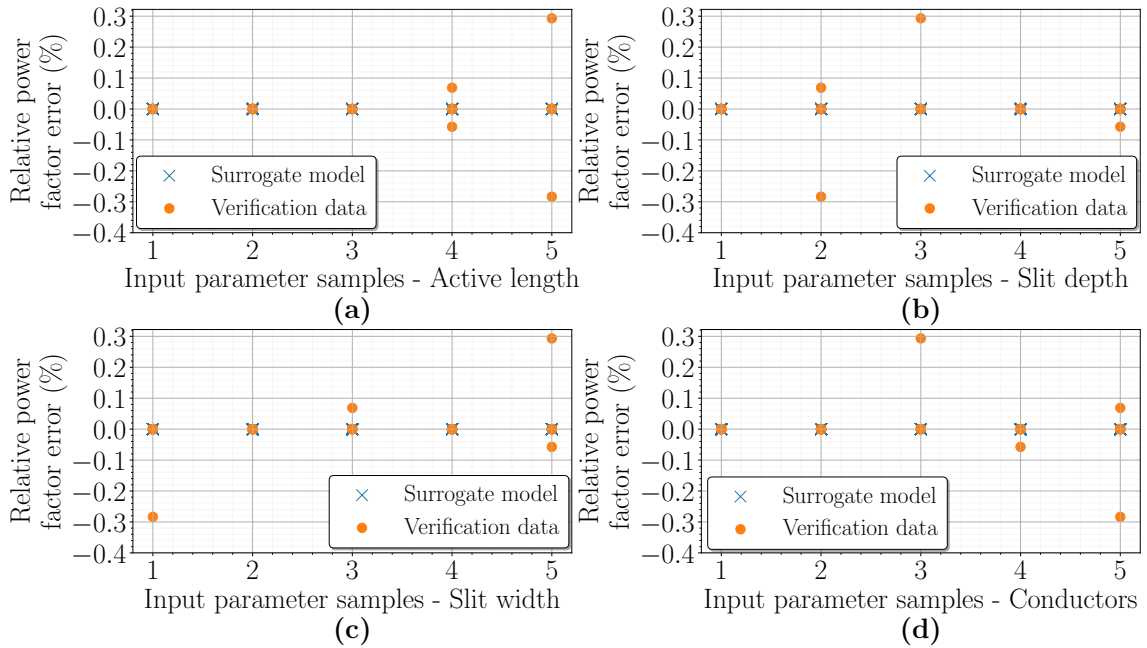


Fig. 6.6: The dependence of relative power factor error of the surrogate model on samples of: Active length of the machine (a), Rotor slit depth (b), Rotor slit width (c), and Number of stator conductors (d).

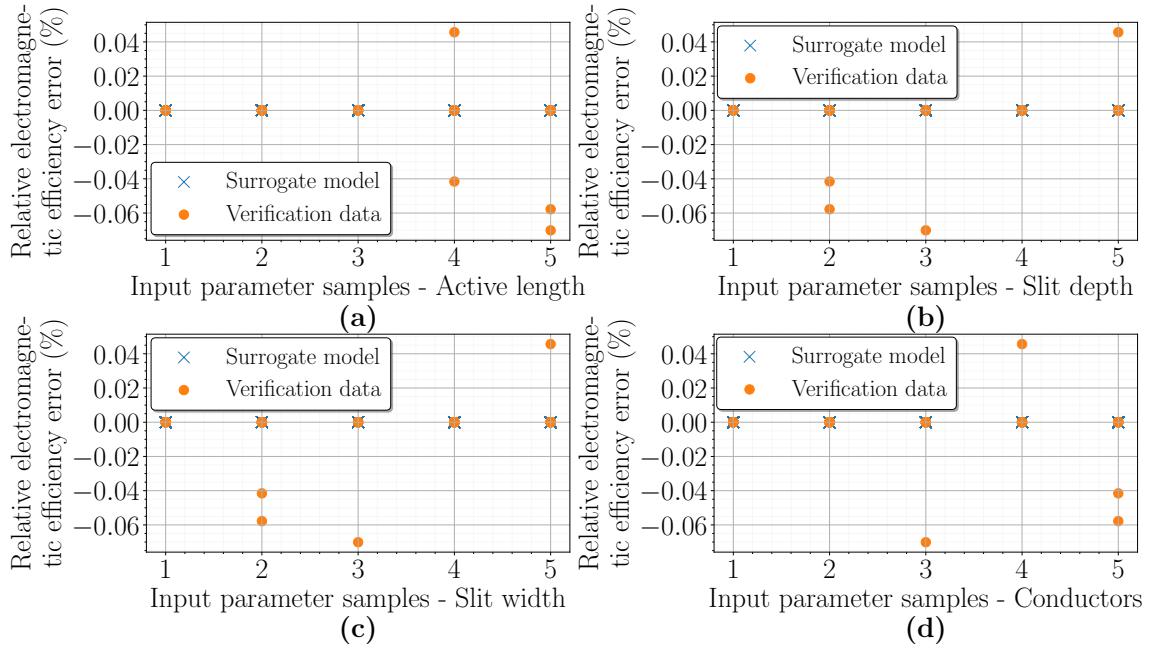


Fig. 6.7: The dependence of relative electromagnetic efficiency error of the surrogate model on samples of: Active length of the machine (a), Rotor slit depth (b), Rotor slit width (c), and Number of stator conductors (d).

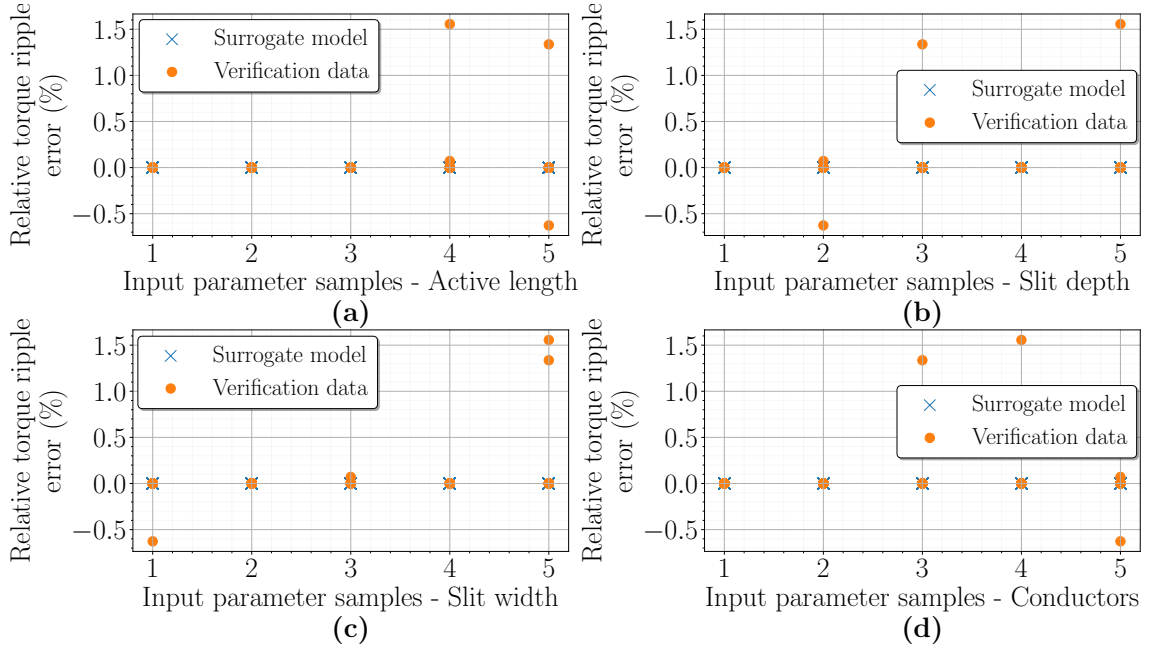


Fig. 6.8: The dependence of relative torque ripple error of the surrogate model on samples of: Active length of the machine (a), Rotor slit depth (b), Rotor slit width (c), and Number of stator conductors (d).

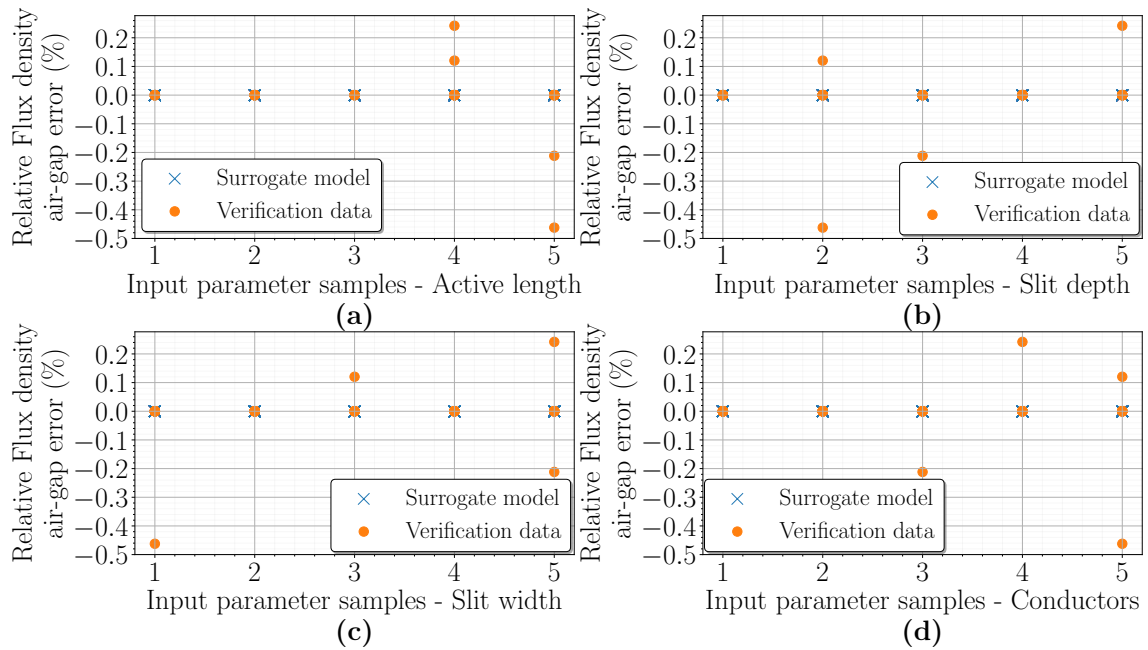


Fig. 6.9: The dependence of relative fundamental component of flux density in the air-gap error of the surrogate model on samples of: Active length of the machine (a), Rotor slit depth (b), Rotor slit width (c), and Number of stator conductors (d).

To determine the possible increase and improvement of the overall machine performance, several graphs were created directly from all the initial training data. All values for the selected simulation output parameter were plotted on the y-axis and all samples for the given machine input parameter were plotted on the x-axis. So again subplots have been created for all machine input parameters. This is essentially a sensitivity analysis of the machine that was presented in section 6.2. Except that here it shows the potential increase in machine performance with the following optimization that will be discussed later. And in addition, the simulation results are affected by all possible sample combinations of machine input parameters. These graphs are shown in Fig. 6.10 - 6.14.

The machine torque (Fig. 6.10) can be increased up to approximately $13 Nm$. It can be seen in the graphs that the machine achieves the highest torque with large rotor slit depths, narrow rotor slit width, and small number of stator conductors. This is in accordance with the results of the sensitivity analysis. But, as the active length of the machine increases, the torque should also increase. However, the machine has the highest torque in the second sample of the active machine length. This is due to the saturation of the machine, which is shown in Fig. 6.14. For the initial sampling of the active length of the machine and the number of stator conductors, certain samples were selected. However, this leads to a much higher saturation of the machine at certain combinations, with flux

densities up to $1.2T$ in the air-gap. Which can be seen in the graphs, where as the active length of the machine increases the saturation of the machine decreases and as the number of stator conductors decreases the saturation increases. But for the depth and width of the rotor slits, the saturation is almost the same over their entire range. To maintain the recommended air-gap flux density of $0.7 - 0.9 T$, some combination of active machine length and number of stator conductors must be maintained. This is not respected here, but the following optimization will take this recommended limit into account. For the rest of the graphs, the same rules apply as for the sensitivity analysis. That is, with increasing active length of the machine, deeper and narrower rotor slits, and increasing number of stator conductors, the overall power factor (Fig. 6.11) of the machine improves. The power factor of the machine is able to reach a value of up to 0.55. The same rules applies for electromagnetic efficiency of the machine (Fig. 6.12). For torque ripple (Fig. 6.13), the situation is different. As the active length of the machine increases, the torque ripple decreases. As the active length of the machine increases, the torque ripple decreases, which is consistent with the predictions and previous results. But it increases considerably with higher rotor slit depth. This is due to some combination of machine input parameters and the largest contributor is the low number of stator conductors. Which can also be seen in the graph. As the width of the rotor slits decreases, the torque ripple decreases, which is expected. The highest value of torque ripple is 140%, which is unacceptable and must be reduced as much as possible during optimization.

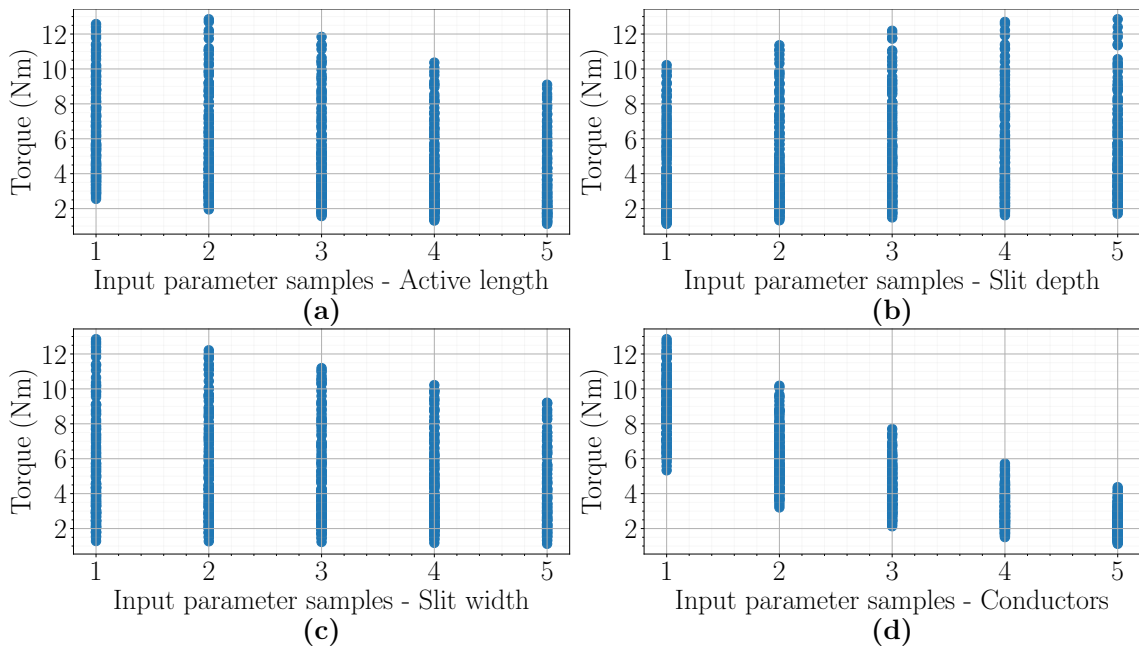


Fig. 6.10: The torque dependence on samples of: Active length of the machine (a), Rotor slit depth (b), Rotor slit width (c), and Number of stator conductors (d) for all values from initial training data.

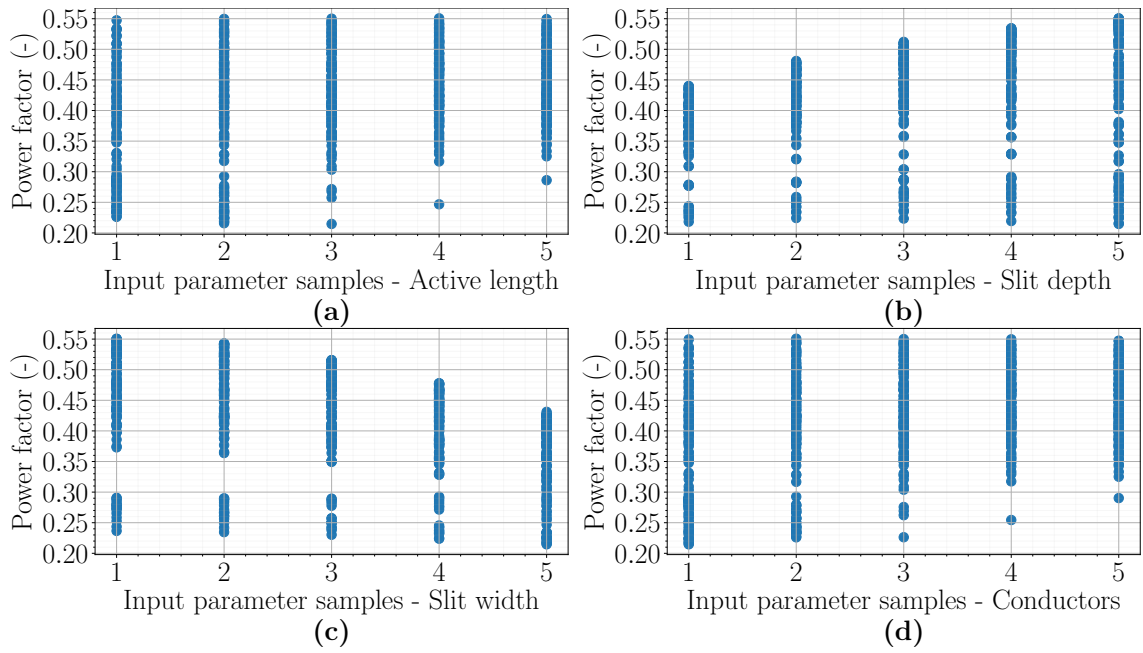


Fig. 6.11: The power factor dependence on samples of: Active length of the machine (a), Rotor slit depth (b), Rotor slit width (c), and Number of stator conductors (d) for all values from initial training data.

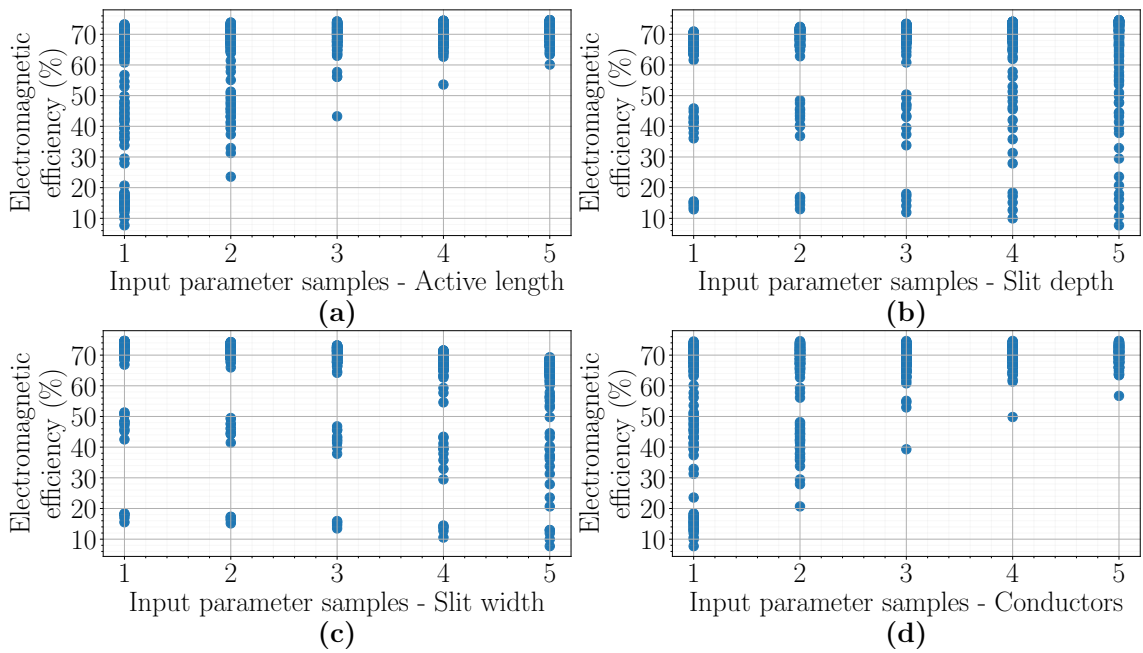


Fig. 6.12: The electromagnetic efficiency dependence on samples of: Active length of the machine (a), Rotor slit depth (b), Rotor slit width (c), and Number of stator conductors (d) for all values from initial training data.

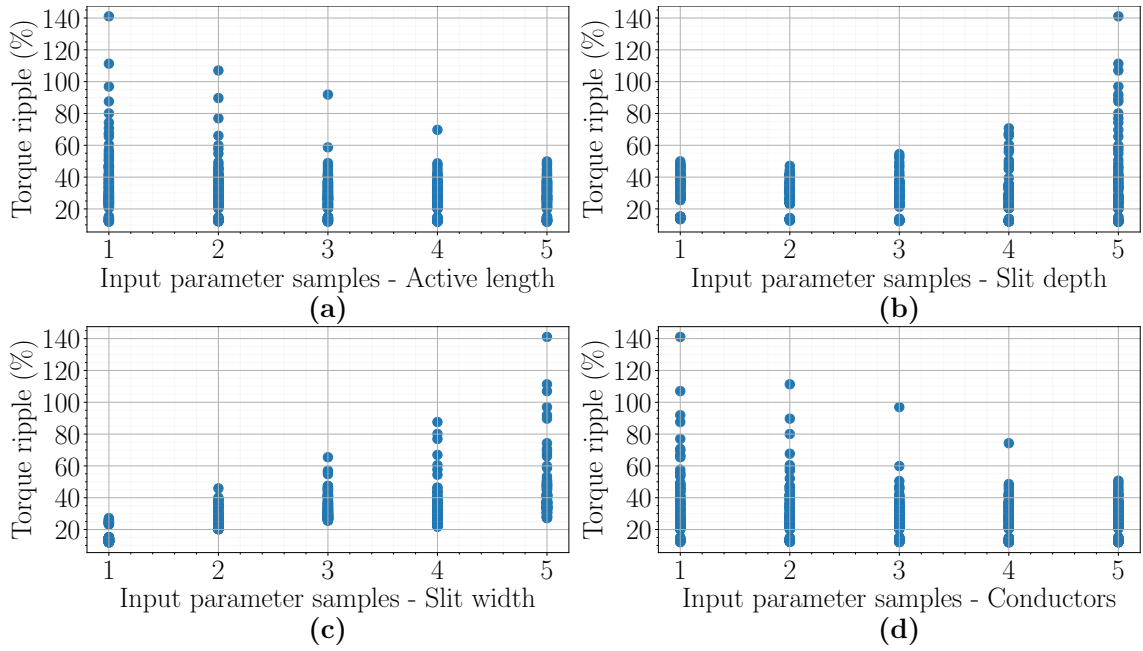


Fig. 6.13: The torque ripple dependence on samples of: Active length of the machine (a), Rotor slit depth (b), Rotor slit width (c), and Number of stator conductors (d) for all values from initial training data.

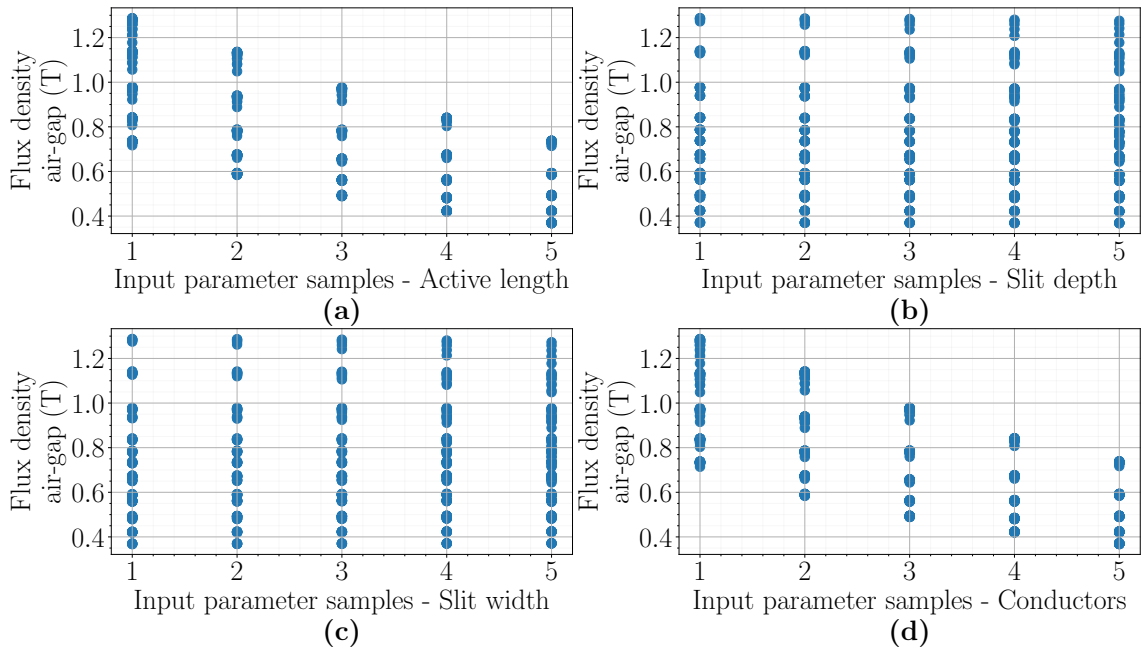


Fig. 6.14: The fundamental component of flux density in the air-gap dependence on samples of: Active length of the machine (a), Rotor slit depth (b), Rotor slit width (c), and Number of stator conductors (d) for all values from initial training data.

Finally, the relationships and correlations between the individual machine parameters were calculated within the display of the above graphs. This is mainly to determine how much the parameters are affected by each other and if one parameter increases or decreases with another. For these purposes, Pearson's R and covariance coefficients were used. Pearson's R coefficient is already known from use on the surrogate model. The covariance is very similar and its principle is to find a linear relationship between two sets of data. Unlike Pearson's R coefficient, its value has no limit. Both parameters were calculated in Python based on the procedure described in [167].

Table 6.3 shows how the output parameters of the machine simulation have a strong linear relationship with each other. Thus, Pearson's R coefficient was applied here and only to the training data on the surrogate models. On the diagonal of the table values it can be seen that the values are equal to 1. In other words, the corresponding parameters grow linearly, which is logical. The other values then take values between -1 and 1 , indicating the strength of the linear relationship between the parameters. This means that, for example, the flux density in the air gap has a relatively strong relationship with the machine torque, as its value is close to 1. So as the flux density in the air gap increases, the machine torque also increases. This hypothesis has been confirmed above. In another example, as the electromagnetic efficiency increases, the value of the flux density in the air gap decreases. The value of the coefficient in this case is close to -1 . And it can also be seen that the size of the torque has very little effect on the size of the torque ripple. Which means that the value of Pearson's R coefficient is close to 0. The same rules apply to the other parameters, the difference is that the values of their Pearson's R coefficients differ.

The same procedure was done for the surrogate model verification data. The only difference is that the values in the table are different because the total number of data was lower than in the previous case. The values for the verification data are given in Table 6.4 and are for verification purposes only.

Table 6.3: Determination of the strength of the linear relationship between machine output parameters using Pearson's R coefficient for training data.

Parameter	Torque	Power factor	Efficiency	Torque ripple	Flux density
Torque	1.00000	-0.42254	-0.55627	0.09109	0.88363
Power factor	-0.42254	1.00000	0.78518	-0.70816	-0.62358
Efficiency	-0.55627	0.78518	1.00000	-0.62803	-0.72316
Torque ripple	0.09109	-0.70816	-0.62803	1.00000	0.27485
Flux density	0.88363	-0.62358	-0.72316	0.27485	1.00000

Tabel 6.4: Determination of the strength of the linear relationship between machine output parameters using Pearson's R coefficient for verification data.

Parameter	Torque	Power factor	Efficiency	Torque ripple	Flux density
Torque	1.00000	-0.47624	-0.59543	0.01499	0.90144
Power factor	-0.47624	1.00000	0.74772	-0.66132	-0.62154
Efficiency	-0.59543	0.74772	1.00000	-0.55425	-0.73721
Torque ripple	0.01499	-0.66113	-0.55425	1.00000	0.20215
Flux density	0.90144	-0.62154	-0.73721	0.20215	1.00000

The last two tables show the correlation between input and output parameters of the machine, for all initial training data. Table 6.5 shows the values for the strength of the linear coupling between input and output parameters, where Table 6.6 shows the values for the linear coupling between input and output parameters. Both tables show statistically the same value, only the scale of their values differs. So this means that if some parameters calculated using the coefficient for Pearson's R will have a very similar number (where the numbers differ most far beyond the decimal point) the coefficient for covariance can detect this difference much better. Otherwise, essentially the same rules for coefficient values apply as in previous tables. So for example, if the number of stator conductors increases, the torque decreases. Or that, the depth of the rotor slits has almost no effect on the torque ripple. And the torque ripple increases as the width

Tabel 6.5: Determination of the strength of the linear relationship between machine input and output parameters using Pearson's R coefficient for all data.

Parameter	Torque	Power factor	Efficiency	Torque ripple	Flux density
Active length	-0.36817	0.39138	0.47482	-0.19413	-0.69470
Slit depth	0.16693	0.26876	0.03490	-0.00904	-0.02006
Slit width	-0.16499	-0.45290	-0.20946	0.63171	-0.00998
Conductors	-0.84592	0.38221	0.42500	-0.17095	-0.69226

Tabel 6.6: Determination of the linear relationship between machine input and output parameters using covariance coefficient for all data.

Parameter	Torque	Power factor	Efficiency	Torque ripple	Flux density
Active length	-13852.083	10588.077	15164.026	-3358.571	-22393.131
Slit depth	7177.716	8309.431	1273.875	-178.809	-739.135
Slit width	-9656.481	-19059.112	-10405.883	17000.433	-500.342
Conductors	-31827.353	10339.975	13573.282	-2957.608	-22314.730

of the rotor slits increases. These tables therefore serve for a deeper analysis of the machine behaviour in terms of statistics and the possible discovery of relationships between individual parameters that were not found in the sensitivity analysis.

Based on all the results obtained, it was concluded that the surrogate models for the case study machine are applicable for this type of application and very accurate. The surrogate models were therefore ready for further use to optimize the machine design. The next chapter will discuss the use of surrogate models for machine optimization as well as active learning of surrogate models.

7 Optimization of the case study induction machine with a solid rotor using surrogate model and active learning of surrogate model

7.1 Selecting a suitable optimization algorithm for a case study machine with a solid rotor

To optimize the machine design, it was necessary to select the proper optimization algorithm. For the purpose of optimization of the design of the case study induction machine with a solid rotor, there are many suitable optimization algorithms such as stochastic algorithms [168], evolutionary algorithms [169], genetic algorithms [170], particle swarm optimization [171], and others. Hence, there are many optimization algorithms for optimizing engineering problems, each with different characteristics. Based on the large selection of optimization algorithms, either a Python script could be created to optimize the machine for this work, or there was the option of using existing programs that use one of the above optimization algorithms.

For the purposes of this master thesis the SymSpace program was chosen. Developed at the Linz center of mechatronics (LCM), it is a tool not only for the calculation and optimization of electrical machines, but also for other engineering, mathematical and physical purposes. It is essentially an integration platform that can connect multiple external programs to communicate with each other and automate their processes and tasks. With Optimizer, which is part of SymSpace, it can optimize any machine design or other problem with multi-objective optimization. In Publication [172], the developers of the program show its advantages and the method of acceleration of the calculation and optimization of the PMSM design. So the main advantage of SymSpace and Optimizer is that it can automate the process and optimization of machine design. Moreover, the optimization algorithm in this program is very well fine-tuned. In case of creating a custom optimization script, debugging it could be complicated and take a longer time. For the purpose of this master thesis, it is not necessary to create an optimization script, but rather to find the best machine design using a surrogate model with the help of any optimization algorithm. The disadvantage of this program, however, is that it is designed to optimize machine design using FEM-based programs. The program is designed in such a way that it takes longer to run each individual calculation, due to FEA analysis. So finding the best machine design for optimization takes longer for each calculation. But the surrogate model is an approximated function, so the calculation of each machine design is instantaneous. For this reason, optimizing the machine design using SymSpace and Optimizer using surrogate models is much slower than using an

optimization script. As mentioned for the purposes of this work, this is not an important characteristic. More information regarding SymSpace and Optimizer, including their features and capabilities, is provided in [173] and [174].

The Optimizer itself does not contain only one optimization algorithm, but has multiple options to choose from, in order to make efficient optimization. Its main optimization algorithm, is MOEA, which is further divided into:

- **DECMO** - differential evolution-based, the co-evolutionary multi-objective optimization algorithm [175]
- **SPEA2** - the strength Pareto evolutionary algorithm [176]
- **NSGA-II** - the non-dominated sorting genetic algorithm [177], [178]

In this work, the DECMO was used for the optimization of the machine.

Since Optimizer has slower calculations of each machine design during optimization, it was convenient to save all surrogate models in a pickle file created with Python. According to [179], pickle file is used for serializing and de-serializing Python object structures, also called marshalling or flattening. Serialization refers to the process of converting an object in memory to a byte stream that can be stored on disk or sent over a network. Later on, this character stream can then be retrieved and de-serialized back to a Python object. However, Pickle file is not compressed file. Pickle file is in fact useful in application where some degree of persistency of data is required. So basically, if python program is in some state, this state can be saved to a file on disk. For this reason, pickle file is very useful in machine learning algorithms, where they can be saved without the need of training them each time all over again. In the case of this work, all surrogate models were saved in pickle file, which decreased time in overall optimization of the machine design. The [180] shows full documentation and use in Python.

7.2 Optimization process of the case studies with a solid rotor

The first step of the optimization process, was to create a SymSpace file that contained all needed input parameters and other constants. The inputs therefore include:

- Active length of the machine,
- Number of stator conductors,
- Rotor slits depth,
- Rotor slits width,

- Other constant values of machine geometry and coefficients,
- Base values of output parameters of the machine.

The first four parameters were already declared and described and they change during optimization. The last two, however, serve as a basis for calculating the price of the machine and converting the calculated output parameters to a per unit system. Thus, do not change during optimization. The reason for converting calculated machine output parameters to a per unit system is that it is much easier to see which parameter is improving or deteriorating with each calculated design during optimization. As a result, this means that the given graphs in optimization can be imaginatively divided into four quadrants, where one quadrant lead to optimal machine designs and the remaining ones lead to deterioration in overall machine performance, therefore to worse machine designs. The base values for converting the output values to a per unit system were considered from Chapter 5 of Table 5.1. In addition, the previously mentioned pickle file, which includes all surrogate models, was imported to SymSpace and used to calculate the output parameters. In this way it is possible to calculate the output parameters of the machine and its price instantly. All machine output parameters that SymSpace calculates, both their absolute value and the value in the per unit system, are:

- Torque,
- Power factor,
- Electromagnetic efficiency,
- Torque ripple,
- Fundamental component of the flux density in the air-gap,
- Price of the machine.

The graphical environment of SymSpace including the created input and output parameters of the calculated machine and ready for optimization of machine design is shown in Fig. 7.1.

The created SymSpace file was then imported into Optimizer, where it was necessary to define settings for the optimization. The first step was to specify constraints for input parameters of the machine. Based on the selected constraints and possibly the given input parameter step, the Optimizer evaluates how many combinations they have. Thus, in some cases, it can reveal the total length of the optimization. The constraints for the input parameters, with their step and all possible number of combinations, are then listed in Table 7.1. If the step value is 0, it means that the step is not defined.

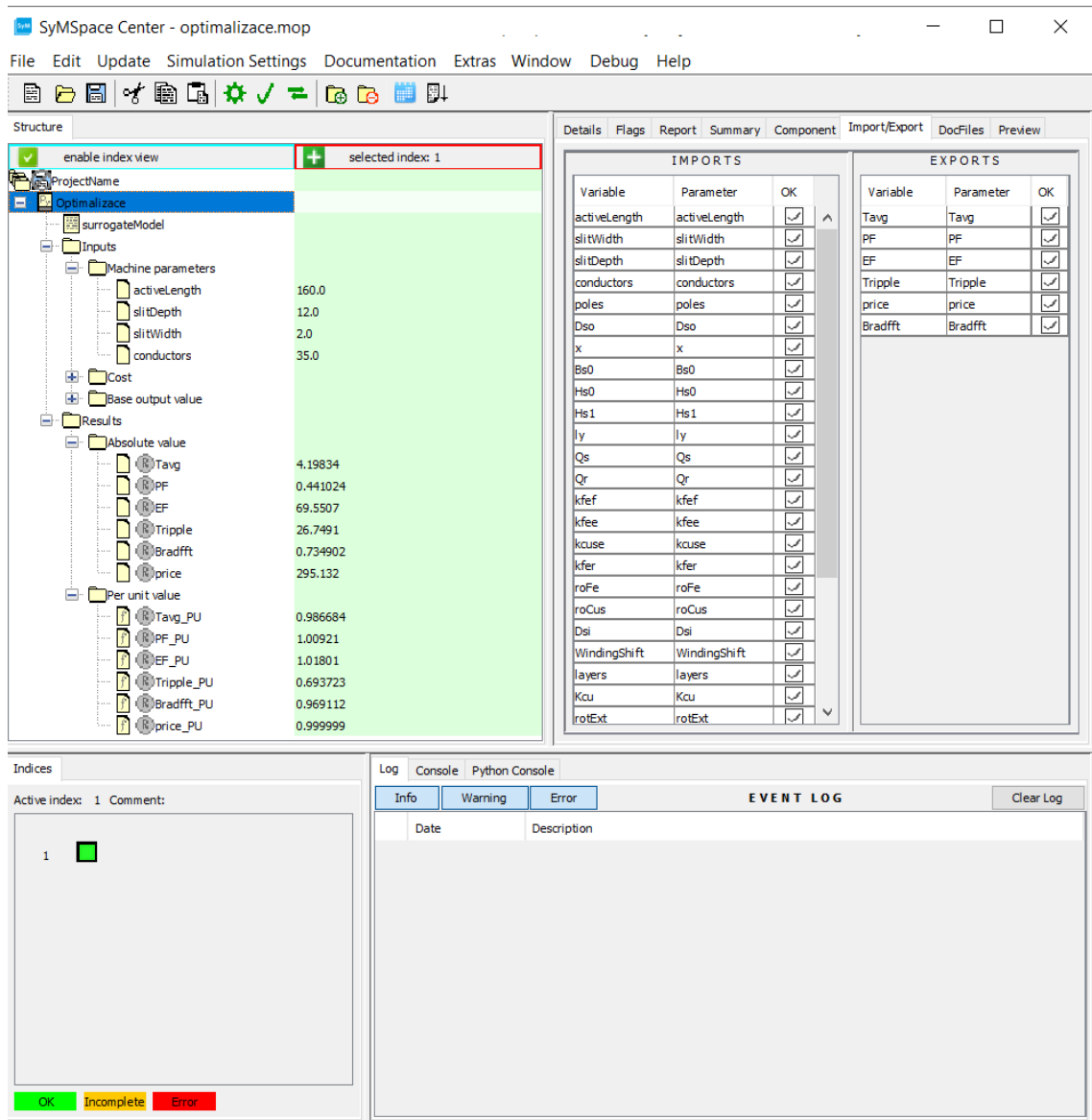


Fig. 7.1: Demonstration of the SymSpace graphical environment and the created input and output parameters of the calculated case study machine.

Table 7.1: Determination of input parameter constraints including their step and possible combinations during optimization.

Parameter	Min	Step	Max	Combinations
Active length	120	0	240	∞
Slit depth	9	0	21	∞
Slit width	0.6	0	2.7	∞
Conductors	23	1	47	25

As for the next step, the optimization objectives had to be determined during the optimization setup. This is for the reason to determine which calculated output parameter of the machine should have its value maximized, minimized or left unchanged by the Optimizer. In addition, the Optimizer can consider all output parameters together when optimizing. So it tries to find the optimal balance between them. For initial optimization, it is not necessary to set constraints on the output parameters of the machine. This can be done when it is finished, which will be explained later. All optimization objectives and constraints on machine output parameters are listed in Table 7.2. Table 7.3 shows the names of all output parameters in the Optimizer.

Table 7.2: Determination of optimization objectives and output parameter constraints in per unit system for the initial optimization.

Parameter	Objective	Min constraint	Max constraint
Torque	MAX	-	-
Power factor	MAX	-	-
Electromagnetic efficiency	MAX	-	-
Torque ripple	MIN	-	-
Flux density in the air-gap	NONE	-	-
Price of the machine	NONE	-	-

Table 7.3: Naming of machine output parameters, their absolute value and their value in per unit system, in Optimizer.

Parameter	Per unit system	Absolute values
Torque	Tavg_PU	Tavg
Power factor	PF_PU	PF
Electromagnetic efficiency	EF_PU	EF
Torque ripple	Tripple_PU	Tripple
Flux density in the air-gap	Bradfft_PU	Bradfft
Price of the machine	price_PU	price

The optimizer is then set up to use the DECMO optimization algorithm as discussed in the previous section. When the Optimizer was started, the individual machine calculations were performed sequentially. This is because this type of optimization is faster as it involves instantaneous calculations. When the number of Pareto fronts was sufficient, the optimization was stopped. All suitable Pareto fronts from the optimization were subsequently extracted from the Optimizer and the selected samples from it used for re-evaluation in Ansys maxwell. From the obtained recalculated simulation results, Python was used to determine how large the deviation was between the surrogate model values

and the simulations. Accordingly, either new surrogate models were created and reused for the new optimization or the final machine designs were calculated. This process is therefore iterative and is an active learning of surrogate models. Diagram in the Fig. 7.2 shows whole workflow of optimization of the case study machine with active learning of the surrogate models, which was described above. Normally the number of iterations is around 2 to 3, but it can vary based on the application. In the next section, the results of the first optimization of the machine and the possible re-training of surrogate models will be presented. In the next section, the results of the first optimization of the machine and the possible re-learning of surrogate models will be presented.

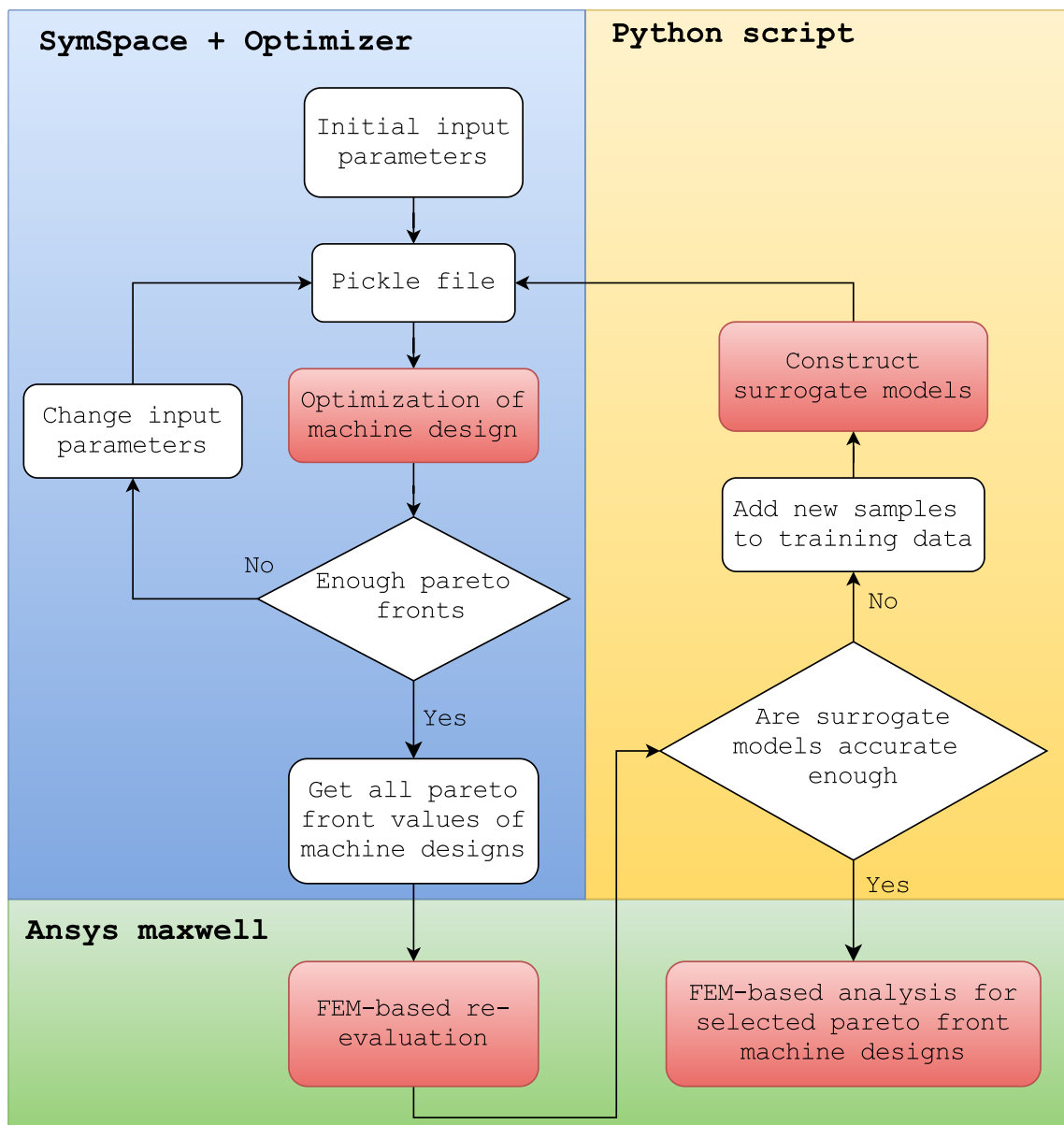


Fig. 7.2: Block diagram for the process of machine design optimization using surrogate model and its active learning.

7.3 Results of the first optimization of the case study machine with a solid rotor

Since the objective of the optimization for the case study machine is not specified in the assignment of this thesis, three states of final designs were considered for the machine during optimization:

- Design with the highest possible **electromagnetic efficiency**,
- Design with the highest possible **torque**,
- Design with the lowest possible **price of the machine** considering the highest possible **torque**.

The initial optimization then took about a day. The total number of calculated entries was around 200,000 of which there were approximately 10,000 Pareto fronts in total. This means that only 5% of the input geometries meet the condition specified in the setup. Due to the speed of calculation of the individual optimization entry, the total number of all calculated entries is relatively low. This is also due to the fact that Optimizer has a problem with storing a large number of computed entries, since it is made for conventional optimization with FEM-based calculations, where much fewer entries are assumed. Conventional optimization can often only compute around 5,000 entries, and the total duration is in the range of weeks to months, where the speed of computation depends very much on the computer setup or computing server setup. Optimization using the surrogate model can be run even on a weaker computer setup. Thus, it can be seen that machine optimization using surrogate models is much faster compared to conventional optimization. But despite the relatively small number of total calculated inputs, it is in fact more than enough to optimize the machine. For a case study machine this is absolutely sufficient and as previously stated Optimizer has a very well tuned optimization algorithm.

The initial optimization for the main optimization objectives of the machine without any constraints displayed in a per unit system is shown in Fig. 7.3. Dark blue dots indicate values for Pareto fronts, while light blue dots indicate optimization inputs that do not satisfy the optimization conditions. A value equal to 1 in the graphs indicates the original values of the machine output parameters. So, it can be seen that if the value for torque, electromagnetic efficiency and power factor is higher than 1, it is an improvement in machine performance. For the torque ripple it is the opposite, the desired value is less than 1. It is clear that there is not much room for improvement for electromagnetic efficiency and power factor. Although the difference does not seem to be too big in the result it can greatly affect the performance of the machine. On the other hand,

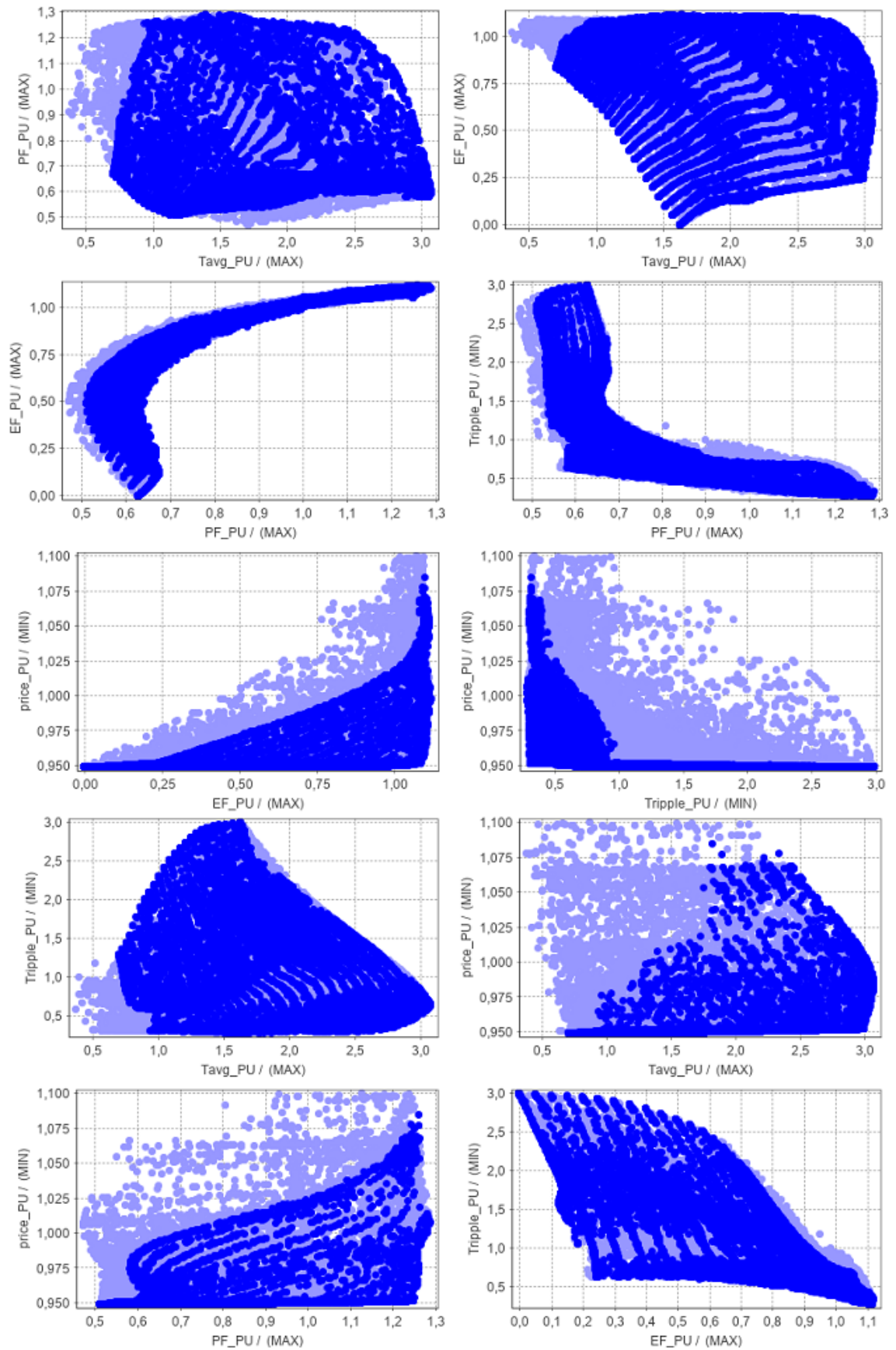


Fig. 7.3: Initial optimization results for the main optimization objectives of the case study machine without any constraints in Optimizer, displayed in a per unit system.

there can be a significant improvement in torque and torque ripple. Both parameters will therefore be most evident in the final analysis of the optimized machine. The price of the machine then indicates by how much the price can be reduced compared to the original design, which can be taken into account for possible serial production. The price of the original machine design was valued at approximately 295 euros. It can be seen that a significant part of Pareto fronts is below the price of the original machine design. So a reduction in the price of the machine can be achieved despite the improvement in its output parameters. The same graphs, but with output parameters presented in absolute values, are listed in the appendix.

Fig. 7.4 shows the distribution of input parameters and their number of uses in the Optimizer during initial optimization. This is only a confirmation of the previously defined theory and the results obtained so far with the sensitivity analysis of the machine. Nevertheless, some conclusions can also be drawn for machine performance and optimization behavior. It would be expected that the Optimizer would try to increase the active length of the machine to increase torque and efficiency, instead it mainly uses the lowest limit of the active length of the machine. This parameter is therefore strongly influenced by the optimization objective to reduce the price. With a small active machine length, it tries to increase the machine torque by using a small number of stator conductors which increases the overall saturation of the machine. The depth of the rotor slits here satisfies the predetermined hypotheses, but tries to go to both extremes when optimizing the width of the rotor slits. The left extreme limit focuses mainly on increasing the overall performance of the machine, while the right limit focuses on reducing the price of the machine. Thus, when the price of the machine is included in the optimization, some predefined hypotheses may not be directly applicable here because of it.

However, the whole optimization was done without any constraints on the output parameters, which greatly affects the saturation of the machine. With the small active length of the machine and the low number of stator conductors, there is a large over-saturation of the machine. This can be seen in Fig. 7.5, where the graphs show the dependence of the flux density in the air-gap on each of the other output parameters. In this case, the output parameters are given in absolute values. Graphs showing these values in the per unit system are provided in the appendix. Here, the parameters in absolute values better reveal whether the magnitude of the flux density in the air-gap meets a previously defined range. The flux density in the air-gap here reaches values of up to $1.3T$ which significantly exceeds the recommended limit. For this reason, it is necessary to apply a constraints to these results for the output parameters of the machine.

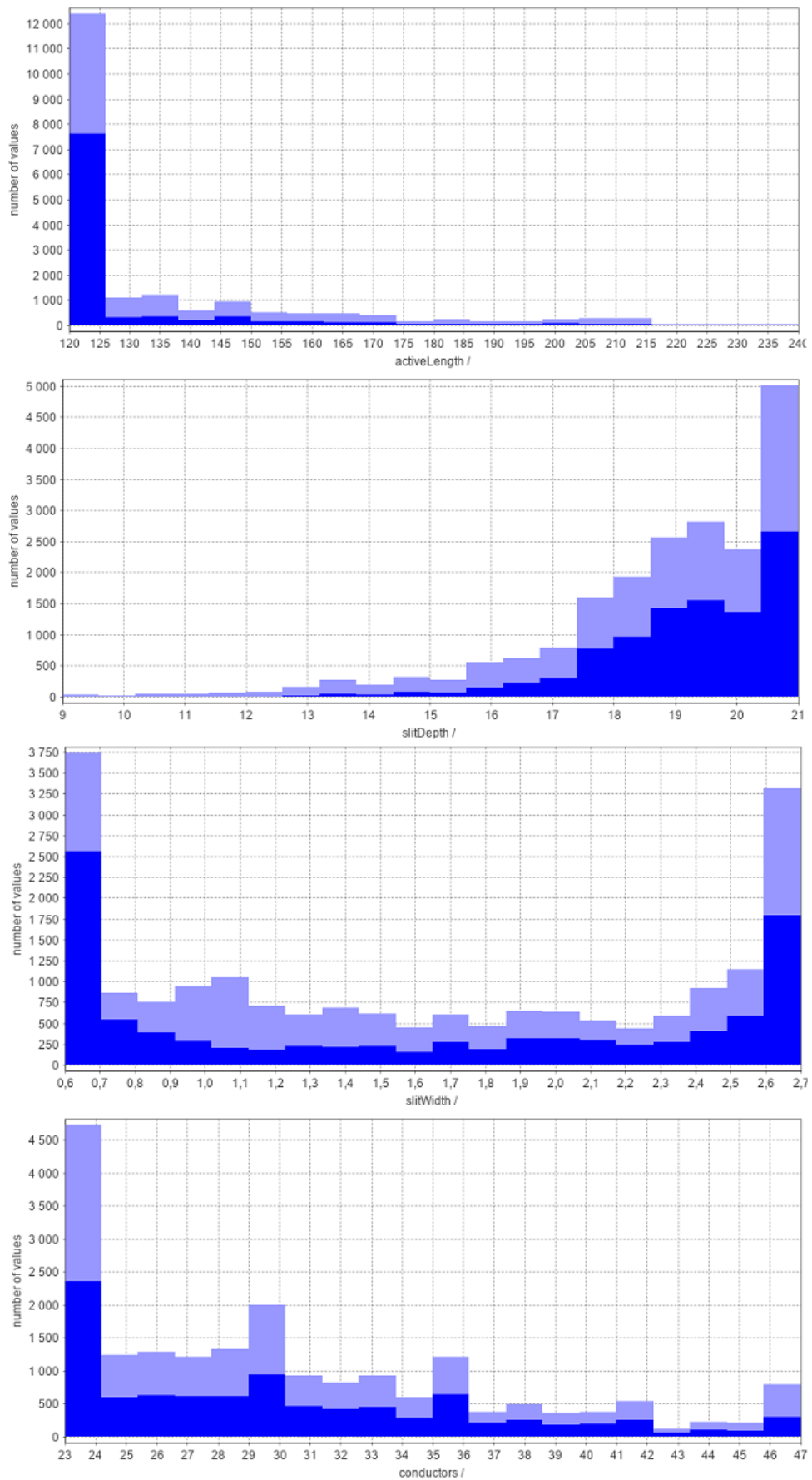


Fig. 7.4: Distribution of input parameters and their number of uses in the Optimizer in the initial optimization without any constrains.

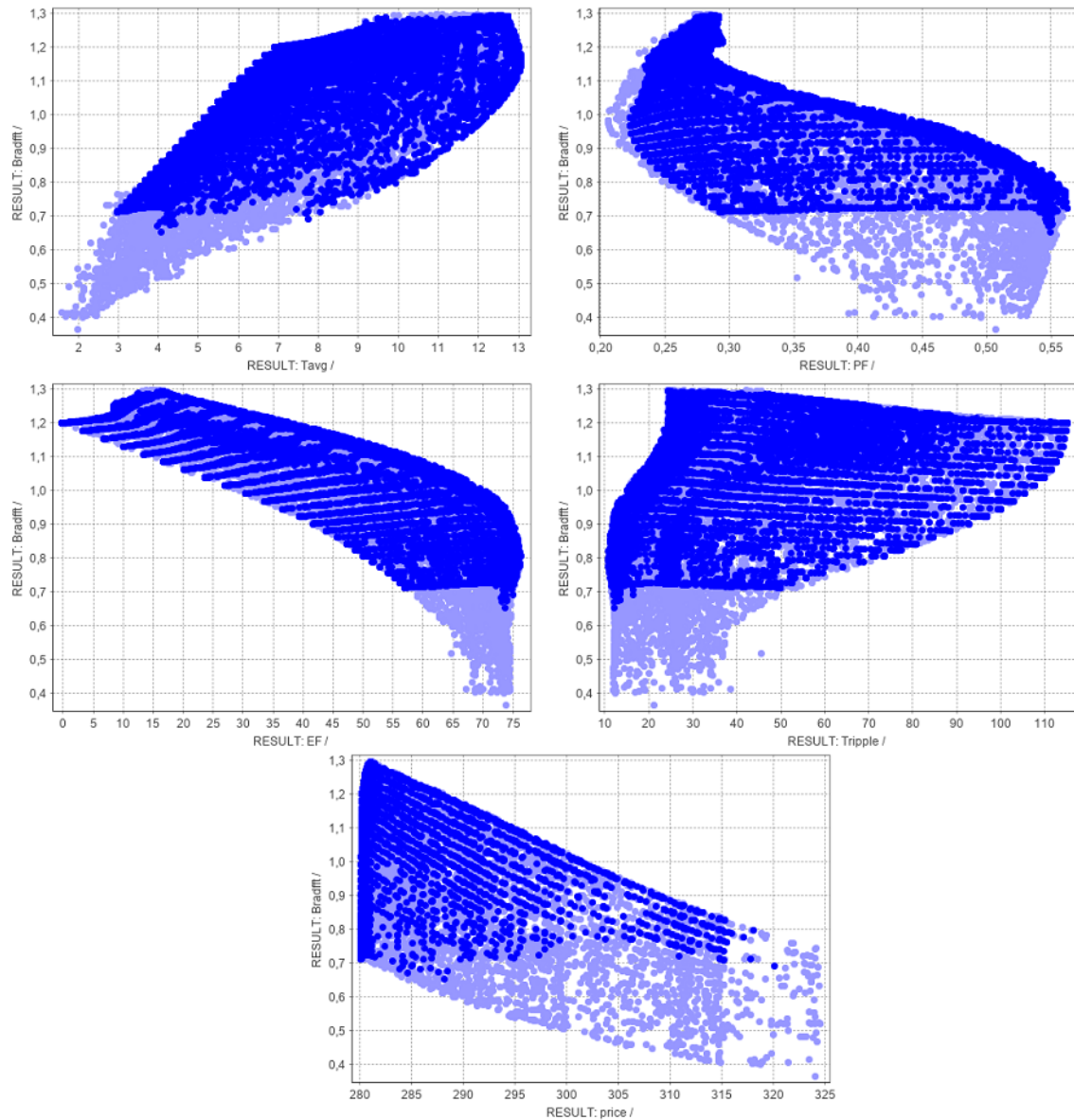


Fig. 7.5: The flux density in the air-gap as a function of other output parameters in the initial optimization results of the machine without any constraints in Optimizer.

Another advantage of Optimizer is that it can filter out existing results, which is exactly the case needed here. Basically, it is just a matter of duplicating an existing optimization and changing the constraints on the output parameters. New constraints of the output parameters in per unit system for the optimization is shown in Table 7.4. For torque, power factor, electromagnetic efficiency and torque ripple, the limits are obvious as they improve the performance of the machine. The limit for the flux density in the air-gap is based on recommended values, while the price is again without limits as it is not a very important factor and the Optimizer could potentially filter out machine designs that are significant and could meet the predefined condition. When the duplicated optimization is started, the existing results are opened, where those members of

the Pareto front that previously met the optimization conditions are now shown as not meeting the conditions. Thus, there is no need to run a new optimization, which is the point of this step.

Table 7.4: Determination of optimization objectives and output parameter constraints in per unit system for the results of the initial optimization.

Parameter	Objective	Min constraint	Max constraint
Torque	MAX	1	∞
Power factor	MAX	1	∞
Electromagnetic efficiency	MAX	1	∞
Torque ripple	MIN	0	1
Flux density in the air-gap	NONE	0.923	1.187
Price of the machine	NONE	-	-

With the defined constraints on the output parameters, the total number of Pareto fronts was reduced from 15,000 to 875. Which is a significant reduction in all possible usable machine designs and accounts for only 0.4375% of all the calculated combinations. The reduced Optimizer results presented in the per unit system are shown in Fig. 7.6. It can be seen that despite the reduction in the total number of optimization results, there are still many machine designs that show significantly better performance than the original machine design. This reduction is mainly due to the saturation in the machine, which was also significantly reduced, as can be seen in Fig. 7.7. All limits of the machine output parameters presented in absolute values obtained from the reduced optimization results are given in Table 7.5. It is possible to see a significant improvement in the torque or torque ripple of the machine. However, it depends on the combination of input parameters that determine which output parameter of the machine will be most affected. What matters most is the trade-off between the input and output parameters. The rest of the obtained results of the initial optimization in the Optimizer, whether displayed in absolute values or per unit of the system, are shown in the appendix.

Table 7.5: Limits of machine output parameter values in absolute values obtained from reduced results of the initial optimization in the Optimizer.

Parameter	Unit	Min value	Max value
Torque	Nm	4.256	11.166
Power factor	—	0.437	0.563
Electromagnetic efficiency	%	69.215	76.368
Torque ripple	%	10.763	27.470
Flux density in the air-gap	T	0.7	0.9
Price of the machine	€	280.38	318.07

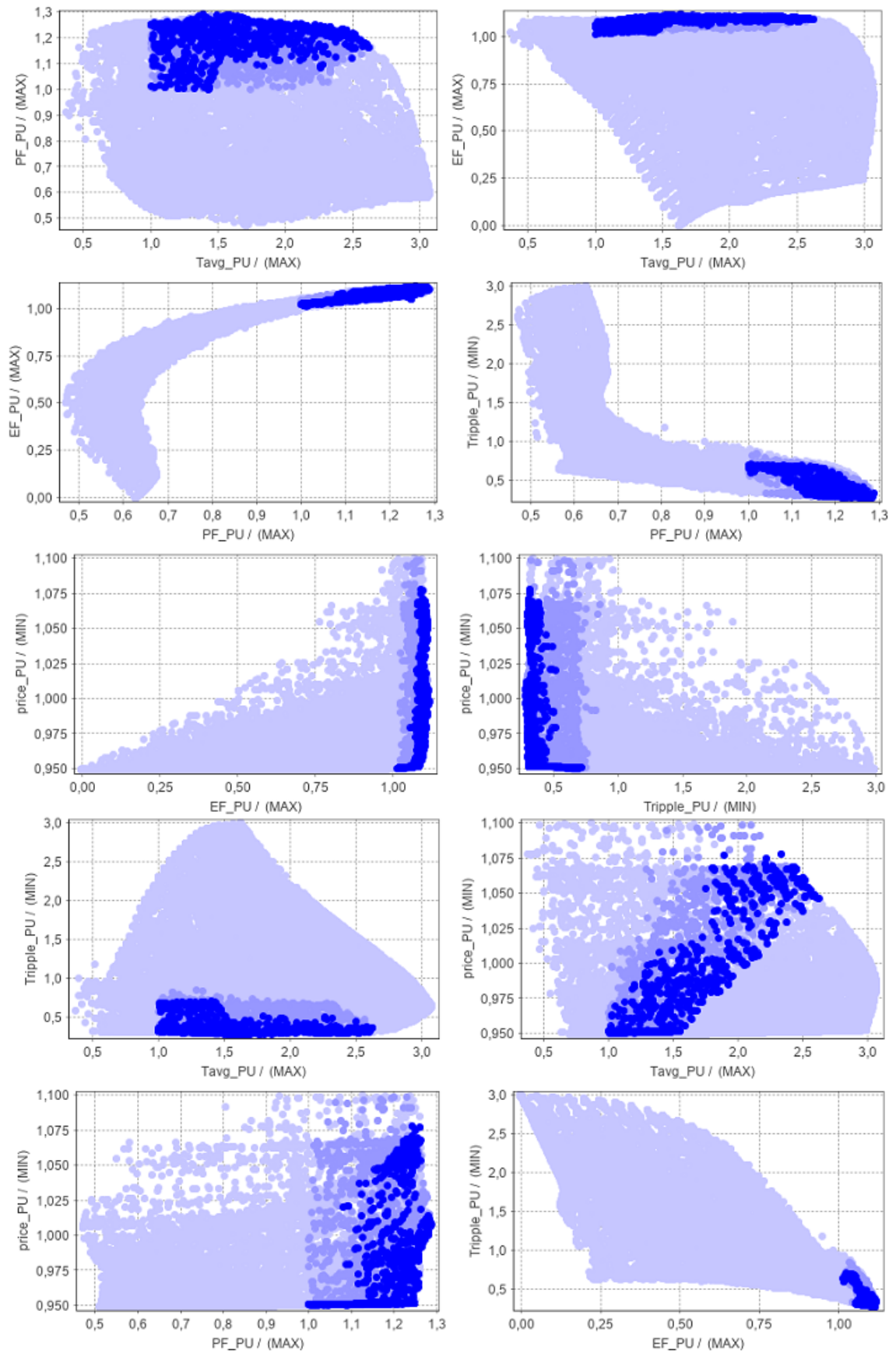


Fig. 7.6: Initial optimization results for the main optimization objectives of the case study machine with defined constraints in Optimizer, displayed in a per unit system.

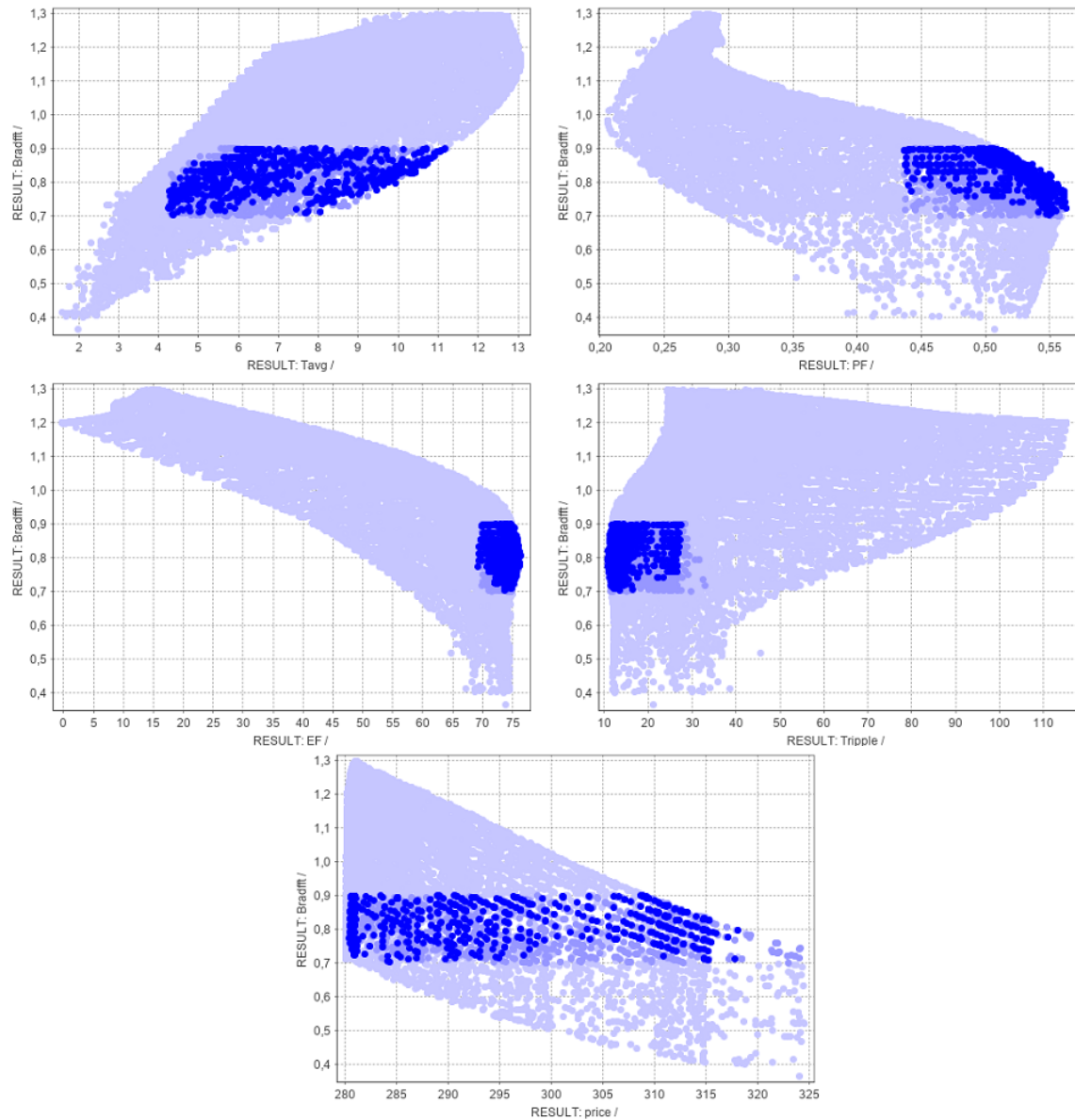


Fig. 7.7: The flux density in the air-gap as a function of other output parameters in the initial optimization results of the machine with defined constraints in Optimizer.

At this point, it was necessary to verify the results of the surrogate models from the optimization using FEM-based re-evaluation. It was therefore essential to select appropriate samples from the optimization results that were used for re-evaluation. As discussed in Chapter 3, it is possible to approach the selection of samples from the optimization results in multiple ways. In the case of this work, samples of machine designs were selected in a way that agrees with the 3 states of the machine declared at the very beginning of this section. This way it can be verified how accurate the surrogate models are in these desired locations. Based on each machine state, 50 samples were selected from the optimization results and re-evaluated using FEM simulations. The total number of re-evaluated results is therefore 150, where the total simulation time

took about a day and a half. The process of verifying the surrogate models is exactly the same as in Chapter 6, Section 6.4. But, the accuracy of the surrogate models was tested separately for each machine state.

To determine the accuracy of the surrogate models, existing learning data and newly obtained corresponding re-evaluated verification data were used, where comparison between them, considering the machine has the highest electromagnetic efficiency, is shown in Fig. 7.8. It is clear that the results of the surrogate models and their verification after optimization show less accuracy than in the case of their initial construction in Chapter 6. This is of course due to a different combination of verification data. However, based on the Pearson's R coefficient for the torque and flux density in the air-gap, it can be seen that the surrogate models are relatively accurate in these output parameters. The power factor and torque ripple have a smaller coefficient value and thus become more inaccurate, whereas the electromagnetic efficiency itself, which is the main concern of optimization, has even a negative coefficient value. The reason for the smaller values of Pearson's R coefficients is that these machine output parameters were evaluated by surrogate models at their outer limit. This was expected, since the evaluated output parameters of surrogate models usually fail at their limit and are inaccurate. Therefore, Pearson's R coefficient for the torque and flux density in the air-gap has a high value because their values were not evaluated at the limit of the surrogate models but at their midpoint. A negative Pearson's R value of the electromagnetic efficiency coefficient of the machine means that the obtained verification values are lower than those evaluated.

The Pearson's R coefficient is therefore not very reliable for revealing the accuracy of the surrogate models and serves only as guideline value. The verification data are mainly concentrated in a small part of the results of the surrogate models training data. This means that even the Pearson's R coefficient itself was computed on this small section and not over the entire range of the surrogate model. Therefore, the torque and flux density in the air-gap of the machine has a high coefficient value since their results are more spread out. A much better indicator for determining the accuracy of surrogate models is to establish the relative error between the evaluated surrogate model results and the verification results of FEM calculations. This way, the overall range of relative errors of all surrogate models is obtained, which will help identify whether the surrogate models need to be actively taught further. Graphs showing the relative error as a function of the input parameter will not be shown here. These are the same graphs as in Chapter 6, but in this case, there would be far more. They are therefore listed in the appendix. As a substitute, a table showing the total range of errors for all the output parameters of the surrogate models is provided in Table 7.6. The flux density in the air-gap and torque have quite a small relative deviation, which is desirable. The power factor and electromagnetic

efficiency already have a much higher deviation and the estimated values of the torque ripple are essentially inaccurate. So the surrogate models fail here.

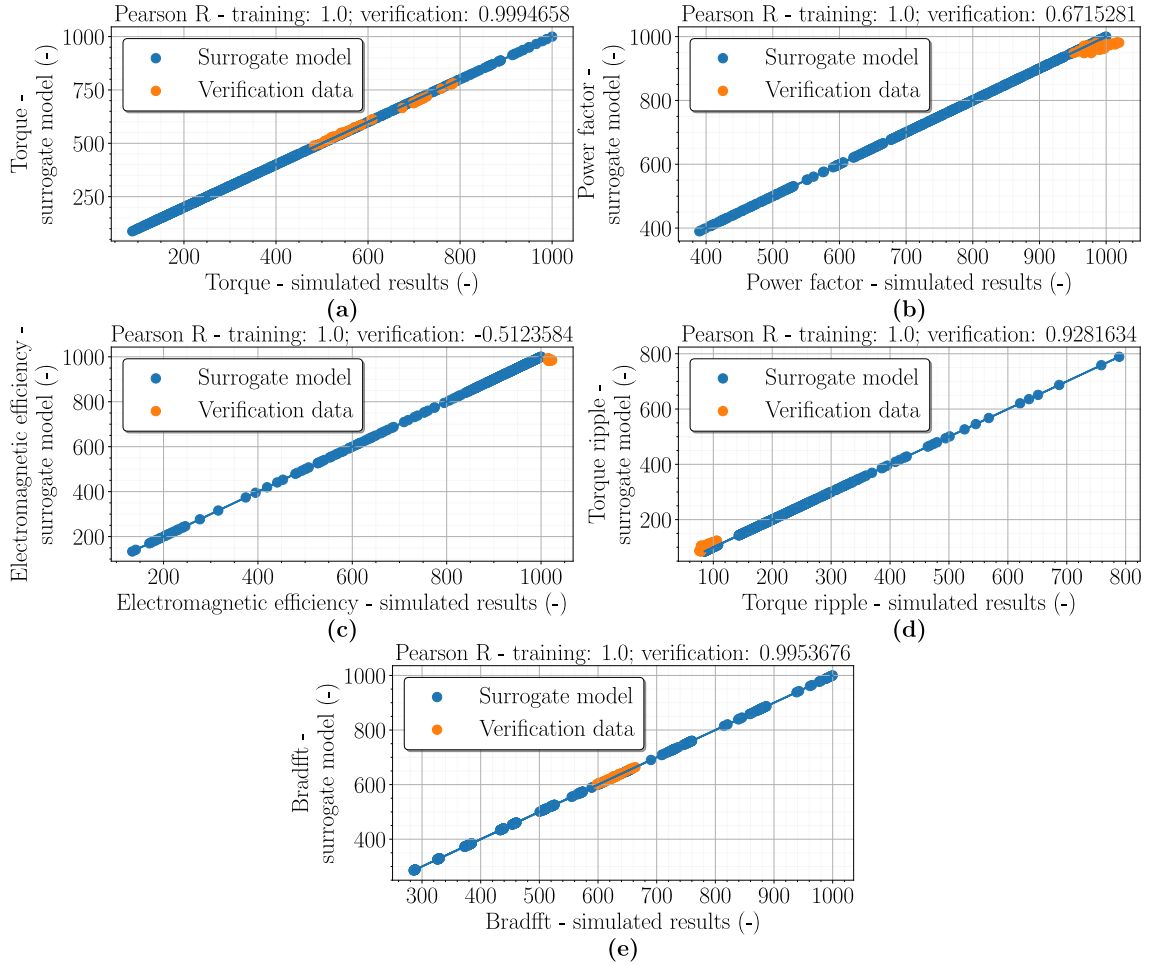


Fig. 7.8: Verification of the accuracy of the surrogate models using the results obtained from the initial optimization, where the verification samples are oriented to the highest possible electromagnetic efficiency of the machine for Torque (a), Power factor (b), Electromagnetic efficiency (c), Torque ripple (d), and Fundamental component of the flux density in the air-gap (e).

Table 7.6: Errors of the surrogate model results after re-evaluation of the initial optimization results with respect to the highest electromagnetic efficiency of the machine.

Parameter	Unit	Min error	Max error
Torque	%	-1.652	1.700
Power factor	%	-0.467	3.785
Electromagnetic efficiency	%	2.261	3.761
Torque ripple	%	-7.856	-33.327
Flux density in the air-gap	%	0.236	-0.722

The same procedure was consequently applied to the remaining 2 machine states. Verification of the accuracy of the surrogate models with verification samples for the highest machine torque is shown in Fig. 7.9. It can be seen from the graphs that the evaluated machine output parameters using surrogate models are more accurate here than in the previous case. Even the machine torque, which was the main objective of the optimization, was very well evaluated by the surrogate models. However, the electromagnetic efficiency of the machine again has a negative Pearson's coefficient value. This indicates again that the validation data has a lower value than those evaluated by the surrogate model. Overall, the surrogate models are more accurate, in this case, as evidenced by Table 1, which shows the range of deviation of all machine output parameters is given in Table 7.7. However, the torque ripple again has a very large deviation. So surrogate models have failed here again.

It remains to verify the last considered state of the machine, where the machine has lowest price with highest possible torque. In this case, the state of the machine is not considered in its outer limits, so surrogate models should be much more accurate in this case. This assumption is confirmed in Fig. 7.10. The values of Pearson's R coefficients are highest here, even for the electromagnetic efficiency of the machine, where the value of the coefficient here is not negative. But their values indicate that the surrogate models are rather accurate on average. Which is not wanted and as stated the coefficient value should be as close to 1 as possible. However, the deviations of the surrogate models are not very large in this case, as shown in Table 1. Output parameters such as torque, power factor and machine flux density in the air-gap of the machine have even the lowest deviation of all cases. But again the evaluated torque ripple fails here.

Based on the results obtained from the verification of all surrogate models for all 3 machine states, it can be concluded that the surrogate models are relatively accurate. However, they could be even more accurate and the evaluation of the ripple moment failed in any case. So in this case it is advisable to further learn surrogate models and perform the machine optimization again. The training of the surrogate models was essentially done in this case by taking all 150 verification samples and embedding them all into the existing surrogate model learning data. With the new learning data, new surrogate models were created and subsequently stored in pickle files. The process of the second optimization was then the same as here and its results are presented in the following section.

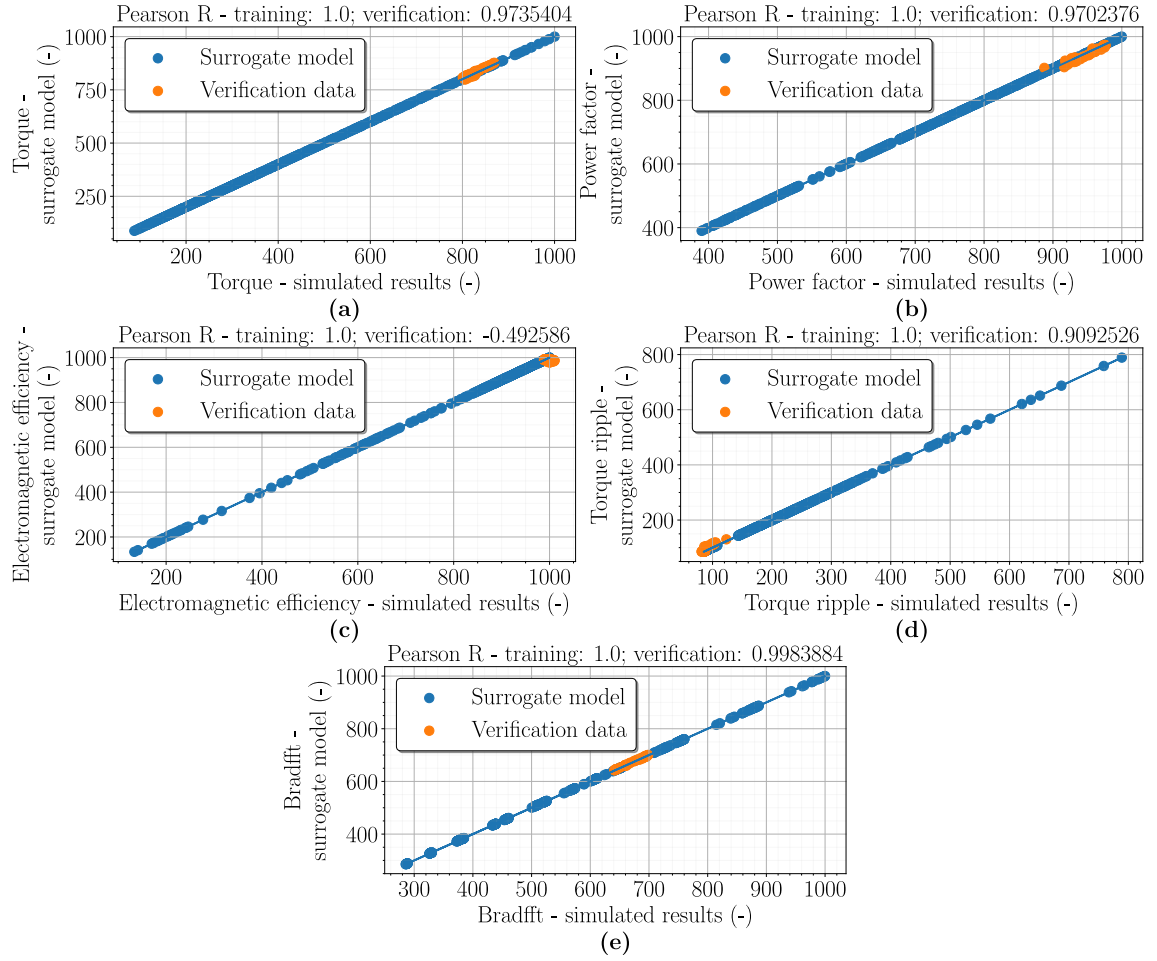


Fig. 7.9: Verification of the accuracy of the surrogate models using the results obtained from the initial optimization, where the verification samples are oriented to the highest possible torque of the machine for Torque (a), Power factor (b), Electromagnetic efficiency (c), Torque ripple (d), and Fundamental component of the flux density in the air-gap (e).

Table 7.7: Errors of the surrogate model results after re-evaluation of the initial optimization results with respect to the highest torque of the machine.

Parameter	Unit	Min error	Max error
Torque	%	1.194	-1.275
Power factor	%	1.349	-1.611
Electromagnetic efficiency	%	-0.310	2.515
Torque ripple	%	1.284	-20.740
Flux density in the air-gap	%	0.268	-0.424

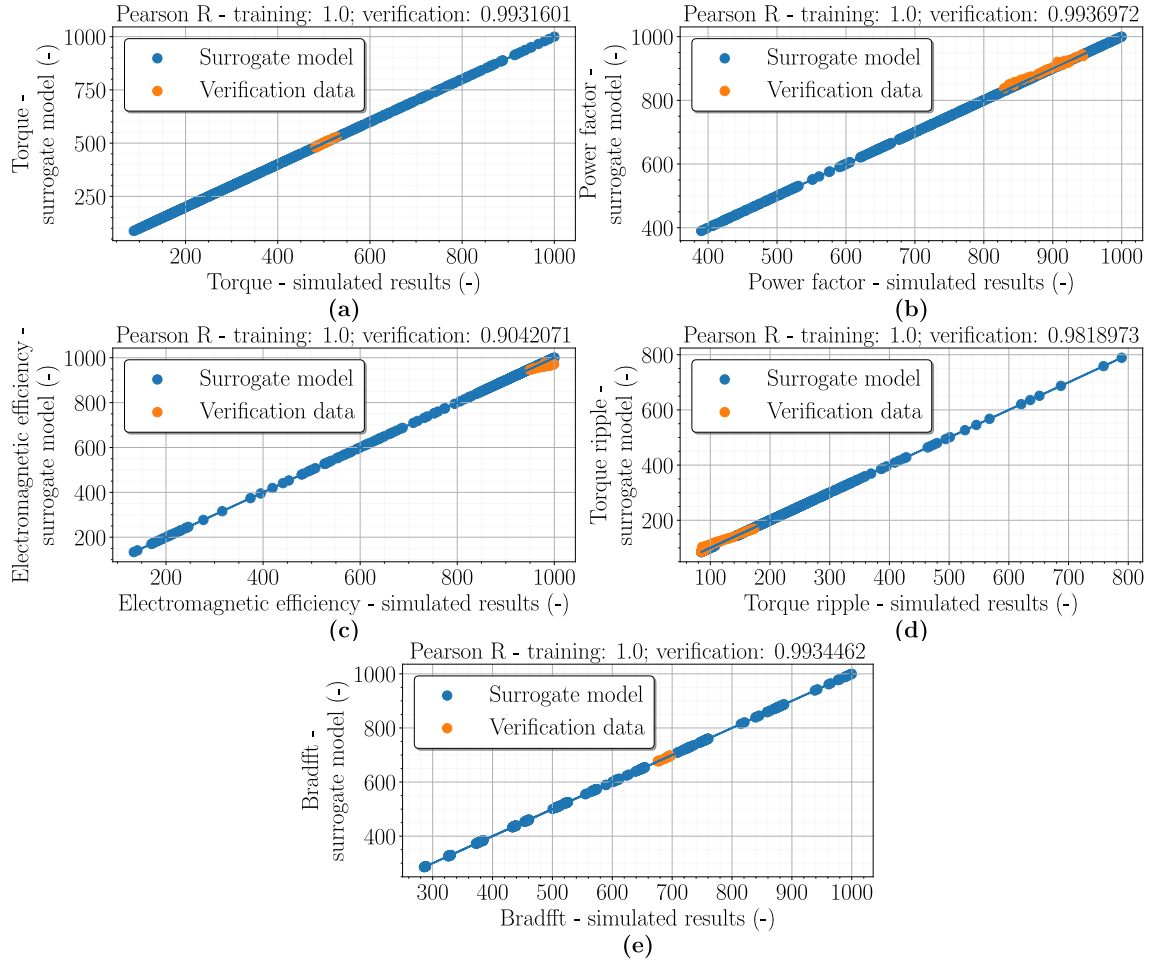


Fig. 7.10: Verification of the accuracy of the surrogate models using the results obtained from the initial optimization, where the verification samples are oriented to the lowest price of the machine with respect to the highest torque of the machine for Torque (a), Power factor (b), Electromagnetic efficiency (c), Torque ripple (d), and Fundamental component of the flux density in the air-gap (e).

Table 7.8: Errors of the surrogate model results after re-evaluation of the initial optimization results with respect to the lowest price of the machine considering the highest possible torque of the machine.

Parameter	Unit	Min error	Max error
Torque	%	0.385	-0.570
Power factor	%	0.511	-1.606
Electromagnetic efficiency	%	0.320	2.826
Torque ripple	%	2.534	-18.844
Flux density in the air-gap	%	-0.189	0.278

7.4 Results of the second optimization of the case study machine with a solid rotor

The process of the second optimization is basically the same as the initial one, that is, some steps and results in this section will be skipped. All the important results that will not be presented here, either from the optimizations or from the verification of the accuracy of the surrogate models, will be presented in the appendix. That being said, the second optimization took about a day and the total number of calculated entries was again around 200,000 of which there were approximately only 8,700 Pareto fronts in total. So in this case the total number of suitable machine designs is considerably lower at around 4.35%. With the defined constraints on the output parameters, the total number of Pareto fronts was additionally reduced to approximately 725, corresponding to only 0.3625% of all calculated combinations. Hence, it can be seen that further learning of surrogate models has reduced the total number of possible machine designs in its optimization.

The results of the second optimization, with defined constraints and displayed in per unit system, are shown in Fig. 7.11. The course of the results of the second optimization is basically the same as in the initial one. This is confirmed in Fig. 7.12, where the values for the absolute value of the flux density in the air-gap are given. More important, however, are the outer limits to which optimization has reached. Table 7.9 shows the outer limits of the optimization results with already defined limits of the output parameters. The outer limits for torque and torque ripple are here almost the same. For electromagnetic efficiency and power factor, this minimal change in the outer limit is relatively significant, as the machine does not have much room for improvement for these two parameters. Therefore, it can be observed that further learning of the surrogate models will indeed affect the optimization results and possibly reduce the achievable extreme limits of those output parameters that were too out of line with the results of the surrogate models in the previous optimization when verifying the accuracy.

Table 7.9: Limits of machine output parameter values in absolute values obtained from reduced results of the second optimization in the Optimizer.

Parameter	Unit	Min value	Max value
Torque	Nm	4.255	11.140
Power factor	—	0.438	0.554
Electromagnetic efficiency	%	69.044	74.960
Torque ripple	%	11.624	27.115
Flux density in the air-gap	T	0.7	0.9
Price of the machine	€	280.40	324.51

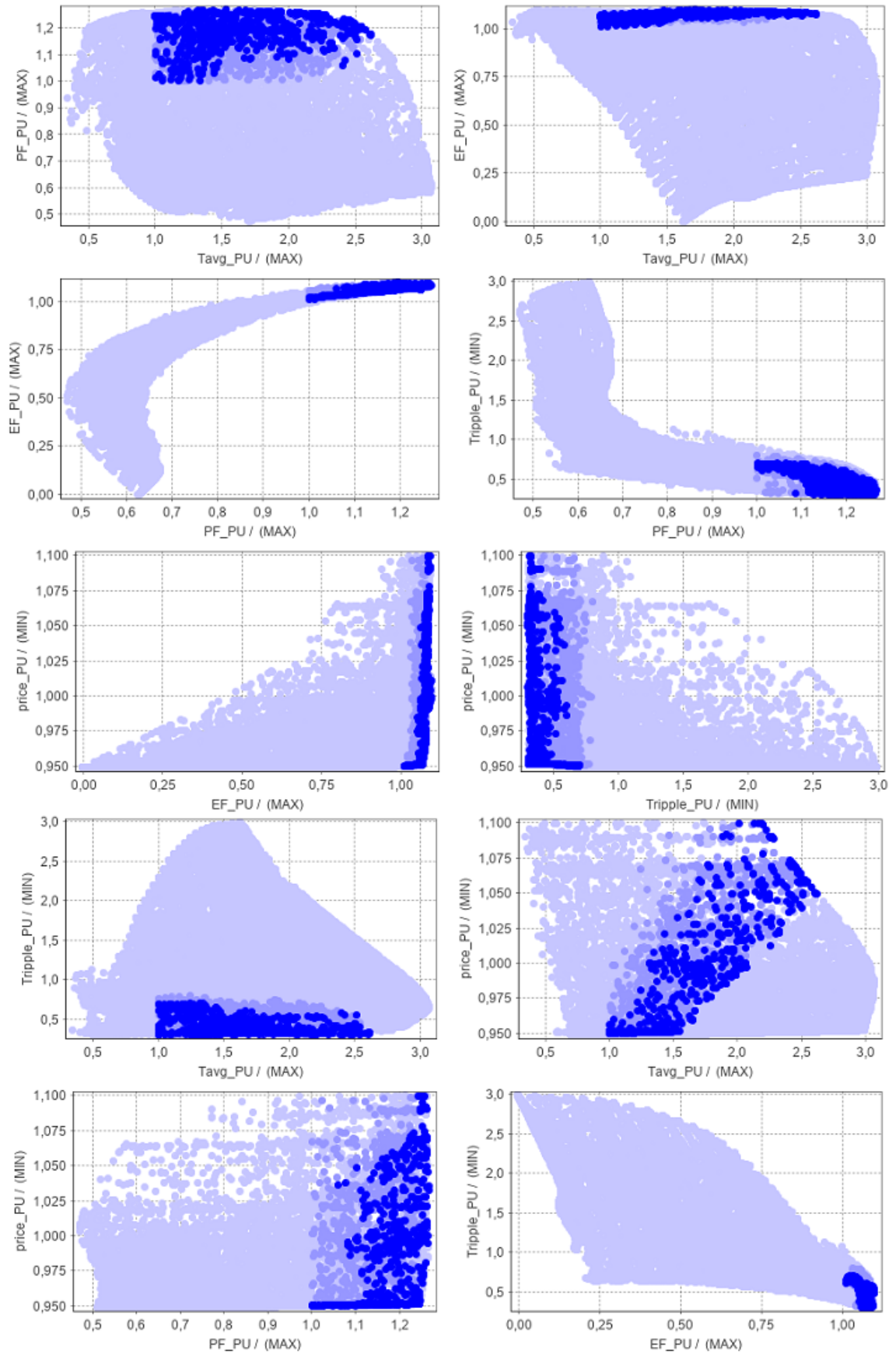


Fig. 7.11: Second optimization results for the main optimization objectives of the case study machine with defined constraints in Optimizer, displayed in a per unit system.

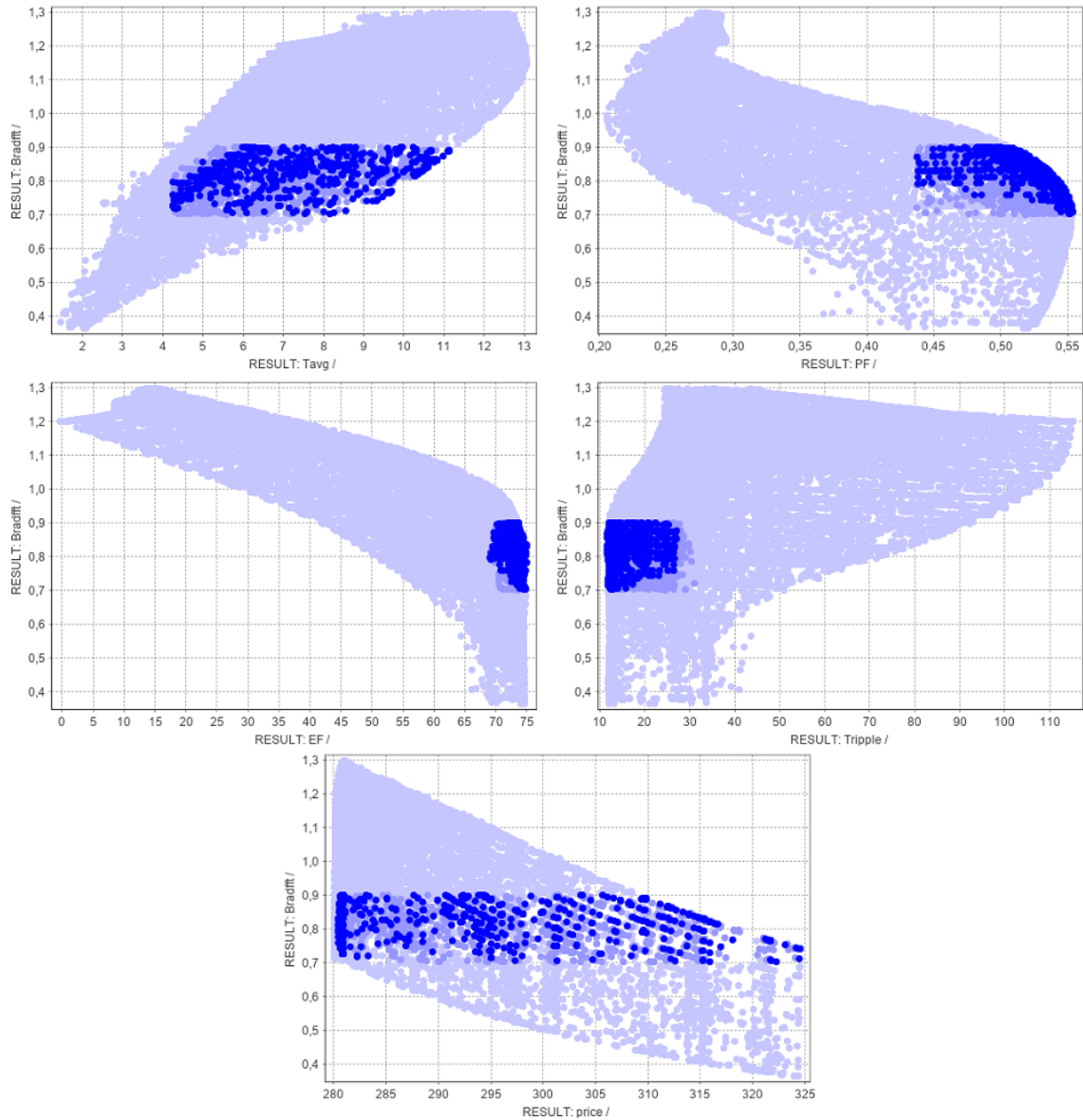


Fig. 7.12: The flux density in the air-gap as a function of other output parameters in the second optimization results of the machine with defined constraints in Optimizer.

Verification of the accuracy of the surrogate models after the second optimization was again performed for 3 machine states, where a total of 150 corresponding samples were calculated as verification data. It took about a day and a half to calculate all the samples again. To verify the accuracy of the surrogate models themselves, Fig. 7.13 shows a comparison of the evaluated values of the surrogate models and the verification data, for the machine state considering the highest possible electromagnetic efficiency. Pearson's R coefficients of the output parameters have a significantly higher value in this case and are much closer to the value of 1 which is desired. Except for the electromagnetic efficiency of the machine itself, whose values again reach the outer limit of the surrogate models and the result is actually somewhat lower, as indicated by

the verification data. Therefore, the coefficient here is again negative, but more close to 1 than in the previous case. That the surrogate models are considerably more accurate in this state is shown in Table 7.10, which shows their deviations. The deviation of all evaluated output parameters has been reduced by up to several percent and the deviation of the torque ripple has been even reduced by up to 20%. Consequently, apart from the torque ripple, the evaluated output parameters of the surrogate models are quite accurate. However, the torque ripple does not show such a large deviation.

A comparison of the accuracy of the surrogate models in terms of the highest possible machine torque is shown in Fig. 7.14. For this machine state, the output parameters have very good value of Pearson's R coefficients without any output parameter having a negative coefficient. This is an indication of their high accuracy. However, in order to make the models as accurate as possible, the value of the coefficients should ideally be closest to the 1 (as for example 0.9999). But their lower value is due to the small scatter of the verification samples, which was explained in the previous section. Nevertheless, the deviations of the surrogate models are very small, as shown in Table 7.11. For most output parameters the deviation is around 1%, which is a very good result and a significant improvement over the initial optimization. The torque ripple deviation is only 5% smaller, which is not such a dramatic improvement.

In the last state of the machine, verification of the accuracy of the surrogate models, it could be considered that here again the models will have the best results as they are not at their outer limits. This is partially confirmed in Fig. 7.15, which shows the accuracy of the surrogate models. Here the Pearson's R coefficients of the output parameters have by far the best values close to 1. For this machine state, surrogate models are very accurate. The opposite situation is observed for the electromagnetic efficiency of the machine, where it has a smaller coefficient value than in the case of the original optimization. But this is not as important as the deviation of surrogate models. The deviation of the surrogate models for this machine state is given in Table 7.12, where the deviation of the output parameters is again around 1%. With the exception of torque ripple, which has a deviation of around 12%.

From the obtained results of the accuracy verification of surrogate models, the average deviation of most output parameters is around 1 – 2%. For the torque ripple, the deviation is around 10 – 15%. Such a high deviation is most likely due to insufficient sampling of the input parameter when creating the initial learning data for all models. Therefore, if the overall deviation were to be reduced, the total number of input parameter samples would have to be increased to e.g. 7 or more. However, it is possible that with further learning of the surrogate models, the deviation would be greatly reduced.

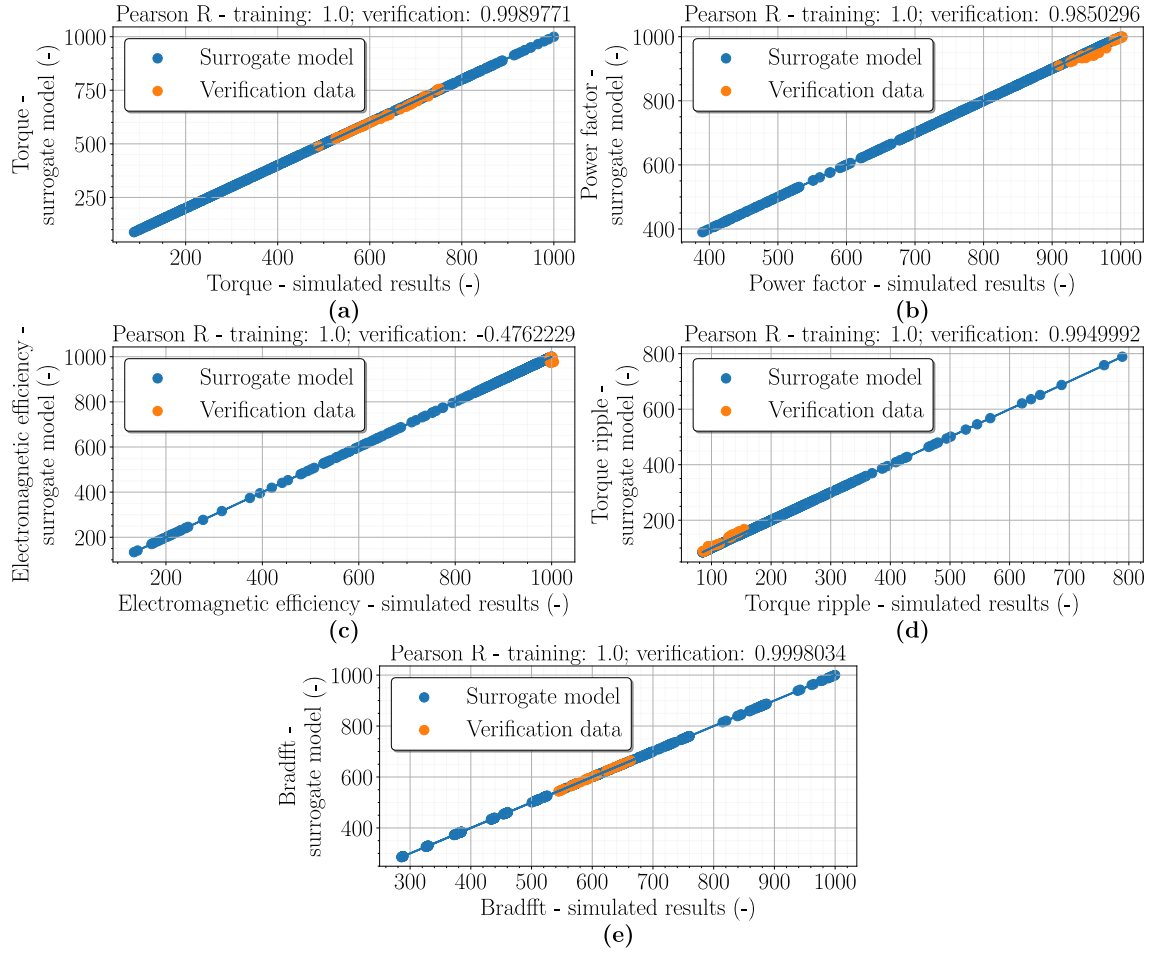


Fig. 7.13: Verification of the accuracy of the surrogate models using the results obtained from the second optimization, where the verification samples are oriented to the highest possible electromagnetic efficiency of the machine for Torque (a), Power factor (b), Electromagnetic efficiency (c), Torque ripple (d), and Fundamental component of the flux density in the air-gap (e).

Table 7.10: Errors of the surrogate model results after re-evaluation of the second optimization results with respect to the highest electromagnetic efficiency of the machine.

Parameter	Unit	Min error	Max error
Torque	%	-0.791	1.314
Power factor	%	-0.138	2.055
Electromagnetic efficiency	%	-0.050	2.755
Torque ripple	%	0.940	-12.511
Flux density in the air-gap	%	-0.265	0.300

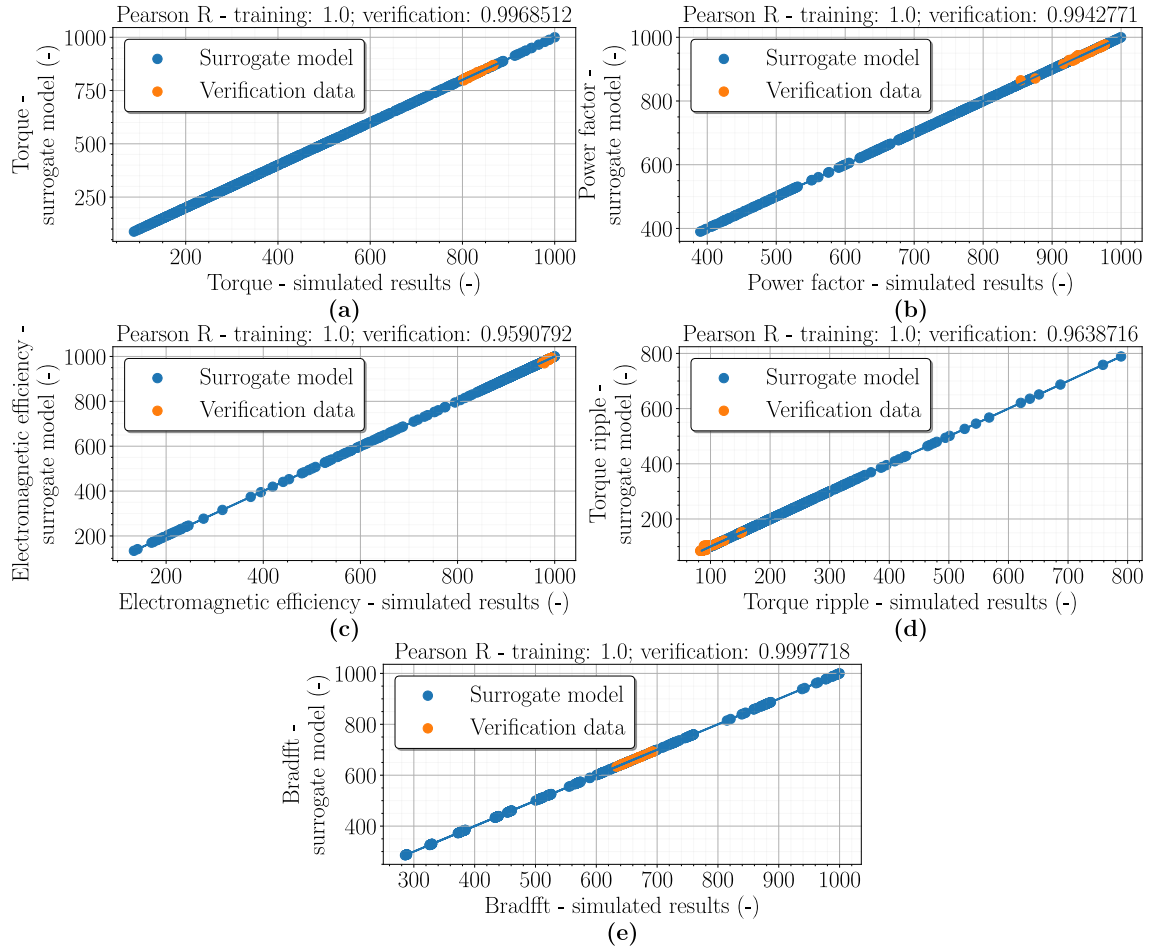


Fig. 7.14: Verification of the accuracy of the surrogate models using the results obtained from the second optimization, where the verification samples are oriented to the highest possible torque of the machine for Torque (a), Power factor (b), Electromagnetic efficiency (c), Torque ripple (d), and Fundamental component of the flux density in the air-gap (e).

Table 7.11: Errors of the surrogate model results after re-evaluation of the second optimization results with respect to the highest torque of the machine.

Parameter	Unit	Min error	Max error
Torque	%	-0.512	0.676
Power factor	%	0.573	-1.245
Electromagnetic efficiency	%	-0.157	0.951
Torque ripple	%	5.091	-15.611
Flux density in the air-gap	%	-0.129	0.213

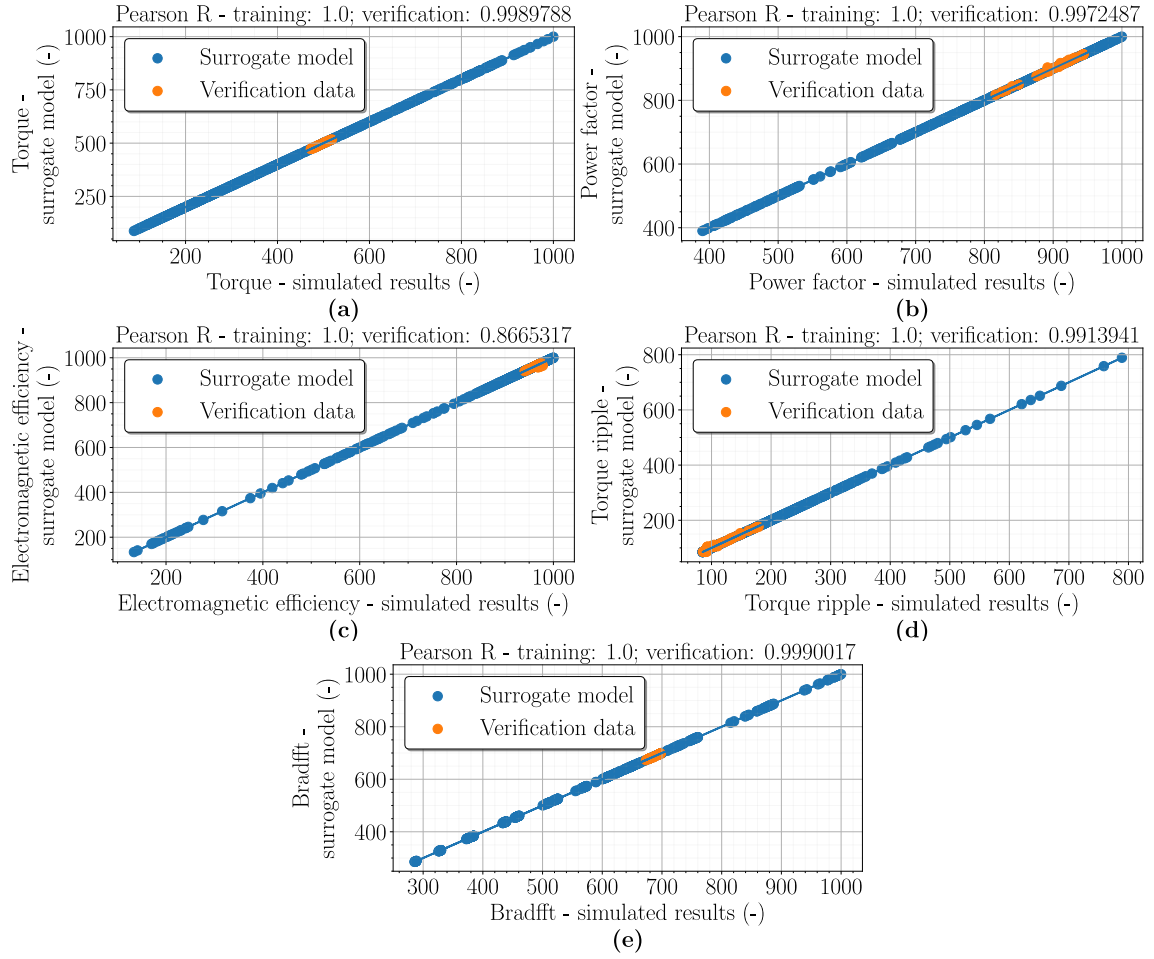


Fig. 7.15: Verification of the accuracy of the surrogate models using the results obtained from the second optimization, where the verification samples are oriented to the lowest price of the machine with respect to the highest torque of the machine for Torque (a), Power factor (b), Electromagnetic efficiency (c), Torque ripple (d), and Fundamental component of the flux density in the air-gap (e).

Table 7.12: Errors of the surrogate model results after re-evaluation of the second optimization results with respect to the lowest price of the machine considering the highest possible torque of the machine.

Parameter	Unit	Min error	Max error
Torque	%	-0.352	0.499
Power factor	%	0.354	-1.274
Electromagnetic efficiency	%	-0.088	1.369
Torque ripple	%	6.096	-11.818
Flux density in the air-gap	%	-0.042	0.314

Except for the evaluated torque ripple, surrogate models are very accurate. At this point, it would be reasonable to continue to learn surrogate models to make them even more accurate, but it would be the same process as so far. Moreover, the deviation of the results in surrogate models will be always present. The goal of this work is not to make the surrogate models as accurate as possible, but rather to introduce them, show how to work with them, and use them to optimise the design of the case study electrical machine with a solid rotor. Therefore, it was decided at this point that, despite the high deviations of the evaluated torque ripple, the final optimized machine designs were selected that respect the 3 machine states determined in the first optimization. A comparison of the original design and the optimized case study machine designs is shown in Fig. 7.16. It can be observed that the width of the rotor slits is much narrower in each optimized design. The same is true for the depth of the rotor slits, which are much deeper. This is in accordance with the pre-established theory and the results obtained from the sensitivity analysis.

A comparison of all input parameters of all machine designs, including their prices, is shown in Fig. 7.13. It is interesting that the design of the machine with the highest possible electromagnetic efficiency, apart from the depth and width of the rotor slits, has almost the same other parameters as the original design. The situation is different in the case of designing a machine with the highest possible torque, where all input parameters are significantly varied to achieve the highest possible torque. However, the final values of the input parameters are influenced by the optimization objective with the reduction of the machine price. If this optimization objective were not applied, the active length of the machine would be considerably higher. Finally, the design of the machine with the lowest cost but with respect to the highest achievable torque is presented. Here, the active length of the machine is reduced considerably in order to reduce the price as much as possible. However, despite the low active machine length, the other input parameters are adjusted from optimization to have better machine performance than the original machine design. As a bonus is also a lower price of the machine, which at first glance may not be that much lower than the original design, but in series production it would make a big difference.

Finally, the evaluated output parameters of the surrogate models were compared with the simulated values to show their deviation, for all optimized machine designs. In terms of designing a machine with the highest possible electromagnetic efficiency, the following differences are listed in Table 7.14. The deviations are a bit higher, especially for power factor and electromagnetic efficiency, where they are around 2%. The torque ripple has a deviation of up to 8.5%. Torque and flux density in the air-gap has a very small deviation which is good. Surrogate models are therefore not as accurate for this

machine condition, but are still usable. The situation is different when it comes to designing a machine with the highest possible torque. All machine output parameters, except torque ripple, have a deviation below 1%. This is very good and desirable. Surrogate models are very accurate in these cases. In the last machine design, all deviations of all output parameters are below 1%. Thus, in this case it is a perfect match between the evaluated and simulated results. Even the torque ripple has a very small deviation. This is to be expected, as the machine was not optimized at its outer limits.

Overall, it is here confirmed that the surrogate models have good accuracy, except for some cases of output parameters where the deviations are larger. However, this could be improved either by further surrogate model learning or by creating a completely new sampling scheme for the initial surrogate model learning. But that is not the aim of this work. In addition to the newly calculated machine designs, it has also been shown that optimization using surrogate models is considerably shorter than conventional optimization. If the total net time to find the optimal machine design is calculated, with the assumption that for this particular procedure the sensitivity analysis took approximately one week, the calculation of the initial learning data for the surrogate models also took one week, each subsequent optimization took one day, and the final verification of the results of each optimization took approximately one and a half a day. That makes 19 days in total to find all 3 suitable machine designs. For comparison, if conventional optimization was used and the total number of designs computed during optimization was considered to be 5,000, considering 10 parallel computations at a time (which were also performed in this work), where one computation of machine design took approximately 3 hours, the total time required for all computations during optimization would be approximately 2 months. So the time gain is over one month. Nevertheless, it is not guaranteed that conventional optimization would find these machine designs and could lead to overall worse variants. Moreover, out of a total of 5,000 calculated samples, there would be far fewer suitable Pareto fronts than if surrogate models were used. Moreover, optimization using surrogate models is capable of calculating up to 200,000 or much more machine designs. This is a great advantage. While the advantage of conventional optimization is that the computed designs have accurate results, it takes much longer. If further learning of surrogate models were considered, let's assume two more iterations, the total time to find the optimal machine designs would be 24 days. The time gain is still over one month, and it is highly likely that the results obtained after optimization would have considerably less deviation. In the case of an electrical machine with a solid rotor, optimization using surrogate models is therefore highly advantageous. The next chapter will deal with electromagnetic analysis and comparison of all optimized machine designs with the original one.

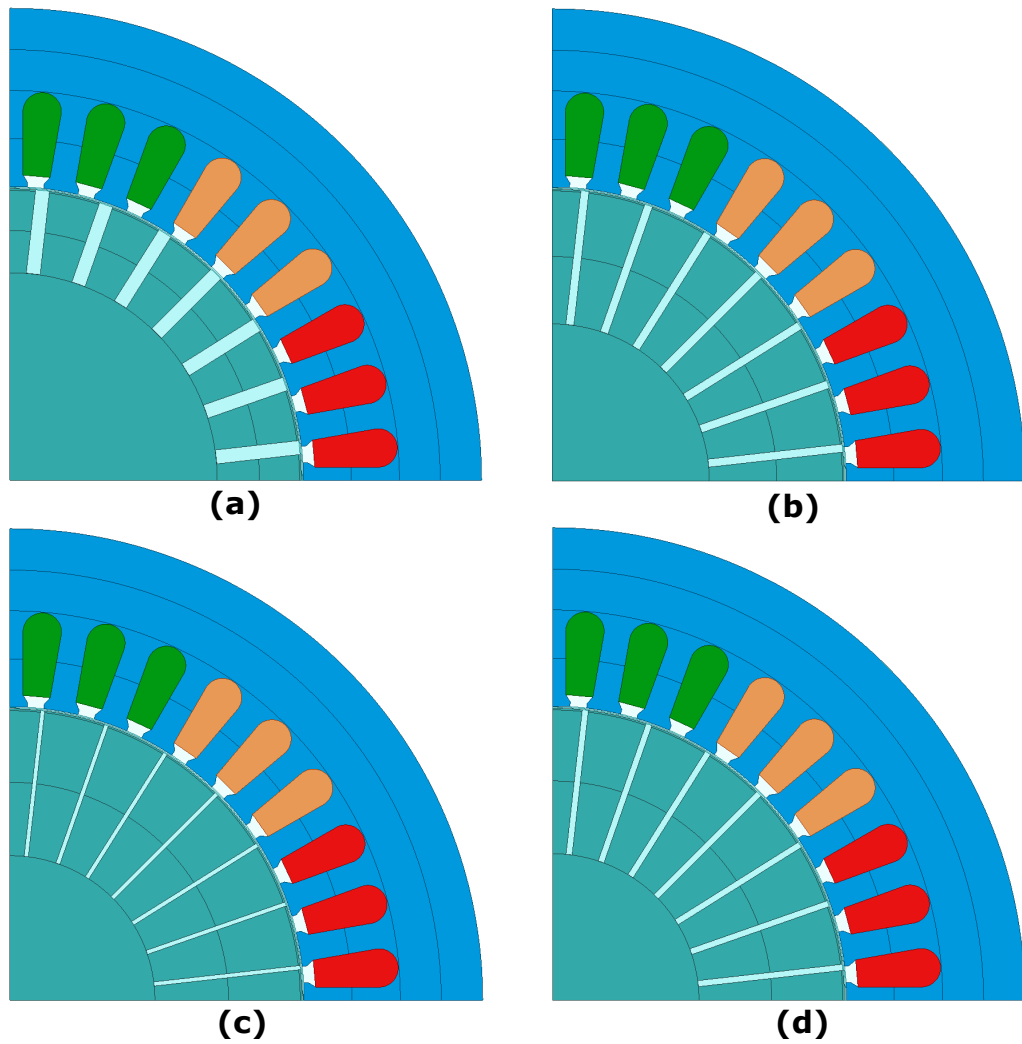


Fig. 7.16: Comparison of the original machine design (a) with optimized machine designs focusing on: the highest possible electromagnetic efficiency (b), the highest possible torque (c) and the lowest machine price respecting the highest achievable torque (d).

Table 7.13: Comparison of input parameters and machine price with the original design and optimized machine designs respecting the highest possible electromagnetic efficiency, the highest possible torque and the lowest machine price with respect to the highest possible torque.

Parameter	Unit	Original	Efficiency	Torque	Price
Active length of the machine	<i>mm</i>	160	159.03	199.35	127.73
Number of stator conductors	–	35	31	23	37
Rotor slit depth	<i>mm</i>	12	19.256	21	20.782
Rotor slit width	<i>mm</i>	2	1.159	0.6	0.875
Price of the machine	€	295.13	294.84	309.75	282.51

Tabel 7.14: Comparison of the evaluated values of the surrogate models with the simulated values of the machine after the optimization considering the highest possible electromagnetic efficiency.

Parameter	Surrogate model	Simulation	Deviation [%]
Torque [Nm]	7.259	7.237	0.303
Power factor [–]	0.523	0.513	1.912
Electromagnetic efficiency [%]	74.960	72.948	2.684
Torque ripple [%]	18.892	20.511	-8.570
Flux density in the air-gap [T]	0.829	0.831	-0.241

Tabel 7.15: Comparison of the evaluated values of the surrogate models with the simulated values of the machine after the optimization considering the highest possible torque.

Parameter	Surrogate model	Simulation	Deviation [%]
Torque [Nm]	11.140	11.168	-0.251
Power factor [–]	0.515	0.512	0.583
Electromagnetic efficiency [%]	73.359	73.558	-0.271
Torque ripple [%]	12.329	12.983	-5.305
Flux density in the air-gap [T]	0.888	0.890	-0.225

Tabel 7.16: Comparison of the evaluated values of the surrogate models with the simulated values of the machine after the optimization considering the lowest price with the respect to the highest possible torque.

Parameter	Surrogate model	Simulation	Deviation [%]
Torque [Nm]	6.608	6.634	-0.393
Power factor [–]	0.501	0.503	-0.399
Electromagnetic efficiency [%]	72.355	72.329	0.036
Torque ripple [%]	17.845	17.898	-0.297
Flux density in the air-gap [T]	0.886	0.886	0.012

8 Electromagnetic analysis of optimized designs of case study IM with solid rotors

The electromagnetic analysis of the optimized case study machine designs is exactly the same as in Chapter 5. Of course, it is made for each machine design separately. For simplicity, the individual optimized designs, according to their selected states, will be referred to as:

- **Original design** - Initial design of the case study machine
- **Design 1** - Optimized machine design that has the highest possible electromagnetic efficiency
- **Design 2** - Optimized machine design that has the highest possible torque
- **Design 3** - Optimized machine design that has the lowest possible cost with respect to the highest torque

The first characteristic is Torque vs. Speed and is shown in Fig. 8.1. It remains true for all machine designs that the starting torque is high. This means that all designs have high rotor impedance. However, it can be seen that each optimized machine design shows better performance than the original machine design. So Design 3 has a better torque curve in the working area than the original design, but its starting torque is almost the same. Design 2 has a better torque curve than design 3, but in the working area the machines have almost the same torque course. Design 3, however, has the best possible torque curve of all the designs, including the working area of the machine. But it does not exhibit the same torque as the original induction machine with a squirrel cage at its rated speed, the parameters of which are given in Chapter 4. However, its performance is closest to that of the original machine.

In this case, the characteristics from Fig. 5.2 and Fig. 5.3 in Chapter 5 have been split into multiple graphs. This is for better clarity and reading from the graphs. Otherwise, there would be up to 12 curves in one graph, which would be very cluttered. The first characteristic in Fig. 8.2 shows the dependence of the electromagnetic efficiency on the output power. Here, again, it can be seen that all optimised machine designs have higher achievable machine output power. The highest available power is for: Design 3 1325 W, Design 2 1480 W and Design 1 2180 W, compared to the original design which has a maximum output power of 860 W. Design 3 is therefore capable of achieving more than twice the output power of the original machine design. In terms of electromagnetic efficiency, all optimised designs are again better. Design 3 achieves the highest electromagnetic efficiency of approximately 73.44%, but almost follows the

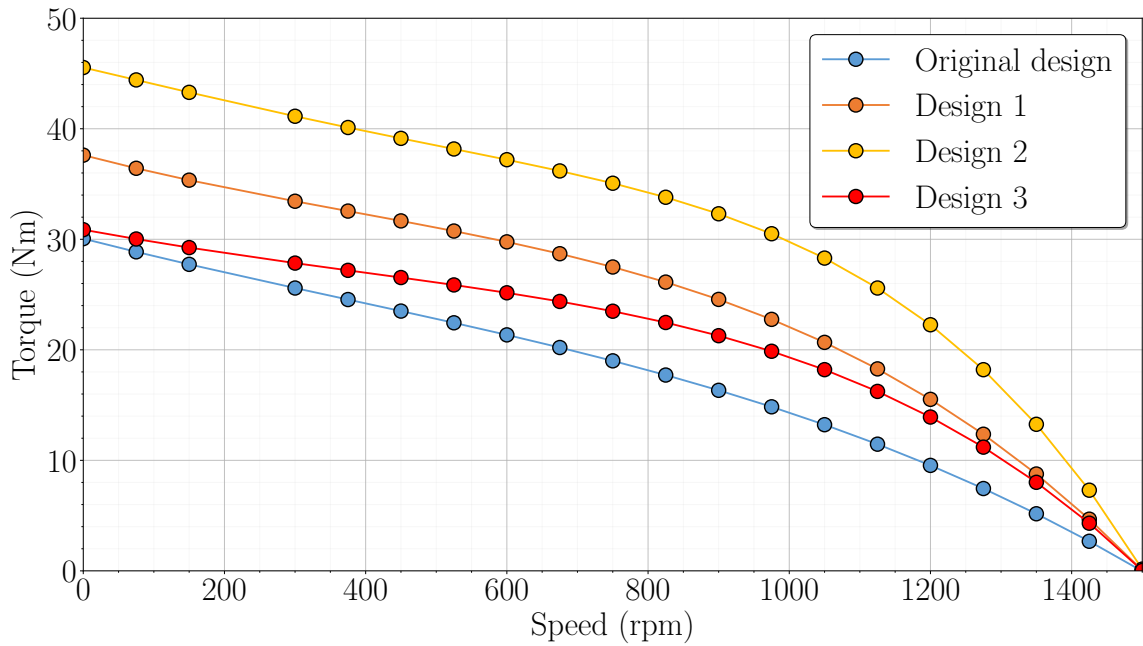


Fig. 8.1: Torque-speed characteristics of the original and optimized designs of the IM with an axially slitted solid rotor.

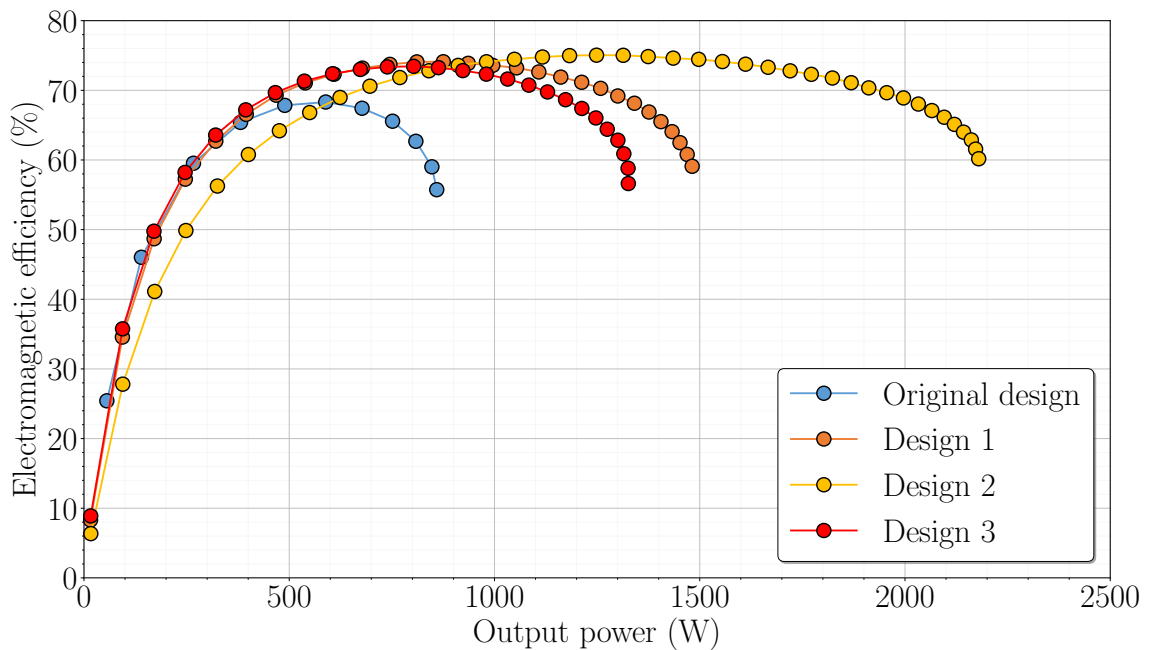


Fig. 8.2: Electromagnetic efficiency vs. Output power characteristics of the original and optimized designs of the IM with an axially slitted solid rotor.

efficiency curve of design 2, which is optimized to have the highest efficiency at the selected speed. The highest efficiency of Design 2 is approximately 74.1 %. However, the highest efficiency is achieved by design 1, where it reaches an efficiency of up to 75.05 %. This efficiency is achieved at a higher output power of the machine. From

the values obtained, it seems that design 1 achieves the highest possible value of electromagnetic efficiency of the machine. Compared to the original machine design, which had a peak electromagnetic efficiency value of around 68.32 %, this is an increase of up to 7 % for design 1 machines.

Another characteristic in Fig. 8.3 is the dependence of the phase current on the output power. It can be seen here that the phase current has increased considerably in the case of the optimized machine designs. Hence, this means that the current and linear current density of the stator slot has also considerably increased. Design 3 and design 2 have more or less the same phase current pattern of the curve, where the only thing that changes is the highest value at higher output power of the machine. For design 3, the highest value of phase current is approximately 4.934 A and for design 2 is approximately 5.216 A. More or less, the phase current values of both machine designs are not that high compared to the original machine design. But the situation with design 1 is very different. Its phase current values are more than double those of the original machine design and the phase current is even higher as the output power increases. For comparison, the highest phase current value of the original machine design at its highest output power is 3.471 A, where design 1 has a phase current value of 7.949 A at its highest output power. This therefore means much higher values of current and linear current density in the stator slot for design 1. Thus, for design 1,

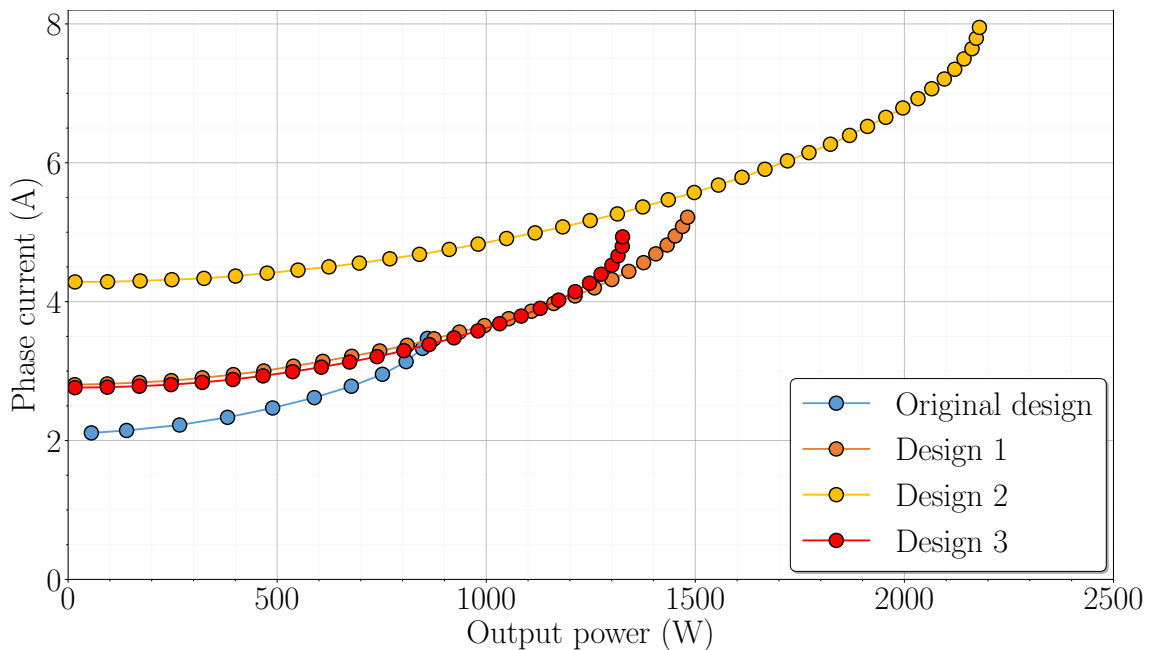


Fig. 8.3: Phase current vs. Output power characteristics of the original and optimized designs of the IM with an axially slitted solid rotor.

a suitable machine operating point would have to be selected or the stator winding

temperature could be very high.

The last characteristic for this type of graph is given in Fig. 8.4, which shows the dependence of the power factor on the output power of the machine. It can be seen here that the maximum power factor value is approximately the same for all machine designs. The main difference is in achieving the maximum power factor value at different values of the machine output power. The original design achieves a maximum power factor of 0.615, design 3 0.668, design 2 0.674, and design 1 0.641. The highest power factor value is therefore achieved by design 2. The highest possible achievable value of the machine is therefore around this power factor value.

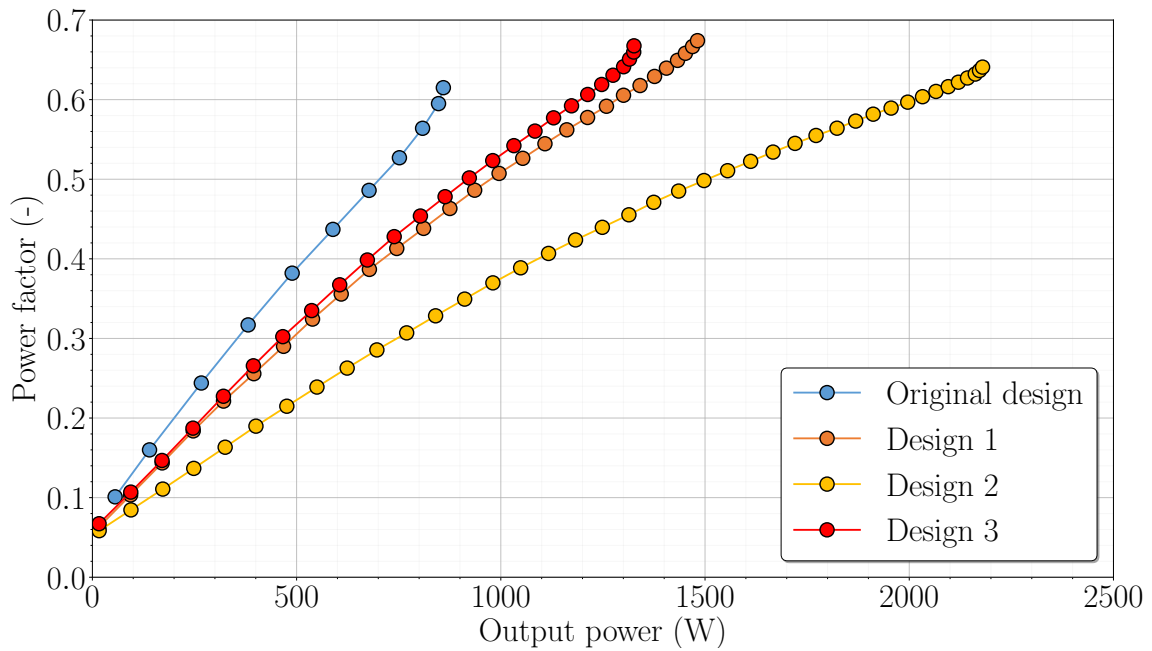


Fig. 8.4: Power factor vs. Output power characteristics of the original and optimized designs of the IM with an axially slitted solid rotor.

The machine losses for all designs are also listed here. The characteristic in Fig. 8.5 shows the dependence of the stator core losses on the output power. Optimized machine designs have an basically linear course of this type of losses with increasing output power. On the other hand, the losses in the original machine design decrease with output power. Design 3 has the lowest losses in the stator core, while design 1 has the highest losses. The characteristic in Fig. 8.6 shows the dependence of rotor losses on output power. All machine designs are then found to have a quadratic distribution of rotor losses with increasing machine output power. Here, the original machine design achieves the lowest rotor losses, while design 1 achieves the highest. The last characteristic is shown in Fig. 8.7, which represents the dependence of the losses in the stator winding on the output power. All machine designs again have a quadratic loss profile

with increasing output power, as in the previous case. Again, the original machine design has the lowest losses and design 1 has the highest. Most losses are concentrated for all machine designs in the rotor, which is expected.

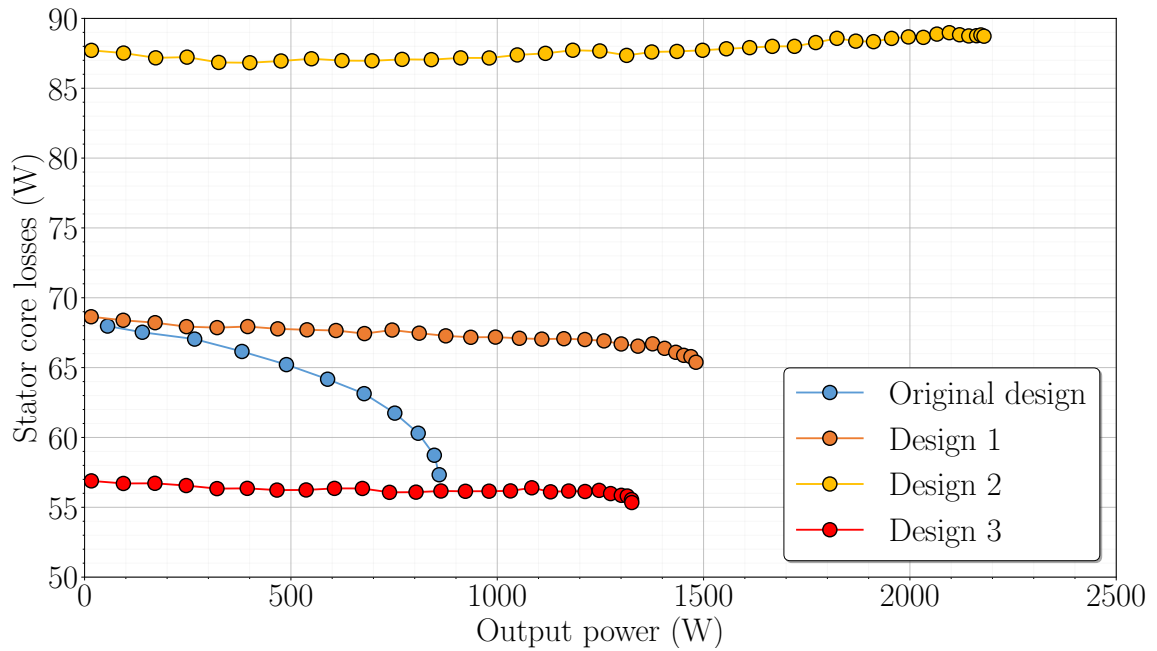


Fig. 8.5: Stator core losses vs. Output power characteristics of the original and optimized designs of the IM with an axially slitted solid rotor.

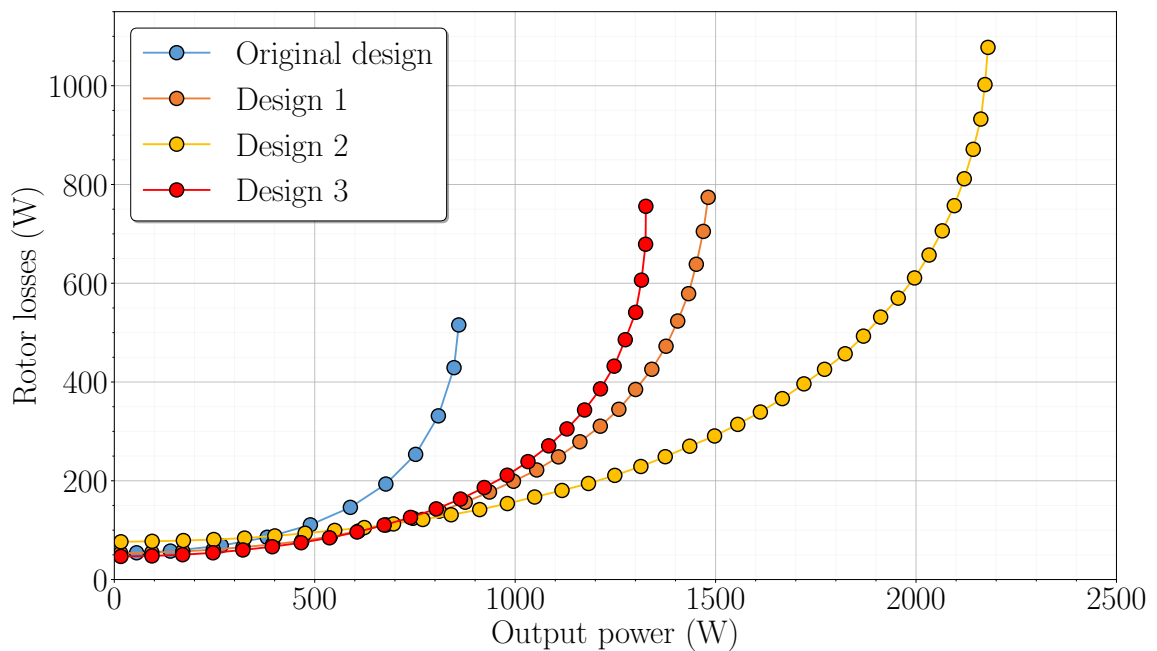


Fig. 8.6: Rotor losses vs. Output power characteristics of the original and optimized designs of the IM with an axially slitted solid rotor.

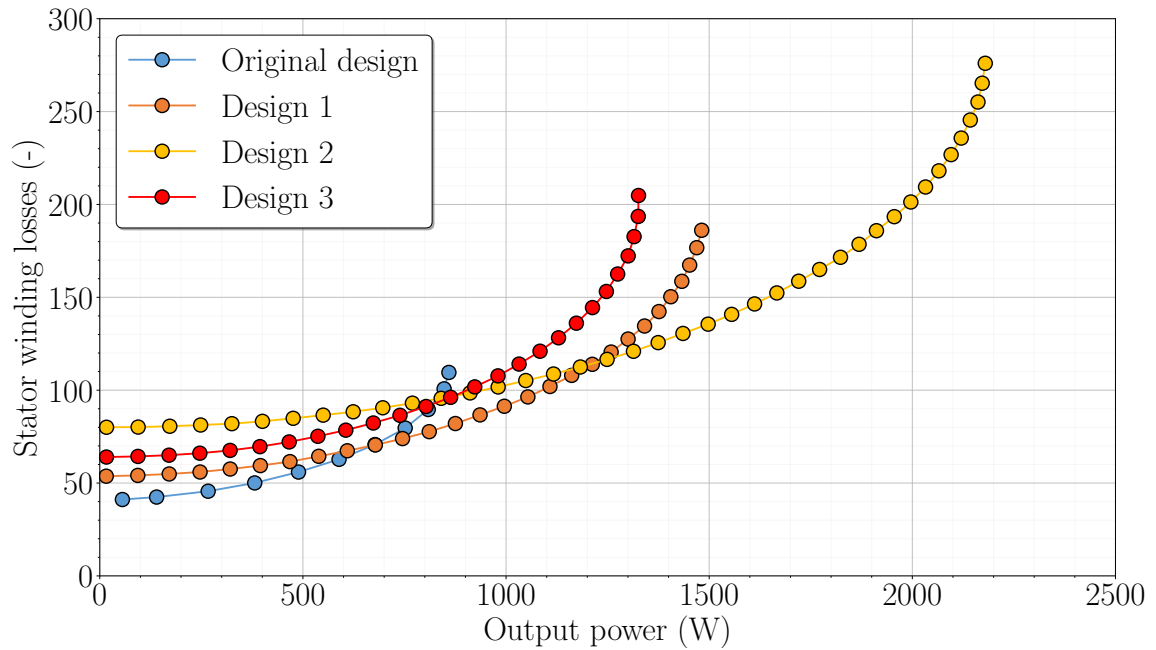


Fig. 8.7: Stator winding losses vs. Output power characteristics of the original and optimized designs of the IM with an axially slitted solid rotor.

As a further comparison, all machine designs were calculated at the assumed constant speed of 1322rpm, or at the operating point of the machine. All the given machine performance values are given in Table 8.1.

Table 8.1: Performance of analyzed original and optimized designs of the case study IM with an axially slitted solid rotor at the selected operating point.

Parameter	Unit	Performance			
		Original	Design 1	Design 2	Design 3
Torque	Nm	4.231	11.168	7.237	6.634
Torque ripple	%	28.562	12.983	20.511	17.898
Speed	rpm	1322	1322	1322	1322
Output power	W	585.8	1546.1	1001.8	918.4
Phase current (rms)	A	2.609	5.681	3.677	3.481
Power factor	–	0.432	0.512	0.513	0.503
Electromagnetic efficiency	%	69.32	73.56	72.95	72.33
Air-gap flux density	T	0.737	0.890	0.831	0.886
Stator core losses	W	63.58	86.97	66.44	55.68
Rotor losses	W	136.25	328.10	212.79	193.96
Stator winding losses	W	59.43	140.74	92.29	101.72

Based on the values obtained, it can be seen how much better the optimized machine designs perform. It is clear that design 1 is superior to all other designs in torque, torque ripple and output power. It even has the highest electromagnetic efficiency despite the fact that design 2 should have it. This is due to the inaccuracy and error of surrogate models, which will always be present. This error could be reduced by further iterations of active learning of surrogate models. For the purposes of this work, however, it is not necessary to have such accurate surrogate models and thus these results are sufficient enough. It can be seen that the power factor of the optimized machine designs is approximately the same at this operating point, but is noticeably higher compared to the original machine design. Here it can also be seen that the machine is more saturated in the optimized designs compared to the original machine design. The distribution of losses also corresponds to those shown in the previous graphs. The original design has the lowest losses and design 1 has the highest losses. Overall, the optimized design 1 of the case study IM with a solid rotor shows the best possible results. At its operating point, it even achieves the same output power as the original machine with a squirrel cage.

To further verify the results, the flux density distributions throughout the whole machine were displayed. The distribution of the flux density throughout the whole machine for all machine designs is shown in Fig. 8.8. Here it is confirmed that all optimized machine designs have higher saturation than the original machine design. Design 1 (Fig. 8.8 (c)) and Design 3 (Fig. 8.8 (d)) have the highest saturation. Which is again confirmed from the Table 8.1.

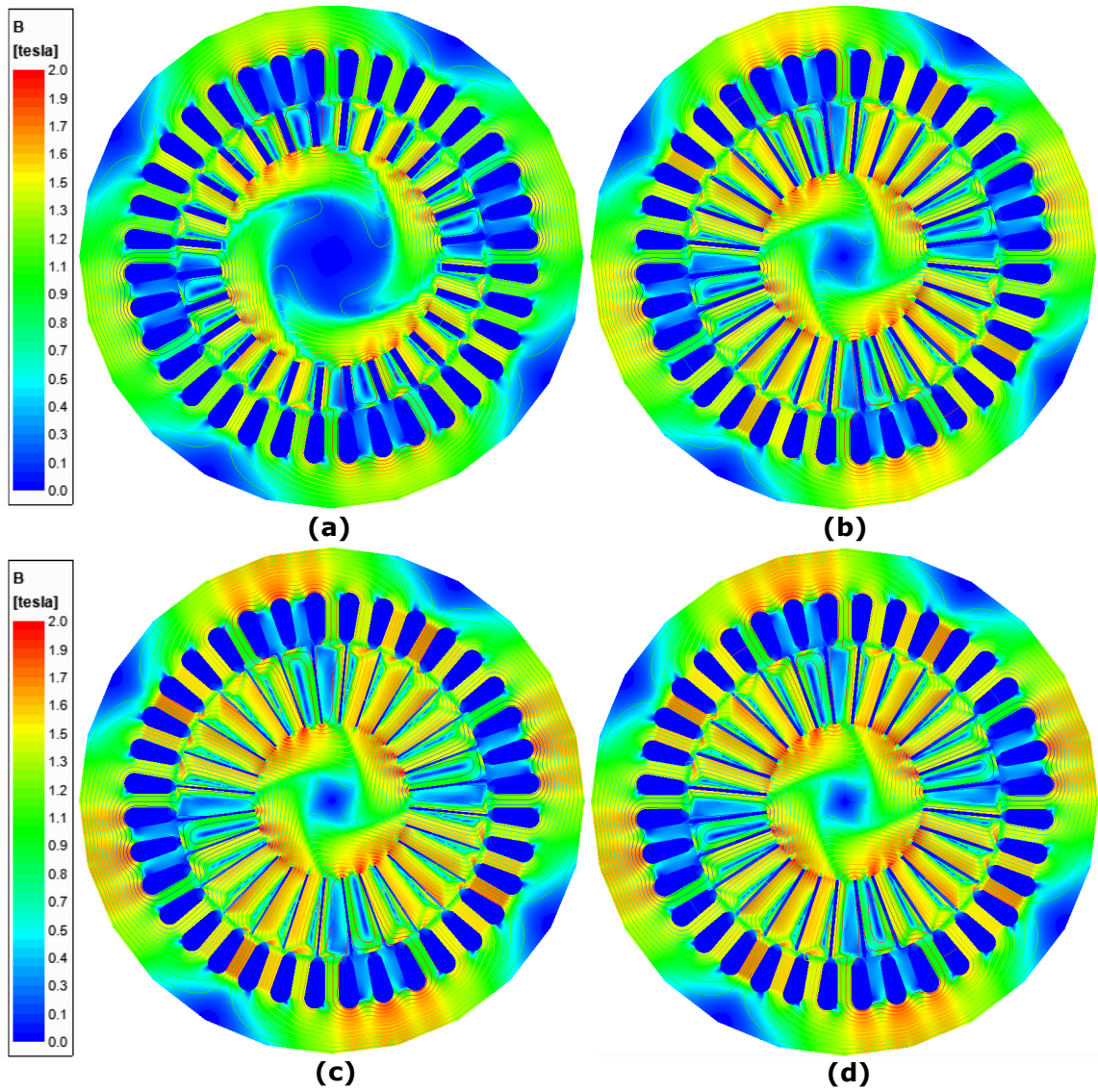


Fig. 8.8: Distribution of magnetic flux density in the whole machine with a solid rotor for: Original design (a), Design 2 (b), Design 1 (c), Design 3 (d).

Conclusion

This Master's thesis deals with the electromagnetic analysis and modeling of a solid rotor induction machine. Today, more and more electric machines with solid rotors are used in industry, especially in the area and applications that require high speeds. The high-speed electrical machines with solid rotors provide at a higher speed high efficiency, great mechanical properties, mechanical robustness, they require less space due to no need for an additional gearbox, have better electromagnetic parameters and are energy efficient with less impact on economics and ecology, compared to the conventional induction machine with a squirrel cage and gearbox. Right now, several types of electrical machines with solid rotors exist, for example permanent magnet brushless machines, induction machines, synchronous reluctance machines and others. Overall, the most used type of high-speed electrical machines with solid rotors are induction machines. Their main advantage is the price, mostly simple geometry and production, the robustness of the solid rotor, great mechanical properties, great resistance to high temperatures and high efficiency and great electromagnetic performance at a higher speed. Of course, they have some disadvantages such as lower power, high rotor loss and others. But the advantages of this machine outweigh the disadvantages. For this type of electrical machine with solid rotors exists several types of solid rotors and applications. For rotor types, for example, they are smooth rotors, slitted rotors or with a squirrel cage rotors. The use of high-speed electrical machines with solid rotors in the application is for example in turbomolecular pumps, gas compressors, microturbines and others. The first chapter provides all the detailed information regarding all the things described above.

The second chapter dealt mainly with the possibilities of calculating electrical induction machines with solid rotors. In the first section, possible analytical methods were described and discussed. However, as stated here, all analytical methods are either very complex with a focus on one specific type of rotor (often smooth), or use simplifications and empirical formulas, which often reduce the accuracy of the calculation compared to the measured values. It is also stated why this is the case with the given practical examples. The next section presents another possibility of calculation and design of electrical machines with solid rotors. And these are FEM programs with modern numerical methods. To calculate the machine, a 3D simulation in FEM programs was first considered because it captures all 3D aspects of the electromagnetic model. If the simulation is set up correctly, it gives the best results compared to the measured one. However, as mentioned, 3D simulation is extremely time consuming and requires the necessary amount of experience with this simulation. Therefore, another type of simulation was proposed, namely 2D. The problem with this type of simulation is that

it does not include all 3D aspects of a real machine, such as end regions of the solid rotor. Thus, the simulation results are not valid and are over-optimistic. For this reason, correction end-effect factors were proposed, which includes the effect of the end-region and the curvature of the rotor currents at these ends. This section deals with problems with 2D simulations of electrical machines with solid rotors, the introduction of correction end-effect factors and their comparison, and the use of correction end-effect factors in the simulation.

The third chapter mainly dealt with surrogate modelling and its general theory. Surrogate modeling is basically an approximation of the dependencies between the input and output dependencies of a system, where surrogate models are created based on these relationships. In other words, surrogate models could be described as statistical models that are built using a given approximation function from machine-learned data. In this thesis, it was stated that there are several approximation functions as the basis of surrogate models, where each function has its given application. These models then predict the output values of the system based on the input parameters. As a result, this greatly speeds up the calculation of such system's output parameters, where their evaluation is essentially instantaneous. This is best used in optimization, where the combination of surrogate models and the optimization algorithm can achieve significant time gains compared to conventional optimization, which is usually performed using FEM analysis. However, the disadvantage of using surrogate models is that they are only suitable for systems that have few input parameters, that is, around 10. The surrogate modeling process consists of 4 main steps, including sampling, output evaluations, surrogate model construction, and active learning of surrogate models. The use of surrogate models, which include medical, electronics, mechanical and other applications, was also presented in this paper. Hence, it is also suitable for electrical machine with solid rotor.

The fourth chapter, deals with the used electrical machine with a solid rotor and its subsequent simulation in 2D using a correction end-effect factor. As a case study machine, a 3-phase induction machine with a squirrel cage was used. Here, the rotor was replaced with an axially slitted solid rotor. The main goal was to analyze the machines using a correction end-effect factor and a possible comparison of their performance with the original machine. For the analysis, 3 programs were used: python, Ansys maxwell and FreeCAD. This chapter additionally contains all the necessary information on stator and rotor geometries, the algorithm of the python script and the reasons why these programs were used, or the general settings of the programs.

The fifth chapter deals with the achieved results from simulations of both machines.

The first is the torque-speed characteristic in Fig. 5.1, which shows that the machine fail indisputably compared to the original machine. In the next characteristics in Fig. 5.2, was shown Efficiency, Phase current and Power factor vs Output power characteristics of the electrical machine with the axially slitted solid rotor. The machine achieved a maximum output power of 860 *W*. The machine reached the maximal output power at higher slips, as expected. However, the machine did not reach the output power of the original machine. Overall it could not reach the electromagnetic parameters of the original machine, as expected. Losses vs output power characteristics was shown in Fig. 5.3. Finally, an operating point was selected for the machine, which was then used for further use in creating a surrogate model for the machine. The total machine performance at this operating point was shown in Table 5.1. Additionally, the distribution of magnetic flux density in the whole machine is shown in Fig. 5.4 at the given operating point in steady-state.

After electromagnetic analysis of the selected induction machine with solid rotor, surrogate modeling was applied to this machine, which is described in sixth chapter. This operation consisted of several steps, where the first step was the determination of the total number of input parameters of the machine. The total number of input parameters was set to 8, which meets the condition for the recommended value of maximum input parameters for surrogate modeling. All machine input parameters are listed in section 6.1. Based on the selected input parameters, their maximum possible limit range was also determined, which would be beneficial for improving the overall performance of the machine. Using all input parameters and their specified limit ranges, a sensitivity analysis of the machine was performed. From the sensitivity analysis, it was found that the performance of the machine can be increased significantly, but also some input parameters can be discarded for surrogate modelling as they have either very little or no effect on the performance of the machine or they are perfectly designed in their original form. Thus, the total number of input parameters has been reduced from 8 to 4, which will greatly simplify surrogate modeling. The results of the sensitivity analysis are shown in Fig. 6.3. Subsequently, a sampling scheme was chosen to serve as the basis for the learning data of the surrogate models. Here, the Box-Behnken scheme was chosen, where the total number of learning samples was determined to be 625. Each sample took approximately 3-4 hours to calculate using FEM-based analysis. The last step was to create the surrogate models for the case study machine itself. This involved selecting the correct approximation function that would correctly approximate the values obtained from the initial learning data. The Radial basis function proved to be the best choice for approximating the learning data. The Radial basis function approximation works on the base of the spline function, which has a great advantage and can be used for many applications. As it turned out the Radial

basis function is a good choice for this machine case and the surrogate models created showed very high accuracy. The rest of the chapter then deals with the surrogate models created, their accuracy and the possible achievable performance of the machine.

The seventh chapter focused on machine optimization. For optimization, SymSpace and Optimizer were chosen, which have very good optimization properties and are very well tuned. They even contain up to 3 optimization algorithms to choose from. Their advantage is therefore easy use of them. For machine optimization, 3 machine designs were considered which include: the design with the highest possible electromagnetic efficiency of the machine, the design with the highest possible machine torque and the design with the lowest machine cost considering the highest possible machine torque. The machine optimization took approximately one day and approximately 200,000 machine designs were calculated, of which only 10,000 were Pareto queues. The Pareto fronts were further reduced to approximately 875 to meet appropriate output limits. The results of the first optimization are shown in Fig. 7.6 and Fig. 7.7. Further in the chapter, the accuracy of the surrogate models was verified, where 150 verification samples were computed and took approximately a day and a half to compute. These samples were used to investigate the outliers of the surrogate models, where the models were found to be relatively accurate, but further learning was appropriate. So a second and final optimization of the machine was done, which also took about a day and the optimization calculated about 200,000 machine designs. The number of Pareto fronts was around 8,700 and were further reduced to 725. The results of the second optimization were presented in Fig. 7.11 and Fig. 7.12. After calculating another 150 validation samples and using them to verify the accuracy of the surrogate models, it was concluded that the surrogate models have very good accuracy except for the torque ripple. However, the torque ripple could be further improved by further learning of the surrogate model or by developing a new sampling scheme. The optimized machine designs were shown in Fig. 7.16, where for each machine design the differences between the surrogate model values and the simulated values are shown in Table 7.14 - Table 7.16. It has also been shown that optimization using surrogate models significantly reduces the time required for machine optimization compared to conventional optimization. In this case, the optimization took approximately 19 days whereas a conventional optimization with a much smaller number of total computed machine designs would take two months.

Finally, an electromagnetic analysis of the optimized machine designs was performed in Chapter eight, where the results were compared with the original machine design. The process of electromagnetic analysis was the same as in the fifth chapter, but for each machine design separately. The whole electromagnetic analysis showed that all three optimized machines have better performance than the original machine

design, which was expected. However, it turned out that the best machine design was the one that had the highest achievable machine torque. In some aspects, in terms of performance, it even came close to the original machine with a squirrel cage. However, despite this, it has worse parameters and considerably more slip, which was expected.

In conclusion, surrogate modeling is a very suitable method for optimizing an electrical machine with a solid rotor, since this type of machine has a small number of input parameters. If surrogate models are used correctly it is possible to achieve their high accuracy. It is also possible to considerably improve machine performance using optimization with the combination of surrogate models in a much shorter period of time, than with conventional optimization.

References

- [1] Vladimír Bílek. “Electromagnetic analysis of the solid rotor electrical machine”. Semester thesis. Brno University of Technology, Faculty of electrical engineering, communication, Department of Power Electrical, and Electronic Engineering, 2021. URL: <https://www.vutbr.cz/studenti/zav-prace/detail/131135>.
- [2] Tuomo Aho. “Electromagnetic design of a solid steel rotor motor for demanding operation environments”. PhD thesis. Lappeenranta University of Technology., 2007.
- [3] P. D. Agarwal. “Eddy-current losses in solid and laminated iron”. In: *Transactions of the American Institute of Electrical Engineers, Part I: Communication and Electronics* 78.2 (1959), pp. 169–181. DOI: [10.1109/TCE.1959.6372977](https://doi.org/10.1109/TCE.1959.6372977).
- [4] J. C. Wilson. “Theory of solid rotor induction machine”. PhD thesis. University of Colorado., 1969.
- [5] P. H. Trickey. “Induction Motor Resistance Ring Width”. In: *Transactions of the American Institute of Electrical Engineers* 55.2 (1936), pp. 144–150. DOI: [10.1109/TAIEE.1936.5057231](https://doi.org/10.1109/TAIEE.1936.5057231).
- [6] H. Yee. “Effects of finite length in solid-rotor induction machines”. In: *Proceedings of the Institution of Electrical Engineers* 118.8 (1971), pp. 1025–1033. DOI: [10.1049/piee.1971.0204](https://doi.org/10.1049/piee.1971.0204).
- [7] H. Yee and T. Wilson. “Saturation and finite-length effects in solid-rotor induction machines”. In: *Proceedings of the Institution of Electrical Engineers* 119.7 (1972), pp. 877–882. DOI: [10.1049/piee.1972.0181](https://doi.org/10.1049/piee.1972.0181).
- [8] I. Woolley and B. J. Chalmers. “End effects in unlaminated-rotor induction machines”. In: *Proceedings of the Institution of Electrical Engineers* 120.6 (1973), pp. 641–646. DOI: [10.1049/piee.1973.0141](https://doi.org/10.1049/piee.1973.0141).
- [9] B. J. Chalmers and I. Woolley. “General theory of solid-rotor induction machines”. In: *Proceedings of the Institution of Electrical Engineers* 119.9 (1972), pp. 1301–1308. DOI: [10.1049/piee.1972.0258](https://doi.org/10.1049/piee.1972.0258).

- [10] R. L. Russell and K. H. Norsworthy. “Eddy Current and Wall Losses in Screened Rotor Induction Motors”. In: *Proceedings of the Institution of Electrical Engineers* 105A.20 (1958), pp. 163–173.
- [11] Jussi Hupponen. “High-speed solid-rotor induction machine-electromagnetic calculation and design”. PhD thesis. Lappeenranta University of Technology., 2004.
- [12] L. Papini, C. Gerada, D. Gerada, and A. Mebarki. “High speed solid rotor induction machine: Analysis and performances”. In: *2014 17th International Conference on Electrical Machines and Systems (ICEMS)*. 2014, pp. 2759–2765. DOI: [10.1109/ICEMS.2014.7013968](https://doi.org/10.1109/ICEMS.2014.7013968).
- [13] W. Han, D. Kim, J. Kim, Y. Kim, and S. Jung. “Multi-simplex algorithm applied to FEM based optimal design of electric machine”. In: *2016 IEEE Conference on Electromagnetic Field Computation (CEFC)*. 2016, pp. 1–1. DOI: [10.1109/CEFC.2016.7816298](https://doi.org/10.1109/CEFC.2016.7816298).
- [14] R. Lateb, J. Enon, and Lionel Durantay. “High speed, high power electrical induction motor technologies for integrated compressors”. In: Dec. 2009, pp. 1 –5. DOI: [10.1109/ICEMS.2009.5382960](https://doi.org/10.1109/ICEMS.2009.5382960).
- [15] A. Tenconi, S. Vaschetto, and A. Vigliani. “Electrical Machines for High-Speed Applications: Design Considerations and Tradeoffs”. In: *IEEE Transactions on Industrial Electronics* 61.6 (2014), pp. 3022–3029. DOI: [10.1109/TIE.2013.2276769](https://doi.org/10.1109/TIE.2013.2276769).
- [16] Hao Zhou and Fengxiang Wang. “Comparative study on high speed induction machine with different rotor structures”. In: *2007 International Conference on Electrical Machines and Systems (ICEMS)*. 2007, pp. 1009–1012.
- [17] Ma Xiaohe, Su Rong, Tseng King Jet, Wang Shuai, Zhang Xiaolong, V. Vaiyapuri, G. Chandana, G. Amit, and N. Sivakumar. “Review of high speed electrical machines in gas turbine electrical power generation”. In: *TENCON 2015 - 2015 IEEE Region 10 Conference*. 2015, pp. 1–9. DOI: [10.1109/TENCON.2015.7372765](https://doi.org/10.1109/TENCON.2015.7372765).
- [18] J. B. Bartolo, H. Zhang, D. Gerada, L. De Lillo, and C. Gerada. “High speed electrical generators, application, materials and design”. In: *2013 IEEE Workshop on Electrical Machines Design, Control and Diagnosis (WEMDCD)*. 2013, pp. 47–59. DOI: [10.1109/WEMDCD.2013.6525164](https://doi.org/10.1109/WEMDCD.2013.6525164).
- [19] T. Aho, V. Sihvo, J. Nerg, and J. Pyrhonen. “Rotor Materials for Medium-Speed Solid-Rotor Induction MotorS”. In: *2007 IEEE International Electric Machines Drives Conference*. Vol. 1. 2007, pp. 525–530. DOI: [10.1109/IEMDC.2007.382722](https://doi.org/10.1109/IEMDC.2007.382722).

- [20] P. Lindh, P. Immonen, C. Di, M. Degano, and J. Pyrhönen. “Solid-Rotor Material Selection for Squirrel-Cage High-Speed Solid-Rotor Induction Machine”. In: *IECON 2019 - 45th Annual Conference of the IEEE Industrial Electronics Society*. Vol. 1. 2019, pp. 1357–1361. DOI: [10.1109/IECON.2019.8926736](https://doi.org/10.1109/IECON.2019.8926736).
- [21] J. Pyrhonen, J. Nerg, P. Kurronen, and U. Lauber. “High-speed, 8 MW, solid-rotor induction motor for gas compression”. In: *2008 18th International Conference on Electrical Machines*. 2008, pp. 1–6. DOI: [10.1109/ICELMACH.2008.4799819](https://doi.org/10.1109/ICELMACH.2008.4799819).
- [22] Yoseph Gessese Mekuria. “Development of a High Speed Solid Rotor Asynchronous Drive fed by a Frequency Converter System”. PhD thesis. TU Darmstadt., 2013.
- [23] J. F. Gieras and J. Saari. “Performance Calculation for a High-Speed Solid-Rotor Induction Motor”. In: *IEEE Transactions on Industrial Electronics* 59.6 (2012), pp. 2689–2700. DOI: [10.1109/TIE.2011.2160516](https://doi.org/10.1109/TIE.2011.2160516).
- [24] Jussi Lähteenmäki. “Design and Voltage Supply of High-Speed Induction Machines”. PhD thesis. Helsinki University of Technology., 2002.
- [25] D. T. McGuinness, M. O. Gulbahce, and D. A. Kocabas. “A performance comparison of different rotor types for high-speed induction motors”. In: *2015 9th International Conference on Electrical and Electronics Engineering (ELECO)*. 2015, pp. 584–589. DOI: [10.1109/ELECO.2015.7394606](https://doi.org/10.1109/ELECO.2015.7394606).
- [26] D. T. McGuinness, M. O. Gulbahce, and D. A. Kocabas. “Novel rotor design for high-speed solid rotor induction machines”. In: *2015 9th International Conference on Electrical and Electronics Engineering (ELECO)*. 2015, pp. 579–583. DOI: [10.1109/ELECO.2015.7394607](https://doi.org/10.1109/ELECO.2015.7394607).
- [27] T. Aho, J. Nerg, and J. Pyrhonen. “The Effect of the Number of Rotor Slits on the Performance Characteristics of Medium-Speed Solid Rotor Induction Motor”. In: *2006 3rd IET International Conference on Power Electronics, Machines and Drives - PEMD 2006*. 2006, pp. 515–519.
- [28] L. Jinning, F. Fengli, et al. “Calculation of Magnetic Fields and Rotor Parameters for Induction Motors with Slitted Solid Rotor”. In: *Electric Energy Conference 1987: An International Conference on Electric Machines and Drives; Proceedings*. Institution of Engineers, Australia. 1987, pp. 306–310.
- [29] Y. Gessese and A. Binder. “Axially slitted, high-speed solid-rotor induction motor technology with copper end-rings”. In: *2009 International Conference on Electrical Machines and Systems*. 2009, pp. 1–6. DOI: [10.1109/ICEMS.2009.5382761](https://doi.org/10.1109/ICEMS.2009.5382761).

- [30] T. Aho, J. Nerg, and J. Pyrhonen. “Analysing the effect of the rotor coating on the rotor losses of medium-speed solid-rotor induction motor”. In: *International Symposium on Power Electronics, Electrical Drives, Automation and Motion, 2006. SPEEDAM 2006*. 2006, pp. 103–107. DOI: [10.1109/SPEEDAM.2006.1649752](https://doi.org/10.1109/SPEEDAM.2006.1649752).
- [31] D. T. McGuinness, M. O. Gulbahce, and D. A. Kocabas. “Novel rotor design for high-speed solid rotor induction machines”. In: *2015 9th International Conference on Electrical and Electronics Engineering (ELECO)*. 2015, pp. 579–583. DOI: [10.1109/ELECO.2015.7394607](https://doi.org/10.1109/ELECO.2015.7394607).
- [32] M. O. Gulbahce, D. T. McGuinness, and D. A. Kocabas. “Shielded axially slitted solid rotor design for high-speed solid rotor induction motors”. In: *IET Electric Power Applications* 12.9 (2018), pp. 1371–1377. DOI: [10.1049/iet-epa.2018.5210](https://doi.org/10.1049/iet-epa.2018.5210).
- [33] S. L. Ho, S. Niu, and W. N. Fu. “A Novel Solid-Rotor Induction Motor With Skewed Slits in Radial and Axial Directions and Its Performance Analysis Using Finite Element Method”. In: *IEEE Transactions on Applied Superconductivity* 20.3 (2010), pp. 1089–1092. DOI: [10.1109/TASC.2010.2040031](https://doi.org/10.1109/TASC.2010.2040031).
- [34] T. Aho, J. Nerg, and J. Pyrhonen. “Analyzing the Effect of the Rotor Slit Depth on the Electric and Mechanical Performance of a Solid-Rotor Induction Motor”. In: *Int. Review of Electr. Engineering IREE* 1.4 (2006), pp. 516–524. DOI: [10.1109/TASC.2010.2040031](https://doi.org/10.1109/TASC.2010.2040031).
- [35] T. Mauffrey, J. Pradurat, L. Durantay, and J. Fontini. “Comparison of 5 different squirrel cage rotor designs for large high speed induction motors”. In: *PCIC Europe 2013*. 2013, pp. 1–9.
- [36] A. Tenconi, S. Vaschetto, and A. Vigliani. “Electrical Machines for High-Speed Applications: Design Considerations and Tradeoffs”. In: *IEEE Transactions on Industrial Electronics* 61.6 (2014), pp. 3022–3029. DOI: [10.1109/TIE.2013.2276769](https://doi.org/10.1109/TIE.2013.2276769).
- [37] D. Zhang, R. An, C. He, L. Bu, and T. Wu. “Electromagnetic design of a megawatt high efficiency high speed solid rotor induction motor”. In: *2017 IEEE International Electric Machines and Drives Conference (IEMDC)*. 2017, pp. 1–8. DOI: [10.1109/IEMDC.2017.8002095](https://doi.org/10.1109/IEMDC.2017.8002095).
- [38] M. Centner and U. Schafer. “Optimized Design of High-Speed Induction Motors in Respect of the Electrical Steel Grade”. In: *IEEE Transactions on Industrial Electronics* 57.1 (2010), pp. 288–295. DOI: [10.1109/TIE.2009.2029523](https://doi.org/10.1109/TIE.2009.2029523).
- [39] E. Kurvinen, C. Di, I. Petrov, R. P. Jastrzebski, D. Kepsu, and J. Pyrhönen. “Comparison of the Performance of Different Asynchronous Solid-Rotor Constructions in a Megawatt-Range High-Speed Induction Motor”. In: *2019 IEEE International Electric Machines Drives Conference (IEMDC)*. 2019, pp. 820–825. DOI: [10.1109/IEMDC.2019.8785288](https://doi.org/10.1109/IEMDC.2019.8785288).

- [40] W. Chou, Y. Liang, L. Gao, and D. Wang. “Research on eddy current losses algorithm in solid rotor of high speed squirrel cage induction motor”. In: *IET Electric Power Applications* 14.6 (2020), pp. 1023–1029. DOI: [10.1049/iet-epa.2019.0884](https://doi.org/10.1049/iet-epa.2019.0884).
- [41] J. Barta, N. Uzhegov, P. Losak, C. Ondrusek, M. Mach, and J. Pyrhönen. “Squirrel-Cage Rotor Design and Manufacturing for High-Speed Applications”. In: *IEEE Transactions on Industrial Electronics* 66.9 (2019), pp. 6768–6778. DOI: [10.1109/TIE.2018.2879285](https://doi.org/10.1109/TIE.2018.2879285).
- [42] J. Barta, C. Ondrusek, P. Losak, and R. Vlach. “Design of high-speed induction machine for the 6 kW, 120 000 rpm helium turbo-circulator”. In: *2016 XXII International Conference on Electrical Machines (ICEM)*. 2016, pp. 1552–1558. DOI: [10.1109/ICELMACH.2016.7732730](https://doi.org/10.1109/ICELMACH.2016.7732730).
- [43] Y. Gessese, A. Binder, and B. Funieru. “Analysis of the effect of radial rotor surface grooves on rotor losses of high speed solid rotor induction motor”. In: *SPEEDAM 2010*. 2010, pp. 1762–1767. DOI: [10.1109/SPEEDAM.2010.5544763](https://doi.org/10.1109/SPEEDAM.2010.5544763).
- [44] D. Gerada, A. Mebarki, N. L. Brown, C. Gerada, A. Cavagnino, and A. Boglietti. “High-Speed Electrical Machines: Technologies, Trends, and Developments”. In: *IEEE Transactions on Industrial Electronics* 61.6 (2014), pp. 2946–2959. DOI: [10.1109/TIE.2013.2286777](https://doi.org/10.1109/TIE.2013.2286777).
- [45] B. Eberleh and T. Hartkopf. “A high speed induction machine with two-speed transmission as drive for electric vehicles”. In: *International Symposium on Power Electronics, Electrical Drives, Automation and Motion, 2006. SPEEDAM 2006*. 2006, pp. 249–254. DOI: [10.1109/SPEEDAM.2006.1649779](https://doi.org/10.1109/SPEEDAM.2006.1649779).
- [46] T. Epskamp, B. Butz, and M. Doppelbauer. “Design and analysis of a high-speed induction machine as electric vehicle traction drive”. In: *2016 18th European Conference on Power Electronics and Applications (EPE'16 ECCE Europe)*. 2016, pp. 1–10. DOI: [10.1109/EPE.2016.7695691](https://doi.org/10.1109/EPE.2016.7695691).
- [47] D. Gerada, D. Borg-Bartolo, A. Mebarki, C. Micallef, N. L. Brown, and C. Gerada. “Electrical machines for high speed applications with a wide constant-power region requirement”. In: *2011 International Conference on Electrical Machines and Systems*. 2011, pp. 1–6. DOI: [10.1109/ICEMS.2011.6073480](https://doi.org/10.1109/ICEMS.2011.6073480).
- [48] D. Diallo, M. E. H. Benbouzid, and A. Makouf. “A fault-tolerant control architecture for induction motor drives in automotive applications”. In: *IEEE Transactions on Vehicular Technology* 53.6 (2004), pp. 1847–1855. DOI: [10.1109/TVT.2004.833610](https://doi.org/10.1109/TVT.2004.833610).

- [49] B. H. Kenny, P. E. Kascak, R. Jansen, T. Dever, and W. Santiago. “Control of a high-speed flywheel system for energy storage in space applications”. In: *IEEE Transactions on Industry Applications* 41.4 (2005), pp. 1029–1038. DOI: [10.1109/TIA.2005.851021](https://doi.org/10.1109/TIA.2005.851021).
- [50] H. A. Toliyat, S. Talebi, P. McMullen, Co Huynh, and A. Filatov. “Advanced high-speed flywheel energy storage systems for pulsed power applications”. In: *IEEE Electric Ship Technologies Symposium, 2005*. 2005, pp. 379–386. DOI: [10.1109/ESTS.2005.1524703](https://doi.org/10.1109/ESTS.2005.1524703).
- [51] Y. Suzuki, A. Koyanagi, M. Kobayashi, and R. Shimada. “Novel applications of the flywheel energy storage system”. In: *Energy* 30.11 (2005). International Symposium on CO₂ Fixation and Efficient Utilization of Energy (CandE 2002) and the International World Energy System Conference (WESC-2002), pp. 2128 –2143. ISSN: 0360-5442. DOI: <https://doi.org/10.1016/j.energy.2004.08.018>. URL: <http://www.sciencedirect.com/science/article/pii/S0360544204003718>.
- [52] A. Boglietti, A. Cavagnino, A. Tenconi, and S. Vaschetto. “Key design aspects of electrical machines for high-speed spindle applications”. In: *IECON 2010 - 36th Annual Conference on IEEE Industrial Electronics Society*. 2010, pp. 1735–1740. DOI: [10.1109/IECON.2010.5675417](https://doi.org/10.1109/IECON.2010.5675417).
- [53] R. Abebe, M. Di Nardo, D. Gerada, G. L. Calzo, L. Papini, and C. Gerada. “High speed drives review: Machines, converters and applications”. In: *IECON 2016 - 42nd Annual Conference of the IEEE Industrial Electronics Society*. 2016, pp. 1675–1679. DOI: [10.1109/IECON.2016.7793721](https://doi.org/10.1109/IECON.2016.7793721).
- [54] “Novel applications of the flywheel energy storage system”. In: *Energy* 30.11 (2005). International Symposium on CO₂ Fixation and Efficient Utilization of Energy (CandE 2002) and the International World Energy System Conference (WESC-2002), pp. 2128 –2143. ISSN: 0360-5442. DOI: <https://doi.org/10.1016/j.energy.2004.08.018>. URL: <http://www.sciencedirect.com/science/article/pii/S0360544204003718>.
- [55] O. Bottauscio, F. Casaro, M. Chiampi, S. Giors, C. Maccarrone, and M. Zucca. “High-Speed Drag-Cup Induction Motors for Turbo-Molecular Pump Applications”. In: *IEEE Transactions on Magnetics* 42.10 (2006), pp. 3449–3451. DOI: [10.1109/TMAG.2006.879446](https://doi.org/10.1109/TMAG.2006.879446).
- [56] Bangcheng Han, Ziyuan Huang, and Yun Le. “Design aspects of a large scale turbomolecular pump with active magnetic bearings”. In: *Vacuum* 142 (2017), pp. 96 –105. ISSN: 0042-207X. DOI: <https://doi.org/10.1016/j.vacuum.2016.12.010>. URL: <http://www.sciencedirect.com/science/article/pii/S0042207X16307515>.

- [57] W Becker and J Henning. “Problems with turbomolecular pumps in magnetic fields”. In: *Journal of Vacuum Science and Technology* 15.2 (1978), pp. 768–770.
- [58] W. L. Soong, G. B. Kliman, R. N. Johnson, R. A. White, and J. E. Miller. “Novel high-speed induction motor for a commercial centrifugal compressor”. In: *IEEE Transactions on Industry Applications* 36.3 (2000), pp. 706–713. DOI: [10.1109/28.845043](https://doi.org/10.1109/28.845043).
- [59] W. L. Soong, G. B. Kliman, R. N. Johnson, R. A. White, and J. E. Miller. “Novel high-speed induction motor for a commercial centrifugal compressor”. In: *IEEE Transactions on Industry Applications* 36.3 (2000), pp. 706–713. DOI: [10.1109/28.845043](https://doi.org/10.1109/28.845043).
- [60] N. Uzhegov, J. Barta, J. Kurfürst, C. Ondrusek, and J. Pyrhönen. “Comparison of high-speed electrical motors for a turbo circulator application”. In: *2016 XXII International Conference on Electrical Machines (ICEM)*. 2016, pp. 688–694. DOI: [10.1109/ICELMACH.2016.7732601](https://doi.org/10.1109/ICELMACH.2016.7732601).
- [61] R. Lateb, J. Enon, and L. Durantay. “High speed, high power electrical induction motor technologies for integrated compressors”. In: *2009 International Conference on Electrical Machines and Systems*. 2009, pp. 1–5. DOI: [10.1109/ICEMS.2009.5382960](https://doi.org/10.1109/ICEMS.2009.5382960).
- [62] N. Uzhegov, A. Smirnov, C. H. Park, J. H. Ahn, J. Heikkinen, and J. Pyrhönen. “Design Aspects of High-Speed Electrical Machines With Active Magnetic Bearings for Compressor Applications”. In: *IEEE Transactions on Industrial Electronics* 64.11 (2017), pp. 8427–8436. DOI: [10.1109/TIE.2017.2698408](https://doi.org/10.1109/TIE.2017.2698408).
- [63] Giampaolo Buticchi, David Gerada, Luigi Alberti, Michael Galea, Pat Wheeler, Serhiy Bozhko, Sergei Peresada, He Zhang, Chengming Zhang, and Chris Gerada. “Challenges of the optimization of a high-speed induction machine for naval applications”. In: *Energies* 12.12 (2019), p. 2431.
- [64] N. W. Frank and H. A. Toliyat. “Gearing ratios of a magnetic gear for marine applications”. In: *2009 IEEE Electric Ship Technologies Symposium*. 2009, pp. 477–481. DOI: [10.1109/ESTS.2009.4906554](https://doi.org/10.1109/ESTS.2009.4906554).
- [65] M. E. Elbuluk and M. D. Kankam. “Potential starter/generator technologies for future aerospace applications”. In: *IEEE Aerospace and Electronic Systems Magazine* 12.5 (1997), pp. 24–31. DOI: [10.1109/62.587815](https://doi.org/10.1109/62.587815).
- [66] G. J. Atkinson, B. C. Mecrow, A. G. Jack, D. J. Atkinson, P. Sangha, and M. Benarous. “The Analysis of Losses in High-Power Fault-Tolerant Machines for Aerospace Applications”. In: *IEEE Transactions on Industry Applications* 42.5 (2006), pp. 1162–1170. DOI: [10.1109/TIA.2006.880869](https://doi.org/10.1109/TIA.2006.880869).

- [67] P. E. Kakosimos, A. G. Sarigiannidis, M. E. Beniakar, A. G. Kladas, and C. Gerada. “Induction Motors Versus Permanent-Magnet Actuators for Aerospace Applications”. In: *IEEE Transactions on Industrial Electronics* 61.8 (2014), pp. 4315–4325. DOI: [10.1109/TIE.2013.2274425](https://doi.org/10.1109/TIE.2013.2274425).
- [68] J. Pyrhönen. *The High-speed Induction Motor: Calculating the Effects of Solid-rotor Material on Machine Characteristics*. Acta polytechnica Scandinavica: El. Finnish Academy of Technology, 1991, p. 84. ISBN: 9789516663329.
- [69] Dieter Gerling and Gurakuq Dajaku. “Comparison of different calculation methods for the induction motor with multilayer rotor structure”. In: *Proc. Int. Conf. Elect. Mach.(ICEM)*. 2004, pp. 4–8.
- [70] M. Markovic and Y. Perriard. “An analytical solution for the torque and power of a solid-rotor induction motor”. In: *2011 IEEE International Electric Machines Drives Conference (IEMDC)*. 2011, pp. 1053–1057. DOI: [10.1109/IEMDC.2011.5994746](https://doi.org/10.1109/IEMDC.2011.5994746).
- [71] V. Räsänen, S. Suuriniemi, S. Kurz, and L. Kettunen. “Rapid Computation of Harmonic Eddy-Current Losses in High-Speed Solid-Rotor Induction Machines”. In: *IEEE Transactions on Energy Conversion* 28.3 (2013), pp. 782–790. DOI: [10.1109/TEC.2013.2268278](https://doi.org/10.1109/TEC.2013.2268278).
- [72] M. R. Shah and Sang Bin Lee. “Rapid analytical optimization of eddy-current shield thickness for associated loss minimization in electrical Machines”. In: *IEEE Transactions on Industry Applications* 42.3 (2006), pp. 642–649. DOI: [10.1109/TIA.2006.873671](https://doi.org/10.1109/TIA.2006.873671).
- [73] M. Mirzaei, M. Mirsalim, and S. E. Abdollahi. “Analytical Modeling of Axial Air Gap Solid Rotor Induction Machines Using a Quasi-Three-Dimensional Method”. In: *IEEE Transactions on Magnetics* 43.7 (2007), pp. 3237–3242. DOI: [10.1109/TMAG.2007.894215](https://doi.org/10.1109/TMAG.2007.894215).
- [74] Luca Papini and Clare Gerada. “ANALYTICAL-NUMERICAL MODELLING OF SOLID ROTOR INDUCTION MACHINE”. In: *ELECTRIMACS 2014* (May 2014).
- [75] M. S. Sarma. “Electromagnetic Fields in Solid-Rotor Induction Motor”. In: *IEEE Transactions on Aerospace and Electronic Systems* AES-12.5 (1976), pp. 572–576. DOI: [10.1109/TAES.1976.308258](https://doi.org/10.1109/TAES.1976.308258).
- [76] Q. Wei, F. Yu, Z. Xi, and L. Shuo. “Analysis on electromagnetic field of an Axial-Flux Solid Aluminum Rotor Induction Motor”. In: *2011 International Conference on Electrical Machines and Systems*. 2011, pp. 1–4. DOI: [10.1109/ICEMS.2011.6073521](https://doi.org/10.1109/ICEMS.2011.6073521).

- [77] M. Jagiela and T. Garbiec. “Evaluation of Rotor-End Factors in Solid-Rotor Induction Motors”. In: *IEEE Transactions on Magnetics* 48.1 (2012), pp. 137–142. DOI: [10.1109/TMAG.2011.2167019](https://doi.org/10.1109/TMAG.2011.2167019).
- [78] T. Reichert, T. Nussbaumer, and J.W. Kolar. “Complete analytical solution of electromagnetic field problem of high-speed spinning ball”. In: *Journal of Applied Physics* 112.10 (2012). DOI: [10.1063/1.4765676](https://doi.org/10.1063/1.4765676).
- [79] J. Bašta and V.M. Kucevalov. *Elektrické stroje s plnými rotory - Teorie a výpočet*. ČESKOSLOVENSKÁ AKADEMIE VĚD. ACADEMIA/Praha, 1980. ISBN: 4-158633-13005/80.
- [80] A. Boglietti, R. I. Bojoi, A. Cavagnino, P. Guglielmi, and A. Miotto. “Analysis and Modeling of Rotor Slot Enclosure Effects in High-Speed Induction Motors”. In: *IEEE Transactions on Industry Applications* 48.4 (2012), pp. 1279–1287. DOI: [10.1109/TIA.2012.2199270](https://doi.org/10.1109/TIA.2012.2199270).
- [81] L. Papini and C. Gerada. “Sensitivity analysis of magnetizing inductance in solid rotor induction machine”. In: *2016 19th International Conference on Electrical Machines and Systems (ICEMS)*. 2016, pp. 1–6.
- [82] S. Guo, L. Zhou, and T. Yang. “An analytical method for determining circuit parameter of a solid rotor induction motor”. In: *2012 15th International Conference on Electrical Machines and Systems (ICEMS)*. 2012, pp. 1–6.
- [83] D. Popa and D. Fodorean. “Design and performances evaluation of a high speed induction motor used for the propulsion of an electric vehicle”. In: *2014 International Symposium on Power Electronics, Electrical Drives, Automation and Motion*. 2014, pp. 88–93. DOI: [10.1109/SPEEDAM.2014.6871981](https://doi.org/10.1109/SPEEDAM.2014.6871981).
- [84] Nikita Uzhegov. “High-speed solid-rotor induction machine - calculation program”. MA thesis. Finland: Lappeenranta University Of Technology, Faculty of Technology, 2012.
- [85] J. Klíma and O. Vitek. “Analysis of high-speed induction motor”. In: *Proceedings of the 16th International Conference on Mechatronics - Mechatronika 2014*. 2014, pp. 85–91. DOI: [10.1109/MECHATRONIKA.2014.7018240](https://doi.org/10.1109/MECHATRONIKA.2014.7018240).
- [86] C. Mellak, H. Gruebler, H. T. Eickhoff, J. Deuringer, K. Krischan, and A. Muetze. “Control-Based Performance Improvements of a Single-Phase Induction Machine with a Large Air Gap and a Copper-Coated Solid Rotor”. In: *2019 IEEE International Electric Machines Drives Conference (IEMDC)*. 2019, pp. 1539–1544. DOI: [10.1109/IEMDC.2019.8785385](https://doi.org/10.1109/IEMDC.2019.8785385).

- [87] K. Boughrara, F. Dubas, and R. Ibtouen. “2-D Analytical Prediction of Eddy Currents, Circuit Model Parameters, and Steady-State Performances in Solid Rotor Induction Motors”. In: *IEEE Transactions on Magnetics* 50.12 (2014), pp. 1–14. DOI: [10.1109/TMAG.2014.2342666](https://doi.org/10.1109/TMAG.2014.2342666).
- [88] Matthew N. O. SADIKU. *Numerical Techniques in Electromagnetics*. 2nd ed. Boca Raton: CRC Press, 2000, p. 760. ISBN: 0-8493-1395-3.
- [89] Claes JOHNSON. *Numerical Solution of Partial Differential Equations by the Finite Element Method*. 1st ed. Cambridge: Cambridge University Press, 1987, p. 278. ISBN: 0-521-347-580.
- [90] Jorma LUOMI. *Finite elements method for electrical machines*. 1st ed. Göteborg: Chalmers University of Technology, Department of Electrical Machines and Power Electronics, 1993, pp. 1–176.
- [91] Ramón Bargallo. *Finite elements for electrical engineering*. Tech. rep. Universitat Politècnica de catalunya, Electrical engineering department, 2006.
- [92] S. S. RAO. *The finite element method in engineering*. 4th ed. Boston, MA: Elsevier/Butterworth Heinemann, 2004, p. 657. ISBN: 0750678283.
- [93] O. C a Robert L. TAYLOR ZIENKIEWICZ. *The finite element method*. 5th ed. Boston: Butterworth-Heinemann, 2000, p. 708. ISBN: 0750650494.
- [94] J. Yang, P. Liu, C. Ye, L. Wang, X. Zhang, and S. Huang. “Multidisciplinary Design of High-Speed Solid Rotor Homopolar Inductor Machine for Flywheel Energy Storage System”. In: *IEEE Transactions on Transportation Electrification* (2020), pp. 1–1. DOI: [10.1109/TTE.2020.3033375](https://doi.org/10.1109/TTE.2020.3033375).
- [95] G. Khanduri, S. Kalra, and V. Agrawal. “Rotor core material and end ring length analysis for Solid-Rotor high speed Induction Motor”. In: *2014 Students Conference on Engineering and Systems*. 2014, pp. 1–6. DOI: [10.1109/SCES.2014.6880082](https://doi.org/10.1109/SCES.2014.6880082).
- [96] M. S. M. Valtonen, D. S. A. Parviainen, and J. Pyrhonen. “Electromagnetic field analysis of 3D structure of axial-flux solid-rotor induction motor”. In: *International Symposium on Power Electronics, Electrical Drives, Automation and Motion, 2006. SPEEDAM 2006*. 2006, pp. 174–178. DOI: [10.1109/SPEEDAM.2006.1649766](https://doi.org/10.1109/SPEEDAM.2006.1649766).
- [97] Bishal Silwal. “Computation of eddy currents in a solid rotor induction machine with 2-D and 3-D FEM”. MA thesis. Finland: Aalto University, School of electrical engineering, Department of Electrical engineering, 2012.
- [98] J. Ikäheimo, J. Kolehmainen, T. Käsäkangas, V. Kivelä, and R. R. Moghaddam. “Synchronous High-Speed Reluctance Machine With Novel Rotor Construction”. In: *IEEE Transactions on Industrial Electronics* 61.6 (2014), pp. 2969–2975. DOI: [10.1109/TIE.2013.2253077](https://doi.org/10.1109/TIE.2013.2253077).

- [99] M. Lefik, K. Komez, E. Napieralska-Juszczak, D. Roger, and P. A. Napieralski. "Synchronous High-Speed Reluctance Machine With Novel Rotor Construction". In: *COMPEL - The international journal for computation and mathematics in electrical and electronic engineering* 39.4 (2019), pp. 1111–1119. DOI: [10.1108/COMPEL-10-2018-0405](https://doi.org/10.1108/COMPEL-10-2018-0405).
- [100] D. Gerada, A. Mebarki, N. L. Brown, H. Zhang, and C. Gerada. "Design, modelling and testing of a high speed induction machine drive". In: *2012 IEEE Energy Conversion Congress and Exposition (ECCE)*. 2012, pp. 4649–4655. DOI: [10.1109/ECCE.2012.6342188](https://doi.org/10.1109/ECCE.2012.6342188).
- [101] A. Al-Timimy, M. Al-Ani, M. Degano, P. Giangrande, C. Gerada, and M. Galea. "Influence of rotor endcaps on the electromagnetic performance of high-speed PM machine". In: *IET Electric Power Applications* 12.8 (2018), pp. 1142–1149. DOI: [10.1049/iet-epa.2017.0811](https://doi.org/10.1049/iet-epa.2017.0811).
- [102] M. Mirzayee, M. Mirsalim, H. Gholizad, and S. Javadi arani. "Combined 3D Numerical and Analytical Computation Approach for Analysis and Design of High Speed Solid Iron Rotor Induction Machines". In: *6th International Conference on Computational Electromagnetics*. 2006, pp. 1–2.
- [103] J. P. Ducreux and G. Nicolas. "Finite length effects study in massive iron rotors using 3D electromagnetic field computation". In: *IEEE Transactions on Magnetics* 31.3 (1995), pp. 2096–2099. DOI: [10.1109/20.376458](https://doi.org/10.1109/20.376458).
- [104] J. J. Pyrhonen, J. K. Nerg, T. Aho, and P. T. Kurrnen. "Solid rotor end effects - Analytic and experimental results for high-power high-speed machines". In: *IEEE EUROCON 2009*. 2009, pp. 688–695. DOI: [10.1109/EURCON.2009.5167708](https://doi.org/10.1109/EURCON.2009.5167708).
- [105] K. P. P. Pillai. "Fundamental-frequency eddy-current loss due to rotating magnetic field. Part 1: Eddy-current loss in solid rotors". In: *Proceedings of the Institution of Electrical Engineers* 116.3 (1969), pp. 407–410. DOI: [10.1049/piee.1969.0079](https://doi.org/10.1049/piee.1969.0079).
- [106] T. Aho, J. Nerg, and J. Pyrhonen. "Optimizing the Axial Length of the Slitted Solid Iron Rotor". In: *2007 2nd IEEE Conference on Industrial Electronics and Applications*. 2007, pp. 255–259. DOI: [10.1109/ICIEA.2007.4318410](https://doi.org/10.1109/ICIEA.2007.4318410).
- [107] D. O’Kelly. "Theory and performance of solid - rotor induction and hysteresis machines". In: *Proceedings of the Institution of Electrical Engineers* 123.5 (1976), pp. 421–428. DOI: [10.1049/piee.1976.0094](https://doi.org/10.1049/piee.1976.0094).
- [108] T. Aho, J. Nerg, and J. Pyrhonen. "Experimental and Finite Element Analysis of Solid Rotor End Effects". In: *2007 IEEE International Symposium on Industrial Electronics*. 2007, pp. 1242–1247. DOI: [10.1109/ISIE.2007.4374776](https://doi.org/10.1109/ISIE.2007.4374776).

- [109] J. Pyrhonen, J. Nerg, P. Kurronen, and U. Lauber. “High-Speed High-Output Solid-Rotor Induction-Motor Technology for Gas Compression”. In: *IEEE Transactions on Industrial Electronics* 57.1 (2010), pp. 272–280. DOI: [10.1109/TIE.2009.2021595](https://doi.org/10.1109/TIE.2009.2021595).
- [110] Mohamed Amine Bouhlef, John T. Hwang, Nathalie Bartoli, Rémi Lafage, Joseph Morlier, and Joaquim R.R.A. Martins. “A Python surrogate modeling framework with derivatives”. In: *Advances in Engineering Software* 135 (2019), p. 102662. ISSN: 0965-9978. DOI: <https://doi.org/10.1016/j.advengsoft.2019.03.005>. URL: <https://www.sciencedirect.com/science/article/pii/S0965997818309360>.
- [111] Shuai Guo. *An introduction to Surrogate modeling, Part I: fundamentals*. URL: <https://towardsdatascience.com/an-introduction-to-surrogate-modeling-part-i-fundamentals-84697ce4d241>. (accessed: 26.4.2021).
- [112] Cai Li, Ren Lei, Wang Yongheng, Xie Wenxian, Zhu Guangyu, and Gao Hao. “Surrogate models based on machine learning methods for parameter estimation of left ventricular myocardium”. In: *Royal Society Open Science* (2021). DOI: <http://doi.org/10.1098/rsos.201121>.
- [113] Xinhua Liu, Ningning Wang, Kun Wang, Shumei Chen, Shuaishuai Sun, Zhixiong Li, and Weihua Li. “A new AI-surrogate model for dynamics analysis of a magnetorheological damper in the semi-active seat suspension”. In: *Smart Materials and Structures* 29.3 (2020), p. 037001. DOI: [10.1088/1361-665x/ab6ba5](https://doi.org/10.1088/1361-665x/ab6ba5). URL: <https://doi.org/10.1088/1361-665x/ab6ba5>.
- [114] Mustafa Berke Yelten, Ting Zhu, Slawomir Koziel, Paul D. Franzon, and Michael B. Steer. “Demystifying Surrogate Modeling for Circuits and Systems”. In: *IEEE Circuits and Systems Magazine* 12.1 (2012), pp. 45–63. DOI: [10.1109/MCAS.2011.2181095](https://doi.org/10.1109/MCAS.2011.2181095).
- [115] Nestor V Queipo, Javier V Goicochea, and Salvador Pintos. “Surrogate modeling-based optimization of SAGD processes”. In: *Journal of Petroleum Science and Engineering* 35.1 (2002), pp. 83–93. ISSN: 0920-4105. DOI: [https://doi.org/10.1016/S0920-4105\(02\)00167-5](https://doi.org/10.1016/S0920-4105(02)00167-5). URL: <https://www.sciencedirect.com/science/article/pii/S0920410502001675>.
- [116] Kevin McBride and Kai Sundmacher. “Overview of Surrogate Modeling in Chemical Process Engineering”. In: *Chemie Ingenieur Technik* 91.3 (2019), pp. 228–239. DOI: <https://doi.org/10.1002/cite.201800091>. URL: <https://onlinelibrary.wiley.com/doi/abs/10.1002/cite.201800091>.

- [117] Luning Sun, Han Gao, Shaowu Pan, and Jian-Xun Wang. “Surrogate modeling for fluid flows based on physics-constrained deep learning without simulation data”. In: *Computer Methods in Applied Mechanics and Engineering* 361 (2020), p. 112732. ISSN: 0045-7825. DOI: <https://doi.org/10.1016/j.cma.2019.112732>. URL: <https://www.sciencedirect.com/science/article/pii/S004578251930622X>.
- [118] Iveta Lolová. “Topology optimization of the line-start synchronous machines”. Master’s thesis. Brno University of Technology, Faculty of electrical engineering, communication, Department of Power Electrical, and Electronic Engineering, 2020. URL: <https://www.vutbr.cz/studenti/zav-prace/detail/125799>.
- [119] Mattia De’ Michieli Vitturi, A. Neri, and S. Barsotti. “PLUME-MoM 1.0: A new integral model of volcanic plumes based on the method of moments”. In: *Geoscientific Model Development* 8 (Aug. 2015), pp. 2447–2463. DOI: [10.5194/gmd-8-2447-2015](https://doi.org/10.5194/gmd-8-2447-2015).
- [120] Maryam Foroughi, Hassan Nasab, Reza Shokoohi, M. H. Ahmadi Azqhandi, Azam Nadali, and Ashraf Mazaheri. “Ultrasound-assisted sorption of Pb(II) on multi-walled carbon nanotube in presence of natural organic matter: an insight into main and interaction effects using modelling approaches of RSM and BRT”. In: *RSC Advances* 9 (Jan. 2019), pp. 16083–16094. DOI: [10.1039/C9RA02881A](https://doi.org/10.1039/C9RA02881A).
- [121] Wei-Liem Loh. “On Latin hypercube sampling”. In: *The Annals of Statistics* 24.5 (1996), pp. 2058–2080. DOI: [10.1214/aos/1069362310](https://doi.org/10.1214/aos/1069362310). URL: <https://doi.org/10.1214/aos/1069362310>.
- [122] Aleš Florian. “An efficient sampling scheme: Updated Latin Hypercube Sampling”. In: *Probabilistic Engineering Mechanics* 7.2 (1992), pp. 123–130. ISSN: 0266-8920. DOI: [https://doi.org/10.1016/0266-8920\(92\)90015-A](https://doi.org/10.1016/0266-8920(92)90015-A). URL: <https://www.sciencedirect.com/science/article/pii/026689209290015A>.
- [123] Michael Stein. “Large Sample Properties of Simulations Using Latin Hypercube Sampling”. In: *Technometrics* 29.2 (1987), pp. 143–151. DOI: [10.1080/00401706.1987.10488205](https://doi.org/10.1080/00401706.1987.10488205). URL: <https://amstat.tandfonline.com/doi/abs/10.1080/00401706.1987.10488205>.
- [124] D.E. Huntington and C.S. Lyrintzis. “Improvements to and limitations of Latin hypercube sampling”. In: *Probabilistic Engineering Mechanics* 13.4 (1998), pp. 245–253. ISSN: 0266-8920. DOI: [https://doi.org/10.1016/S0266-8920\(97\)00013-1](https://doi.org/10.1016/S0266-8920(97)00013-1). URL: <https://www.sciencedirect.com/science/article/pii/S0266892097000131>.
- [125] J.C. Helton and F.J. Davis. “Latin hypercube sampling and the propagation of uncertainty in analyses of complex systems”. In: *Reliability Engineering & System Safety* 81.1 (2003), pp. 23–69. ISSN: 0951-8320. DOI: [https://doi.org/10.1016/S0951-8320\(03\)00013-1](https://doi.org/10.1016/S0951-8320(03)00013-1).

8320(03)00058-9. URL: <https://www.sciencedirect.com/science/article/pii/S0951832003000589>.

- [126] Kaan Yetilmezsoy, Sevgi Demirel, and Robert J. Vanderbei. “Response surface modeling of Pb(II) removal from aqueous solution by *Pistacia vera* L.: Box–Behnken experimental design”. In: *Journal of Hazardous Materials* 171.1 (2009), pp. 551–562. ISSN: 0304-3894. DOI: <https://doi.org/10.1016/j.jhazmat.2009.06.035>. URL: <https://www.sciencedirect.com/science/article/pii/S0304389409009480>.
- [127] J. Prakash Maran, S. Manikandan, K. Thirugnanasambandham, C. Vigna Nivetha, and R. Dinesh. “Box–Behnken design based statistical modeling for ultrasound-assisted extraction of corn silk polysaccharide”. In: *Carbohydrate Polymers* 92.1 (2013), pp. 604–611. ISSN: 0144-8617. DOI: <https://doi.org/10.1016/j.carbpol.2012.09.020>. URL: <https://www.sciencedirect.com/science/article/pii/S0144861712009289>.
- [128] N. Aslan and Y. Cebeci. “Application of Box–Behnken design and response surface methodology for modeling of some Turkish coals”. In: *Fuel* 86.1 (2007), pp. 90–97. ISSN: 0016-2361. DOI: <https://doi.org/10.1016/j.fuel.2006.06.010>. URL: <https://www.sciencedirect.com/science/article/pii/S0016236106002201>.
- [129] S.L.C. Ferreira, R.E. Bruns, H.S. Ferreira, G.D. Matos, J.M. David, G.C. Brandão, E.G.P. da Silva, L.A. Portugal, P.S. dos Reis, A.S. Souza, and W.N.L. dos Santos. “Box–Behnken design: An alternative for the optimization of analytical methods”. In: *Analytica Chimica Acta* 597.2 (2007), pp. 179–186. ISSN: 0003-2670. DOI: <https://doi.org/10.1016/j.aca.2007.07.011>. URL: <https://www.sciencedirect.com/science/article/pii/S0003267007011671>.
- [130] De qiang Li, Xin Jia, Zhong Wei, and Zhi yong Liu. “Box–Behnken experimental design for investigation of microwave-assisted extracted sugar beet pulp pectin”. In: *Carbohydrate Polymers* 88.1 (2012), pp. 342–346. ISSN: 0144-8617. DOI: <https://doi.org/10.1016/j.carbpol.2011.12.017>. URL: <https://www.sciencedirect.com/science/article/pii/S0144861711011325>.
- [131] Shuai Guo. *An introduction to Surrogate modeling, Part II: case study*. (accessed: 29.4.2021).
- [132] S. H. Kim and F. Boukouvala. “Machine learning-based surrogate modeling for data-driven optimization: a comparison of subset selection for regression techniques”. In: *Optimization Letters* 14.4 (2020), 989–1010. DOI: [10.1007/s11590-019-01428-7](https://doi.org/10.1007/s11590-019-01428-7). URL: <https://doi.org/10.1007/s11590-019-01428-7>.

- [133] Saman Razavi, Bryan A. Tolson, and Donald H. Burn. “Review of surrogate modeling in water resources”. In: *Water Resources Research* 48.7 (2012). DOI: <https://doi.org/10.1029/2011WR011527>. URL: <https://agupubs.onlinelibrary.wiley.com/doi/abs/10.1029/2011WR011527>.
- [134] Mikhail Belyaev, Evgeny Burnaev, Ermek Kapushev, Maxim Panov, Pavel Prikhodko, Dmitry Vetrov, and Dmitry Yarotsky. “GTApprox: Surrogate modeling for industrial design”. In: *Advances in Engineering Software* 102 (2016), pp. 29–39. ISSN: 0965-9978. DOI: <https://doi.org/10.1016/j.advengsoft.2016.09.001>. URL: <https://www.sciencedirect.com/science/article/pii/S0965997816303696>.
- [135] Karel Crombecq, Luciano De Tommasi, Dirk Gorissen, and Tom Dhaene. “A novel sequential design strategy for global surrogate modeling”. In: *Proceedings of the 2009 Winter Simulation Conference (WSC)*. 2009, pp. 731–742. DOI: [10.1109/WSC.2009.5429687](https://doi.org/10.1109/WSC.2009.5429687).
- [136] J.W. Bandler, Qingsha Cheng, D.H. Gebre-Mariam, K. Madsen, F. Pedersen, and J. Sondergaard. “EM-based surrogate modeling and design exploiting implicit, frequency and output space mappings”. In: *IEEE MTT-S International Microwave Symposium Digest, 2003*. Vol. 2. 2003, 1003–1006 vol.2. DOI: [10.1109/MWSYM.2003.1212538](https://doi.org/10.1109/MWSYM.2003.1212538).
- [137] Shuai Guo. *An introduction to surrogate modeling, Part III: beyond basics*. (accessed: 29.4.2021).
- [138] A. G. Asuero, A. Sayago, and A. G. González. “The Correlation Coefficient: An Overview”. In: *Critical Reviews in Analytical Chemistry* 36.1 (2006), pp. 41–59. DOI: [10.1080/10408340500526766](https://doi.org/10.1080/10408340500526766). URL: <https://doi.org/10.1080/10408340500526766>.
- [139] Xin Chen, Haofei Zhou, and Yumeng Li. “Effective design space exploration of gradient nanostructured materials using active learning based surrogate models”. In: *Materials & Design* 183 (2019), p. 108085. ISSN: 0264-1275. DOI: <https://doi.org/10.1016/j.matdes.2019.108085>. URL: <https://www.sciencedirect.com/science/article/pii/S0264127519305234>.
- [140] Prasanna Balaprakash, Robert B. Gramacy, and Stefan M. Wild. “Active-learning-based surrogate models for empirical performance tuning”. In: *2013 IEEE International Conference on Cluster Computing (CLUSTER)*. 2013, pp. 1–8. DOI: [10.1109/CLUSTER.2013.6702683](https://doi.org/10.1109/CLUSTER.2013.6702683).
- [141] Handing Wang, Yaochu Jin, and John Doherty. “Committee-Based Active Learning for Surrogate-Assisted Particle Swarm Optimization of Expensive Problems”. In: *IEEE Transactions on Cybernetics* 47.9 (2017), pp. 2664–2677. DOI: [10.1109/TCYB.2017.2710978](https://doi.org/10.1109/TCYB.2017.2710978).

- [142] Gerd Bramerdorfer, Alexandru-Ciprian Zăvoianu, Siegfried Silber, Edwin Lughofer, and Wolfgang Amrhein. “Possibilities for Speeding Up the FE-Based Optimization of Electrical Machines—A Case Study”. In: *IEEE Transactions on Industry Applications* 52.6 (2016), pp. 4668–4677. DOI: [10.1109/TIA.2016.2587702](https://doi.org/10.1109/TIA.2016.2587702).
- [143] Alexandru-Ciprian Zăvoianu, Gerd Bramerdorfer, Edwin Lughofer, Siegfried Silber, Wolfgang Amrhein, and Erich Peter Klement. “Hybridization of multi-objective evolutionary algorithms and artificial neural networks for optimizing the performance of electrical drives”. In: *Engineering Applications of Artificial Intelligence* 26.8 (2013), pp. 1781–1794. ISSN: 0952-1976. DOI: <https://doi.org/10.1016/j.engappai.2013.06.002>. URL: <https://www.sciencedirect.com/science/article/pii/S0952197613001036>.
- [144] *FreeCAD Your own 3D parametric modeler*. URL: <https://www.freecadweb.org/>. (accessed: 2.5.2020).
- [145] *Getting started*. URL: https://wiki.freecadweb.org/Getting_started. (accessed: 2.5.2020).
- [146] *Maxwell 2D User’s Guide*. Edition: REV6.0. ANSYS Inc. 2020.
- [147] *Maxwell 3D User’s Guide*. Edition: REV6.0. ANSYS Inc. 2020.
- [148] *ANSYS Electronics Desktop: Scripting Guide*. ANSYS Inc. 2015. URL: <http://www.ece.uprm.edu/~rafaelr/inel6068/HFSS/scripting.pdf>.
- [149] *Typical data for SURA® M470-50A*. URL: <https://www.tatasteeleurope.com/ts/sites/default/files/m470-50a.pdf>. (accessed: 2.5.2021).
- [150] Ji-Hyun Kim, Sunil Kim, and J.P. Hong. “Extrapolating B-H Curve Data using Common Electrical Steel Characteristics for High Magnetic Saturation Applications”. In: *Journal of Magnetism* 20 (Sept. 2015), pp. 258–264. DOI: [10.4283/JMAG.2015.20.3.258](https://doi.org/10.4283/JMAG.2015.20.3.258).
- [151] Aghuinyue Umenei, Yevgen Melikhov, and David Jiles. “Models for Extrapolation of Magnetization Data on Magnetic Cores to High Fields”. In: *IEEE Transactions on Magnetics - IEEE TRANS MAGN* 47 (Dec. 2011), pp. 4707–4711. DOI: [10.1109/TMAG.2011.2159616](https://doi.org/10.1109/TMAG.2011.2159616).
- [152] *Python*. URL: <https://www.python.org/>. (accessed: 2.5.2021).
- [153] J. Pyrhonen, T. Jokinen, and V. Hrabovcova. *Design of Rotating Electrical Machines*. Wiley, 2009, p. 538. ISBN: 9780470740088.
- [154] Rickard Sjoegren. *pyDOE2: An experimental design package for python*. URL: <https://pypi.org/project/pyDOE2/>. (accessed: 6.5.2021).

- [155] Izabella Surowiec, Ludvig Vikström, Gustaf Hector, Erik Johansson, Conny Vikström, and Johan Trygg. “Generalized Subset Designs in Analytical Chemistry”. In: *Analytical Chemistry* 89.12 (2017). PMID: 28497952, pp. 6491–6497. DOI: [10.1021/acs.analchem.7b00506](https://doi.org/10.1021/acs.analchem.7b00506). URL: <https://doi.org/10.1021/acs.analchem.7b00506>.
- [156] Abraham Lee. *pyDOE: The experimental design package for python*. URL: <https://pythonhosted.org/pyDOE/>. (accessed: 6.5.2021).
- [157] Vaclav Skala. “Fast Interpolation and Approximation of Scattered Multidimensional and Dynamic Data Using Radial Basis Functions”. In: *WSEAS Transaction on Mathematics* 12.5 (2013), pp. 501–511. URL: <http://hdl.handle.net/11025/11330>.
- [158] Karl Rohr and Stefan Würz. “An extension of thin-plate splines for image registration with radial basis functions”. In: *2012 9th IEEE International Symposium on Biomedical Imaging (ISBI)*. 2012, pp. 442–445. DOI: [10.1109/ISBI.2012.6235579](https://doi.org/10.1109/ISBI.2012.6235579).
- [159] I. Boztosun, A. Charafi, M. Zerroukat, and K. Djidjeli. “Thin-plate spline radial basis function scheme for advection-diffusion problems”. In: *Electronic Journal of Boundary Elements* BETEQ 2001.2 (2002), pp. 267–282. URL: <https://eprints.soton.ac.uk/22112/>.
- [160] M. D. Buhmann. “Radial basis functions”. In: *Acta Numerica* 9 (2000), 1–38. DOI: [10.1017/S0962492900000015](https://doi.org/10.1017/S0962492900000015).
- [161] M. J. D. Powell. “Recent research at Cambridge on radial basis functions”. In: *New Developments in Approximation Theory*. Ed. by Manfred W. Müller, Martin D. Buhmann, Detlef H. Mache, and Michael Felten. Basel: Birkhäuser Basel, 1999, pp. 215–232. ISBN: 978-3-0348-8696-3.
- [162] Song Xiang, Ze yang Bi, Shao xi Jiang, Yao xing Jin, and Ming sui Yang. “Thin plate spline radial basis function for the free vibration analysis of laminated composite shells”. In: *Composite Structures* 93.2 (2011), pp. 611–615. ISSN: 0263-8223. DOI: <https://doi.org/10.1016/j.compstruct.2010.08.018>. URL: <https://www.sciencedirect.com/science/article/pii/S0263822310002849>.
- [163] Natasha Flyer and Grady B. Wright. “A radial basis function method for the shallow water equations on a sphere”. In: *Proceedings of the Royal Society A: Mathematical, Physical and Engineering Sciences* 465.2106 (2009), pp. 1949–1976. DOI: [10.1098/rspa.2009.0033](https://doi.org/10.1098/rspa.2009.0033). URL: <https://royalsocietypublishing.org/doi/abs/10.1098/rspa.2009.0033>.

- [164] Mohamed Amine Bouhlef, John T. Hwang, Nathalie Bartoli, Rémi Lafage, Joseph Morlier, and Joaquim R.R.A. Martins. “A Python surrogate modeling framework with derivatives”. In: *Advances in Engineering Software* 135 (2019), p. 102662. ISSN: 0965-9978. DOI: <https://doi.org/10.1016/j.advengsoft.2019.03.005>. URL: <https://www.sciencedirect.com/science/article/pii/S0965997818309360>.
- [165] SciPy. URL: <https://docs.scipy.org/doc/scipy/reference/index.html>. (accessed: 9.5.2021).
- [166] SciPy interpolate RBF. URL: <https://docs.scipy.org/doc/scipy/reference/generated/scipy.interpolate.Rbf.html>. (accessed: 9.5.2021).
- [167] Jason Brownlee. *How to Calculate Correlation Between Variables in Python*. URL: <https://machinelearningmastery.com/how-to-use-correlation-to-understand-the-relationship-between-variables/>. (accessed: 9.5.2021).
- [168] M. Montaz Ali, Charoenchai Khompatraporn, and Zelda B. Zabinsky. “A Numerical Evaluation of Several Stochastic Algorithms on Selected Continuous Global Optimization Test Problems”. In: *Journal of Global Optimization* 31 (2005), 635–672. ISSN: 1573-2916. DOI: [10.1007/s10898-004-9972-2](https://doi.org/10.1007/s10898-004-9972-2). URL: <https://doi.org/10.1007/s10898-004-9972-2>.
- [169] Thomas Bäck and Hans-Paul Schwefel. “An Overview of Evolutionary Algorithms for Parameter Optimization”. In: *Evolutionary Computation* 1.1 (Mar. 1993), pp. 1–23. ISSN: 1063-6560. DOI: [10.1162/evco.1993.1.1.1](https://doi.org/10.1162/evco.1993.1.1.1). URL: <https://doi.org/10.1162/evco.1993.1.1.1>.
- [170] Mitsuo Gen and Runwei Cheng. *Genetic Algorithms and Engineering Optimization*. Frontmatter. John Wiley & Sons, Ltd, 1999, p. 512. ISBN: 9780470172261. DOI: <https://doi.org/10.1002/9780470172261.fmatter>. URL: <https://onlinelibrary.wiley.com/doi/abs/10.1002/9780470172261.fmatter>.
- [171] Riccardo Poli, James Kennedy, and Tim Blackwell. “Particle swarm optimization”. In: *Swarm Intelligence* 1.1 (2007), 33–57. ISSN: 1935-3820. DOI: [10.1007/s11721-007-0002-0](https://doi.org/10.1007/s11721-007-0002-0). URL: <https://doi.org/10.1007/s11721-007-0002-0>.
- [172] Siegfried Silber, Werner Koppelstätter, Günther Weidenholzer, Gordan Segon, and Gerd Bramerdorfer. “Reducing Development Time of Electric Machines with SyMSpace”. In: *2018 8th International Electric Drives Production Conference (EDPC)*. 2018, pp. 1–5. DOI: [10.1109/EDPC.2018.8658312](https://doi.org/10.1109/EDPC.2018.8658312).
- [173] Linz center of mechatronics. *SYMSPACE – THE SYSTEM MODEL SPACE*. URL: <https://www.lcm.at/en/project/symspace-the-system-model-space/>. (accessed: 14.5.2021).

- [174] Linz center of mechatronics. *WHAT IS SYMSPACE® AND HOW DOES IT WORK?* URL: <https://symspace.lcm.at/>. (accessed: 14.5.2021).
- [175] Alexandru-Ciprian Zăvoianu, Edwin Lughofer, Gerd Bramerdorfer, Wolfgang Amrhein, and Erich Peter Klement. “DECMO2: a robust hybrid and adaptive multi-objective evolutionary algorithm”. In: *Soft Computing* 19 (2015). ISSN: 1433-7479. DOI: [10.1007/s00500-014-1308-7](https://doi.org/10.1007/s00500-014-1308-7). URL: <https://doi.org/10.1007/s00500-014-1308-7>.
- [176] Eckart Zitzler, Marco Laumanns, and Lothar Thiele. “SPEA2: Improving the strength pareto evolutionary algorithm”. In: *TIK-Report* 103 (2001). DOI: <https://doi.org/10.3929/ethz-a004284029>.
- [177] K. Deb, A. Pratap, S. Agarwal, and T. Meyarivan. “A fast and elitist multiobjective genetic algorithm: NSGA-II”. In: *IEEE Transactions on Evolutionary Computation* 6.2 (2002), pp. 182–197. DOI: [10.1109/4235.996017](https://doi.org/10.1109/4235.996017).
- [178] K. Deb, A. Pratap, S. Agarwal, and T. Meyarivan. “A fast and elitist multiobjective genetic algorithm: NSGA-II”. In: *IEEE Transactions on Evolutionary Computation* 6.2 (2002), pp. 182–197. DOI: [10.1109/4235.996017](https://doi.org/10.1109/4235.996017).
- [179] Théo Vanderheyden. *Pickle in Python: Object Serialization*. URL: <https://www.datacamp.com/community/tutorials/pickle-python-tutorial>. (accessed: 15.5.2021).
- [180] Python. *pickle — Python object serialization*. URL: <https://docs.python.org/3/library/pickle.html>. (accessed: 15.5.2021).

List of symbols and abbreviations

Symbol	Description	Unit
β_ν	Constant (real number) dependent on the space harmonic	$[m^{-1}]$
λ_j	Weights coefficients	$[-]$
μ_0	Permeability of vacuum	$[Hm^{-1}]$
μ_r	Relative permeability of material	$[-]$
μ	Permeability of a material	$[Hm^{-1}]$
ν_{ave}	Average value of higher harmonic component	$[-]$
ν	Number of a space harmonic	$[-]$
ρ_c	Cylindrical shell region resistivity	$[\Omega]$
ρ_{er}	End region resistivity	$[\Omega]$
σ	Electrical conductivity of a material	$[Sm^{-1}]$
σ_{Corr}	Corrected conductivity of the solid rotor material	
τ_p	Pole pitch	$[m]$
$\tau_{p\nu}$	Average pole pitch of the stator slot harmonic fields	$[m]$
φ	Basis function	$[-]$
φ_s	Phase shift of total machine impedance measured at stator terminals	$[\circ]$
φ_r	Phase shift of total rotor impedance	$[\circ]$
Ψ_a	Phase flux linkage	$[Wb]$
Ω	Mechanical angular velocity of the rotor	$[rads^{-1}]$
ω, ω_s	Angular frequency of the stator field	$[rads^{-1}]$
ω_r	Angular frequency of the rotor fields	$[rads^{-1}]$
ω_p	Angular frequency of the penetrating field	$[rads^{-1}]$
A	Interpolation matrix containing radial functions	$[-]$
B_s	Saturation value of magnetic field flux density	$[T]$
B	Magnetic flux density	$[T]$
b	Vector of values	$[-]$
C_R	Damping of the rotor	$[N \cdot m \cdot s \cdot rad^{-1}]$
C	Constant determining type of material used for end-rings	$[-]$
c	Adaptation coefficient	$[-]$
$cos\varphi$	Power factor	$[-]$
$cos\varphi_r$	Power factor of the rotor	$[-]$
D_{out}	Outer diameter of the rotor without the thicker layer of the copper coating	$[m]$
D_{in}	Inner diameter of the rotor	$[m]$

Symbol	Description	Unit
D_r	Outer rotor diameter	[m]
d_{Cu}	Thickness of the copper coat	[m]
d	Penetration depth of magnetic field	[m]
$E_1(s)$	Electromotive force (slip dependent)	[V]
f	Supply frequency	[Hz]
$f(x)$	General radial basis function	[-]
H_0	Peak value of the sinusoidal applied surface field strength	[Am ⁻¹]
H	Magnetic field strength	[Am ⁻¹]
H_{Slit}	Height of rotor slits	[m]
H_{Slot}	Height of stator slots	[m]
I_0	Magnetizing current	[A]
I_1	Stator phase input current	[A]
J	Current density	[Am ⁻²]
I_2'	Secondary current in the rotor frame	[A]
I_m	Stator peak current	[A]
k_{Aho}	Slip-correction factor by Aho	[-]
k_{er}	Complex corrective end-effect factor	[-]
$k_{O'Kelly}$	Corrective end-effect factor by O'Kelly	[-]
k_{PAN}	Slip-correction factor	[-]
$k_{R,\nu=1}$	Corrective end-effect factor for fundamental field for radial grooves by Russell	[-]
$k_{R,\nu}$	Corrective end-effect factor for higher harmonic fields for radial grooves by Russell	[-]
$k_{R,eq}$	Average equivalent corrective end-effect factor for radial grooves by Russell	[-]
k_{RN}	Corrective end-effect factor by Russell-Northworthy	
$k_{Russell}$	Corrective end-effect factor by Russell	[-]
$k_{Russell,M}$	Modified corrective end-effect factor by Russell	[-]
$k_{Trickey}$	Corrective end-effect factor by Trickey	[-]
k_{tot}	Total correction factor for the solid rotor	[-]
k_t	Correction factor for a thicker part of the copper coat	[-]
$k_{Woolley}$	Corrective end-effect factor by Woolley	[-]
k_{Yee}	Corrective end-effect factor by Yee	[-]
k_z	Corrective end-effect factor for a smooth solid rotor	[-]
k	General corrective end-effect factor	[-]
L_1	Magnetizing inductance (Stator inductance)	[H]

Symbol	Description	Unit
l_{gap}	Length of the air gap	[m]
L_r	Whole rotor length	[m]
L	Length of the active part of the rotor	[m]
l_s	Half of the active stator-pack length	[m]
l_{end}	Length of the rotor end beyond the active stator pack	[m]
l_{FeV}	Distance between the radial grooves	[m]
M_{Mech}	Mechanical friction moment of the solid rotor	[Nm]
m	Number of phases	[-]
$N'_2(s), L_{r\sigma}$	Leakage inductance expressed in the rotor frame (slip dependent)	[H]
N_s	Number of stator conductors	[-]
n_s	Synchronous rotational speed	[rpm]
n	Rotational speed of the rotor	[rpm]
$P_k(x)$	Polynomial added to radial basis function	[-]
P_{Mech}	Mechanical friction losses of the solid rotor	[W]
P_{tr}	Active power of the high-speed IM with solid rotor	[W]
p	Pole pair number	[-]
Q_1	Number of stator slots	[-]
Q_2	Number of rotor bars/slits	[-]
Q_{tr}	Reactive power of the high-speed IM with solid rotor	[Var]
R_s	Stator phase resistance	[Ω]
$R'_2(s)$	Equivalent resistance expressed in the rotor frame (slip dependent)	[Ω]
$R_{\text{tot,ef}}$	Resistive part of the total calculated machine impedance	[Ω]
R_r	Resistance of the solid rotor	[Ω]
$R_{r,\text{act}}$	Resistance of the active part of the solid rotor	[Ω]
$R_{r,\text{er}}$	Resistance of the rotor end regions	[Ω]
r_{ave}	Average rotor radius	[m]
s	Slip of the rotor	[-]
S_{tr}	Apparent power of the high-speed IM with solid rotor	[VA]
$T_{\text{em}}(s)$	Electromagnetic torque (slip dependent)	[Nm]
t_{ov}	Thickness of the copper coat at the rotor end regions	[m]
V_1	Stator phase input voltage	[V]
W_{Slit}	Width of rotor slits	[m]
W_{Slot}	Width of stator slits	[m]
w_{ov}	Length of the copper coat at the rotor end region	[m]

Symbol	Description	Unit
$X_{\text{tot,ef}}$	Reactance part of the total calculated machine impedance	$[\Omega]$
$X_{\text{tot,er}}$	Measured reactance error at stator terminals	$[\Omega]$
$X_{\text{r,act}}$	Reactance of the active part of the solid rotor	$[\Omega]$
$X_{\text{r,er}}$	Reactance of the rotor end regions	$[\Omega]$
x	Vector of coefficients	$[-]$
y_{slit}	Slit depth	$[m]$
$Z'_2(s)$	Impedance of the solid rotor (slip dependent)	$[\Omega]$
$Z_{\text{ef,tot}}$	Impedance of machine calculated with two-dimensional approach with end factor resistivity correction	$[\Omega]$
Z_{fix}	Corrected solid rotor impedance	$[\Omega]$
$Z_{\text{meas,tot}}$	Total machine impedance measured at stator terminals	$[\Omega]$
Z_{r}	Total impedance of the solid rotor	$[\Omega]$
$Z_{\text{op}}(s)$	Impedance of the solid rotor parallel to magnetizing inductance (slip dependent)	$[\Omega]$
z_{er}	End region thickness	$[m]$

Abbreviations	Description
CAD	Computer-aided design
CPM	Claw pole machine(s)
EGR	Exhaust gas recirculation
FEA	Finite element analysis
FEM	Finite element method
FFT	Fast Fourier transformation
GUI	Graphical user interface
HM	Homopolar machine(s)
IEP	Integrated electric propulsion
IFEPE	Integrated full electric propulsion
IM	Induction machine(s)
MEA	More electric aircraft
MEE	More electric engine
MOEA	Multi-objective evolutionary algorithms
NiMH	Nickel–metal hydride
PMBM	Permanent magnet brushless machine(s)
PMSM	Permanent magnet synchronous machine(s)
SRM	Switch reluctance machine(s)
Syn. RM	Synchronous reluctance machine(s)
RBF	Radial basis function
TPS	Thin-plate spline

List of Appendices

Appendix A - Overview of all correction end-effect factors	185
Appendix B - Material data for stator sheet	189
Appendix C - The rest of the results from the sensitivity analysis simulations of the case study machine	190
Appendix D - The rest of the results from the initial optimization of the case study machine in Optimizer	191
Appendix E - The rest of the results from the second optimization of the case study machine in Optimizer	196
Appendix F - All data used to determine the accuracy of surrogate models after the initial optimization in Optimizer	204
Appendix G - All data used to determine the accuracy of surrogate models after the second optimization in Optimizer	212

Appendix A - Overview of all correction end-effect factors

Table A1: Overview of all end-effect correction factors for a solid rotor

Description	End-effect factor formula	Conductivity correction	Reference
Trickey's end-effect correction factor for a solid rotor	$k_{\text{Trickey}} = \frac{p}{2} \left[\frac{1 + \left(\frac{D_{\text{in}}}{D_r}\right)^p}{1 - \left(\frac{D_{\text{in}}}{D_r}\right)^p} \right], \quad D_{\text{in}} = D_r - 2y_{\text{slit}}$	$\sigma_{\text{Corr}} = k_{\text{Trickey}} \cdot \sigma$	[5]
Yee's end-effect correction factor for a solid rotor	$k_{\text{Yee}} = \frac{aL_r \left(1 + \coth\left(\frac{aL_r}{2}\right)\right)}{aL_r \left(1 + \coth\left(\frac{aL_r}{2}\right)\right) - 2}, \quad a = \frac{\pi}{\tau_p}$	$\sigma_{\text{Corr}} = k_{\text{Yee}} \cdot \sigma$	[7]
Woolley's end-effect correction factor for a solid rotor	$k_{\text{Woolley}} = \left[\frac{1}{2} \left(Q_1 + \sqrt{Q_1^2 + 4k_1 \cdot \tanh\left(\frac{pL_r}{D_r}\right)} \right) \right],$ $Q_1 = 1 - \left(\frac{D_r}{pL_r} + k_1\right) \tanh\left(\frac{pL_r}{D_r}\right), \quad k_1 = \frac{z_{\text{er}}\rho_c}{y_{\text{slit}}\rho_{\text{er}}}$	$\sigma_{\text{Corr}} = k_{\text{Woolley}} \cdot \sigma$	[8]
O'Kelly's end-effect correction factor for a solid rotor	$k_{\text{O'Kelly}} = \frac{L_r}{L_r + \frac{\pi\tau_{\text{ave}}}{p}}$	$\sigma_{\text{Corr}} = k_{\text{O'Kelly}} \cdot \sigma$	[107]

Description	End-effect factor formula	Conductivity correction	Reference
Frequency dependent Yee's end-effect correction factor for a solid rotor	$K_{\text{Yee,M}} = 1 + \frac{2}{a \cdot L_r \cdot \left(\coth \left(\lambda \cdot \frac{L_r}{2} \right) + \frac{a \cdot \coth \left(\gamma \cdot \frac{L_r}{2} \right)}{\gamma} - \frac{2 \cdot a}{L_r \cdot \gamma^2} \right)},$ $a = \frac{\pi}{\tau_p}, \lambda = \sqrt{j \cdot \omega_r \cdot \mu \cdot \sigma}, \gamma = \sqrt{a^2 + \frac{\lambda}{l_{\text{gap}} \cdot \mu_r}}$	$\sigma_{\text{Corr}} = k_{\text{Yee}} \cdot \sigma$	[7]
Russell's end-effect correction factor for a solid rotor	$k_{\text{Russell}} = 1 - \frac{2\tau_p}{\pi L_r} \tanh \left(\frac{\pi L_r}{2\tau_p} \right)$	$\sigma_{\text{Corr}} = k_{\text{Russell}} \cdot \sigma$	[10]
Modified Russell's end-effect correction factor for a solid rotor	$k_{\text{Russell,M}} = 1 - \frac{\tau_p}{\pi l_s} \frac{\tanh \left(\frac{\pi l_s}{\tau_p} \right)}{\left(1 + \tanh \left(\frac{\pi l_s}{\tau_p} \right) \tanh \left(\frac{\pi l_{\text{end}}}{\tau_p} \right) \right)}$	$\sigma_{\text{Corr}} = k_{\text{Russell,M}} \cdot \sigma$	[109]
End-effect correction factor for a solid smooth rotor with a copper coating	$k_z = 1 + \frac{2\tau_p}{\pi L}$	$\sigma_{\text{Corr}} = \frac{1}{k_z^2} \cdot \sigma$	[23]

Description	End-effect factor formula	Conductivity correction	Reference
Russell-Northworthy's correction end-effect factor for a copper coating of a smooth solid rotor	$k_{RN} = 1 - \frac{\tanh(0.5\beta_\nu L)}{0.5\beta_\nu L [1 + k_t \tanh(0.5\beta_\nu L) \tanh(\beta_\nu w_{ov})]},$ $k_t = 1 + \frac{1.2(t_{ov} - d_{Cu})}{d_{Cu}}, \quad \beta_\nu = \nu \frac{\pi}{\tau_p}$	$\sigma_{Corr} = k_{RN} \cdot \sigma$	[23]
End-effect correction factor for a solid rotor with a high-conductive end rings	$k_e = 1 + C \cdot (\alpha - 1), \quad \alpha = \frac{1}{k_{Russell}} = \frac{1}{1 - \frac{2\tau_p}{\pi L} \tanh\left(\frac{\pi L}{2\tau_p}\right)}$	$\sigma_{Corr} = k_e \cdot \sigma$	[22], [29]
End-effect correction factor for a solid rotor with a radial grooves	$k_{R,\nu=1} = 1 - \frac{2 \cdot \tau_p}{\pi \cdot l_{Fe\nu}} \tanh\left(\frac{\pi \cdot l_{Fe\nu}}{2 \cdot \tau_p}\right),$ $k_{R,\nu} = 1 - \frac{2 \cdot \tau_{p\nu}}{\pi \cdot l_{Fe\nu}} \tanh\left(\frac{\pi \cdot l_{Fe\nu}}{2 \cdot \tau_{p\nu}}\right),$ $\tau_{p\nu} = \frac{\tau_p}{\nu_{ave}}, \quad k_{R,eq} = \frac{k_{R,\nu=1} + k_{R,\nu}}{2}$	$\sigma_{Corr} = k_{R,eq} \cdot \sigma$	[22], [43]

Tabel A2: Overview of all slip correction factors for a solid rotor

Description	Slip correction end-effect factor formula	Total correction factor	Reference
Slip correction end-effect factor by Aho	$k_{\text{Aho}} = \left(\frac{n}{n_s}\right)^4$	$k_{\text{tot}} = k \cdot k_{\text{Aho}}$	[108]
Slip correction end-effect factor by Pyrhonen, Aho, Nerg	$k_{\text{PAN}} = 1 - c \cdot \omega_r^{\frac{3}{4}}$	$k_{\text{tot}} = k \cdot k_{\text{PAN}}$	[109]

Appendix B - Material data for stator sheet

Typical data for SURA® M470-50A

T	W/kg at 50 Hz	VA/kg at 50 Hz	A/m at 50 Hz	W/kg at 100 Hz	W/kg at 200 Hz	W/kg at 400 Hz
0,1	0,03	0,10	52	0,13	0,19	0,52
0,2	0,12	0,28	68	0,42	0,76	1,98
0,3	0,25	0,49	77	0,78	1,58	4,16
0,4	0,42	0,72	84	1,21	2,62	6,90
0,5	0,61	0,98	91	1,71	3,86	10,3
0,6	0,82	1,27	98	2,26	5,29	14,3
0,7	1,05	1,59	106	2,86	6,94	19,2
0,8	1,30	1,94	114	3,59	8,86	25,2
0,9	1,57	2,34	124	4,30	11,2	32,3
1,0	1,87	2,79	136	5,22	13,7	40,6
1,1	2,21	3,34	152	6,04	16,6	50,4
1,2	2,59	4,02	178	7,29	19,9	61,7
1,3	3,01	4,97	224	8,32	23,7	74,6
1,4	3,53	6,65	326	9,72	28,1	89,9
1,5	4,13	11,2	630	11,4	32,7	105
1,6	4,78	27,6	1612			
1,7	5,39	74,2	3963			
1,8	5,82	163	7773			

Loss at 1.5 T , 50 Hz, W/kg	4,13
Loss at 1.0 T , 50 Hz, W/kg	1,87
Anisotropy of loss, %	6
Magnetic polarization at 50 Hz	
H = 2500 A/m, T	1,63
H = 5000 A/m, T	1,71
H = 10000 A/m, T	1,83
Coercivity (DC), A/m	85
Relative permeability at 1.5 T	1600
Resistivity, $\mu\Omega\text{cm}$	33
Yield strength, N/mm ²	250
Tensile strength, N/mm ²	390
Young's modulus, RD, N/mm ²	210000
Young's modulus, TD, N/mm ²	220000
Hardness HV5 (VPN)	120

RD represents the rolling direction
 TD represents the transverse direction
 Values for yield strength (0.2 % proof strength)
 and tensile strength are given for the rolling direction
 Values for the transverse direction are approximately 5% higher



October 2008

Fig. B1: Typical material data for M470-50A.

Appendix C - The rest of the results from the sensitivity analysis simulations of the case study machine

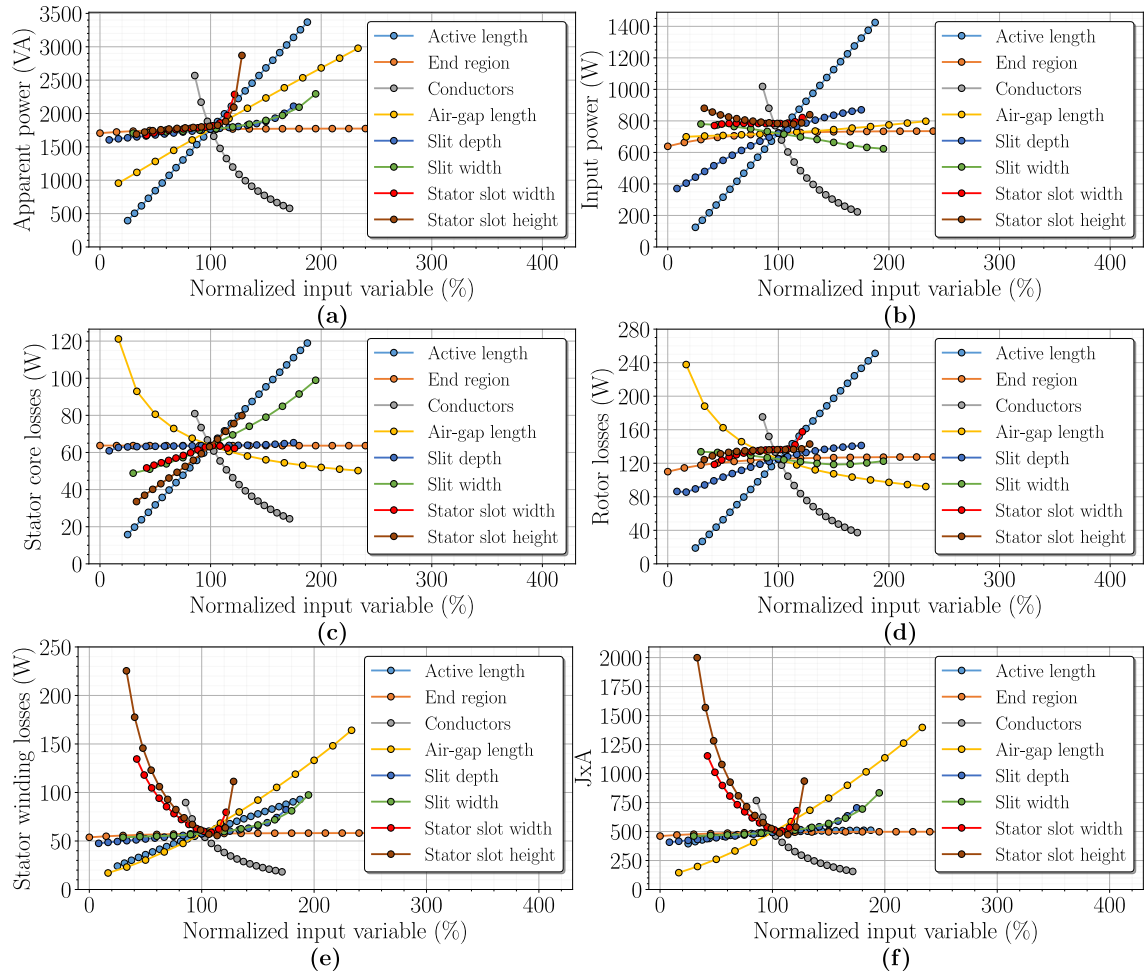


Fig. C1: Rest of the results of sensitivity analysis for the function of: Apparent power (a), Input power (b), Stator core losses (c), Rotor losses (d), Stator winding losses (e), and product of current density and linear current density of the stator slot (f) on normalized value of input variable.

Appendix D - The rest of the results from the initial optimization of the case study machine in Optimizer

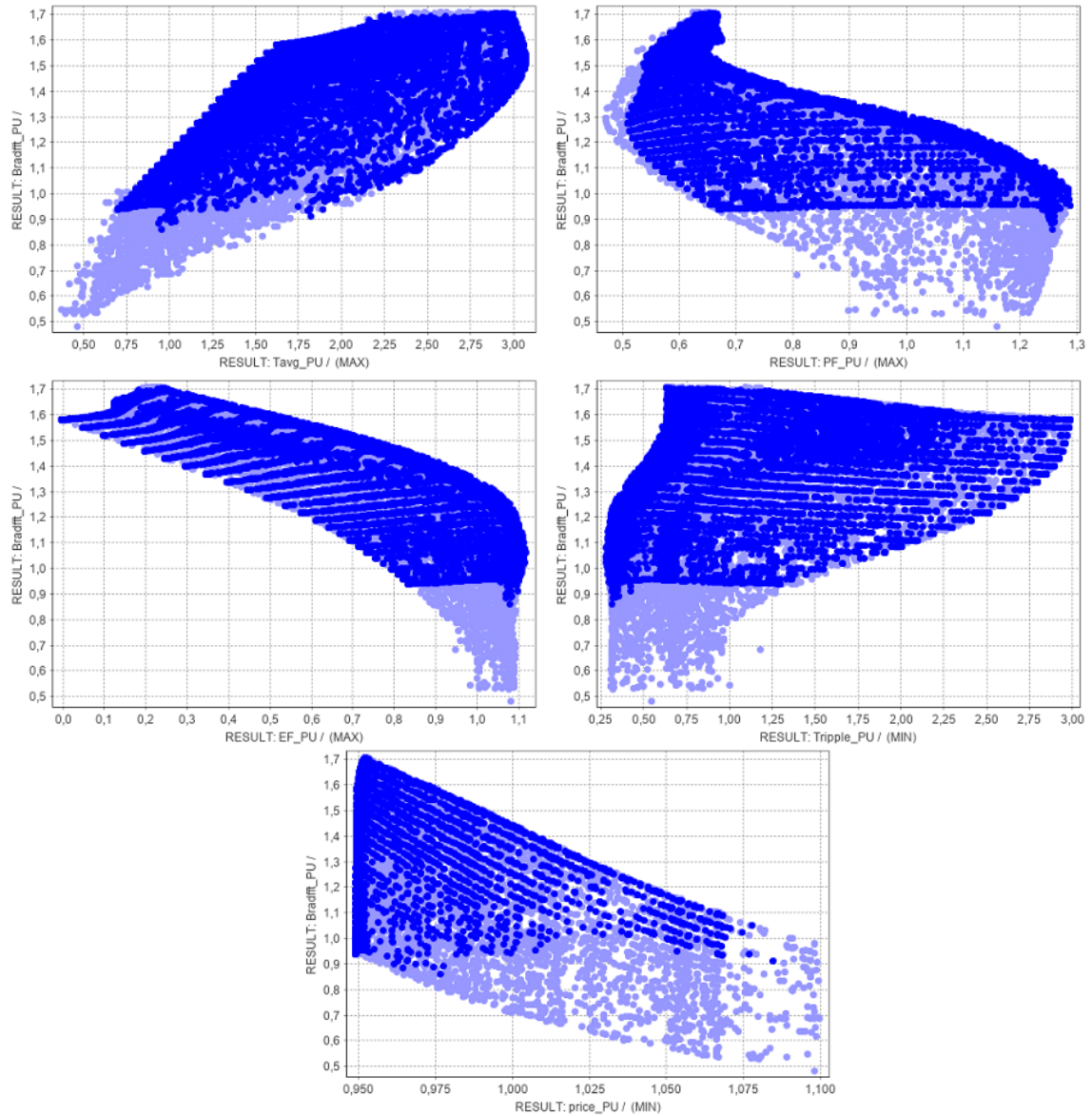


Fig. D1: The flux density in the air-gap as a function of other output parameters in the initial optimization results of the machine without any constraints in Optimizer, displayed in per unit system.

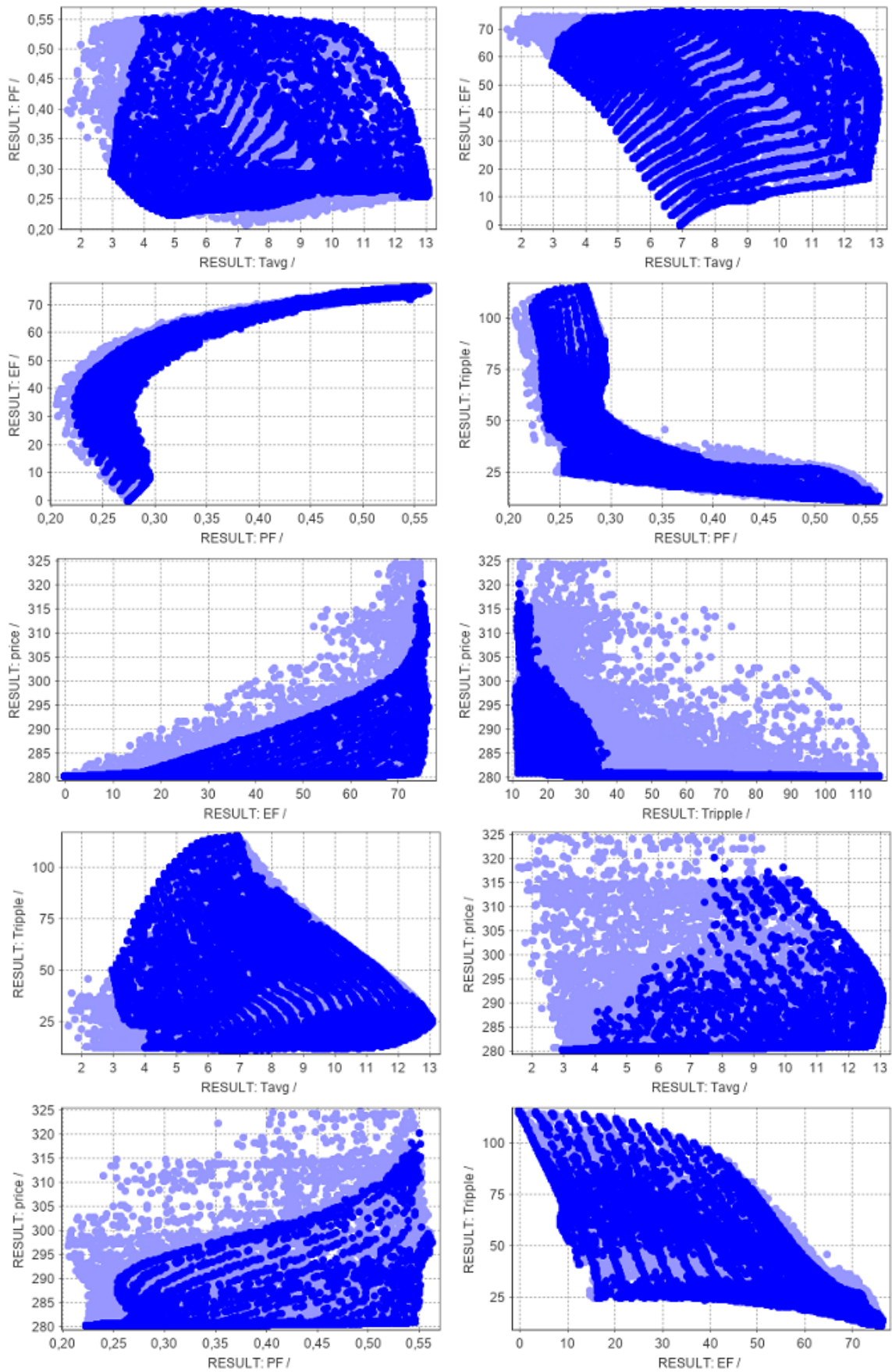


Fig. D2: Initial optimization results for the main optimization objectives of the case study machine without any constraints in Optimizer.

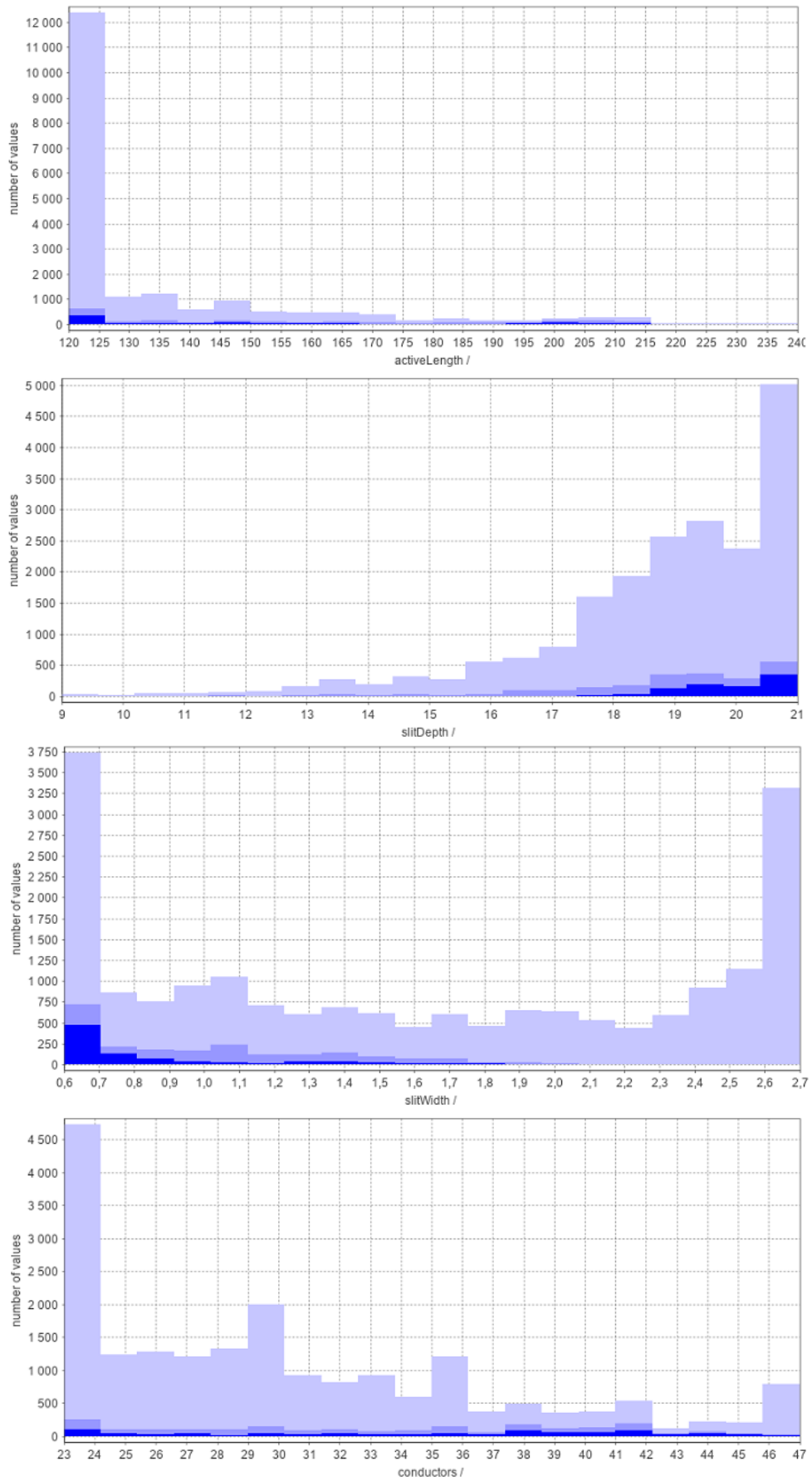


Fig. D3: Distribution of input parameters and their number of uses in the Optimizer in the initial optimization with defined constrains.

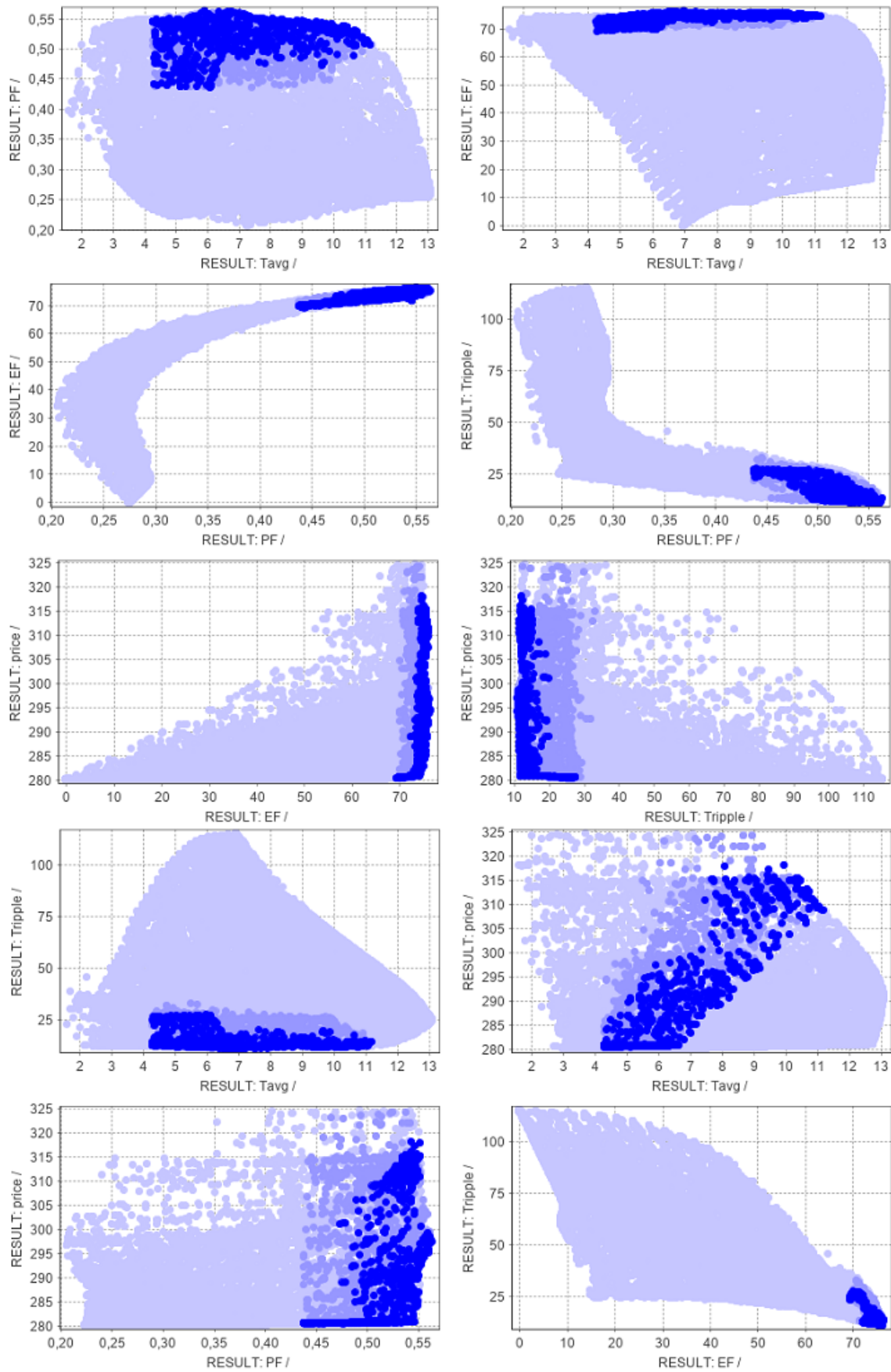


Fig. D4: Initial optimization results for the main optimization objectives of the case study machine with defined constraints in Optimizer.

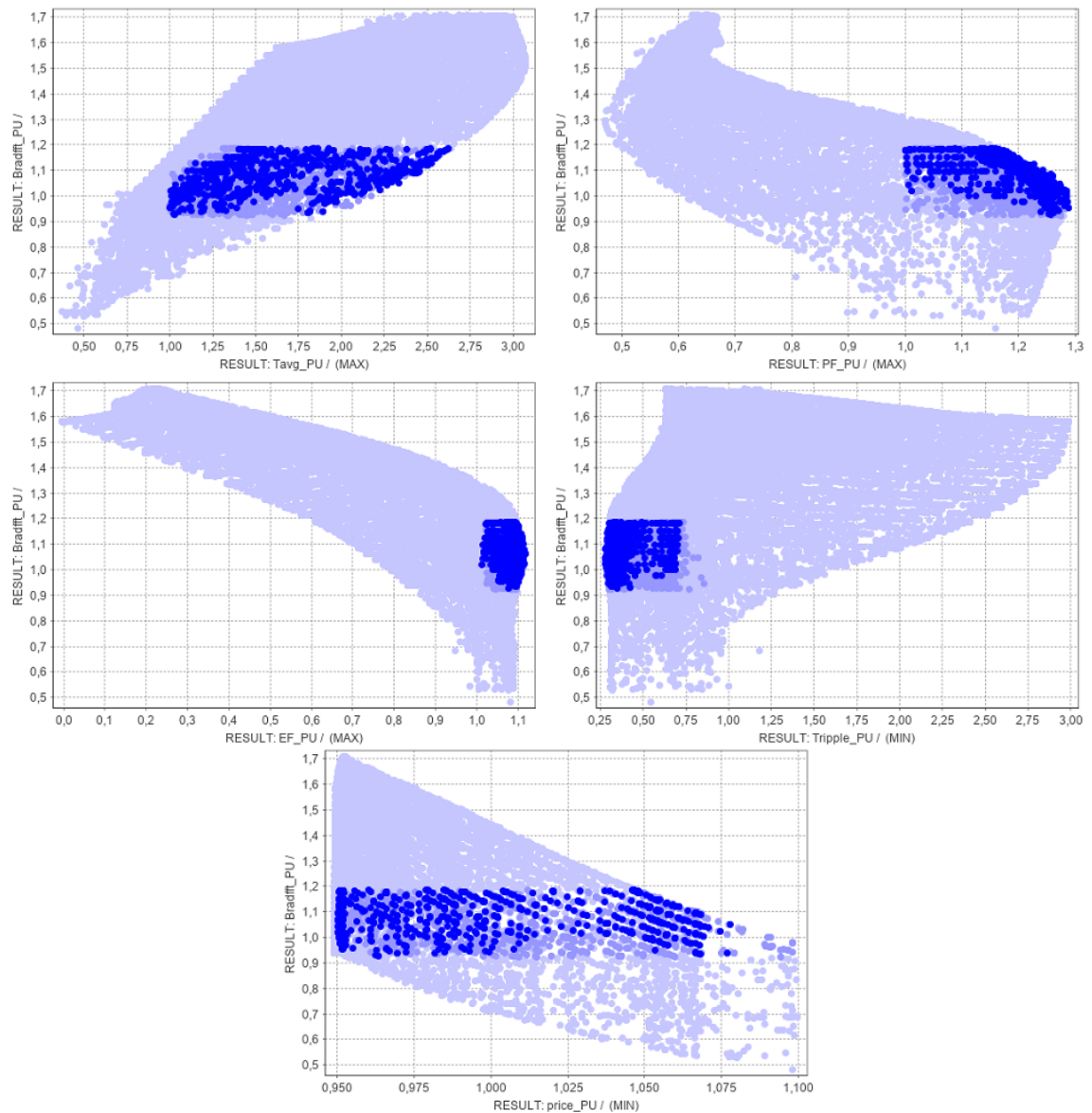


Fig. D5: The flux density in the air-gap as a function of other output parameters in the initial optimization results of the machine with defined constraints in Optimizer, displayed in per unit system.

Appendix E - The rest of the results from the second optimization of the case study machine in Optimizer

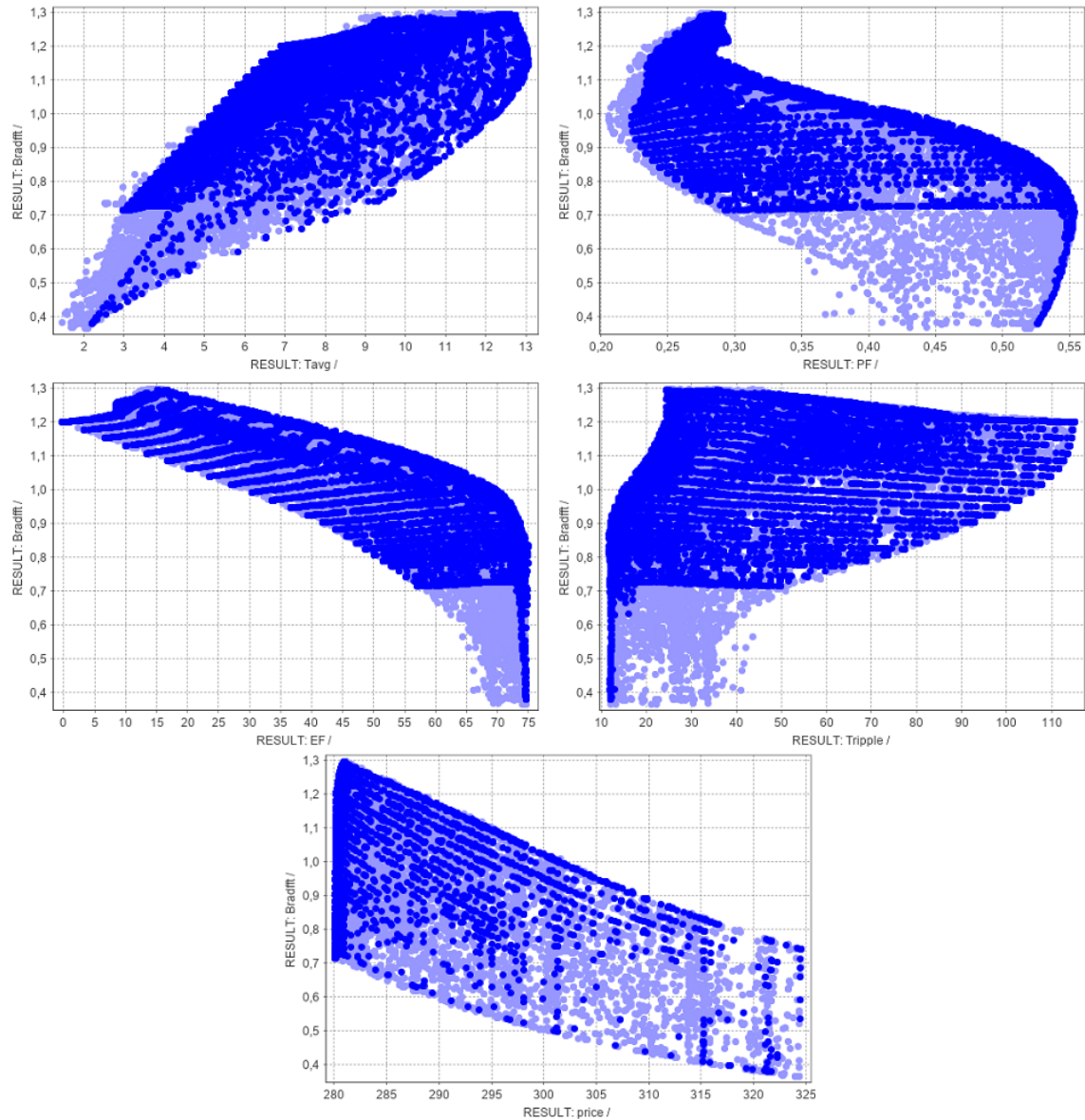


Fig. E1: The flux density in the air-gap as a function of other output parameters in the second optimization results of the machine without any constraints in Optimizer.

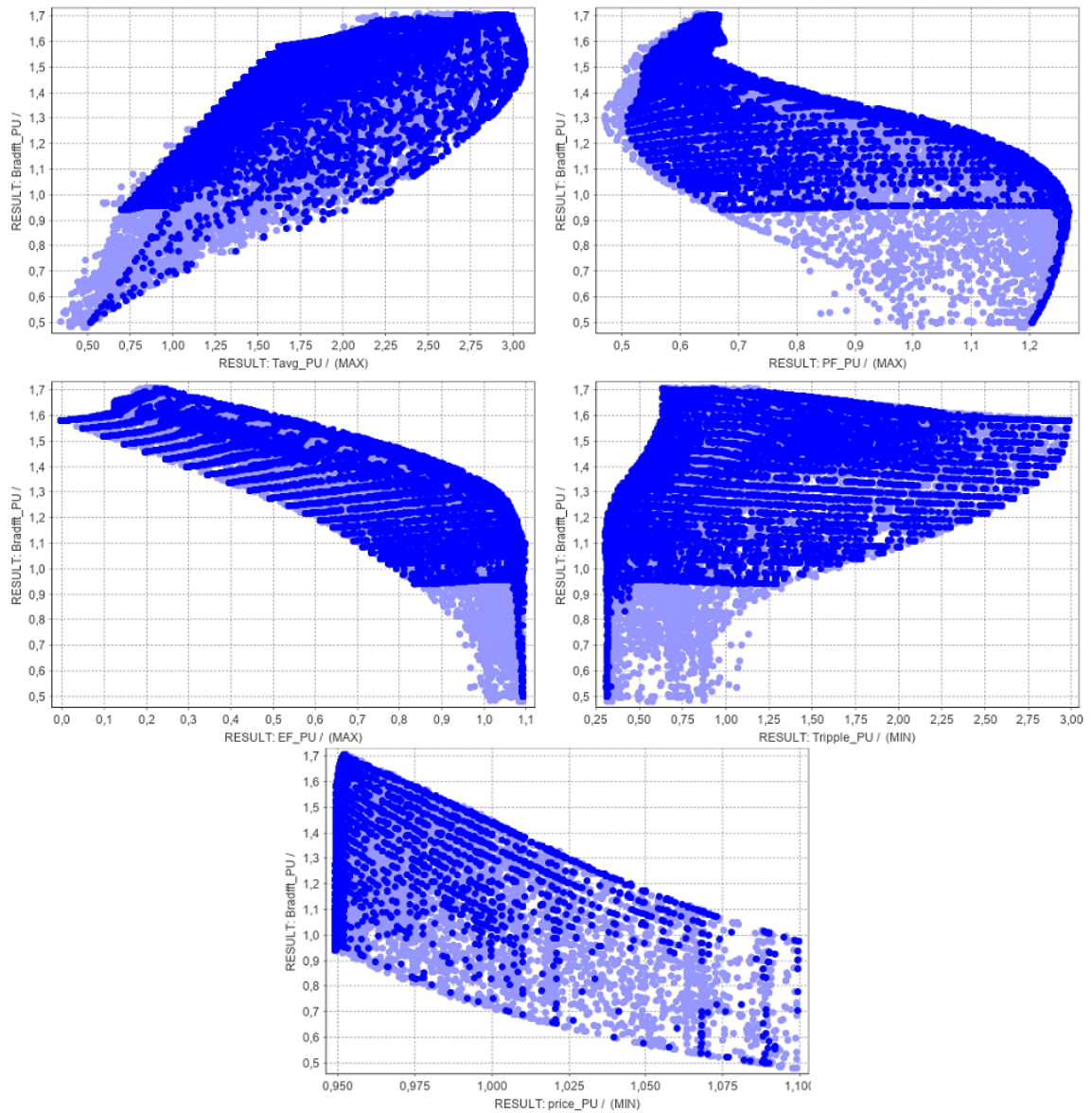


Fig. E2: The flux density in the air-gap as a function of other output parameters in the second optimization results of the machine without any constraints in Optimizer, displayed in per unit system.

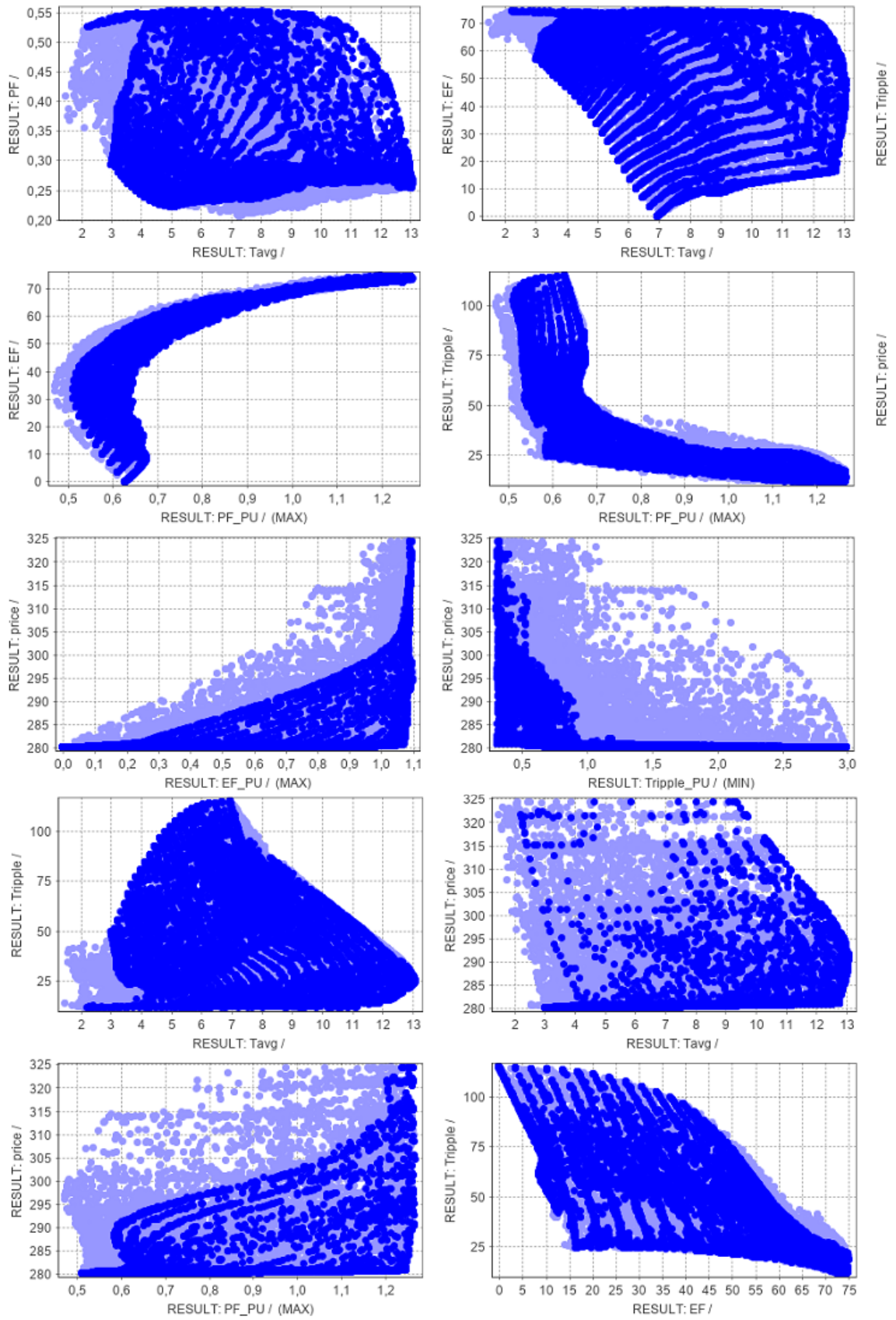


Fig. E3: Second optimization results for the main optimization objectives of the case study machine without any constraints in Optimizer.

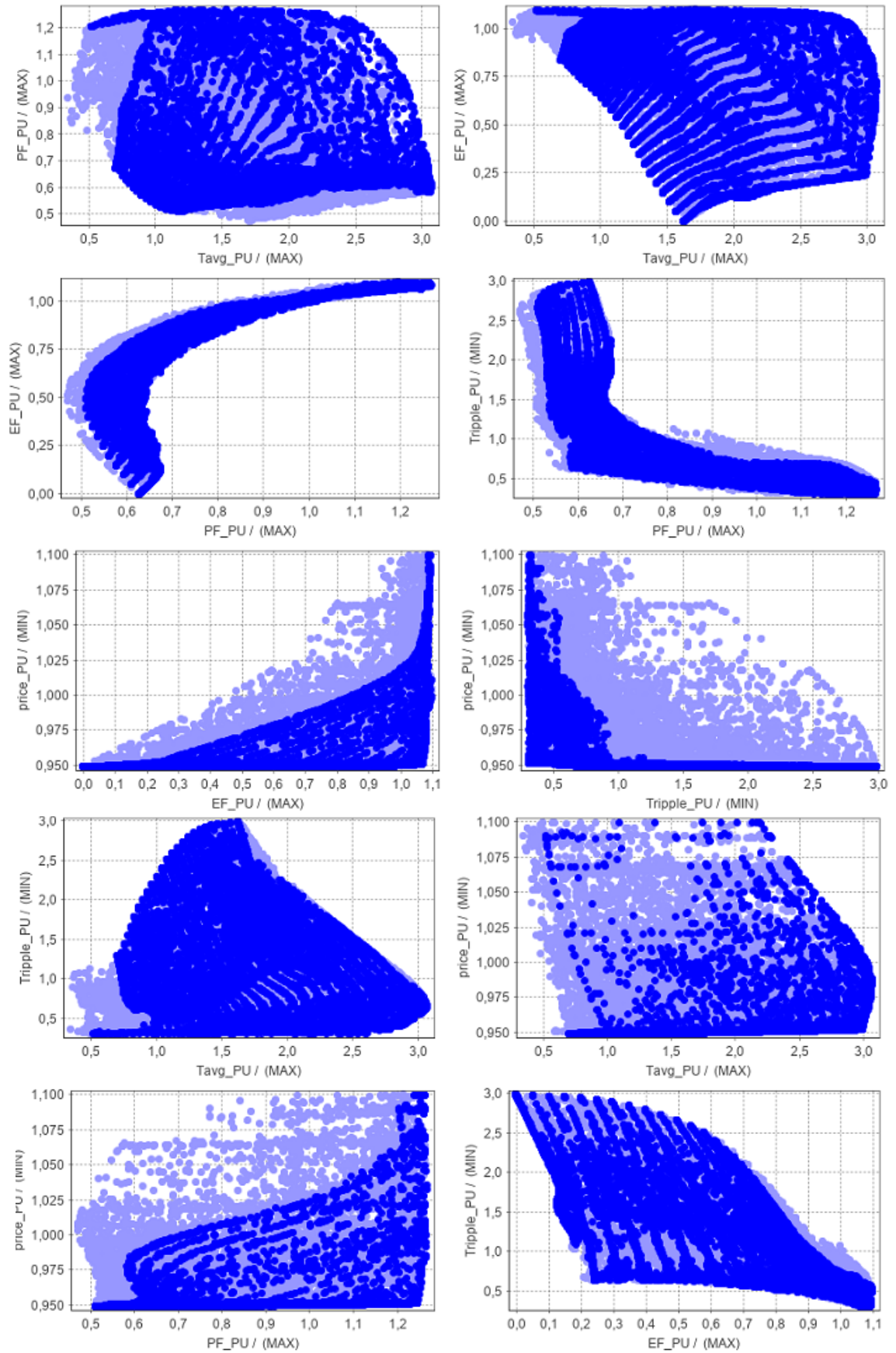


Fig. E4: Second optimization results for the main optimization objectives of the case study machine without any constraints in Optimizer, displayed in per unit system.

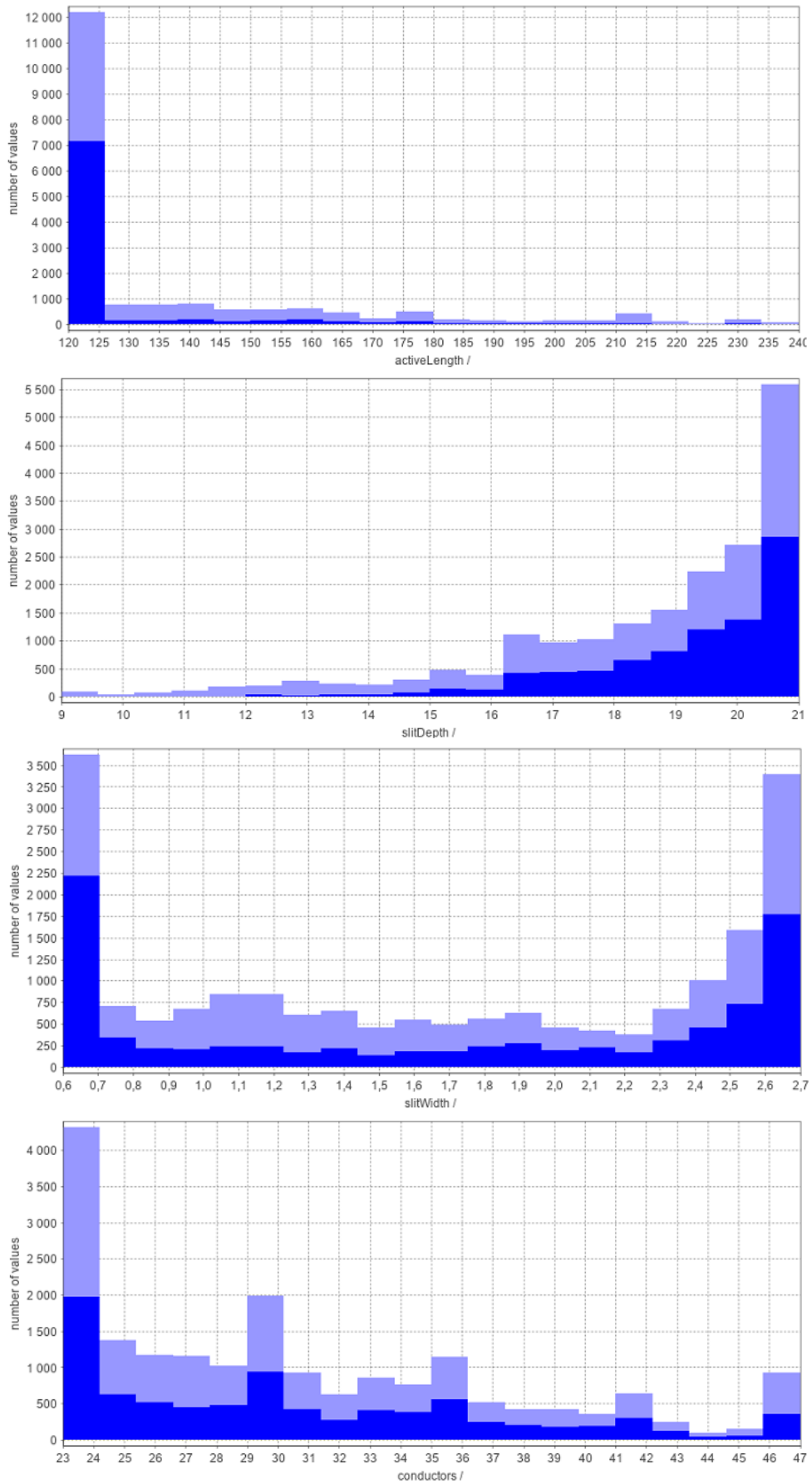


Fig. E5: Distribution of input parameters and their number of uses in the Optimizer in the second optimization without any constrains.

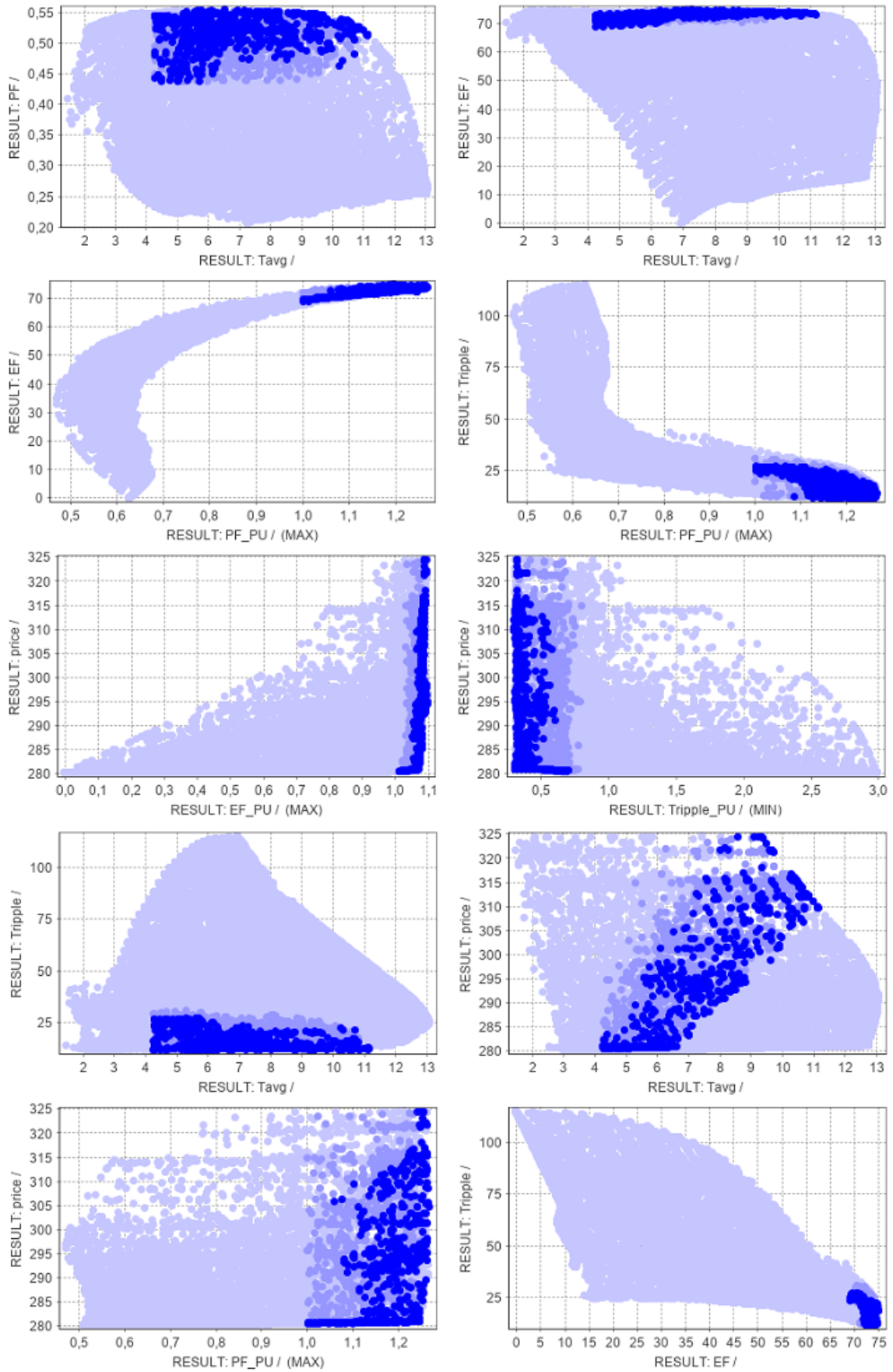


Fig. E6: Second optimization results for the main optimization objectives of the case study machine with defined constraints in Optimizer.

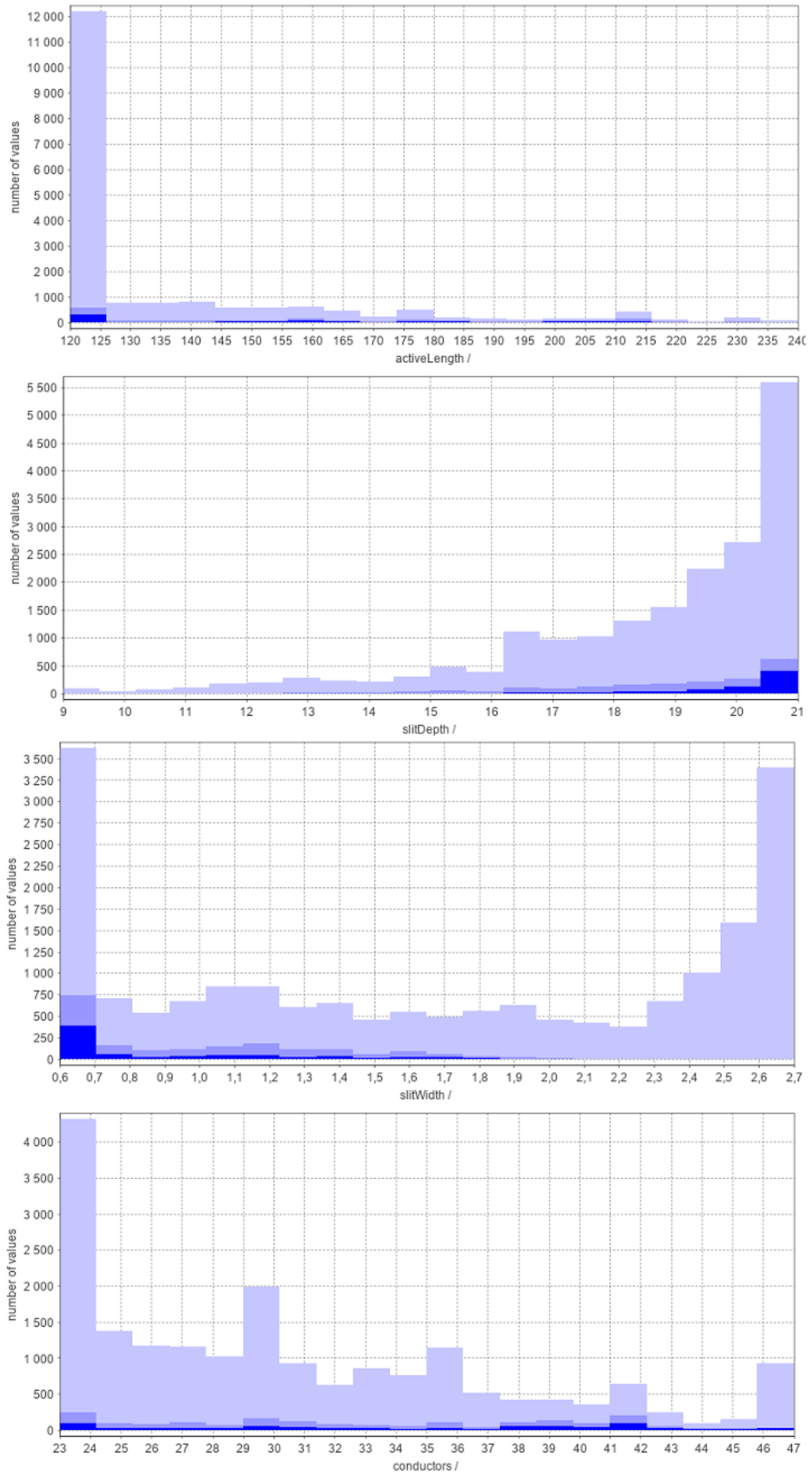


Fig. E7: Distribution of input parameters and their number of uses in the Optimizer in the second optimization with defined constrains.

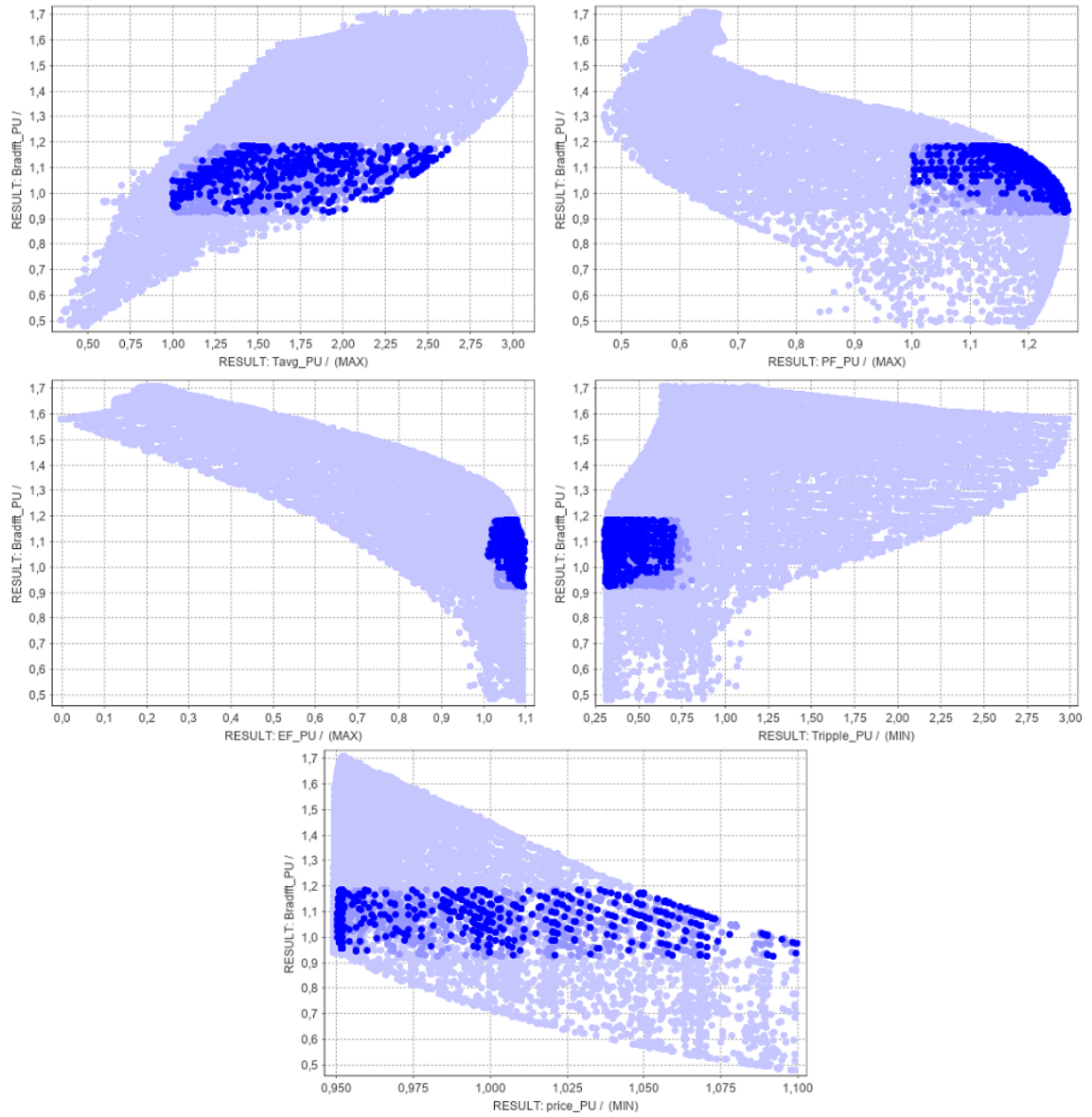


Fig. E8: The flux density in the air-gap as a function of other output parameters in the second optimization results of the machine with defined constraints in Optimizer, displayed in per unit system.

Appendix F - All data used to determine the accuracy of surrogate models after the initial optimization in Optimizer

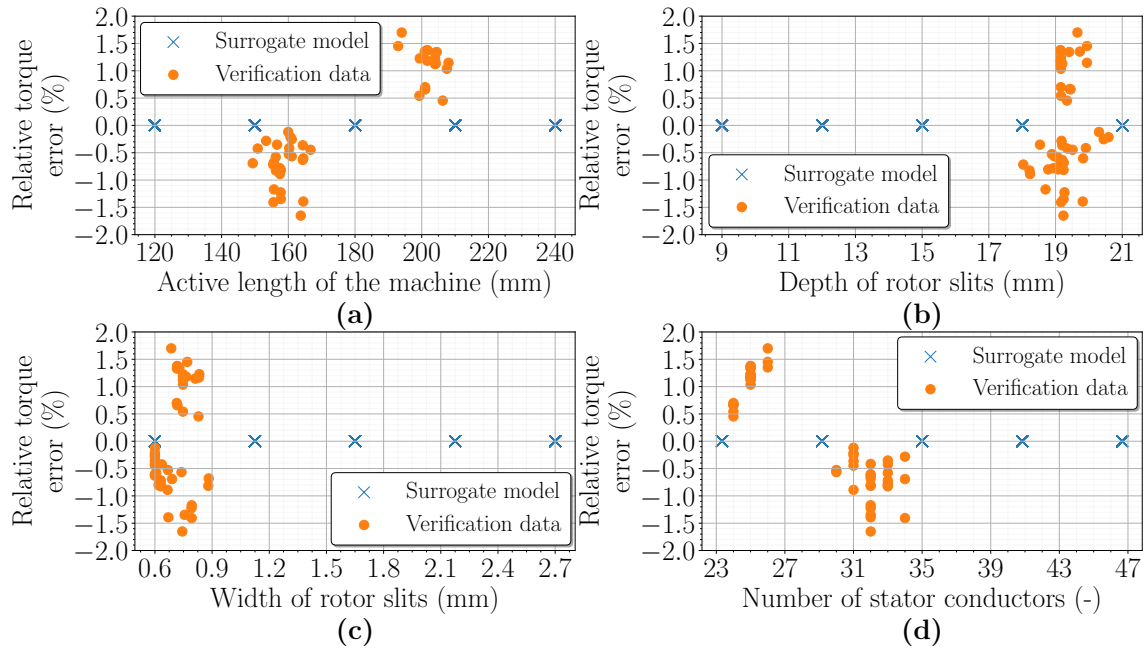


Fig. F1: Dependence of the relative torque error of surrogate models on the input parameter size: Active length of the machine (a), Rotor slit depth (b), Rotor slit width (c), and Number of stator conductors (d), considering the highest possible electromagnetic efficiency of the machine from the initial optimization.

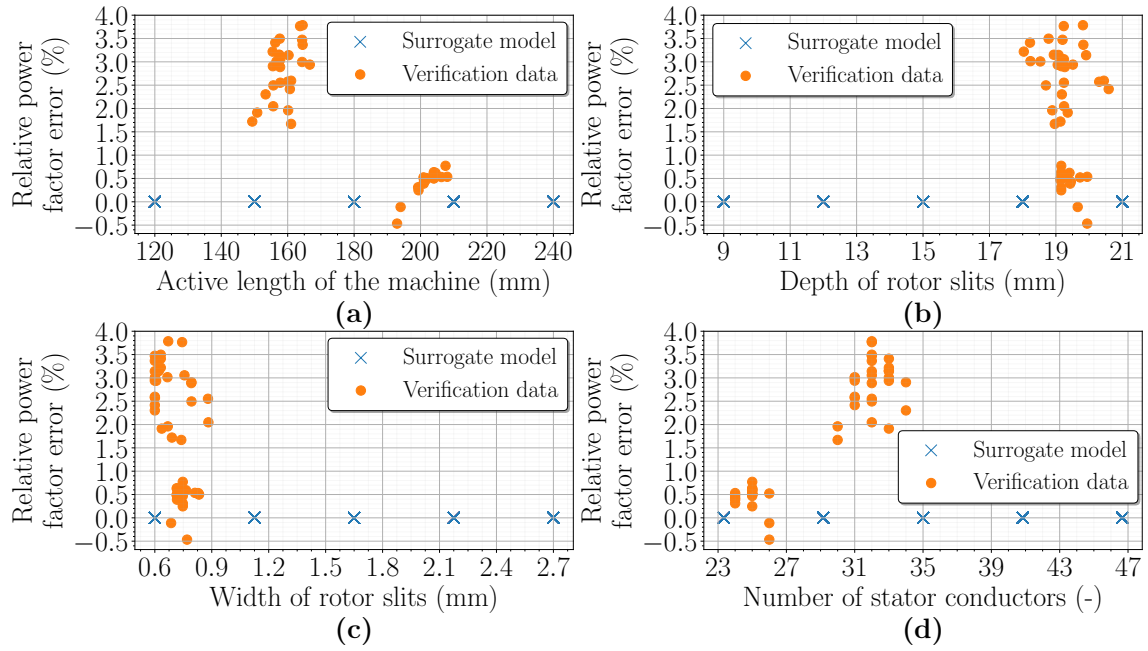


Fig. F2: Dependence of the relative power factor error of surrogate models on the input parameter size: Active length of the machine (a), Rotor slit depth (b), Rotor slit width (c), and Number of stator conductors (d), considering the highest possible electromagnetic efficiency of the machine from the initial optimization.

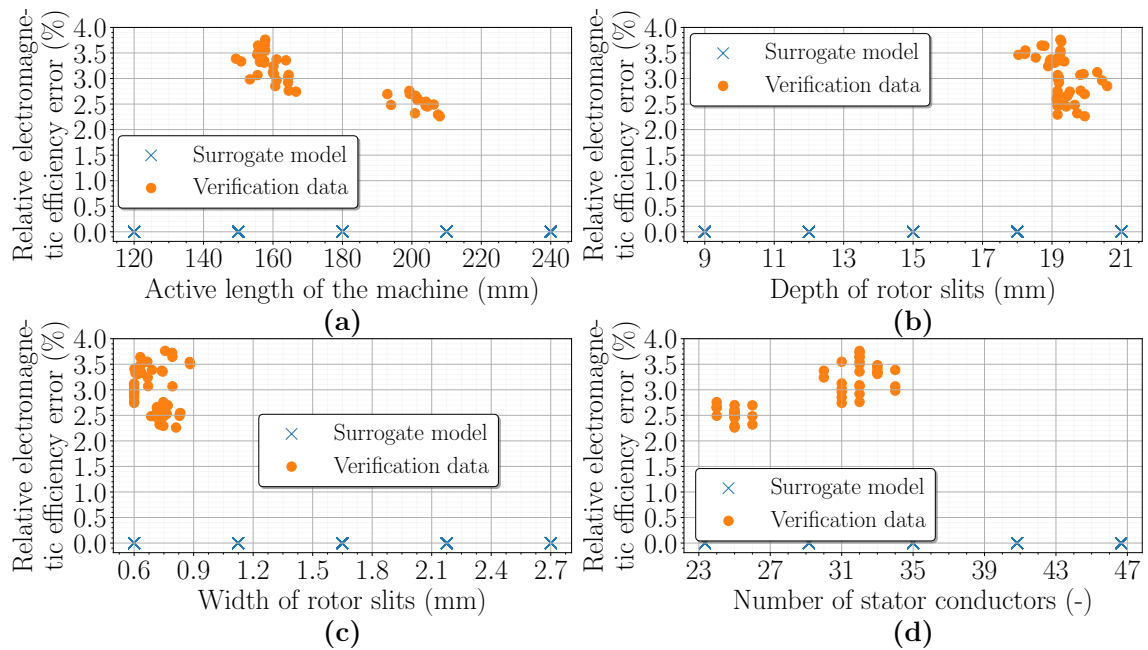


Fig. F3: Dependence of the relative electromagnetic efficiency error of surrogate models on the input parameter size: Active length of the machine (a), Rotor slit depth (b), Rotor slit width (c), and Number of stator conductors (d), considering the highest possible electromagnetic efficiency of the machine from the initial optimization.

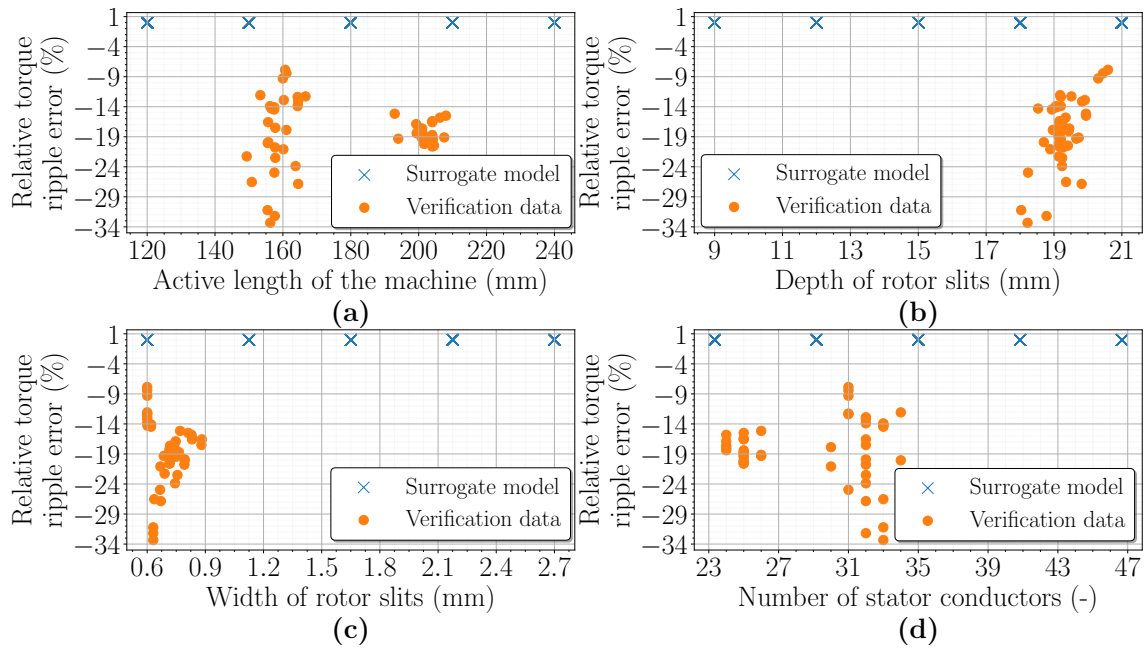


Fig. F4: Dependence of the relative torque ripple error of surrogate models on the input parameter size: Active length of the machine (a), Rotor slit depth (b), Rotor slit width (c), and Number of stator conductors (d), considering the highest possible electromagnetic efficiency of the machine from the initial optimization.

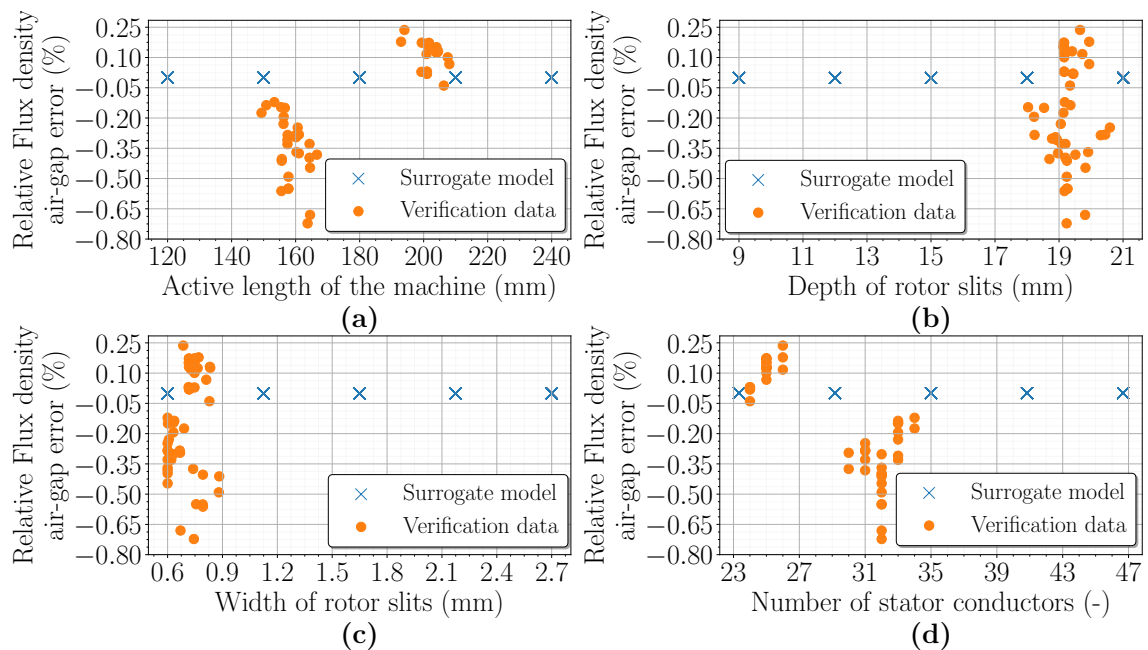


Fig. F5: Dependence of the relative flux density in the air-gap error of surrogate models on the input parameter size: Active length of the machine (a), Rotor slit depth (b), Rotor slit width (c), and Number of stator conductors (d), considering the highest possible electromagnetic efficiency of the machine from the initial optimization.

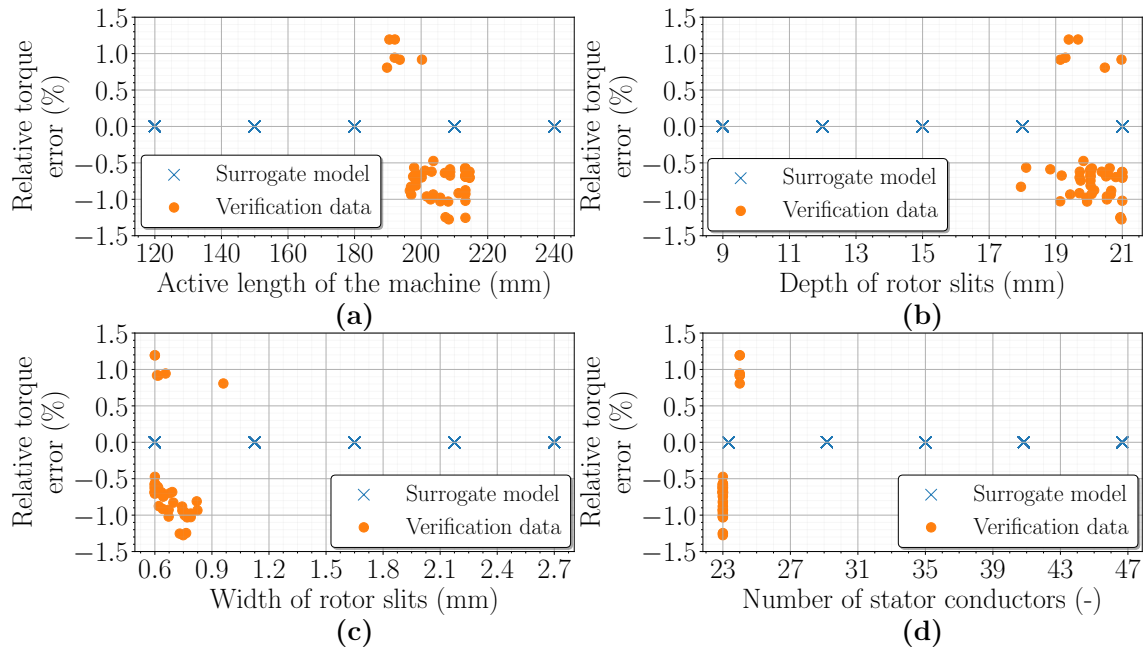


Fig. F6: Dependence of the relative torque error of surrogate models on the input parameter size: Active length of the machine (a), Rotor slit depth (b), Rotor slit width (c), and Number of stator conductors (d), considering the highest possible torque of the machine from the initial optimization.

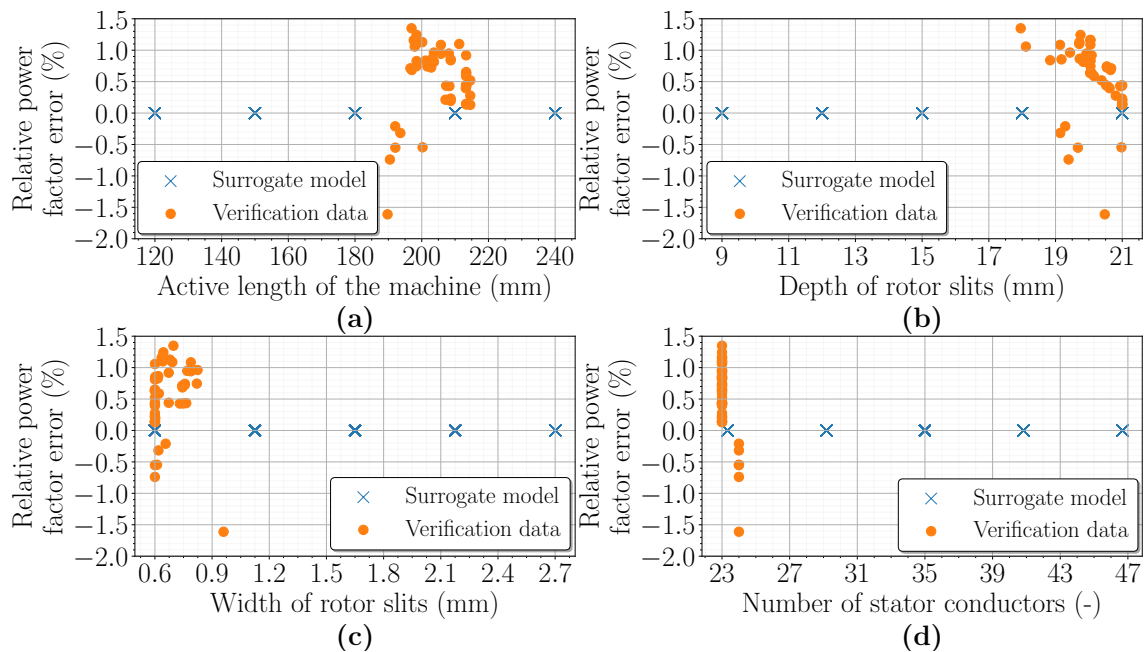


Fig. F7: Dependence of the relative power factor error of surrogate models on the input parameter size: Active length of the machine (a), Rotor slit depth (b), Rotor slit width (c), and Number of stator conductors (d), considering the highest possible torque of the machine from the initial optimization.

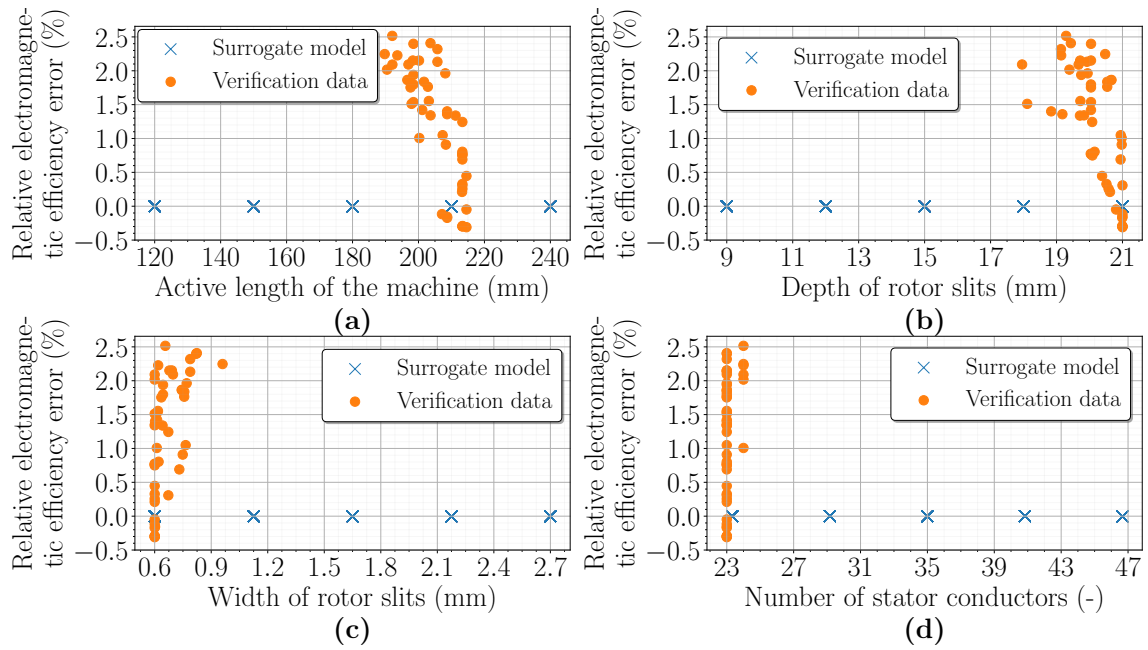


Fig. F8: Dependence of the relative electromagnetic efficiency error of surrogate models on the input parameter size: Active length of the machine (a), Rotor slit depth (b), Rotor slit width (c), and Number of stator conductors (d), considering the highest possible torque of the machine from the initial optimization.

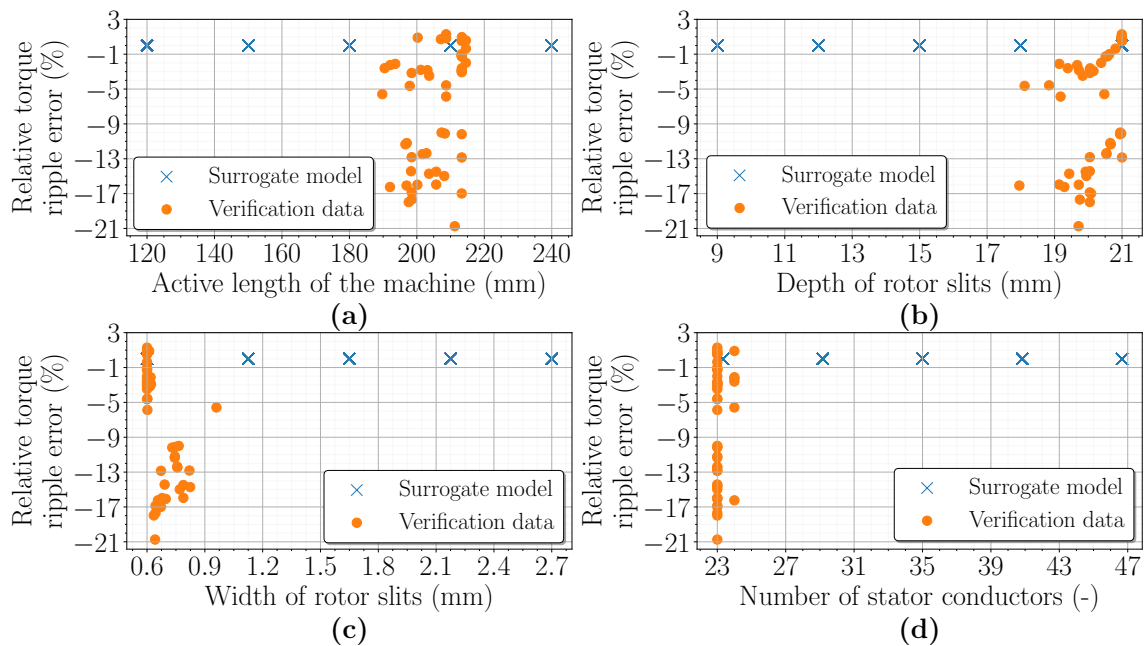


Fig. F9: Dependence of the relative torque ripple error of surrogate models on the input parameter size: Active length of the machine (a), Rotor slit depth (b), Rotor slit width (c), and Number of stator conductors (d), considering the highest possible torque of the machine from the initial optimization.

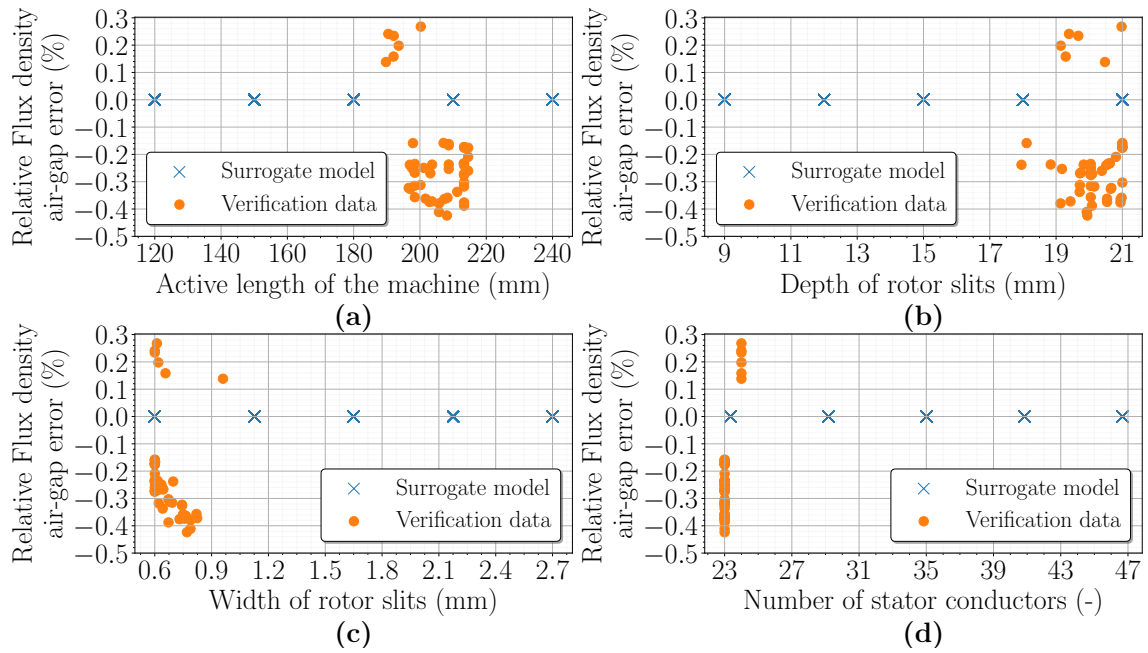


Fig. F10: Dependence of the relative flux density in the air-gap error of surrogate models on the input parameter size: Active length of the machine (a), Rotor slit depth (b), Rotor slit width (c), and Number of stator conductors (d), considering the highest possible torque of the machine from the initial optimization.

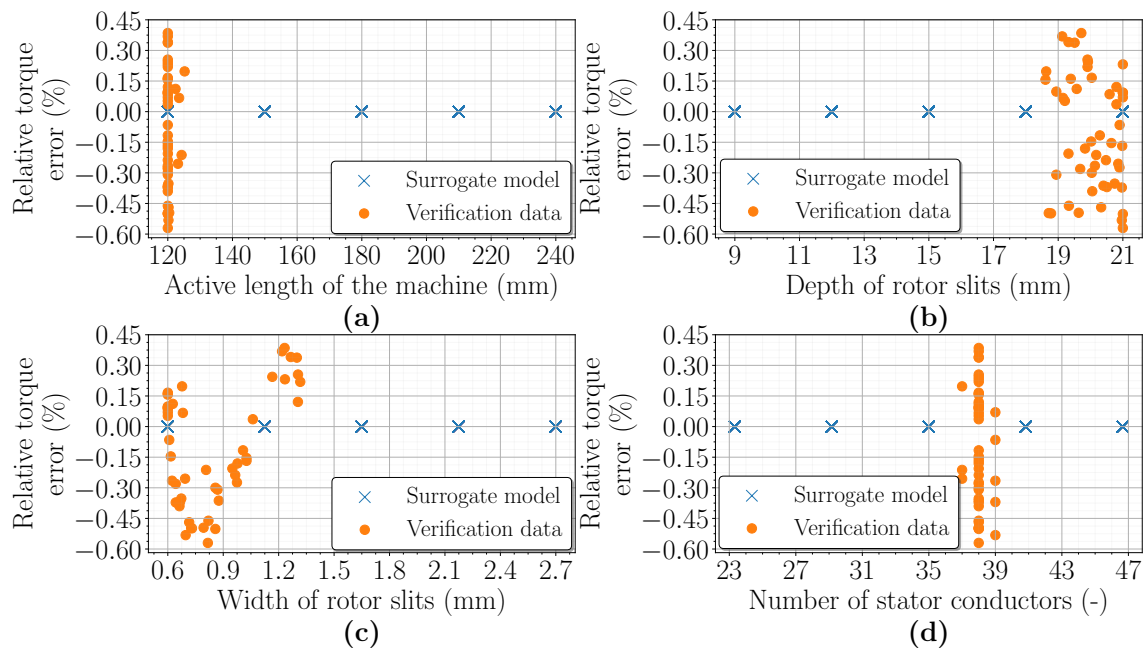


Fig. F11: Dependence of the relative torque error of surrogate models on the input parameter size: Active length of the machine (a), Rotor slit depth (b), Rotor slit width (c), and Number of stator conductors (d), considering the lowest price of the machine with respect to the highest torque of the machine from the initial optimization.

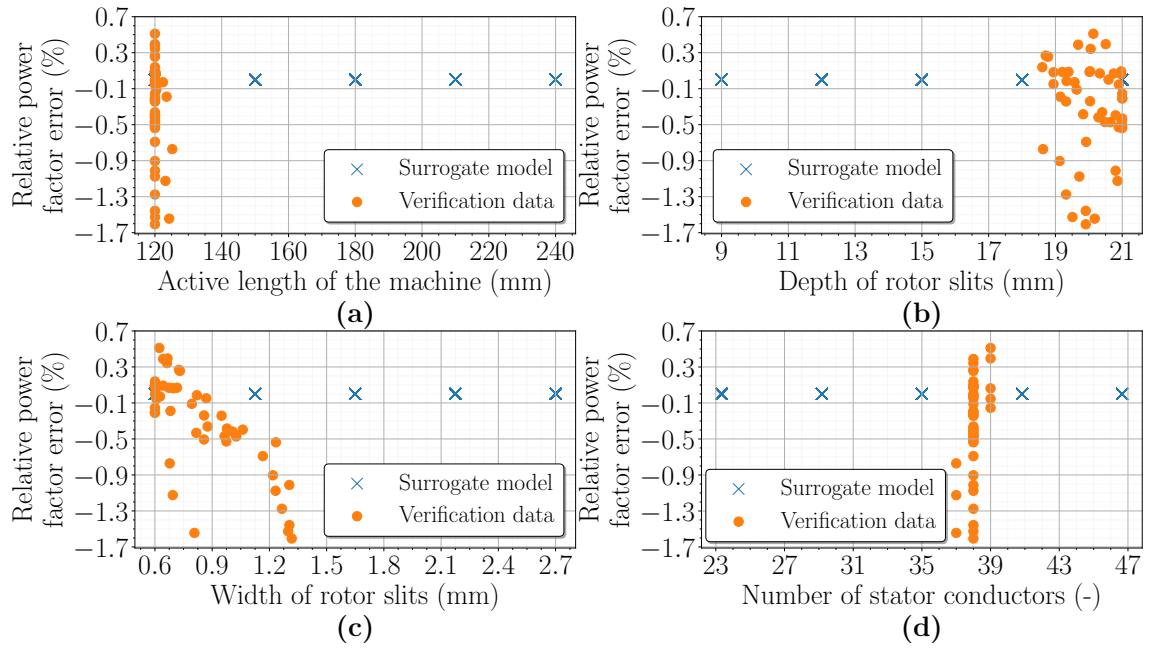


Fig. F12: Dependence of the relative power factor error of surrogate models on the input parameter size: Active length of the machine (a), Rotor slit depth (b), Rotor slit width (c), and Number of stator conductors (d), considering the lowest price of the machine with respect to the highest torque of the machine from the initial optimization.

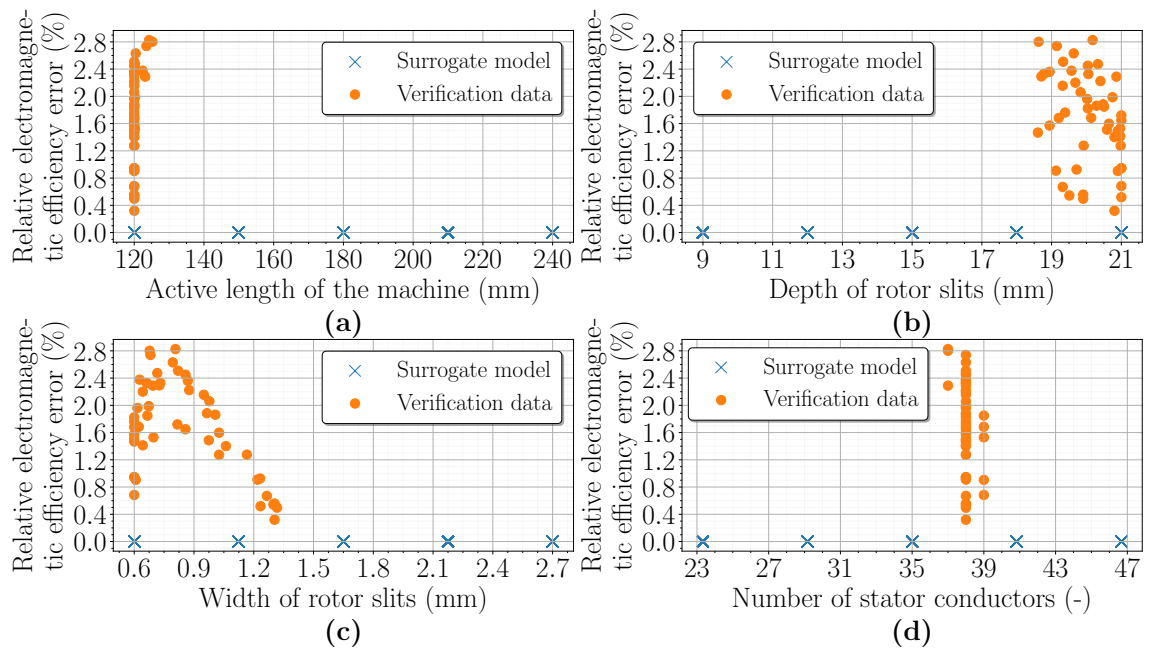


Fig. F13: Dependence of the relative efficiency error of surrogate models on the input parameter size: Active length of the machine (a), Rotor slit depth (b), Rotor slit width (c), and Number of stator conductors (d), considering the lowest price of the machine with respect to the highest torque of the machine from the initial optimization.

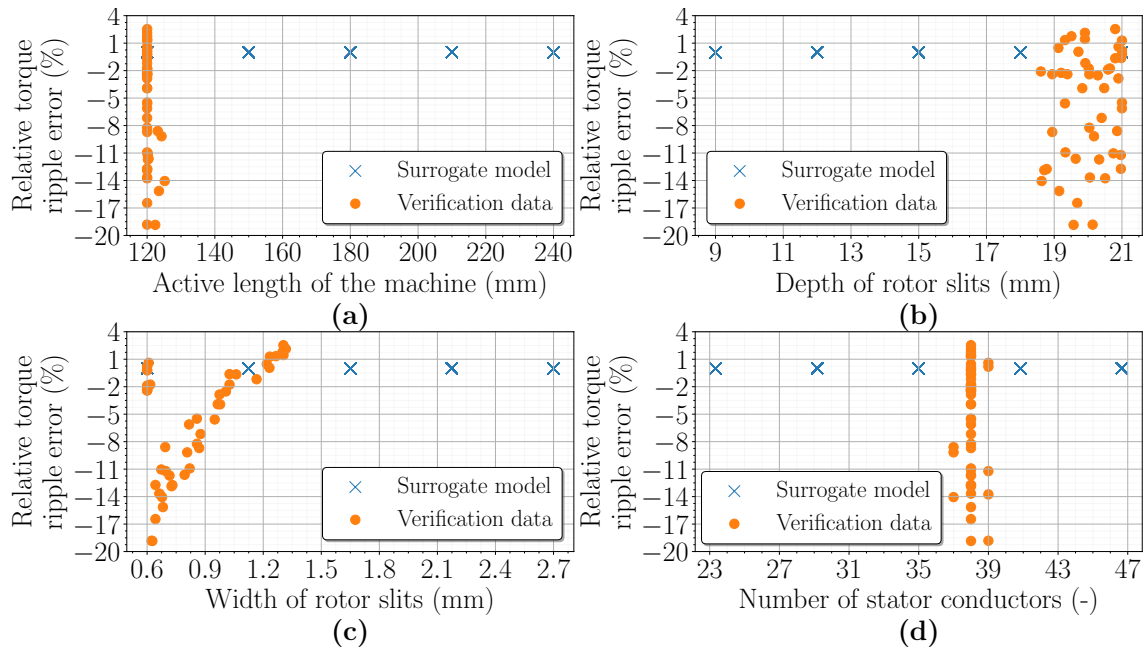


Fig. F14: Dependence of the relative torque ripple error of surrogate models on the input parameter size: Active length of the machine (a), Rotor slit depth (b), Rotor slit width (c), and Number of stator conductors (d), considering the lowest price of the machine with respect to the highest torque of the machine from the initial optimization.

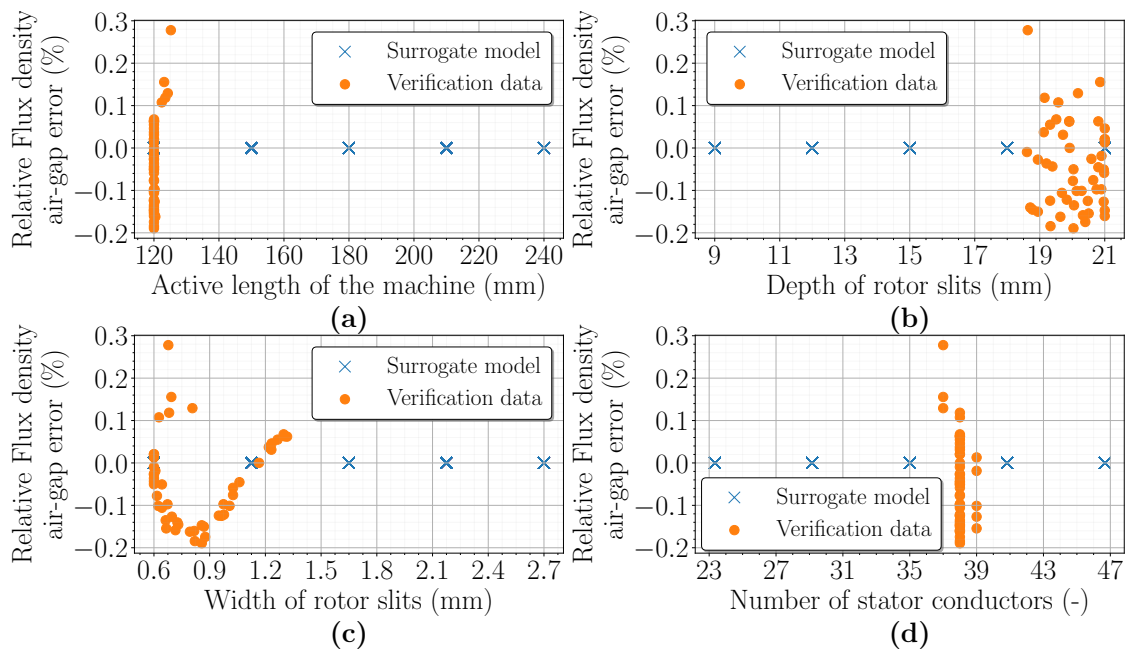


Fig. F15: Dependence of the relative flux density in the air-gap error of surrogate models on the input parameter size: Active length of the machine (a), Rotor slit depth (b), Rotor slit width (c), and Number of stator conductors (d), considering the lowest price of the machine with respect to the highest torque of the machine from the initial optimization.

Appendix G - All data used to determine the accuracy of surrogate models after the second optimization in Optimizer

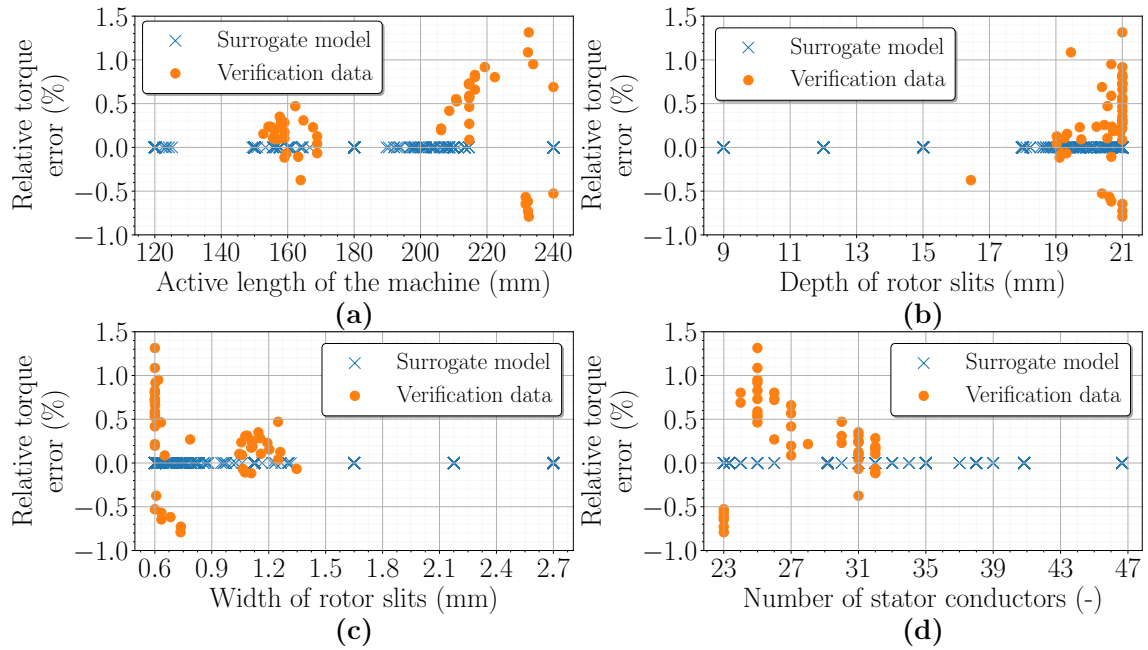


Fig. G1: Dependence of the relative torque error of surrogate models on the input parameter size: Active length of the machine (a), Rotor slit depth (b), Rotor slit width (c), and Number of stator conductors (d), considering the highest possible electromagnetic efficiency of the machine from the second optimization.

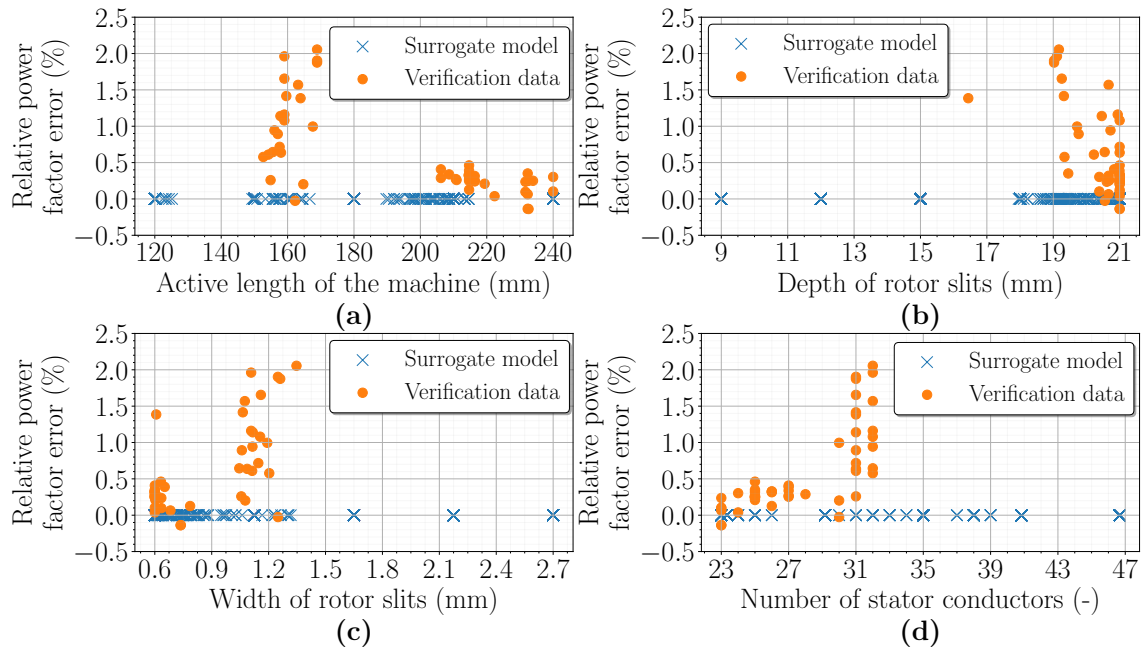


Fig. G2: Dependence of the relative power factor error of surrogate models on the input parameter size: Active length of the machine (a), Rotor slit depth (b), Rotor slit width (c), and Number of stator conductors (d), considering the highest possible electromagnetic efficiency of the machine from the second optimization.

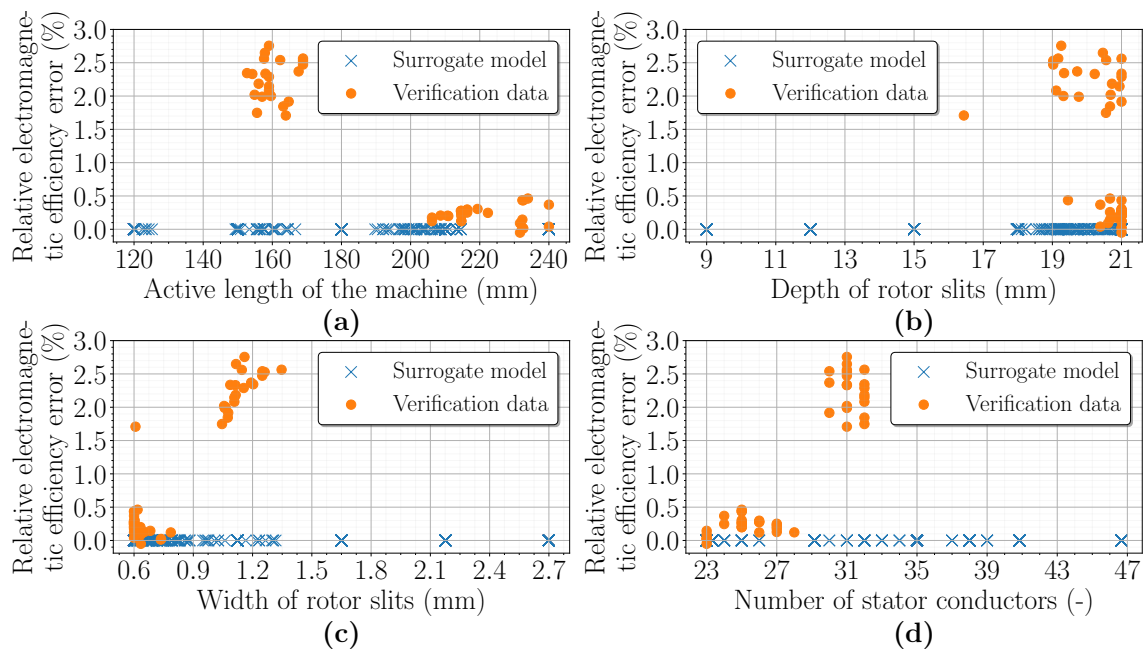


Fig. G3: Dependence of the relative electromagnetic efficiency error of surrogate models on the input parameter size: Active length of the machine (a), Rotor slit depth (b), Rotor slit width (c), and Number of stator conductors (d), considering the highest possible electromagnetic efficiency of the machine from the second optimization.

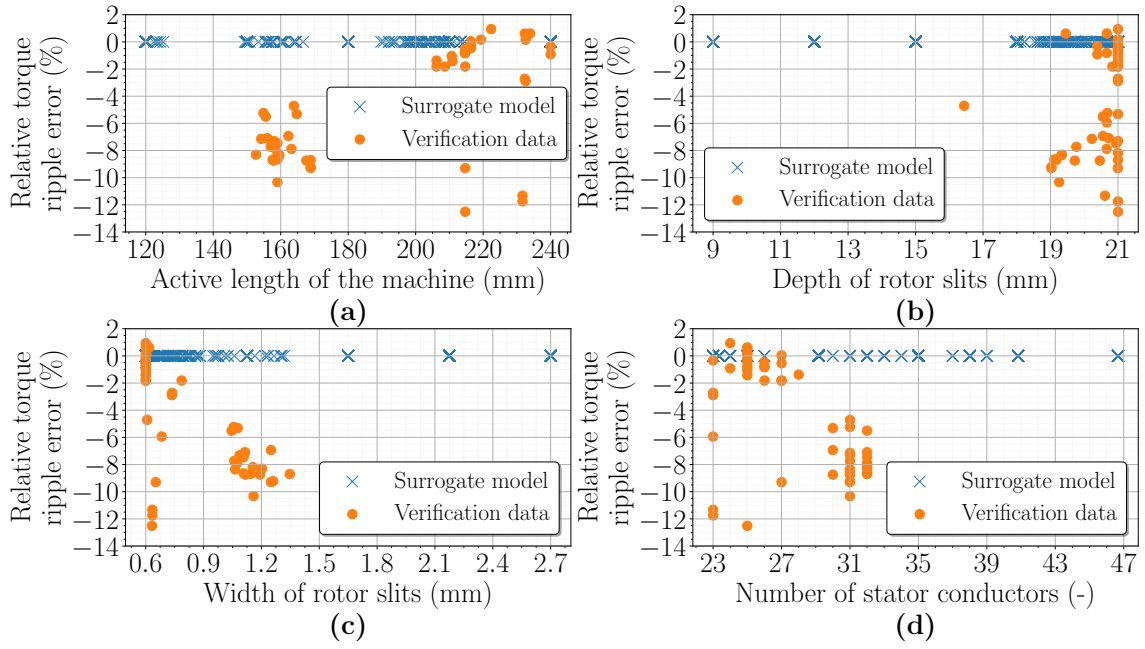


Fig. G4: Dependence of the relative torque ripple error of surrogate models on the input parameter size: Active length of the machine (a), Rotor slit depth (b), Rotor slit width (c), and Number of stator conductors (d), considering the highest possible electromagnetic efficiency of the machine from the second optimization.

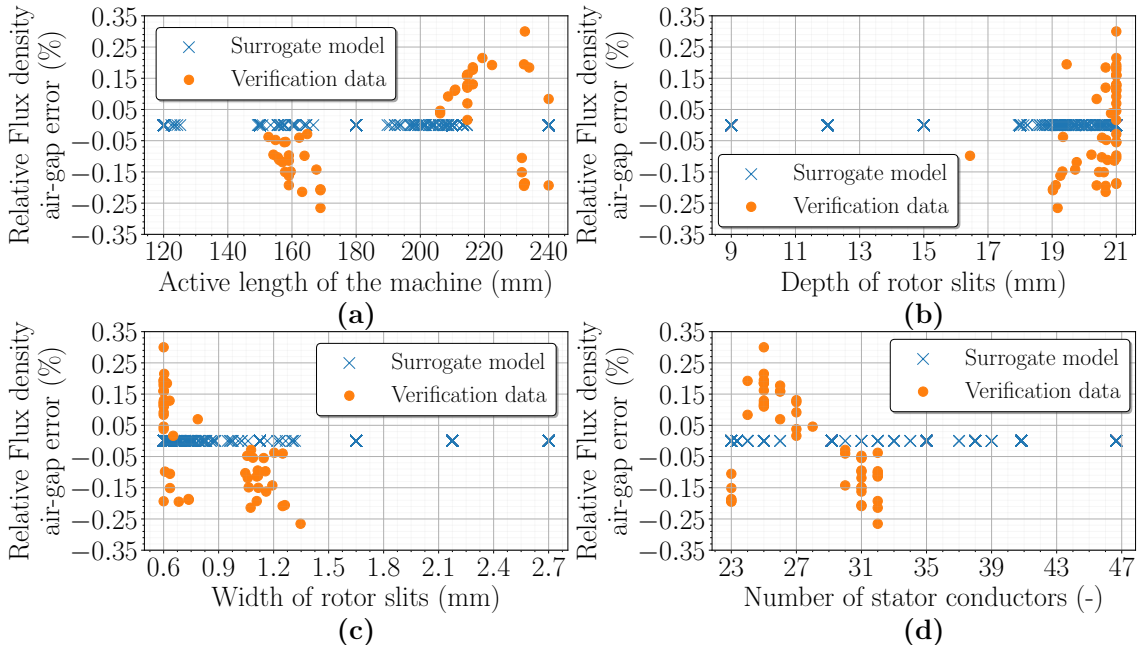


Fig. G5: Dependence of the relative flux density in the air-gap error of surrogate models on the input parameter size: Active length of the machine (a), Rotor slit depth (b), Rotor slit width (c), and Number of stator conductors (d), considering the highest possible electromagnetic efficiency of the machine from the second optimization.

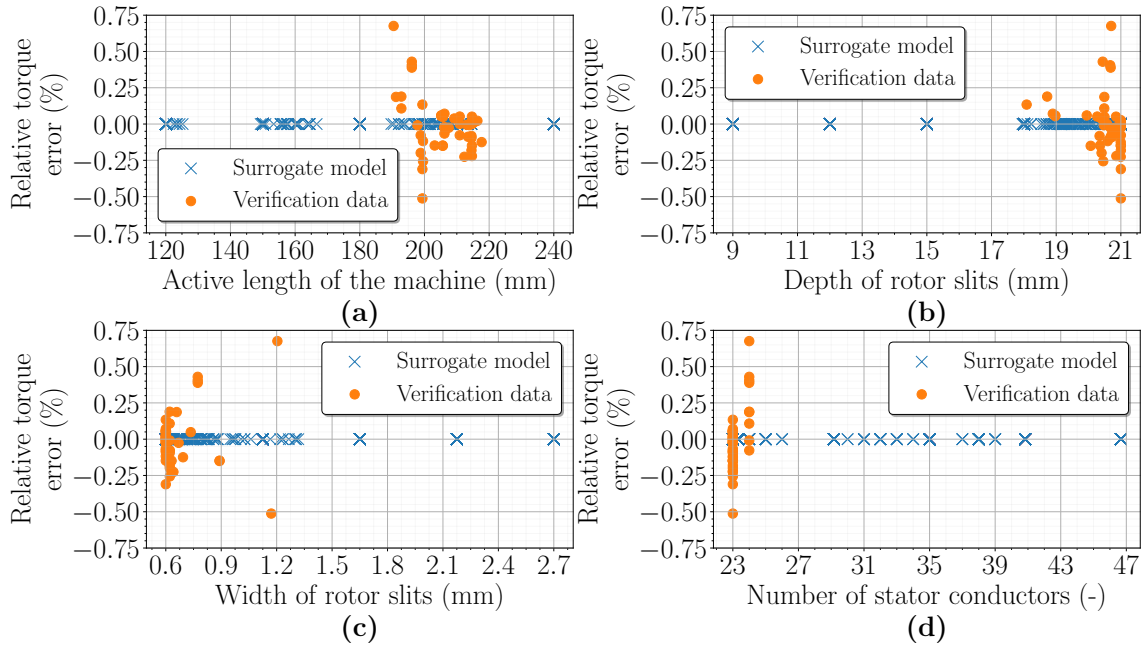


Fig. G6: Dependence of the relative torque error of surrogate models on the input parameter size: Active length of the machine (a), Rotor slit depth (b), Rotor slit width (c), and Number of stator conductors (d), considering the highest possible torque of the machine from the second optimization.

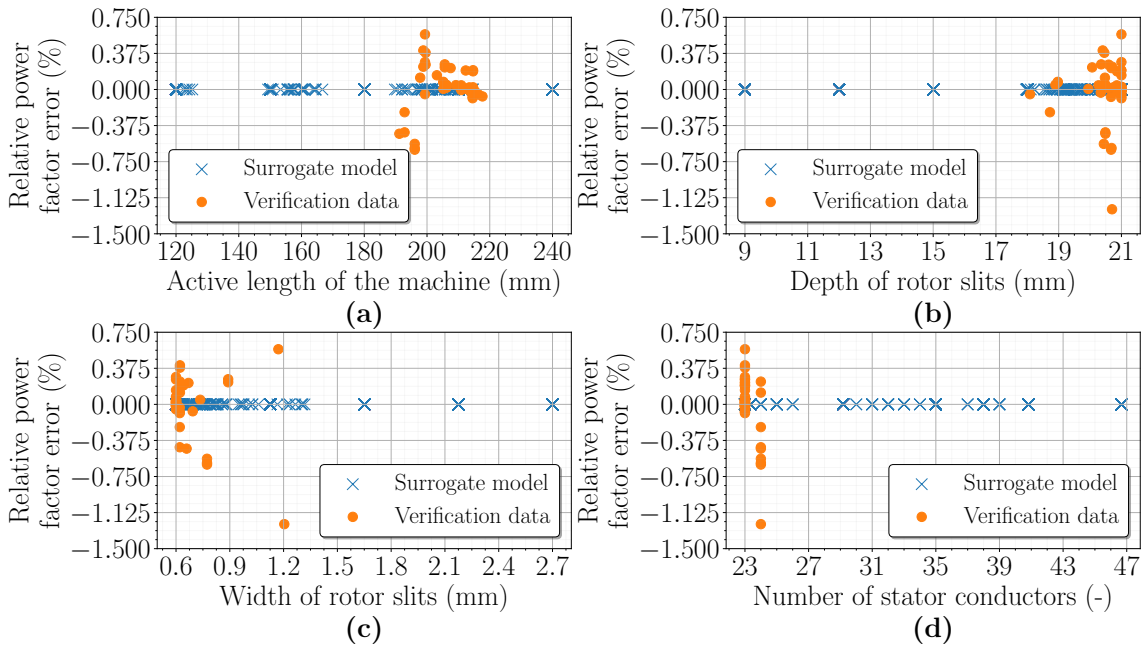


Fig. G7: Dependence of the relative power factor error of surrogate models on the input parameter size: Active length of the machine (a), Rotor slit depth (b), Rotor slit width (c), and Number of stator conductors (d), considering the highest possible torque of the machine from the second optimization.

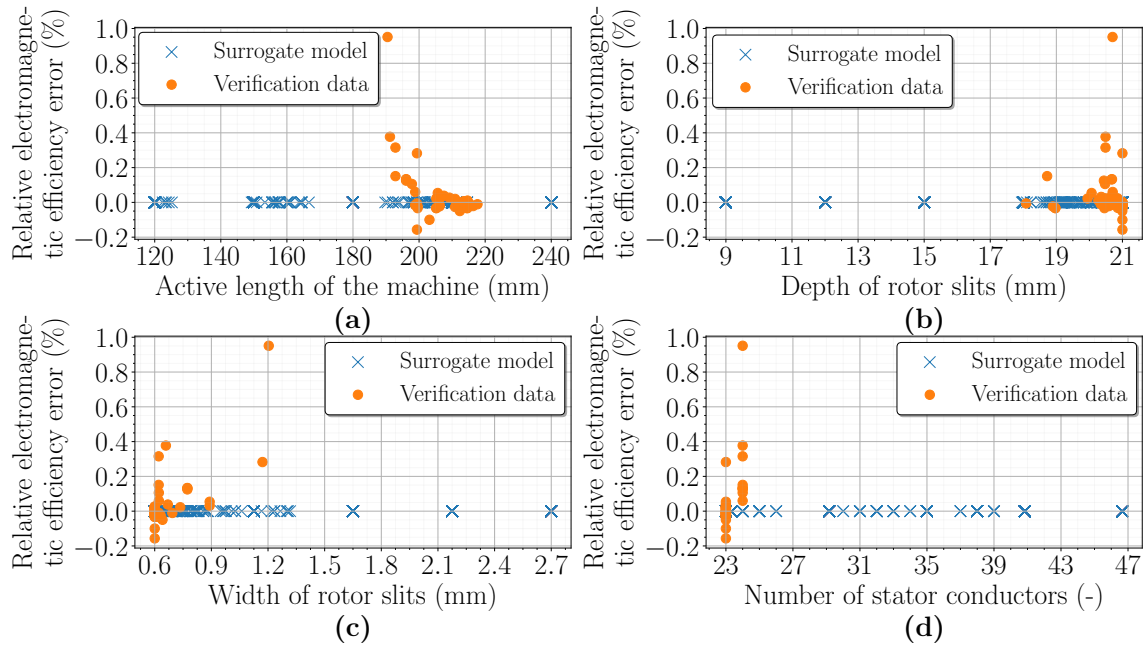


Fig. G8: Dependence of the relative electromagnetic efficiency error of surrogate models on the input parameter size: Active length of the machine (a), Rotor slit depth (b), Rotor slit width (c), and Number of stator conductors (d), considering the highest possible torque of the machine from the second optimization.

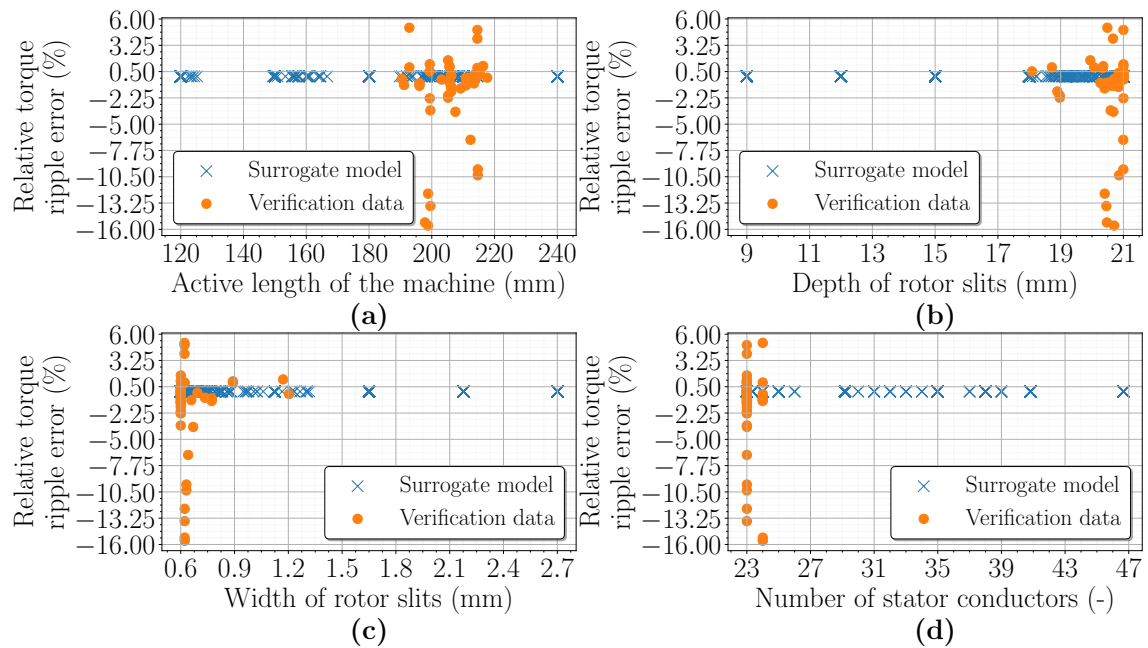


Fig. G9: Dependence of the relative torque ripple error of surrogate models on the input parameter size: Active length of the machine (a), Rotor slit depth (b), Rotor slit width (c), and Number of stator conductors (d), considering the highest possible torque of the machine from the second optimization.

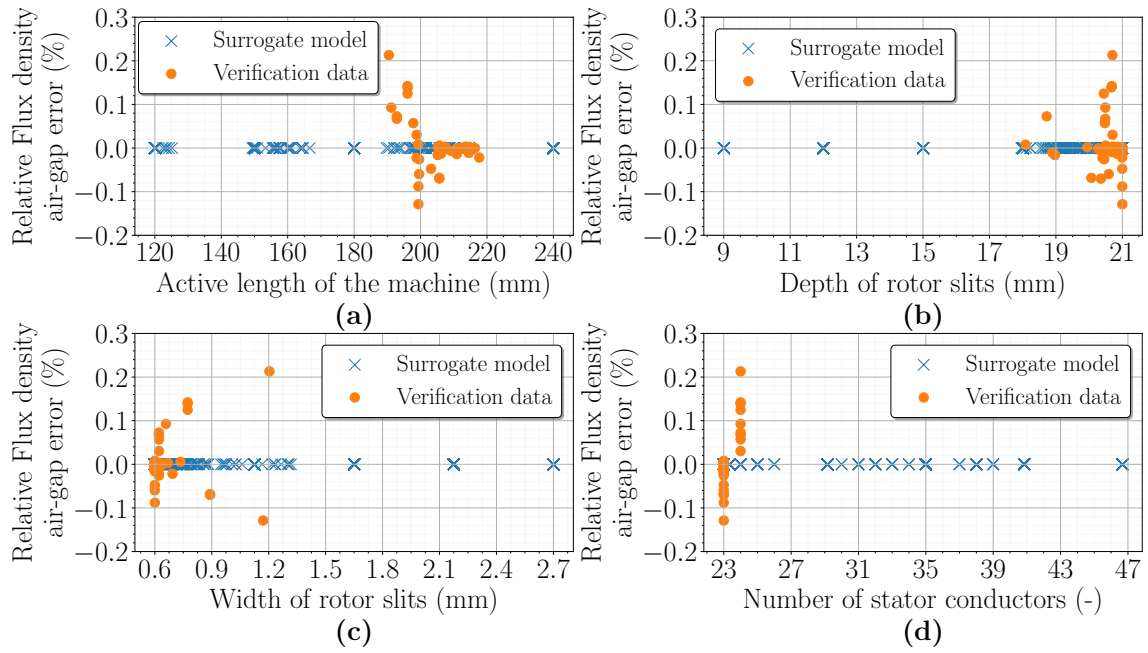


Fig. G10: Dependence of the relative flux density in the air-gap error of surrogate models on the input parameter size: Active length of the machine (a), Rotor slit depth (b), Rotor slit width (c), and Number of stator conductors (d), considering the highest possible torque of the machine from the second optimization.

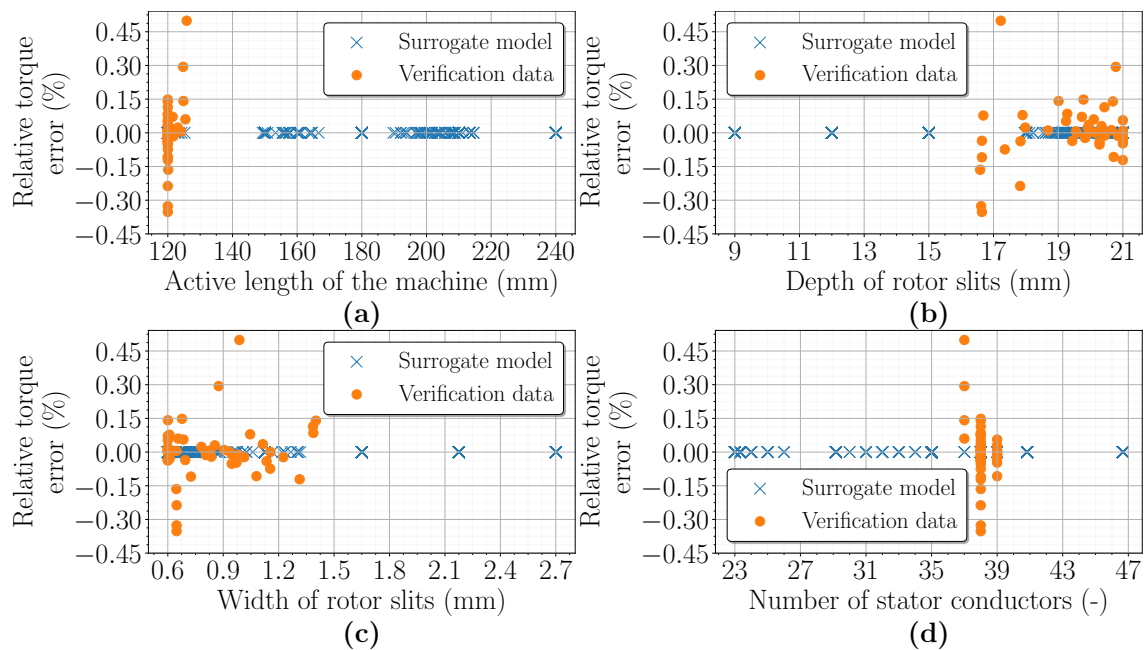


Fig. G11: Dependence of the relative torque error of surrogate models on the input parameter size: Active length of the machine (a), Rotor slit depth (b), Rotor slit width (c), and Number of stator conductors (d), considering the lowest price of the machine with respect to the highest torque of the machine from the second optimization.

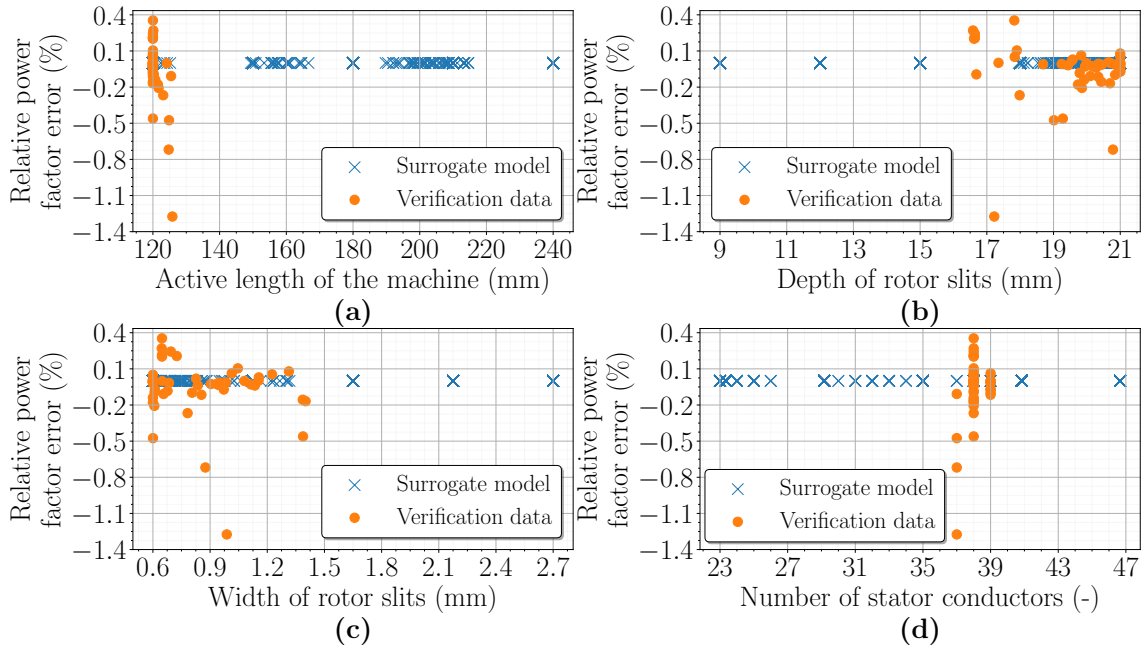


Fig. G12: Dependence of the relative power factor error of surrogate models on the input parameter size: Active length of the machine (a), Rotor slit depth (b), Rotor slit width (c), and Number of stator conductors (d), considering the lowest price of the machine with respect to the highest torque of the machine from the second optimization.

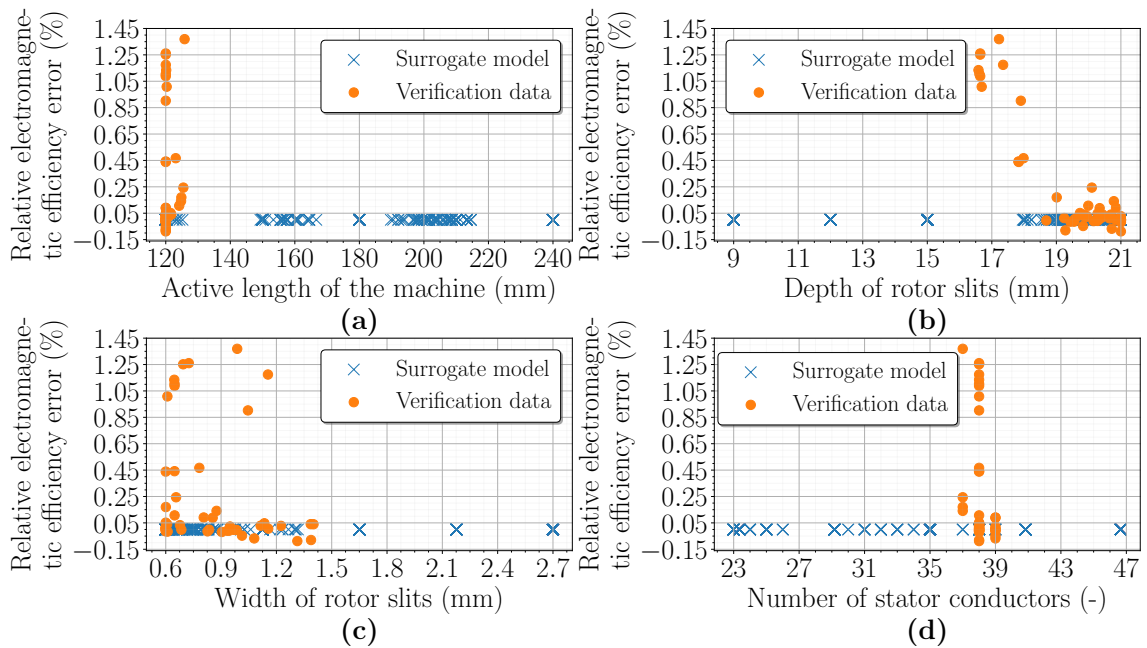


Fig. G13: Dependence of the relative efficiency error of surrogate models on the input parameter size: Active length of the machine (a), Rotor slit depth (b), Rotor slit width (c), and Number of stator conductors (d), considering the lowest price of the machine with respect to the highest torque of the machine from the second optimization.

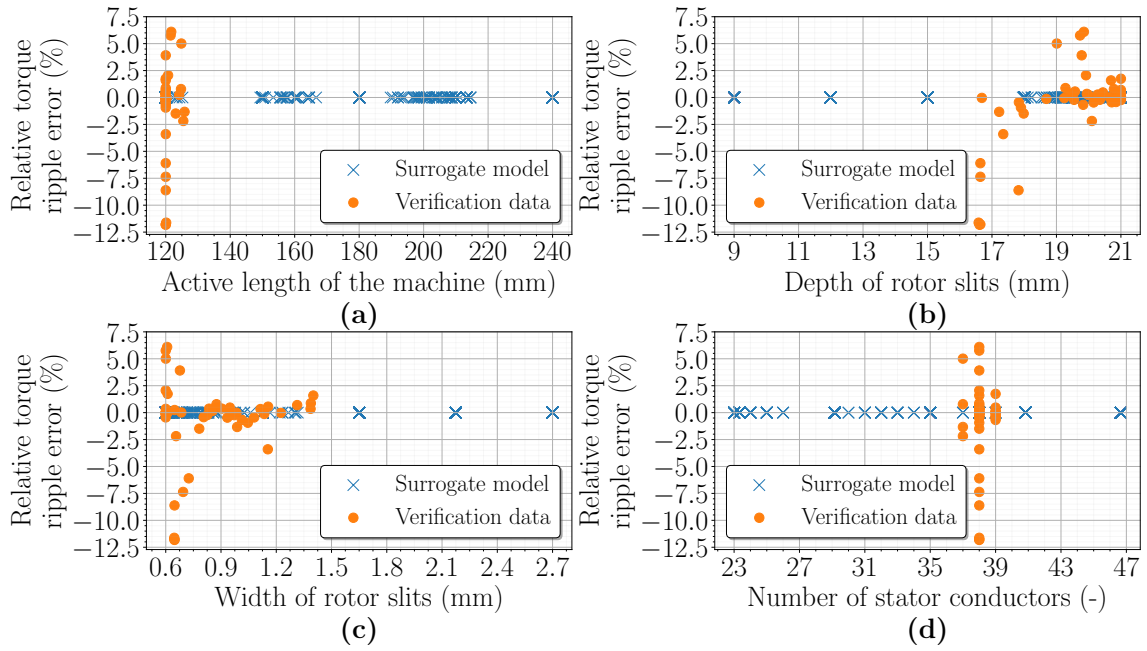


Fig. G14: Dependence of the relative torque ripple error of surrogate models on the input parameter size: Active length of the machine (a), Rotor slit depth (b), Rotor slit width (c), and Number of stator conductors (d), considering the lowest price of the machine with respect to the highest torque of the machine from the second optimization.

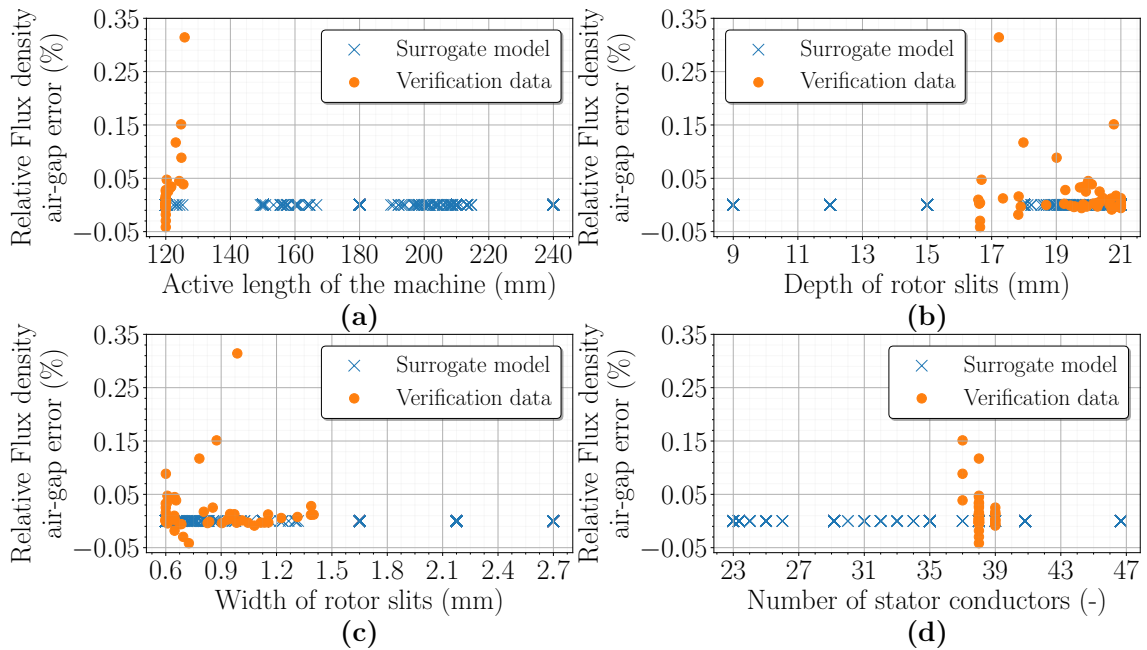


Fig. G15: Dependence of the relative flux density in the air-gap error of surrogate models on the input parameter size: Active length of the machine (a), Rotor slit depth (b), Rotor slit width (c), and Number of stator conductors (d), considering the lowest price of the machine with respect to the highest torque of the machine from the second optimization.